

**H₂ ADSORPTION AND DIRECT METHANE CONVERSION TO
METHANOL ON Cu-EXCHANGED ZEOLITES**

by

Bahar Ipek

A dissertation submitted to the Faculty of the University of Delaware in partial fulfillment of the requirements for the degree of Doctor of Philosophy in Chemical Engineering

Summer 2016

© 2016 Bahar Ipek
All Rights Reserved

ProQuest Number: 10191783

All rights reserved

INFORMATION TO ALL USERS

The quality of this reproduction is dependent upon the quality of the copy submitted.

In the unlikely event that the author did not send a complete manuscript and there are missing pages, these will be noted. Also, if material had to be removed, a note will indicate the deletion.



ProQuest 10191783

Published by ProQuest LLC (2016). Copyright of the Dissertation is held by the Author.

All rights reserved.

This work is protected against unauthorized copying under Title 17, United States Code
Microform Edition © ProQuest LLC.

ProQuest LLC.
789 East Eisenhower Parkway
P.O. Box 1346
Ann Arbor, MI 48106 - 1346

**H₂ ADSORPTION AND DIRECT METHANE CONVERSION TO
METHANOL ON Cu-EXCHANGED ZEOLITES**

by

Bahar Ipek

Approved: _____
Abraham M Lenhoff, Ph.D.
Chair of the Department of Chemical and Biomolecular Engineering

Approved: _____
Babatunde A. Ogunnaike, Ph.D.
Dean of the College of Engineering

Approved: _____
Ann L. Ardis, Ph.D.
Senior Vice Provost for Graduate and Professional Education

I certify that I have read this dissertation and that in my opinion it meets the academic and professional standard required by the University as a dissertation for the degree of Doctor of Philosophy.

Signed:

Raul F. Lobo, Ph.D.
Professor in charge of dissertation

I certify that I have read this dissertation and that in my opinion it meets the academic and professional standard required by the University as a dissertation for the degree of Doctor of Philosophy.

Signed:

Dionisios G. Vlachos, Ph.D.
Member of dissertation committee

I certify that I have read this dissertation and that in my opinion it meets the academic and professional standard required by the University as a dissertation for the degree of Doctor of Philosophy.

Signed:

Yushan Yan, Ph.D.
Member of dissertation committee

I certify that I have read this dissertation and that in my opinion it meets the academic and professional standard required by the University as a dissertation for the degree of Doctor of Philosophy.

Signed:

Craig M. Brown, Ph.D.
Member of dissertation committee

ACKNOWLEDGMENTS

I would first like to thank my supervisor Prof. Dr. Raul F. Lobo for giving an opportunity to do my Ph.D. in his group, for his profound scientific guidance throughout the years, and for his endless scientific support and patience. I am grateful to him for setting a great example for being a fair and professional supervisor and a manager. The numerous conferences, to which I attended by his support added me valuable insight and brought many fruitful discussions and collaborations.

I would like to thank Prof. Dr. Craig M. Brown from National Institute of Standards and Technology Center for Neutron Research, Maryland for his supervision during a valuable period. I am grateful to him for all neutron diffraction and scattering and data analysis methods I learned throughout my Ph.D. study. His perfectionist approach in science, work dedication, and science integrity are the most valued inspirations for me for a lifetime.

I would also like to thank Dr. Rachel A. Pollock and Dr. Matthew R. Hudson for their help in sample preparation and powder diffraction experiments reported in Chapter 2 and Chapter 4. Their help in teaching GSAS are also mostly appreciated.

I would like to thank other members of my defense committee: Prof. Dr. Dionisios G. Vlachos and Prof. Dr. Yushan Yan for spending time on reviewing my thesis and offering valuable comments.

I would like to acknowledge our collaborators at University of Turin —Prof. Silvia Bordiga, Dr. Filippo Giordanino for IR measurements with H₂ adsorption reported in Chapter 2, at University of Wisconsin-Madison —Dr. Florian Goeltl for

theoretical calculations provided in Chapter 4, at Chemical Sciences and Engineering Division, Argonne National Laboratory —Dr. Hacksung Kim for *in situ* Raman measurements reported in Chapter 4, at Department of Chemistry and Biochemistry, University of Delaware —Joseph P. Smith and Prof. Kral S. Booksh for Raman measurements reported in Chapter 4.

The work described in this thesis has been supported by cooperative agreement 70NANB10H256 from NIST, U.S. Department of Commerce. I would like to acknowledge the financial support provided by the Department of Commerce.

My special thanks to Dr. Matthew J. Wulfers and Dr. Shewangizaw Teketel, who started the project of direct methane conversion to methanol using Cu- exchanged small-pore zeolites. The 3-step experiments reported in Chapter 3 are performed by Dr. Shewangizaw Teketel. Dr. Matthew J. Wulfers has spent a valuable time for planning the spectroscopic measurements provided in Chapter 3 and 4. I appreciate all the time and effort he spent on discussions for that project with me. His enthusiasm in research is a value to be greatly acknowledged and to be inspired by.

I would also like to thank Dr. Guangjin Hou from Department of Chemistry and Biochemistry for MAS NMR measurements, Dr. Frank Kriss for SEM training, Gerald Poirer for his help with XRD and Dr. Trong D. Pham for supplying different zeolite samples and synthesis procedures. He will be a memorable colleague with his friendly and lively personality.

I would like to express my gratitude to other existing and previous group members: Maura Koehle, Huibo Sheng, Edward Schreiner, Trishelle Copland-Johnson, Dr. Jason Loiland, Dr. Jang Ho Yun, Dr. Jelvehnaz Mirzababei, Dr. Erisa Saraci, Dr. Efterpi Vasileiadou, Dr. Andrew Foster, Dr. Qingling Liu, Eyas Mahmoud,

Chen-Yu Chou, Dr. Ali Mehdad, Dr. Young Jin Kim for all the support and social time we spent together. Molly, I am grateful for your great company and nice conversations for all the time I spent in Newark as well as in conferences we have been together. Dr. Marta Lean Garcia, I am more than thankful to share an office and each other's company almost three years with you.

Many thanks to technical support team George Whitmyre, Gary Wellmaker, Alan Price, Neilsen Garrett, and to Kathleen Young, Rechilda Alba and Mary Walsh for their administrative support.

Last but not the least; I would like to thank my family; my sister Pinar, my father Ata and my mother Emel, who always supported me realizing my goals and checked on me every day from 5000 miles away, and even coming here for supporting me each time I needed. I cannot imagine a life without you.

And to Murat Torun, who was always at the end of the phone to keep me calm and to keep me going on for the last 5 years. He now knows every detail of SSZ-13 and zeolites, all difficulties in science community and so on. I cherished every day with you or 5000 miles away from you for the last 9 years. I wish to continue to be in each other's heart for a lifetime.

Finally I wish to thank everyone who believed in me on this path I started to become an inspiring professor, to raise curious minds that would be always eager to learn, and to serve to the human society. I hope our efforts in research would help create an equal and sustainable world for everyone, where the greed for oil and power is annihilated.

TABLE OF CONTENTS

LIST OF TABLES	xii
LIST OF FIGURES	xvi
ABSTRACT	xxiv

Chapter

1	INTRODUCTION	1
1.1	Zeolites	2
1.1.1	Zeolites: Definition.....	2
1.1.2	Zeolites: Improved Properties	2
1.1.3	Zeolites: Applications.....	5
1.2	Cu exchanged Zeolites and Applications	7
1.2.1	Catalytic Applications	7
1.2.2	Direct Methane Conversion to Methanol	9
1.2.3	H ₂ Adsorption.....	18
1.3	Cu-SSZ-13: Structural Background	20
1.4	Scope of the Thesis.....	25
2	H ₂ ADSORPTION ON Cu(I) EXCHANGED –SSZ-13	27
2.1	Introduction	27
2.2	Experimental.....	28
2.2.1	Zeolite Synthesis and Ion Exchange.....	28
2.2.1.1	NH ₄ ⁺ Exchange.....	30
2.2.1.2	Na ⁺ Exchange	30
2.2.1.3	Solid State Cu(I)Cl Exchange	31
2.2.1.4	Liquid Phase Cu(I) Exchange.....	33
2.2.2	Analytical Methods	34
2.2.3	Hydrogen Adsorption Experiments.....	35

2.2.4	<i>In situ</i> FTIR Experiments	37
2.2.5	Diffuse Reflectance Infrared Fourier Transform Spectroscopy ..	38
2.2.6	Powder Neutron Diffraction (PND) Experiments	38
2.3	Results and Discussion	39
2.3.1	Material Characterization	39
2.3.2	H ₂ Adsorption Isotherms	43
2.3.3	<i>In situ</i> FTIR Experiments	50
2.3.4	Powder Neutron Diffraction (PND) Experiments	56
2.3.5	Liquid Phase Cu(I) Exchange.....	60
2.4	Conclusion.....	64
3	DIRECT METHANE CONVERSION TO METHANOL ON Cu- EXCHANGED SMALL-PORE ZEOLITES	66
3.1	Introduction	66
3.2	Experimental.....	68
3.2.1	Zeolite Synthesis and Ion Exchange.....	68
3.2.1.1	Na ⁺ Exchange	70
3.2.1.2	Cu(II) Exchange	71
3.2.2	Analytical Methods	72
3.2.3	Methane Conversion Reactions.....	73
3.2.4	Diffuse Reflectance UV–vis Spectroscopy	75
3.2.5	Raman Spectroscopy	76
3.3	Results and Discussion	76
3.3.1	Material Characterization	76
3.3.2	Methanol Formation	78
3.3.3	UV–vis Spectroscopy	81
3.3.4	Raman Spectroscopy	87
3.4	Conclusion.....	93
4	Cu _x O _y CLUSTERS ON Cu-SSZ-13 AND Cu-SSZ-39	95
4.1	Introduction	95
4.2	Methods	96
4.2.1	Zeolite Synthesis and Ion Exchange.....	96

4.2.1.1	Cu(II) exchange	96
4.2.2	Analytical Methods	98
4.2.3	Synchrotron Powder X-ray Diffraction Experiments	98
4.2.4	Diffuse Reflectance UV–vis Spectroscopy	99
4.2.5	<i>In situ</i> Raman Spectroscopy of H-Cu-SSZ-13	100
4.2.6	Raman Spectroscopy of Na-Cu-SSZ-13 and Na-Cu-SSZ-39....	101
4.2.7	Methane Conversion.....	102
4.3	Results and Discussion	103
4.3.1	Material Characterization	103
4.3.2	Synchrotron Powder X-ray Diffraction Experiments	104
4.3.3	Diffuse Reflectance UV–vis Spectroscopy	110
4.3.4	<i>In situ</i> Raman Spectroscopy of H-Cu-SSZ-13	116
4.3.5	Theoretical Calculations	119
4.3.6	Effect of He Activation	124
4.3.7	Precursor for Cu ₂ O ₂ and Cu ₂ O species on Cu-SSZ-13	128
4.3.8	Dehydration Mechanisms and O ₂ Free Route to Cu ₂ O ₂ and Cu ₂ O species.....	130
4.3.9	Reactivity of Cu ₂ O ₂ species.....	136
4.4	Conclusion.....	137
5	CATALYTIC METHANOL FORMATION ON Cu-SSZ-13	139
5.1	Introduction	139
5.2	Experimental.....	141
5.2.1	Zeolite Synthesis and Ion Exchange.....	141
5.2.2	Methane Conversion Experiments	142
5.2.2.1	Equipment.....	142
5.2.2.2	3-Step Cyclic Procedure	142
5.2.2.3	Catalysis Experiments	143
5.2.3	Diffuse Reflectance UV–vis Spectroscopy	143
5.3	Results and Discussion	144
5.3.1	Material Characterization	144
5.3.2	3-step Cyclic Methanol Production: Effect of N ₂ O.....	146
5.3.3	Catalytic Methanol Production.....	147
5.3.4	Diffuse Reflectance UV–vis Spectroscopy	155

5.4	Conclusion.....	158
6	SUMMARY AND OUTLOOK	160
6.1	Summary.....	160
6.2	Outlook.....	165
	REFERENCES	169
Appendix		
A	H ₂ ADSORPTION ON Cu(I)- EXCHANGED SAMPLES	185
A.1	Isosteric Heat of Adsorption Calculations for Cu(I)-exchanged samples	185
A.1.1	Cu(I)-SSZ-13 (Si/Al = 6) Sample.....	185
A.1.2	Cu(I)-[B]-SSZ-13 Sample	188
A.2	Fitting of H ₂ Adsorption Isotherms at -196 °C.....	190
A.3	Powder Neutron Diffraction (PND) Experiments	191
A.4	XRD Analysis of Cu(I)-SSZ-13 (Si/Al = 12) Sample.....	194
B	Cu(II) EXCHANGED SAMPLES FOR METHANOL FORMATION	195
B.1	Cu(II) Acetate Concentration Calibration for UV–vis Spectroscopy....	195
B.2	Methanol Formation on Cu(II)- exchanged Zeolites.....	196
C	Cu _x O _y CHARACTERIZATION ON Cu-SSZ-13 AND Cu-SSZ-39.....	199
C.1	Synchrotron Powder X-ray Diffraction of Cu-SSZ-13	199
C.2	MAS NMR Spectra	205
C.3	DR UV–vis Spectroscopy.....	209
D	CATALYTIC METHANOL SYNTHESIS ON Cu-SSZ-13	211
D.1	CH ₃ OH, CO and CO ₂ Calibrations.....	211
D.1.1	CH ₃ OH calibration of GC FID chromatogram.....	211
D.1.2	CO calibration of GC TCD chromatogram	212
D.1.3	CO ₂ calibration of GC TCD chromatogram	213
D.1.4	CO calibration using Mass Spectrometer	214
D.2	N ₂ O Treatment of Cu-SSZ-13	215
D.3	Catalytic Tests	217

D.4	DR UV-vis Spectra After CH ₄ Treatment Cu-SSZ-13	222
E	PERMISSIONS	223

LIST OF TABLES

Table 1.1:	Catalytic reactions involving Cu- exchanged zeolites.	8
Table 1.2:	Methanol and formaldehyde selectivity and yield values for gas phase CH ₄ partial oxidation in absence or presence of a catalyst	12
Table 1.3:	Direct methanol production amounts observed on different Cu- exchanged zeolites and 3-step procedures.....	16
Table 1.4:	Zeolite structures and pore systems.....	22
Table 2.1:	Refined rhombohedral unit cell parameters (<i>R3m</i>) for prepared Na- and Cu(I)-SSZ-13 zeolites using CelRef Unit-Cell refinement software ¹⁶⁸	41
Table 2.2:	t-plot micropore volumes and chemical compositions of prepared Na- and Cu(I)- samples obtained from ICP-OES and EDX.....	43
Table 2.3:	Total and excess hydrogen adsorption amounts per gram of adsorbent and per cm ³ of pore volume at the equilibrium pressure of 1 atm and temperature of 30 °C	46
Table 2.4:	Bond distances and T–O–T angles obtained via Rietveld Refinement of PND data of bare Cu(I)-SSZ-13 (Si/Al = 6, Cu ₅ Al _{5.14} Si _{30.86} O ₇₂) at - 263 °C (10 K) and 27 °C (300 K),and PND data obtained at -263 °C with D ₂ loading at 27 °C (300 K), <i>R3m</i>	58
Table 2.5:	Chemical composition of Cu(I)-SSZ-13 (Si/Al = 12) prepared by exchanging Cu(I) in acetonitrile, composition obtained by ICP-OES and EDX analysis	61
Table 3.1:	Quantity of materials used in copper (II) ion exchanges and the resulting Cu/Al ratios determined by the UV–vis	72
Table 3.2:	Elemental compositions of the Cu-exchanged samples determined by UV–vis [†] and ICP	78
Table 3.3:	Methanol production amounts on Cu(II)- exchanged samples.	79

Table 3.4:	$d \leftarrow d$ transitions of copper (II) ions in Cu-exchanged zeolites.....	84
Table 3.5:	Experimentally observed Raman vibrations on Cu- exchanged zeolites following O ₂ treatment at 450 °C for 2 h	93
Table 4.1:	Quantity of materials used in copper (II) ion exchanges and the resulting Cu/Al ratios determined by UV–vis	97
Table 4.2:	Elemental analysis of copper(II) acetate-exchanged samples calculated from UV–vis and from ICP-OES. t-plot micropore volumes of H ⁺ -form and Cu(II) exchanged samples are measured with N ₂ adsorption at -196 °C.....	104
Table 4.3:	Cu distribution and bond distances obtained by Rietveld analysis of PXRD data of H _{0.3} Cu _{1.2} Al _{2.7} Si _{33.3} O ₇₂ and H _{1.2} Cu _{2.4} Al ₆ Si ₃₀ O ₇₂ (APS, 17-BM-B, $\lambda = 0.75009 \text{ \AA}$, Trigonal, R-3m) [†]	106
Table 4.4:	Mononuclear and binuclear Cu _x O _y complexes mentioned in the literature and in this work and their spectroscopic features	118
Table 4.5:	Amount of methanol produced by Na-Cu-SSZ-13 (Si/Al = 12, Cu/Al = 0.47) and Na-Cu-SSZ-39 (Si/Al = 10, Cu/Al = 0.48) using O ₂ or He treatments (Experimental details are given in section 4.2.7)	128
Table 5.1:	Elemental analysis of copper(II)acetate exchanged samples [†]	145
Table 5.2:	Methanol production on Cu-SSZ-13 (Si/Al = 12) using N ₂ O or O ₂ as oxidant [†]	147
Table 5.3:	Catalytic CH ₃ OH and CO _x production rates and selectivity values ^a	148
Table A.1:	Toth Adsorption Isotherm Model ($q = q_{max} KP1 + KP1t$) parameters found by fitting Cu(I)-SSZ-13 (Si/Al = 6) hydrogen adsorption isotherm data at a temperature range of 20 °C and 40 °C ...	186
Table A.2:	Sips Model fitting $q = q_{max}(K * P)^{n1} + K * Pn$, for pressure region: 0–0.2 atm R ² :0.9955, 0.9988, 0.9944.....	189
Table A.3:	Linear Model fitting $q = aP + b$ for pressure region: 0.2-1atm, R ² :0.9997, 0.9997, 0.9997	189
Table A.4:	Henry's constant ($q_{max} * K$ - mmol H ₂ g ⁻¹ atm ⁻¹) and other equation parameters found by fitting hydrogen adsorption isotherm data to Toth Model ($q = q_{max} KP1 + KP1/t$)	190

Table A.5:	Atomic Parameters from Rietveld refinement of Cu(I)-SSZ-13 (Si/Al = 6, Cu ₅ Al _{5.14} Si _{30.86} O ₇₂) PND data at -263 °C (10 K) [NCNR, BT-1](Trigonal, R-3m, Goodness of fit parameters $\chi^2 = 1.092$, R _p = 4.57%, wR _p = 5.58%, $\lambda = 2.0787(2)$ Å, a = 13.6192(5) Å, c = 15.0540(8) Å, V = 2418.2(1) Å ³	191
Table A.6:	Atomic Parameters from Rietveld refinement of Cu(I)-SSZ-13 (Si/Al = 6, Cu ₅ Al _{5.14} Si _{30.86} O ₇₂) PND data at 27 °C (300 K) [NCNR, BT-1](Trigonal, R-3m, Goodness of fit parameters $\chi^2 = 0.9949$, R _p = 4.58%, wR _p = 5.56%, $\lambda = 2.0787(2)$ Å, a = 13.6054(5) Å, c = 15.0170(9) Å, V = 2407.3(2) Å ³	192
Table A.7:	Atomic Parameters from Rietveld refinement of Cu(I)-SSZ-13 (Si/Al = 6, Cu ₅ Al _{5.14} Si _{30.86} O ₇₂) PND data obtained at -263 °C (10 K) with D ₂ loading at 27 °C (300 K) [NCNR, BT-1](Trigonal, R-3m, Goodness of fit parameters $\chi^2 = 1.065$, R _p = 4.33%, wR _p = 5.41%, $\lambda = 2.0787(2)$ Å, a = 13.6230(5) Å, c = 15.0347(98) Å, V = 2416.4(2) Å ³	193
Table C.1:	Atomic Parameters from Rietveld refinement of H-Cu-SSZ-13 (Si/Al = 12, Cu/Al = 0.4) data [APS, 17-BM-B](Trigonal, R-3m, Goodness of fit parameters $\chi^2 = 8.099$, R _p = 1.68%, wR _p = 2.24% at 30 °C, $\lambda = 0.75009$ Å, a = 13.5805(1) Å, c = 14.6748(2) Å, V = 2343.89(4) Å ³ ...	199
Table C.2:	Atomic Parameters from Rietveld refinement of H-Cu-SSZ-13 (Si/Al = 12, Cu/Al 0.4, H _{0.3} Cu _{1.2} Al _{2.7} Si _{33.3} O ₇₂) data [APS, 17-BM-B](Trigonal, R-3m, Goodness of fit parameters $\chi^2 = 2.610$, R _p = 1.51%, wR _p = 1.99% at 50 °C, $\lambda = 0.75009$ Å, a = 13.5494(2) Å, c = 14.7720(2) Å, V = 2348.59(8) Å ³	203
Table C.3:	Atomic Parameters from Rietveld refinement of Cu-SSZ-13 (Si/Al = 5, Cu/Al = 0.39, H _{1.2} Cu _{2.4} Al ₆ Si ₃₀ O ₇₂) data [APS, 17-BM-B] (Trigonal, R-3m, Goodness of fit parameters $\chi^2 = 4.211$, R _p = 2.52%, wR _p = 3.59% at 50 °C, $\lambda = 0.75009$ Å, a = 13.4932(5) Å, c = 15.1027(7) Å, V = 2381.3(2) Å ³	204
Table D.1:	Concentrations of methanol in 10 ml toluene solutions and corresponding peak areas obtained at 1.87 min residence time using HP-PLOT Q column.....	211
Table D.2:	Concentrations of CO ₂ and corresponding peak areas obtained at 3.564 min residence time using HayeSep Q column.....	213
Table D.3:	Loaded catalyst weights for catalytic methanol production ^a	218

Table D.4: Effect of methane partial pressure on methane conversion (TOF: mol _{CH₄ converted} mol _{Cu} ⁻¹ h ⁻¹) and methanol production rates at 270 °C on Cu-SSZ-13 (Cu concentration : 0.50 mmol Cu g ⁻¹), feed gas composition: 20– 50% CH ₄ , 30% N ₂ O, 3% H ₂ O, balance He; flow rate: 120 cm ³ min ⁻¹	221
Table D.5: Effect of N ₂ O partial pressure on methane conversion (TOF: mol _{CH₄ converted} mol _{Cu} ⁻¹ h ⁻¹) and methanol production rates at 270 °C on Cu-SSZ-13 (Cu concentration : 0.50 mmol Cu g ⁻¹), feed gas composition: 30% CH ₄ , 3–30% N ₂ O, 3% H ₂ O, balance He; flow rate: 120 cm ³ min ⁻¹	221

LIST OF FIGURES

Figure 1.1:	Schematic representation of extra-framework cation sites in aluminosilicates. M^+ represents a proton (H^+) or a monovalent cation (Na^+ , Li^+ , K^+ , etc.)	5
Figure 1.2:	Conventional methanol production from synthesis gas route	10
Figure 1.3:	Schematic representation of CHA framework and building units. Yellow tetrahedral corners represent Si/Al atoms and red represent shared oxygen atoms.	21
Figure 1.4:	Possible Cu(II) sites on 6MR with two Al sites, reproduced from Godiksen et al. ¹⁴²	25
Figure 2.1:	a) Solid State CuCl exchange set-up b) Schematic representation of the quartz reactor	33
Figure 2.2:	Powder XRD pattern of Na-SSZ-13 (Si/Al=6 & 12), Cu-SSZ-13 (Si/Al=6 & 12) and Cu-[B]-SSZ-13 samples, Cu $K\alpha$, $\lambda = 1.5418 \text{ \AA}$	41
Figure 2.3:	Hydrogen adsorption isotherms for Na- and Cu(I)-samples at 30 °C. Sample names are given in M-SSZ-13/xx format, where M represents the cation type and xx represents the Si/Al ratio.....	45
Figure 2.4:	Hydrogen adsorption isotherms for Na- and Cu(I)-samples at -196 °C. Sample names are given in M-SSZ-13/xx format, where M represents the cation type and xx represents the Si/Al ratio.....	47
Figure 2.5:	Calculated isosteric heat of adsorption versus adsorbed hydrogen amounts on Cu(I)-SSZ-13 (Si/Al = 6) for the temperature range between 20 °C and 40 °C	48
Figure 2.6:	Calculated isosteric heat of adsorption versus adsorbed hydrogen amounts on Cu(I)-[B]-SSZ-13 for the temperature range between 30 °C and 50 °C.....	49

Figure 2.7:	IR spectra in the OH region for samples Cu-SSZ-13 (Si/Al = 12, Cu/Al = 0.44, copper (II) acetate exchanged), Cu(I)-SSZ-13 (Si/Al = 12, Cu/Al = 0.98, CuCl exchanged) and Na-SSZ-13 (Si/Al = 12, Na/Al = 0.76) denoted as H-Cu-SSZ-13, Cu-SSZ-13 and Na-SSZ-13 respectively. The bands indicated by letters are; a & a*: external and internal silanol groups, b & c: hydroxyl groups of extra-framework aluminum, d & e: high frequency and low frequency Brønsted acid sites, f: highly defective silanol nests.....	51
Figure 2.8:	IR spectra of Cu(I)-SSZ-13 (Si/Al = 12, Cu/Al = 0.98) in equilibrium with 40 mbar H ₂ at decreasing temperature from -23 °C (250 K) to -173 °C (100 K), sample was pre-treated <i>in vacuo</i> at 500 °C for 3 h.....	52
Figure 2.9:	IR spectra of Cu(I)-SSZ-13 (Si/Al = 12, Cu/Al = 0.98) in equilibrium with 40 mbar H ₂ at decreasing temperature from -173 °C (100 K) to -258 °C (15 K). a. OH region b. H-H region. Sample was pre-treated <i>in vacuo</i> at 500 °C for 3 h.....	54
Figure 2.10:	IR spectra of Na-SSZ-13 (Si/Al = 12, Na/Al = 0.76) in equilibrium with 40 mbar H ₂ at decreasing temperature from -173 °C (100 K) to -258 °C (15 K). a: OH region, b: HH region. Sample was pre-treated <i>in vacuo</i> at 500 °C for 3 h.....	55
Figure 2.11:	Representation of Cu(I)-SSZ-13 (Si/Al = 6) with two copper position: Cu1 at Site II and Cu2 at Site III'	57
Figure 2.12:	DRIFT spectra of Cu(I)-SSZ-13 (Si/Al = 12) sample prepared by Cu(I) exchange in acetonitrile as temperature was increased from 25 °C (black, hydrated sample) to 450 °C (green, dehydrated sample)	62
Figure 2.13:	DRIFT spectra of Cu(I)-SSZ-13 (Si/Al = 12) sample prepared by Cu(I) exchange in acetonitrile and oxidized at 350 °C for 4 h. The spectra was taken as temperature was increased from 25 °C (black, hydrated sample) to 450 °C (green, dehydrated sample)	64
Figure 3.1:	Temperature profile and gas flow rates used for conversion of methane to methanol on Cu(II) ion-exchanged samples	74
Figure 3.2:	Powder XRD pattern of Cu-SSZ-13 (Si/Al = 12), Cu-SSZ-39 (Si/Al = 10), Cu-SSZ-16 (Si/Al = 6.5) Cu-mordenite, and Cu-ZSM-5 samples, Cu K α , λ = 1.5418 Å	77

Figure 3.3:	Diffuse reflectance UV–vis spectra of Cu- zeolites. Before the spectra were obtained, the samples were heated to 450 °C in flowing O ₂ , hold at 450 °C for 2 h and cooled to 25 °C. Reproduced from Wulfers et al. ⁷¹ with permission from the Royal Society of Chemistry.....	82
Figure 3.4:	Schematic representation of SSZ-13 (CHA), SSZ-16 (AFX) and SSZ-39 (AEI).....	83
Figure 3.5:	Diffuse reflectance UV–vis spectra of a) Cu-ZSM-5 and b) Cu-SSZ-13 (Si/Al = 6). The samples were heated to 450 °C in flowing O ₂ for 2 h, cooled to 25 °C and the flow was diverted to propane. The difference between the spectra taken after propane treatment and O ₂ treatment are shown as purple and orange lines and given above the measured spectra	86
Figure 3.6:	Raman spectra ($\lambda_{\text{ex}} = 532 \text{ nm}$) of Cu-ZSM-5 (Si/Al = 16, Cu/Al = 0.53) activated in O ₂ at 450 °C for 2 h (black) and hydrated at room conditions (blue). Both spectra are taken at 25 °C	88
Figure 3.7:	Raman spectra ($\lambda_{\text{ex}} = 532 \text{ nm}$) of Cu-mordenite (Si/Al = 5, Cu/Al = 0.33) activated in O ₂ at 450 °C for 2 h (black) and hydrated at room conditions (blue). Both spectra are taken at 25 °C	90
Figure 3.8:	Raman spectra ($\lambda_{\text{ex}} = 532 \text{ nm}$) of Cu-SSZ-13 (Si/Al = 12, Cu/Al = 0.47) activated in O ₂ at 450 °C for 2 h (black) and hydrated at room conditions (blue). Both spectra are taken at 25 °C	91
Figure 3.9:	Raman spectra ($\lambda_{\text{ex}} = 532 \text{ nm}$) of Cu-SSZ-39 (Si/Al = 10, Cu/Al = 0.48) activated in O ₂ at 450 °C for 2 h (black) and hydrated at room conditions (blue). Both spectra are taken at 25 °C	92
Figure 4.1:	Powder XRD pattern of H-Cu-SSZ-13 (Si/Al = 5, Cu/Al = 0.39), H-Cu-SSZ-13 (Si/Al = 12, Cu/Al = 0.40) and Na-Cu-SSZ-39 (Si/Al = 10), Cu K α , $\lambda = 1.5418 \text{ \AA}$	103
Figure 4.2:	Schematic of d6MR and 8MR of hydrated and dehydrated Cu-SSZ-13 (Si/Al = 12, Cu/Al = 0.4) at 30 °C refined in space group <i>R-3m</i> (No.166). For illustration purposes, all extra-framework atoms are represented in the same cage on left. The three refined Cu sites found after O ₂ treatment at 450 °C are given on right.	108

- Figure 4.3: Schematic of d6MR and 8MR of dehydrated Cu-SSZ-13 (Si/Al = 5, Cu/Al = 0.39) refined in space group $R-3m$ (No.166). Figures display the four refined Cu sites found after O₂ treatment at 450 °C. Atomic parameters can be found in Table S2.3. 109
- Figure 4.4: DR UV–vis absorption spectra of Cu-SSZ-13 samples in hydrated form and after O₂ treatment at 450 °C for 2 h. Before the spectra were collected, the temperature was reduced to room temperature under O₂ flow..... 111
- Figure 4.5: DR UV–vis absorption spectra of Cu-SSZ-13 (Si/Al = 12, Cu/Al = 0.4) after O₂ treatment at 250 °C, 300 °C, 350 °C, 400 °C and 450 °C. Before the spectra were collected, the temperature was reduced to room temperature under O₂ flow. The difference between the spectra taken at 450 °C and 300 °C is given above the measured spectra. 114
- Figure 4.6: DR UV–vis absorption spectra of Cu-SSZ-13 (Si/Al = 12, Cu/Al = 0.4) after O₂ treatment at 450 °C 2 h, and subsequent CH₄ treatment at 200 °C for 2h. Before the spectra were collected, the temperature was reduced to room temperature under O₂ or CH₄ flow. The difference between the O₂ and CH₄ treated spectra is given above the measured spectra..... 115
- Figure 4.7: *In situ* Raman spectra of O₂ activated (at 450 °C for 2 h) H-Cu-SSZ-13 (Si/Al = 12, Cu/Al = 0.4). Blue and green spectra are taken after indicated time spent in pure O₂ environment. Hydrated H-Cu-SSZ-13 is given for comparison (black)..... 116
- Figure 4.8: Comparison of *in situ* ¹⁸O₂ and ¹⁶O₂ activated Raman spectra of H-Cu-SSZ-13 (Si/Al =12, Cu/Al = 0.4) and H-SSZ-13/12 ¹⁸O₂ activation was performed at 450 °C for 13 h before cooling the samples to 150 °C and 21 °C for spectra measurement (red and blue) and ¹⁶O₂ activation was performed at 450 °C for 2 h before cooling the samples to 21 °C (black) 119
- Figure 4.9: The three different structures with μ^{Cu} within 5 kJ mol⁻¹ of a [CuOH]⁺ site in the zeolite. Si atoms are displayed in yellow, O in red, Cu atoms in blue, Al atoms in silver and H atoms in white. The bond distances are given in units of Å. 121

Figure 4.10: Comparison of experimental and calculated (a) Raman and (b) UV–vis spectra belonging to A, B, and C species (notations are given in Figure 4.9). The experimental Raman spectrum of Cu-SSZ-13 (Si/Al = 12, Cu/Al = 0.4) is given as black line on the left figure. On the right, the difference between the spectra of O ₂ activated Cu-SSZ-13, Si/Al = 12, Cu/Al = 0.4 and Cu/Al = 0.02 is given in black and denoted as ‘exp’.....	123
Figure 4.11: DR UV–vis spectra of Na-Cu-SSZ-13 (Si/Al = 12, Cu/Al = 0.47) and Na-Cu-SSZ-39 (Si/Al = 10, Cu/Al = 0.48) samples after O ₂ and He treatment at 450 °C.....	126
Figure 4.12: a)Raman spectra ($\lambda_{\text{ex}} = 532 \text{ nm}$) of hydrated (blue), O ₂ treated at 450 °C (black) and He treated at 450 °C (green) Na-Cu-SSZ-13 (Si/Al = 12, Cu/Al = 0.47). b) Raman spectra ($\lambda_{\text{ex}} = 532 \text{ nm}$) of hydrated (blue), O ₂ treated at 450 °C (black) and He treated at 450 °C (green) Na-Cu-SSZ-39 (Si/Al = 10, Cu/Al = 0.48)	127
Figure 4.13: DR UV–vis spectra before (red spectrum) and after (blue spectrum) O ₂ admission for Cu(I)-SSZ-13 (Si/Al =12, Cu/Al = 0.4). Green line is the difference of the blue and red spectra showing the additional absorption features formed after O ₂ exposure at 25 °C. The feature observed at 28,500 cm ⁻¹ was caused by a lamp switch in the spectrometer	130
Figure 4.14: Chemical scheme of dehydration on Cu-SSZ-13 as summarized from Borfecchia et al. ¹⁴⁸ and Paolucci et al. ¹⁵⁶ The dashed arrow shows the suggested Cu(II) migration mechanism from 8MR to 6MR as observed by PXRD here.	132
Figure 5.1: Powder XRD pattern of Cu-ZSM-5 (Si/Al = 11.5), Cu-mordenite (Si/Al = 5), Cu K α , $\lambda = 1.5418 \text{ \AA}$	145
Figure 5.2: Arrhenius plot of methane oxidation rate ($\mu\text{mol}_{\text{CH}_4 \text{ converted}} \text{ g}_{\text{zeolite}}^{-1} \text{ h}^{-1}$) of Cu-SSZ-13 at the temperature range of 250 –270 °C. The feed gas mixture for these experiments was: 30% CH ₄ : 30% N ₂ O: 3% H ₂ O balance He at ambient pressure, flow rate 120 cm ³ min ⁻¹ , WHSV = 19,650 g _{feed} g _{cat} ⁻¹ h ⁻¹	150
Figure 5.3: log-log plot of methane oxidation rate versus partial pressure of CH ₄ (between 20265 Pa and 40530 Pa) at 270 °C on Cu-SSZ-13 (feed gas composition: 20– 40% CH ₄ , 30% N ₂ O, 3% H ₂ O, balance He; flow rate: 120 cm ³ min ⁻¹).....	152

Figure 5.4:	log-log plot of methanol formation rate versus partial pressure of N ₂ O (between 3040 Pa and 30400 Pa) at 270 °C on Cu-SSZ-13 (feed gas composition: 30% CH ₄ , 3– 30% N ₂ O, 3% H ₂ O, balance He; flow rate: 120 cm ³ min ⁻¹).....	153
Figure 5.5:	Diffuse reflectance UV–vis spectra of Cu-SSZ-13 (Si/Al = 12) after O ₂ or 30% N ₂ O/He treatment at 270 °C. The spectrum of hydrated Cu-SSZ-13 is provided for comparison. Before each spectrum was collected, the quartz sample holder was cooled to room temperature with continuing N ₂ O/He flow. The spike at 28,500 cm ⁻¹ is an artifact caused by a lamp switch in the spectrometer.	156
Figure 5.6:	Diffuse reflectance UV–vis spectra of Cu-SSZ-13 (Si/Al = 12), Cu-mordenite (Si/Al = 5) and Cu-ZSM-5 (Si/Al = 11.5) following 30% N ₂ O/He treatment at 270 °C. Before each spectrum was collected, the quartz sample holder was cooled to room temperature with continuing N ₂ O/He flow. The spike at 28,500 cm ⁻¹ is an artifact caused by a lamp switch in the spectrometer.	157
Figure 6.1:	Schematic representation of fluidized bed reactors in series for selective methanol production using Cu- exchanged zeolites.....	167
Figure A.1:	Toth Isotherm Model Fitting of the hydrogen adsorption isotherms obtained experimentally at 20, 30 and 40 °C on Cu(I)-SSZ-13 (Si/Al = 6) sample. Y axis represents H ₂ adsorption capacity, mmol H ₂ g _{zeolite} ⁻¹ , X axis represents H ₂ pressure, atm.	186
Figure A.2:	0.13 mmol H ₂ g ⁻¹ isostere least square fitting with a straight line.....	187
Figure A.3:	Hydrogen adsorption experimental data and 95% prediction intervals for the fitted Sips adsorption model for low pressure region (0– 0.2 atm) and 95% prediction intervals for the linear model for high pressure region (0.2–1 atm).....	188
Figure A.4:	Powder XRD pattern of H-SSZ-13 (Si/Al = 12), Cu-SSZ-13 (Si/Al = 12) samples, Cu Kα, λ = 1.5418 Å. Samples were exposed to air during XRD data collection.....	194
Figure B.1:	Absorbance at 776 nm vs Cu(II) acetate concentration least square fitting with a straight line, R ² _{adj} = 0.9966	196
Figure B.2:	The concentration of methanol in the effluent stream (obtained from GC) versus time after admission of steam (at time = 0 min) for Cu(II) exchanged samples from Na ⁺	197

Figure B.3: Ion current versus time (min) obtained from MS analysis of the reactor effluent (for Na-Cu-SSZ-13 (Si/Al = 12, Cu/Al = 0.35)). The dashed line represents the time when the products were started to be observed. $m/z = 44$ is attributed to CO_2 and $m/z = 31$ is attributed to methanol. The produced CO_2 amount is calculated to be $1.6 \mu\text{mol g}^{-1}$ compared to $31 \mu\text{mol CH}_3\text{OH g}^{-1}$ produced methanol, resulting in 95% methanol selectivity.....	198
Figure C.1: a) Refined unit cell parameter a and b) unit cell parameter c and c) volume of the unit cell during dehydration and cooling of H-Cu-SSZ-13 (Si/Al = 12, Cu/Al = 0.4) with O_2 flow. (The unit cell parameters were refined with LeBail refinement)	202
Figure C.2: ^{29}Si single pulse MAS NMR of H-SSZ-13 (Si/Al = 12) obtained at 10 kHz	205
Figure C.3: ^{27}Al single pulse MAS NMR of H-SSZ-13 (Si/Al = 12) obtained at 10 kHz	206
Figure C.4: ^{29}Si single pulse MAS NMR of H-SSZ-13 (Si/Al = 5) obtained at 10 kHz	207
Figure C.5: ^{27}Al single pulse MAS NMR of H-SSZ-13 (Si/Al = 5) obtained at 10 kHz	208
Figure C.6: DR UV-vis spectra before (red spectrum) and after (blue spectrum) O_2 admission for H-Cu ⁺ -SSZ-13 (Si/Al = 12, Cu/Al = 0.4) as given in Figure 4.13. Purple line is the spectra taken after heating the O_2 exposed sample to 450 °C with $20 \text{ cm}^3 \text{ min}^{-1}$ O_2 flow. The feature observed at $28,500 \text{ cm}^{-1}$ was caused by a lamp switch in the spectrometer.	209
Figure C.7: DR UV-vis spectra with (black spectrum) and without (red spectrum) O_2 purifier for H-Cu-SSZ-13 (Si/Al = 12, Cu/Al = 0.4) treated with $20 \text{ cm}^3 \text{ min}^{-1}$ He flow at 450 °C for 4 h. The spectra are taken at 25 °C under flowing He.....	210
Figure D.1: The concentration of methanol in prepared toluene solutions versus observed methanol peak areas at 1.87 min residence time on HP-PLOT Q column at 140 °C.....	212
Figure D.2: The concentration of CO_2 on He versus observed CO_2 peak areas at 3.564 min residence time on HayeSep Q column at 140 °C.....	214

Figure D.3: The molar flow rate of CO assuming 120 cm ³ min ⁻¹ mixture (CO and He) flow versus Ion Current of Pfeiffer OmniStar GSD 320 mass spectrometer.	215
Figure D.4: Mass spectrometer ion current vs time upon 10% N ₂ O treatment of hydrated Cu-SSZ-13 with a heating rate of 5 °C min ⁻¹	216
Figure D.5: Steady state concentration of methanol in the exit stream at 270 °C. Feed: 30% CH ₄ , 30% N ₂ O, 3% H ₂ O balance helium; flow rate 120 cm ³ min ⁻¹ , WHSV = 19,650 g _{feed} g _{cat} ⁻¹ h ⁻¹	217
Figure D.6: Methane oxidation rate (mol _{CH₄ converted} mol _{Cu} ⁻¹ h ⁻¹) versus partial pressure of CH ₄ (between at 20265 Pa and 50662 Pa) at 270 °C on Cu-SSZ-13 (feed gas composition: 20– 50% CH ₄ , 30% N ₂ O, 3% H ₂ O, balance He; flow rate: 120 cm ³ min ⁻¹).....	219
Figure D.7: log-log plot of methanol production rate versus partial pressure of CH ₄ (between at 20265 Pa and 40530 Pa) at 270 °C on Cu-SSZ-13 (feed gas composition: 20– 40% CH ₄ , 30% N ₂ O, 3% H ₂ O, balance He; flow rate: 120 cm ³ min ⁻¹). The order is calculated based on : $r_{CH_3OH} = k_{app} P_{CH_4}^\alpha P_{N_2O}^\beta$	220
Figure D.8: Diffuse reflectance UV–vis spectra of Cu-SSZ-13 (Si/Al =12) following 2 h 30% N ₂ O/He treatment at 270 °C (black) followed by 1 h 30% CH ₄ /He treatment at 270 °C (red). Before each spectrum was collected, the quartz sample holder was cooled to room temperature with continuing N ₂ O/He or CH ₄ /He flow.....	222

ABSTRACT

The adverse impact of atmospheric greenhouse gases and our heavy dependence on petroleum for materials and energy are an urgent call for sustainable methods in energy generation and chemical synthesis. Hydrogen fuel-cell vehicles are zero emission cars that run on compressed hydrogen stored in tanks at 70 MPa. Due to the volume and safety concerns, there is a need for a safer, lightweight and economical onboard hydrogen storage system with a target capacity of 5.5 wt.%.

At the same time, efficient utilization of the increasingly important shale gas via methane conversion into valuable and more easily transportable liquid products in small-scales could help reduce our dependence on petroleum. Current methods for converting methane into chemicals involve synthesis gas production, economical only at large scale. Therefore, direct methane conversion into value added products such as methanol has been an important goal for the field of catalysis. There have been developments in selective methanol production using Cu- exchanged zeolites at mild conditions, however the low yields and the absence of a selective catalytic process leave a large room for research in this field.

In this thesis, both challenges were investigated using Cu-exchanged small-pore zeolites with crystallographic and spectroscopic experiments focused on the material Cu-SSZ-13. H₂ adsorption capacity that more than triple the capacity of the best metal-organic-frameworks (MOFs), reaching 0.05 wt.%, were achieved at 30 °C and 1 atm using Cu(I)-SSZ-13 and Cu(I)-[B]-SSZ-13 with adsorption enthalpy around -20 kJ mol⁻¹. The strong interaction of Cu(I)-SSZ-13 with H₂ was also monitored

using IR spectroscopy and neutron diffraction. In the second part of the thesis, Cu-exchanged SSZ-13, -SSZ-16 and SSZ-39 were tested for methanol formation and found to form methanol in quantities that are more than double the amounts produced by Cu-ZSM-5, the most investigated alternative. The active sites for methane activation on Cu-SSZ-13 and Cu-SSZ-39 were identified using optical spectroscopy and theory, while the optimum conditions for the formation of higher concentrations of the active site were reported. Finally, a new catalytic methanol production process was investigated using CH₄, N₂O, and steam on Cu-SSZ-13, and conditions for achieving higher selectivity were suggested.

Chapter 1

INTRODUCTION

The development of new and sustainable routes for energy generation and chemical production is essential in modern chemistry. High dependence on crude oil is changing with increasing environmental concerns and diminishing oil resources.

Transportation constitutes 27% (27 quadrillion Btu) of the energy consumption in USA, where 92% of the energy is provided from petroleum.¹ Hydrogen can be considered to be the best alternative to petroleum due to its high calorific value ($141790 \text{ kJ kg}^{-1}$)² and it results in zero emissions. However, the low density of hydrogen requires effective and safe hydrogen storage systems for efficient utilization of hydrogen fuel cells. Adsorption materials such as metal organic frameworks and zeolites are considered to have potential to fulfill the target hydrogen storage capacity of $55 \text{ g H}_2 \text{ kg}^{-1}$ set by DOE for 2020.³

A cleaner resource than petroleum for energy generation and chemical production is methane with higher potential in terms of abundance and versatility. It is a desirable chemical feedstock considering its conversion to many value-added products such as methanol. However, current production of value-added chemicals requires energy intensive intermediate manufacture of synthesis gas, which requires temperatures as high as $\sim 900 \text{ }^\circ\text{C}$.⁴ Therefore, there is a considerable interest in one-step economical methane conversion into liquid fuels. Cu- exchanged zeolites are potential candidates for selective methane conversion to methanol at mild temperatures,⁵ and worth investigation for catalytic one-step conversion of methane.

1.1 Zeolites

1.1.1 Zeolites: Definition

Zeolites are crystalline, nanoporous aluminosilicates composed of corner sharing $\text{SiO}_{4/2}$ and $\text{AlO}_{4/2}^-$ tetrahedra as framework components (4/2 indicates that the oxygen atoms are shared between two tetrahedra). The term *zeolite*, meaning boiling stone in Greek, was given by the Swedish chemist Alex Cronstedt in 1756 after observing a mineral stilbite giving steam when heated. The definition of zeolite refers to nanoporous crystalline aluminosilicates, which share a general formula of $\text{M}^{n+}_{x/n} \cdot (\text{AlO}_{4/2})^{-x} (\text{SiO}_{4/2})_y \cdot z \text{H}_2\text{O}$. Aluminophosphates (AIPO) and silicoaluminophosphates (SAPO) that are isostructural with known zeolites are called as zeotypes.⁶

1.1.2 Zeolites: Improved Properties

Zeolites occur naturally and can be synthesized in laboratory. Some examples of the zeolites found in nature are faujasite, ferrierite, chabazite, offretite and erionite. The worldwide total natural zeolite production is estimated to be 2,730,000 ton in 2015.⁷ These natural zeolites can be used in adsorption and separation processes. Nevertheless, they contain impurity phases and their chemical composition is variable, which prevents their widespread application especially in catalysis.

The large-scale use of zeolites as adsorbents and in catalysis was enabled after the introduction of laboratory synthesis of Zeolite A and Zeolite X by Milton in 1959.^{8,9} These zeolites, having Si/Al ratios close to 1, are known as 'low silica zeolites' and can be synthesized with alkaline metal hydroxides or other alkaline metal sources with a synthesis gel formula having M^+/Al ratio close to 1. With introduction of quaternary ammonium hydroxides as structure directing agent (SDA) in ZK-4

synthesis by Kerr in 1966,¹⁰ zeolites with higher Si/Al ratios and different structures were started to be obtained in laboratory.

The highly crystalline zeolites are formed by organization of corner sharing $\text{SiO}_{4/2}$ and $\text{AlO}_{4/2}^-$ tetrahedra around a variety of SDAs (while balancing the negative charge from $\text{AlO}_{4/2}^-$ tetrahedra with either NH_4^+ from SDA or with alkali/ alkaline earth metal cations) resulting in different framework structures composed of secondary building units such as 4 member rings (4MR), 6MR, 8MR, 10MR up to 30MR and larger composite building units such as double 6 member rings (*d6MR*), sodalite cage (*sod*), *mor*, *mfi*, *cha*, *aft*, to name a few. The number of known framework structures reached 231 by April 2016, and seems to increase each year.¹¹ With the usage of different SDA's, zeolites gained unique properties such as tunability of nanopore sizes and composition.

The tunability of pore size ranging from 3.4 to 20 Å¹² provides flexibility in reactant, product or transition state selectivity features of zeolites. The uniform pore openings, in the same range of small molecule sizes, allow zeolites to act as molecular sieves: the molecules having smaller pore diameters are allowed inside the zeolite crystals, while the molecules that are larger are not allowed, thus resulting in reactant selectivity. Similar to the reactant selectivity, the transition state or product selectivity is determined by the size of the cages and channels within the zeolite framework, which can increase the product selectivity by favoring the product that is compatible with the pore size. More information about the shape selectivity feature can be found in the reviews written by Davis¹³ and Weitkamp.¹⁴

Another unique property of zeolites is the tunability of composition that allows a wide range of Al concentration in the framework with Si/Al ratios ranging from 1

(avoiding Al-O-Al linkages by the so-called Loewenstein's rule)¹⁵ to infinity. Increased $(\text{AlO}_{4/2})^-$ concentration (smaller Si/Al ratios) introduces higher number of negative net charges in the siliceous framework. These negative framework charges can be balanced by including H^+ s (resulting in Brønsted acid sites) or more frequently alkali, alkaline earth or transition metal cations as extra-framework cations inside the pores (Figure 1.1). Different kinds of extra-framework cations grant different kinds of functionality to the zeolites, as will be explained in the next subsection. The intriguing property here is to be able to change the maximum allowed concentration of these extra-framework cations simply by changing the Al concentration. The maximum concentration of extra-framework cations can be calculated by the formula given before: i.e., $\text{M}^{n+}_{x/n} \cdot (\text{AlO}_{4/2})^-_x (\text{SiO}_{4/2})_y \cdot z \text{H}_2\text{O}$, provided that there are enough $(\text{AlO}_{4/2})^-$ sites that are in close proximity to each other, allowing energetically favorable coordination of bare cations near these Al sites. In some cases, divalent cations (M^{2+}) are charge compensated by and OH^- anion to form a structure like $[\text{M}(\text{OH})]^+$ that coordinates to isolated Al sites,¹⁶ which can be considered as exceptions to the above formula. More flexibility arises from the ion exchange property of zeolites, which allows them to host different kind of cations at the same time, concentrations of which depend on the favorability of the cations and ion exchange conditions.^{17,18}

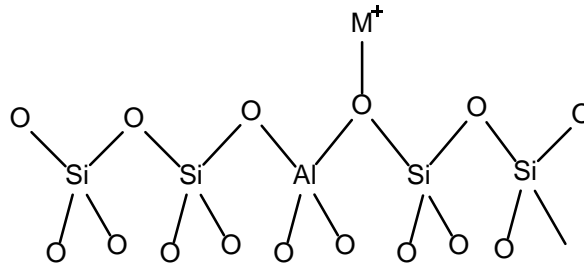


Figure 1.1: Schematic representation of extra-framework cation sites in aluminosilicates. M^+ represents a proton (H^+) or a monovalent cation (Na^+ , Li^+ , K^+ , etc.)

1.1.3 Zeolites: Applications

Zeolites are largely used in a variety of commercial applications relating to adsorption and catalysis. The biggest application of synthetic zeolites in a weight base (73% of total synthetic zeolites) is as detergent builder, in which zeolites are used as ion-exchange reagents.⁶ The following applications are as catalysts (15%) or adsorbents (12%).⁶ Fluid catalytic cracking and hydro-cracking for gasoline and middle distillate making in refinery and petrochemistry industry account for the majority of the synthetic zeolite consumption in catalysis. In these processes, post-synthesis techniques such as dealumination by steaming or leaching are utilized to tune selectivity by changing the acidity of the zeolites.¹⁹ Some other reactions that can be catalyzed by acid zeolites (with Brønsted acid sites) are isomerization and alkylation of hydrocarbons.^{20–22} Readers are encouraged to read reviews from Vermeiren et al.¹⁹ and Marcilly²³ for application of zeolites in refining and petrochemistry.

Some of the zeolite features that make them efficient catalysts are as follows:

- They are non-toxic and non-corrosive.

- Their acidity or mild basicity can be tuned by changing Si/Al ratios either during the synthesis or by post-synthesis methods.
- In addition to the Si/Al ratios that vary the acid site concentration, the acidity level of the sites can be changed by substituting Al trivalent cation by Ga, Fe or B (in decreasing acid strength).²⁴
- Their pore structure allows 1, 2 or 3 dimensional flow of molecules, which enables control of diffusion rates.
- Crystal sizes can be tuned to less than 100 nm and to bigger than 5 μm allowing control of diffusion path length and deactivation.
- Most of the zeolite structures reported to date resist high temperatures ($>400\text{--}800\text{ }^\circ\text{C}$).
- As of this writing, there are 231 zeolite frameworks recognized by IUPAC (International Union of Pure and Applied Chemistry) with different building units that can be utilized for different purposes; however only 13 of them are commercially used in catalysis (AEL, AFY, BEA, CHA, ERI, FAU, FER, LTL, MFI, MOR, MWW, RHO, TON)²⁵

In addition to these appealing features of protonated zeolites, transition metal cation exchanged zeolites introduce additional catalytic features by providing cations with reducible valence states. Methane conversion (C1 chemistry) and environmental catalysis are the fields, in which transition metal exchanged zeolites show promising activity. Among the transition metal cation exchanged zeolites, Cu exchanged zeolites are special since they catalyze many reactions including NO and N_2O decomposition,^{26–35} selective catalytic reduction of NO_x with NH_3 ,^{36–46} hydroxylation of benzene to phenol,^{47–51} and oxidative carbonylation of alcohols.^{52–56}

Alkali metal and alkaline earth metal cation exchanged zeolites, are often used in separation and storage applications including CO_2/N_2 , O_2/N_2 and CH_4/N_2 separations.^{57–60} Degree of polarizability and interaction of stronger/ weaker quadrupole moments of these mixture gases with alkali/ alkaline earth metal cations

enable selective adsorption of specific gases. On the other hand, absence of a dipole moment in many adsorbates and presence of a strong dipole moment of water molecule renders alkali/ alkaline earth metal cation exchanged zeolites (with high Al content) powerful desiccants.

1.2 Cu exchanged Zeolites and Applications

1.2.1 Catalytic Applications

Cu- exchanged zeolites might be the most frequently investigated transition metal cation exchanged zeolites due to its wide range of catalytic applications. Catalytic interest to Cu exchanged zeolites increased after Iwamoto et al.'s report on NO decomposition activity on Cu-Y²⁶ and Cu-ZSM-5²⁷ during the 80's and continued with selective NO_x reduction with hydrocarbons and ammonia, hydroxylation of benzene to phenol, selective oxidation of methane and carbonylation of alcohols (Table 1.1).

Table 1.1: Catalytic reactions involving Cu- exchanged zeolites.

Reaction	Zeolite	Reference
NO decomposition $2NO \rightarrow N_2 + O_2$	Cu-Y	27
	Cu-ZSM-5	27,28,33
N ₂ O decomposition $2N_2O \rightarrow 2N_2 + O_2$	Cu-ZSM-5	29-32
	Cu-X	61
	Cu-Beta	62
NO _x reduction with NH ₃ $2NO + 2NH_3 + \frac{1}{2}O_2 \rightarrow 2N_2 + 3H_2O$ and $NO + 2NH_3 + NO_2 \rightarrow 2N_2 + 3H_2O$	Cu-Y	36
	Cu-ZSM-5	38-41,43
	Cu-Beta	63,64
	Cu-SSZ-13	65-67
Hydroxylation of benzene to phenol $C_6H_6 + \frac{1}{2}O_2 \rightarrow C_6H_6O$	Cu-ZSM-5	47-49,51
Partial oxidation of methane to methanol $CH_4 + \frac{1}{2}O_2 \rightarrow CH_3OH$	Cu-ZSM-5	5,68,69
	Cu-mordenite	5,69,70
	Cu-Beta	69
	Cu-SSZ-13	71
Carbonylation of alcohols $2CH_3OH + CO + \frac{1}{2}O_2 \rightarrow (CH_3O)_2CO + H_2O$	Cu-X	52
	Cu-ZSM-5	53,54
	Cu-Y	56,72,73
	Cu-mordenite	55

Sensitivity of Cu-ZSM-5 to SO₂, H₂O and O₂ poisoning for direct decomposition of NO led to investigation of hydrocarbons, NH₃ or CO as reductants.⁷⁴

This discovery opened the way for Cu exchanged zeolites in the treatment of oxygen-rich exhaust gas from diesel engines. Now, it is well established that Cu- exchanged zeolites show superior activity and selectivity at selective catalytic reduction (SCR) of NO with NH₃ in the low temperature region compared to Fe- exchanged zeolites.⁷⁵ Application of Cu-SSZ-13 in SCR of NO_x with NH₃ resolved important limitations of medium-pore Cu- exchanged zeolites such as a comparatively lower hydrothermal stability of Cu-ZSM-5 and Cu-beta, in addition to achieving high activity and even higher selectivity on Cu-SSZ-13.⁶⁵

Catalytic activity of the transition metal cation exchanged zeolites does not depend only on the type but also on the location of the cation relative to the framework, since the framework oxygen atoms act as *ligands* and affect the electronic and chemical properties of the transition metal cation. Cu cation is special among the transition metal cations since information about Cu coordination environment can be gained relatively easily by using UV-vis spectroscopy and electron paramagnetic resonance (EPR), resulting in a number of articles containing spectroscopic information of Cu exchanged zeolites. Location of the transition metal cation is determined by several factors: One, evidently, is the framework type, and the other factors are the Si/Al ratio and Mⁿ⁺/Al ratio. One interesting common finding in NO, N₂O decomposition reactions and methane oxidation to methanol is that zeolites with relatively higher copper cation concentrations show activity indicating presence of multinuclear copper species in addition to mononuclear Cu sites.

1.2.2 Direct Methane Conversion to Methanol

Methane is the main component of natural gas and it is a very important hydrocarbon feedstock especially considering the increasing shale gas production over

the last decade.⁷⁶ Methanol is a valuable product itself for electricity generation for it can be used in fuel cells, or it can be converted to gasoline or value added chemicals. Conventionally, methanol is produced from synthesis gas that is obtained via methane steam reforming process (Figure 1.2), which has high energy costs due to its endothermicity and the required reaction temperatures ($\sim 900\text{ }^\circ\text{C}$).⁴ These high rates of energy consumption of synthesis gas production account for 60% to 70% of methanol production costs.

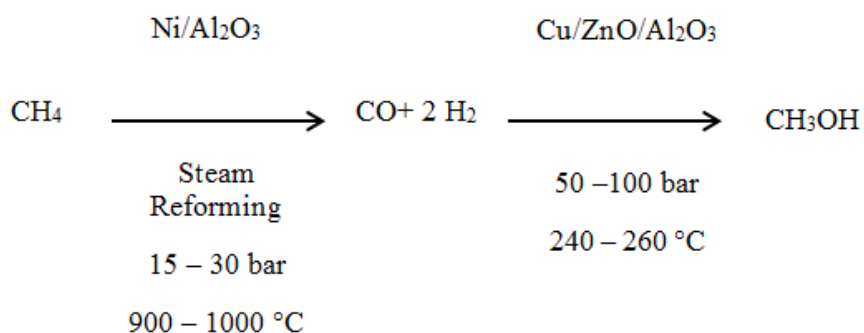


Figure 1.2: Conventional methanol production from synthesis gas route

One-step oxidation of methane to methanol in an environmentally friendly catalytic way is a very attractive but challenging alternative to the industrial two-step methanol formation. The biggest challenge in direct methane oxidation to methanol is achieving high selectivity towards methanol. Methanol (and formaldehyde) has higher reactivity when compared to the methane molecule due to the weaker C–H bonds in methanol (397 kJ mol^{-1}) compared to methane (439 kJ mol^{-1}), resulting in over-

oxidation to CO or CO₂. For this reason, the best yield for methanol production using heterogeneous or homogeneous catalysis that will follow radical chemistry is estimated to be around 5% by Labinger.⁷⁷ And indeed, when we have a look at the methanol + formaldehyde yields obtained at high pressures at gas phase (conditions at which radical reactions are predominant⁷⁸) or using heterogeneous catalysis at lower pressures, we observe yields not surpassing 5% with highest methanol selectivity around 40% (Table 1.2).

In contrast to the homogenous gas phase reactions at high temperatures or supported metal catalysts, biological systems and transition metal cation exchanged zeolites can selectively convert methane to methanol at mild conditions. The methane monooxygenase (MMO) enzyme, found in methanotrophic bacteria, is capable of oxidizing C–H bonds at ambient conditions with the help of the reducing agent NADH (Eq 1.1).^{79,80}



There are two forms of MMO. One is a membrane-bound, particulate form of MMO (pMMO) containing about 12–15 copper atoms between two sites. The location and the mechanism of the copper active site in pMMO is still an area of research. The second form of MMO is the soluble form, which is more stable and easier to purify when compared to pMMO and the active site in sMMO that break C–H bond has been identified as a bis(μ–oxo) diiron center^{81,82}

Table 1.2: Methanol and formaldehyde selectivity and yield values for gas phase CH₄ partial oxidation in absence or presence of a catalyst

Catalyst	Pressure / atm	Temperature / °C	CH ₄ Conversion / %	CH ₃ OH Selectivity / %	HCHO Selectivity / %	(CH ₃ OH + HCHO) Yield / %	Ref
MoO ₃ /SiO ₂	1	650	5.3	0	32	1.6	83
W/SiO ₂	1	650	6.9	0	11.9	0.8	84
V ₂ O ₅ /SiO ₂	1	650	13.5	0	35	4.73	85
V/MCM-41	1	626	5.4	0.2	22	1.20	86
FePO ₄ /SiO ₂	1	600	10	Trace	12	1.2	87
MgBPO/SiO ₂	1	500	8.1	0	22	1.78	88
MoSnP/SiO ₂	1	675	7.2	Trace	64.8	4.67	89
Cu-Fe/ZnO	1	750	2.5	0	10	0.25	90
Ga ₂ O ₃ /MoO ₃	15	455	3.0	22	-	0.66	91
MoO ₃ UO ₂ /SiO ₂ /Al ₂ O ₃	53.3	543	2.2	43	-	0.95	92
No catalyst (quartz lined reactor)	53.3	388	2.6	47	-	1.22	92
No catalyst (Pyrex lined reactor)	49.3	425	5.25	39.3	-	2.06	93
No catalyst (quartz lined reactor)	29.6	400	8.5	23	-	1.96	94
No catalyst (Pyrex lined reactor)	50	433	4	38.1	Trace	1.52	95

Particulate form of MMO consists of the pmoB, pmoA and pmoC subunits.

The active oxidative site is believed to be located in pmoB subunit where there are two different sites, one containing a single copper ion⁹⁶ and a second site with dinuclear

copper site with a Cu–Cu distance of 2.5–2.7 Å (on the basis of extended X-ray absorption fine structure (EXAFS) analysis).⁹⁷ The active dicopper site has been suggested to be a bis(μ -oxo) dicopper center^{98–100} based on the observed Cu–Cu distances. A μ -(η^2 : η^2) peroxy dicopper(II) species has also been suggested based on an absorption feature at 345 nm following the oxidation of soluble fragment of pmoB.¹⁰¹ There are also theoretical studies suggesting transformation of a plausible μ -(η^1 : η^2) peroxy Cu(I)Cu(II) or μ -(η^2 : η^2) peroxy dicopper(II) species into bis(μ -oxo) Cu(II)Cu(III) species⁹⁸ or a (μ -oxo)(μ -hydroxo) Cu(II) Cu(III) species¹⁰² that are theoretically more active for methane conversion to methanol. While the research for identification of this active species is on-going (a comprehensive review on MMO can be found elsewhere),^{103,104} it is desired to develop synthetic biomimetic catalysts for natural gas conversion to methanol.

The other class of agents that can selectively oxidize methane into methanol is transition metal ion (Fe,^{105–109} Co^{110,111} and Cu^{5,68–70,112–114}) exchanged zeolites. Fe exchanged zeolites are known to activate methane with an active oxygen atom known as ‘ α ’ oxygen atom. They are generated by first auto-reducing the Fe exchanged zeolites with an inert flow ($Fe^{III} \rightarrow Fe^{II}$) at temperatures higher than 600 °C¹¹⁵ and then treating the zeolites with N₂O at 200–250 °C (Eq. 1.2).¹⁰⁹



These active sites then can break C–H bonds at room temperature and form (Fe-OCH₃) _{α} groups (Eq. 1.3), which can then produce methanol by hydrolysis (Eq. 1.4) in a step wise manner.^{108,109} Quasi-catalytic and catalytic formation of methanol has

recently been reported on Fe-ZSM-5 by co-feeding methane, N₂O and steam at 275 °C reaching a methanol selectivity of 62%.¹¹⁶ Even though the methanol turn over frequencies with Fe-ZSM-5 are promising for temperatures as low as 200 – 275 °C, the main disadvantage with Fe exchanged zeolites remains to be the high temperature (900 °C) pre-treatment of the catalyst with an inert flow to create (Fe^{II})_α sites.¹¹⁶

Cu-exchanged zeolites have been investigated for selective methanol formation for over a decade starting with a report by Groothaert et al. in 2005.⁵ The activation of methane has been shown on Cu-ZSM-5 with an absorption feature at 22,700 cm⁻¹.^{5,69} that increased in intensity by O₂ treatment (above 350 °C)⁶⁹ and decreased in intensity upon contacting with CH₄ at temperatures starting at 125 °C.⁶⁹ This new reactive species, which was firstly assigned to be a bis(μ-oxo)dicopper(III) species by Groothaert et al.,⁵ has also been shown to play an active role in NO and N₂O decomposition.³³⁻³⁵ In 2009, the same group together with Solomon assigned the species with the related absorption feature at 22,700 cm⁻¹ to a bent mono-(μ-oxo)dicopper(II) species ([Cu-O-Cu]²⁺) based on resonance Raman spectroscopy features and theoretical calculations that are consistent with mono-(μ-oxo)dicopper(II) species.¹¹⁷ Mono-(μ-oxo)dicopper(II) species activate methane on Cu-ZSM-5 at temperatures as low as 125 °C, resulting in a (suggested) methoxy species,^{68,118} which could then be extracted as methanol at room temperature by using a solvent^{5,68} or by flowing steam over the zeolite at 200 °C⁷⁰ with methanol selectivity around 98%.⁵

The earlier procedures for selective methanol formation on Cu-exchanged zeolites included a 3-step cyclic process including:

1. Oxidation of Cu- zeolite at temperatures between 300 °C and 450 °C

2. Methane reaction at the temperature range of 150 °C – 200 °C resulting in a stable bound intermediate
3. Methanol extraction from the surface using steam or solvent

The first step in this process results in Cu_xO_y active species formation on Cu-exchanged zeolites, the identity and location of which is essential for methane activation at mild temperatures. Utilization of O_2 in this step is a major advantage of Cu-exchanged zeolites when compared to Fe-exchanged zeolites where N_2O treatment is compulsory for formation of reactive $(\text{Fe}^{\text{III}}-\text{O}^-)_\alpha$ sites.¹¹⁵

The second step is the methane activation step, which also showed differences for different Cu-exchanged zeolites. Methanol formation was noted on Cu-ZSM-5 and Cu-mordenite with CH_4 activation at 150 °C, whereas Cu-exchanged FER and *BEA showed comparable activity only at 200 °C, suggesting the presence of different Cu_xO_y active species on different frameworks.⁶⁹ Methane contact time also showed differences in methanol production amounts (Table 1.3). Grundner et al. estimated CH_4 contact time of at least 30 min to observe reasonable methanol formation on Cu-mordenite (Table 1.3).¹¹⁴

Methanol could be extracted by dissolving in a solvent or by purging with steam (Table 1.3). Beznis et al. mentioned the positive effect of more polar and protic solvents on methanol extraction amounts, suggesting a proton transfer from the solvent to the surface bound intermediate in the methanol extraction process.⁶⁸ The recent methanol formation procedures often use steam for extracting methanol for the practicability of the process.

Table 1.3: Direct methanol production amounts observed on different Cu- exchanged zeolites and 3-step procedures

Zeolite	Si/Al, Cu/Al	Procedure	CH ₃ OH formation / μmol CH ₃ OH $\text{g}_{\text{zeolite}}^{-1}$	Cu Concen- tration / mmol Cu $\text{g}_{\text{zeolite}}^{-1}$	CH ₃ OH formation / mol CH ₃ OH mol Cu^{-1}	Ref.
Cu-ZSM-5	12, 0.31	100% O ₂ activation at 450 °C overnight, 5% CH ₄ flow at 200 °C for 15 min, methanol extraction in 1:1 H ₂ O:Acetonitrile solution	8.2	0.39	0.002	5
Cu-mordenite	8.8, 0.50	100% O ₂ activation at 450 °C overnight, 5% CH ₄ flow at 150 °C for 15 min, methanol extraction in 1:1 H ₂ O:Acetonitrile solution	6	0.80	0.0075	69
		100% O ₂ activation at 450 °C overnight, 5% CH ₄ flow at 200 °C for 15 min, methanol extraction in 1:1 H ₂ O:Acetonitrile solution	16	0.80	0.02	69
Cu-FER	6.2, 0.42	100% O ₂ activation at 450 °C overnight, 5% CH ₄ flow at 200 °C for 15 min, methanol extraction in 1:1 H ₂ O:Acetonitrile solution	12	0.92	0.013	69
Cu-ZSM-5	17, 0.4	Air activation at 550 °C, 8% CH ₄ flow at 150 °C for 25 min, methanol extraction in ethanol	1.69	0.36	0.0047	68
Cu-mordenite	11, 0.38	100% O ₂ activation at 450 °C 4 h, 5% CH ₄ flow at 200 °C for 20 min, He/H ₂ O flow extraction at 200 °C	13	0.51	0.0255	70
Cu-ZSM-5	12, 0.28	50% NO activation at 150 °C 2 h, 50% CH ₄ flow at 150 °C for 1 h, Ar/H ₂ O flow extraction at 150 °C	0.629	0.35	0.0018	113
		50% N ₂ O activation at 300 °C 2 h, 50% CH ₄ flow at 150 °C for 1 h, Ar/H ₂ O flow extraction at 150 °C	0.690	0.35	0.002	113
Cu-mordenite	11, 0.4	100% O ₂ activation at 450 °C 1 h, 90% CH ₄ flow at 200 °C for 4 h, He/H ₂ O flow extraction at 135 °C	135	0.44	0.306	114
Cu-mordenite	6, 0.35*	1 bar O ₂ at 450 °C 4 h, 1 bar CH ₄ at 200 °C for 30 min, aqueous extraction	45.3	0.74*	0.061	119
		1 bar O ₂ at 450 °C 4 h, 36 bar CH ₄ at 200 °C for 30 min, aqueous extraction	103.3	0.74*	0.140	119
		1 bar O ₂ at 200 °C 13 h, 37 bar CH ₄ at 200 °C for 30 min, aqueous extraction	56.2	0.74*	0.140	119

*Calculated from given Si/Al ratio and Cu wt.% value of 4.7¹¹⁹

The ultimate goal in direct methanol formation from methane is a catalytic process with high methanol selectivity. There have been improvements on the step-wise cyclic process such as implementation of isothermal processes, but a catalytic process has not been developed elsewhere yet. An isothermal step-wise process was reported with Cu-ZSM-5 at 150 °C using NO and N₂O as the oxidant with high methanol selectivity. The reported methanol production amounts were remarkably lower with this process when compared to the methanol amounts obtained by activating Cu-ZSM-5 at 450 °C. Very recently, another isothermal step-wise process at 200 °C has been reported on Cu- mordenite using O₂ as the oxidant and CH₄ with pressures reaching 37 bar which increased methanol production amounts significantly¹¹⁹ (Table 1.3).

One essential component in direct and selective methanol formation on Cu-exchanged zeolites is the Cu_xO_y active site. The identification of Cu_xO_y sites is crucial for developing materials having high concentration of active sites that would produce methanol with higher yields. There has been two Cu_xO_y species identified on Cu-exchanged zeolites so far. One is the mentioned mono-(μ-oxo)dicopper(II) species,¹¹⁷ which has also been identified on Cu- mordenite by Vanelderen et al. (Si/Al = 5) using enhanced Raman spectroscopy¹²⁰ and suggested by Alayon et al. (Si/Al = 11) using UV-vis spectroscopy.^{70,121} The second active species is a tricopper species ([Cu₃O₃]²⁺) reported for Cu-mordenite with a different Si/Al ratio (Si/Al = 11).¹¹⁴ Based on these reports, we can conclude that the differences in Si/Al and Cu/Al ratios and even synthesis methods are expected to result in different Cu species formation.

Overall, the low methanol production yields per Cu cations (Table 1.3) imply formation of the Cu_xO_y active species low in concentration. Spectroscopic techniques

such as Raman spectroscopy and UV–vis spectroscopy often provide information that is specific to species in low concentrations, but a combinatory approach including theoretical calculations should be applied in careful identification of these active species. Together with developing new methanol production processes and Cu_xO_y site identification, understanding the mechanisms for active site formation is among the scopes of this thesis.

1.2.3 H_2 Adsorption

Cu-exchanged zeolites bind to hydrogen molecule strongly at room temperature, making Cu-exchanged zeolites desirable for molecular hydrogen storage at ambient conditions. There is an undeniable need for a safe, lightweight and economical onboard hydrogen storage system with a target capacity of $55 \text{ g H}_2 \text{ kg}^{-1}$ of storing system set by DOE for 2020.³ Physisorption using porous adsorbents can be considered the safest and the most economical method compared to compressed gas (up to 70 MPa), liquid hydrogen storage (at temperatures below 30 K) or hydrogen storage via metal hydrides, which binds hydrogen via chemisorption.¹²²

Physisorption onto nanoporous materials have several advantages including completely reversible adsorption and rapid adsorption kinetics. On the other hand, weak physical interaction of hydrogen with these adsorbents undermines achieving effective hydrogen storage at practical conditions; i.e., at near-ambient temperatures and pressures below 10 MPa. Activated carbons¹²³ and metal organic frameworks (MOFs) having high specific surface areas and pore volumes (up to $6240 \text{ m}^2 \text{ g}^{-1}$, MOF 210),¹²⁴ can adsorb hydrogen with capacities up to $86 \text{ mg H}_2 \text{ g}_{\text{adsorbent}}^{-1}$ by MOF 210¹²⁴ at cryogenic temperatures (and at pressures up to 120 bar). However at ambient conditions; i.e., 298 K and 1 atm, the hydrogen adsorption capacities of metal organic

frameworks do not exceed $0.12 \text{ mg H}_2 \text{ g}_{\text{adsorbent}}^{-1}$ (IRMOF-8)¹²⁵ due to low hydrogen adsorption enthalpies associated with physical adsorbents with high pore volumes such as MOFs (with highest reported hydrogen adsorption enthalpy, $-13.5 \text{ kJ mol}^{-1}$ for CPO-27-Ni)¹²⁶ and activated carbons ($-4 - -6 \text{ kJ mol}^{-1}$).¹²⁷

Having no charge and no dipole, and a relatively small quadrupole moment ($2.21 * 10^{-40} \text{ C m}^{-2}$) and low polarizability ($8.79 * 10^{-41} \text{ C}^2 \text{ m}^2 \text{ J}^{-1}$),¹²⁸ strong hydrogen interaction with the porous adsorbents at ambient conditions depends on strong polarizing centers on these adsorbents. These strong polarizing centers are open metal centers in MOFs and extra-framework cations in zeolites and they are the main adsorption sites for hydrogen adsorption. After saturation of these metal sites, hydrogen adsorption has been shown to proceed on the walls and inside the pores of the porous materials,¹²⁹ which makes materials with narrow pores (to enhance the dispersion forces) a prerequisite for an optimum adsorbent. Small-pore openings of zeolites result in higher dispersion forces on the guest molecules when compared to MOFs, making them more promising adsorbents, however electric field applied by the extra-framework alkali metal ions in zeolite materials are still not enough to induce strong interaction between the hydrogen molecule and the zeolite. Reported hydrogen adsorption enthalpies by alkali and alkali earth metal exchanged zeolites are in the range of -4 to -10 kJ mol^{-1} with exception of $-18.2 \text{ kJ mol}^{-1}$ for Mg/Na-Y.¹³⁰

Another form of interaction with hydrogen is through donor-acceptor orbital interactions as observed in Kubas-type hydrogen complexes^{131,132} that result in an elongated H-H bond length ($0.8-0.9 \text{ \AA}$) and smaller M-H₂ distances than the expected van der Waals contact distance (around 3 \AA)¹²⁸ while still allowing reversible adsorption. Cu(I) cation, when coordinated to zeolite framework, was shown to form

similar dihydrogen complexes even at room temperature, resulting in a strong perturbation of the H–H bond as showed with a bathochromic shift of 1000 cm^{-1} for H–H vibration frequency by IR spectroscopy.¹³³ Hydrogen adsorption on Cu(I)-ZSM-5 was so far investigated by Kazansky et al.,^{133,134} Eckert group,^{135,136} Ramirez-Cuesta et al..¹³⁷ Investigations showed isosteric heat values for hydrogen adsorption at an average temperature of $48\text{ }^{\circ}\text{C}$ on Cu-ZSM-5 between -73 and $-39\text{ kJ mol H}_2^{-1}$ for H_2/Cu : 0.05–0.4).¹³⁵ For cation exchanged zeolites, optimal absolute hydrogen adsorption enthalpy value was predicted to be in the range of $-22 - -25\text{ kJ mol H}_2^{-1}$ (at a loading pressure of 30 bar and desorption pressure of 1.5 bar) at ambient temperature.¹³⁸

The strong interaction of hydrogen with Cu(I) cations coordinated to oxygen atoms of an $\text{AlO}_{4/2}^-$ tetrahedron has been explained by the electron donation from the σ bonding orbital of the H–H bond to the low occupied Cu^+ (4s) orbitals and electron back donation from the $3d_{\pi}$ (Cu^+) to the $\sigma^*(\text{H-H})$ anti bonding orbital.^{133,139,140} Specific Cu(I) position inside the zeolite framework affects the dihydrogen and Cu(I) interaction strength since framework oxygen atoms, to which Cu(I) cation coordinates, increase Cu ($3d_{\pi}$) orbital polarization and to reduce Cu(I) – zeolite repulsion which favors Cu^+ ($3d_{\pi}$) \rightarrow H_2 (σ^*) back donation.^{139,140} For a chabazite framework, hydrogen adsorption enthalpy values are theoretically calculated to be -18 kJ mol^{-1} for Cu(I) located at the window of the 6MR,¹³⁹ which makes Cu(I)-SSZ-13 a potential hydrogen adsorbent at ambient conditions.

1.3 Cu-SSZ-13: Structural Background

SSZ-13 has the chabazite framework type, and it is formed of 6 member rings (6MR) stacked in an AABCC sequence, resulting in an 3-dimensional structure with

an ellipsoidal cage ($7.3 \times 12 \text{ \AA}$)¹⁴¹ (Figure 1.3). The resulting building units of CHA framework are 4-, 6-, and 8- member rings, but practical openings for guest molecules are 8MRs with an opening size of 3.8 \AA . Because of the smaller pore openings, SSZ-13 have advantages such as higher hydrothermal stability or higher selectivity toward specific products when compared to other medium or large pore zeolites such as ZSM-5 (MFI framework, 10MR, 5.6 \AA) or mordenite (MOR framework, 12MR, 7 \AA).

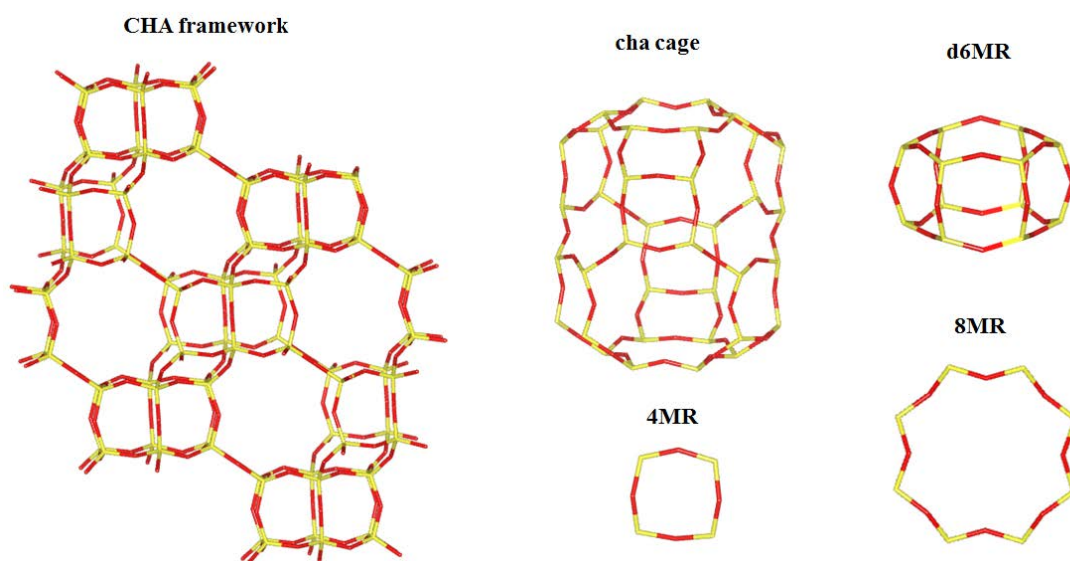


Figure 1.3: Schematic representation of CHA framework and building units. Yellow tetrahedral corners represent Si/Al atoms and red represent shared oxygen atoms.

Si/Al composition for SSZ-13 can be varied between $\text{Si/Al} = 1$ to infinity, but industrially relevant SSZ-13 samples have a Si/Al ratio between 12 and 15, which statistically results in one Al atom in one double-6-member ring, or one Al atom in one chabazite cage even though experimental data suggests random Al distribution

and presence of two Al atoms in one 6MR with Si/Al ratios between 12 and 15.¹⁴² The lower framework density of CHA framework results in higher specific micropore volumes than MFI and MOR frameworks (Table 1.4), which also decreases effective Cu concentration inside CHA pores when compared to MFI and MOR.

Table 1.4: Zeolite structures and pore systems

Zeolite	IZA Framework Code	Largest Pore / member ring	Pore opening / Å	Framework Density / T 1000 Å⁻³	Micropore Volume / cm³ g⁻¹
SSZ-13	CHA	8	3.8	15.1	0.30
ZSM-5	MFI	10	5.6	18.4	0.15
Mordenite	MOR	12	7	17	0.17
Y	FAU	12	7.4	13.3	0.30

Cu exchange onto zeolites can be done in two ways. First one is the aqueous exchange, in which one can use water soluble Cu(II)-nitrate,⁶⁵ sulfate¹⁴³ or acetate salts⁷¹ as copper sources. This method generally results in Cu(II)/Al ratios smaller than 1, but sometimes larger than theoretical maximum of Cu(II)/Al = 0.5 (for one M²⁺ balancing two (AlO_{2/4})⁻ units) depending on the Al distribution of the zeolite.¹⁴⁴ The second method is the solid state exchange in which water insoluble salts such as Cu(I)Cl could be used as the Cu(I) source and exchanged onto the zeolite by heating the CuCl and H-zeolite mixture (or by contacting CuCl vapor to the H-zeolite as in vapor phase exchange method) around 400–500 °C in presence of inert gas flow.^{145–147}

The location of Cu cations on any framework depends on following factors:

- Framework topology
- Al concentration (Si/Al ratio)
- Cu concentration (Cu/Al ratio)
- pH of the exchange solution
- Presence of co-cations

The Al concentration determines the Al distribution within a zeolite, together with the framework topology they affect the possibility of having two $(\text{AlO}_{2/4})^-$ units in close proximity to each other. With two $(\text{AlO}_{2/4})^-$ sites that are in close proximity, dissolved $[\text{Cu}(\text{II})(\text{H}_2\text{O})_6]^{2+}$ aquo complexes can balance the negatively charged oxygen atoms, which further results in monomeric Cu(II) coordination upon dehydration of the zeolite. However, if the zeolite has high Si/Al ratios, which result in higher concentration of isolated $(\text{AlO}_{2/4})^-$ units, then Cu(II) cations can be balanced in form of $[\text{CuOH}]^+$ complexes¹⁴⁸ near single $(\text{AlO}_{2/4})^-$ units. For this kind of Cu arrangement inside the zeolite pores, Cu concentration would also be of importance. The fraction of monomeric Cu(II) or $[\text{CuOH}]^+$ species would depend on energetic favorability of the sites and on the available copper cation concentration. For aqueous Cu(II) exchange, pH of the solution is also reported to be important since pH values higher than 6 result in precipitation of Cu(II) in the solution.¹⁴⁹ Presence of co-cations would also affect the exchange limit and location of Cu(II) depending on the favorability of the cations at those specific locations.

There have been numerous investigations about the location and coordination of Cu cations on SSZ-13. The first structural report has been done by Fickel et al. who showed Cu coordination on the window of the 6MR with a coordination number of 3 (C_{3v} symmetry) and average Cu–O distances of 2.2–2.3 Å.¹⁴³ Korhonen et al.¹⁵⁰ and

Deka et al.¹⁵¹ performed X-ray Absorption Spectroscopy on Cu-SSZ-13 (with Si/Al ratio of 9 and 18 respectively) and also found Cu on the window of 6MR with coordination number of 3 and average Cu–O distances of 1.93 Å and 1.95 Å respectively. This location was theoretically shown to be more favorable for monomeric Cu(II) cations when compared to Cu(II) on 8MR (more favorable by 54–71 kJ mol⁻¹)¹⁵², provided that two (AlO_{2/4})⁻ units reside on the same 6MR or 8MR. Two different distorted tetragonal planar Cu(II) coordination on 6MR have been theoretically suggested for Cu-SSZ-13¹⁴² as well as other frameworks having 6MRs such as FAU.¹⁵³ The Al locations with respect to each other have been reported to be in two ways on a 6MR. One, where two Al atoms are located in –Al–O–(Si–O)–Al– sequence (second-nearest-neighbor position, A in Figure 1.4), and second in –Al–O–(Si–O)₂–Al– sequence (third-nearest-neighbor position, B in Figure 1.4). These two possibilities result in two different EPR signals from Cu-SSZ-13 samples with g₁ factors of 2.325 and 2.328 on SSZ-13.¹⁴² The first Al sequence (where two Al atoms are separated by a single Si atom) is theoretically shown to result in 3 equal Cu–O distances around 1.97 Å and one longer Cu–O coordination around 2.39 Å.¹⁴⁸ In the second sequence, where two Al atoms are located diagonally across each other, 4 near equivalent Cu–O bonds with 2.03 Å are observed.¹⁴⁸

Energetically Cu(II) favors 4-coordination to oxygen atoms, a geometry difficult to achieve at the 8MR. For Cu(II) coordination at 8MR, several reports suggest coordination of [CuOH]⁺ species to single (AlO_{2/4})⁻ unit on 8MR following DFT calculations,^{148,154} FTIR,^{148,155} XAS,^{148,156} and EPR.¹⁴² Borfecchia et al. evaluated occurrence and stability of [CuOH]⁺ species on Cu-SSZ-13 under oxidative and inert environments and suggested a dehydration mechanism involving [CuOH]⁺ species.¹⁴⁸

More insight about the effect of the treatment conditions on Cu coordination and Cu_xO_y species will be given through this dissertation.

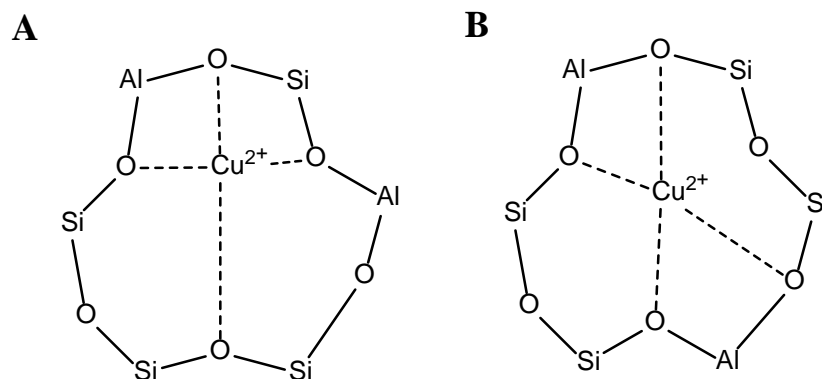


Figure 1.4: Possible Cu(II) sites on 6MR with two Al sites, reproduced from Godiksen et al.¹⁴²

1.4 Scope of the Thesis

The work presented in this thesis focuses on applications of Cu exchanged zeolites, mainly Cu-SSZ-13, in clean energy applications including hydrogen storage and direct methane conversion to methanol. The main aim of the thesis is to investigate Cu-SSZ-13 materials to improve hydrogen storage capacities of porous materials at ambient conditions and also to improve selective methanol production amounts from direct methane conversion.

As described above, Cu(I)-SSZ-13 is a potential H₂ adsorbent at ambient conditions due to the strong interaction between Cu(I) and hydrogen molecule. In Chapter 2, hydrogen adsorption capacities of several Cu(I) exchanged zeolites are tested in addition to the evaluation of site specific adsorption properties of Cu(I)-SSZ-

13 using powder neutron diffraction and FTIR. Different Cu(I) exchange methods are also explored.

Chapter 3 introduces Cu-SSZ-13 together with other small-pore zeolites and zeotypes such as Cu-SSZ-16 and Cu-SSZ-39 in direct methane conversion to methanol. The active site for these zeolites is investigated using UV–vis spectroscopy and Raman spectroscopy.

Chapter 4 provides an in-depth study of Cu-SSZ-13 characterization under oxidative and inert environments. Several *in situ* methods including Synchrotron X-Ray diffraction, UV–vis spectroscopy, Raman spectroscopy are combined with DFT calculations to identify the active species for methanol production on Cu-SSZ-13. Formation mechanism of this active species is also investigated.

Chapter 5 introduces a catalytic methanol production procedure with Cu-exchanged zeolites using N₂O as the oxidant. The effect of temperature, methane, nitrous oxide and water partial pressures on methanol activity and selectivity are explored using Cu-SSZ-13. The activity is compared to other zeolites such as Cu-ZSM-5 and Cu-mordenite. Dioxygen and nitrous oxide are compared as the oxidant for this reaction in terms of selectivity and the formed active species.

Chapter 6 summarizes the results of these studies and suggests further research directions to improve both the H₂ adsorption properties of Cu-SSZ-13 materials and the partial oxidation of methanol.

Chapter 2

H₂ ADSORPTION ON Cu(I) EXCHANGED –SSZ-13

2.1 Introduction

Fuel cell electric vehicles were commercialized in 2015 and use 700 bar compressed hydrogen storage tanks as onboard hydrogen storage systems.¹⁵⁷ The ultimate goal in these vehicles is to develop onboard systems for a driving range greater than 300 miles, and for these onboard systems hydrogen storage capacity of 5.5 wt.% ($40 \text{ g}_{\text{H}_2} \text{ L}_{\text{system}}^{-1}$) at near ambient temperatures and at pressures under 100 bar are targeted. Despite the progress made in metal-organic frameworks (MOFs) with surface areas reaching $6240 \text{ m}^2 \text{ g}^{-1}$ and hydrogen capacities reaching 8.6 wt.% at cryogenic temperatures,¹²⁴ hydrogen uptakes at ambient temperatures currently do not surpass 1.5 wt.% at 100 bar.¹⁵⁸

The reason for low hydrogen adsorption capacities of adsorbents having high surface areas is the weak interaction of hydrogen molecule with the open metal centers. One of the highest binding energies reported is $12.3 \text{ kJ mol}^{-1} \text{ g}$ (with an observed H₂ bathochromic shift about 135 cm^{-1} in its vibrational frequency) on Co₂-*mdobdc* and Ni₂-*mdobdc* samples.¹⁵⁹ Cu(I) exchanged zeolites, on the other hand, result in H₂ adsorption enthalpies between -73 and $-39 \text{ kJ mol H}_2^{-1}$ (on Cu(I)-ZSM-5)¹³⁵ with $\nu(\text{H-H})$ bathochromic shifts near 1000 cm^{-1} .¹³³ This strong interaction between hydrogen and Cu(I) cation has been explained by the combined role of the zeolite framework oxygen atoms and electron back donation from Cu(I) to H₂ molecule. Oxygen atoms, to which Cu(I) cation coordinates, theoretically increase Cu

($3d_{\pi}$) orbital polarization and reduce Cu(I)- zeolite repulsion which favors Cu(I) ($3d_{\pi}$) \rightarrow H₂ (σ^*) back donation.^{139,140}

The most commonly used Cu(I) exchange methods on zeolites are the solid-state^{147,160} or vapor phase exchange^{133,146,161-163} of Cu(I) salts, which result in very high Cu(I) exchange extent up to Cu(I)/Al = 1,¹⁶⁰ however the solid state or vapor phase exchange of CuCl results in Cl residuals inside the zeolite pores.^{147,162,164} Cu(II) exchange in aqueous media, on the other hand, results in Cu(II)/Al ratios always smaller than 1 due to Cu(II) exchange near two Al sites. Therefore, residual free Cu(I) exchange methods that would result in Cu/Al ratios close to one are needed to achieve higher hydrogen adsorption capacities using Cu(I)- exchanged zeolites.

In this chapter, Cu(I)-exchanged SSZ-13 samples with different Si/Al ratios and different Cu(I) exchange methods have been tested for H₂ adsorption at both cryogenic and ambient temperatures and compared to other adsorbents. The hydrogen interaction strength of the prepared zeolites has been investigated using various techniques including powder neutron diffraction and variable temperature infrared spectroscopy. In addition to the solid state CuCl exchange method, Cu(I) exchange in liquid media has also been investigated.

2.2 Experimental

2.2.1 Zeolite Synthesis and Ion Exchange

SSZ-13 with Si/Al = 6 was prepared hydrothermally as reported by Pham et al.¹⁶⁵ A mixture of 10 g sodium silicate solution (Sigma Aldrich, 26.5% SiO₂), 0.32 g of NaOH (Fischer Scientific, >98%) and 24 g de-ionized water was stirred using a magnetic stirrer for 15 minutes at 25 °C. Subsequently, 1 g of Na-Y (Zeolyst CBV100,

Si/Al = 2.47) and 1.6 g of *N,N,N*-trimethyl-1-adamantanammonium iodide were added and stirred for 30 more minutes. The white solution was then transferred to 43 ml Teflon-lined autoclaves (Parr) (under autogenous pressure) and heated at a temperature of 150 °C for 6 days while tumbling the autoclaves at a rate of 45 rpm. The resulting solid crystallites were vacuum filtered and washed with 200 ml de-ionized water three times. The filtered solid (2– 3 g) was dried at 80 °C for 12 h (in air, Fisher Scientific Isotemp Lab Oven) and it was calcined in static air at a temperature of 560 °C for 8 hours (using a bench top muffle furnace, Thermolyne) using a heating rate of 5 °C min⁻¹. The resulting zeolite is designated Na/H-SSZ-13.

SSZ-13 with Si/Al = 12 was prepared by using a gel mixture having a composition of 1SiO₂: 0.035 Al₂O₃: 0.5 TMAdaOH: 20 H₂O. 11.81 g of tetraethyl orthosilicate (Sigma, >98%), 23.58 g of *N,N,N*-trimethyl-1-adamantanammonium hydroxide (TMAdaOH, Sachem Inc., 25 wt.%) and 2.13 g of de-ionized water were stirred for 2 hours at 25 °C. After getting a clear solution, 0.65 g of aluminum triethoxide (Al(OEt)₃, Sigma Aldrich, 97%) was added slowly and stirred for another 2 hours. The mixture was then transferred to Teflon lined autoclaves and heated to a temperature of 150 °C under static condition where it was maintained for 7 days. The resulting crystals were recovered using a centrifuge (International Equipment Company, Centra MP4, 4000 rpm) for 6 min, washed with de-ionized water (200 ml for 1 g) three times and dried at 80 °C for 3 h (in air, Fisher Scientific Isotemp Lab Oven). Formed zeolite was calcined in static air using same conditions used for Si/Al = 6. The resulting zeolite is designated H⁺-SSZ-13.

[B]-SSZ-13 was synthesized using the protocol from Regli et al.¹⁶⁶ 8.961 g of *N,N,N*-trimethyl-1-adamantanamine hydroxide (TMAdaOH, Sachem Inc., 25 wt.%)

was mixed with 17.5 g de-ionized water and 0.215 g H_3BO_3 (Sigma Aldrich, >99.5 wt.%) and stirred at room temperature for 30 minutes until having a homogeneous mixture. Then, 2.613 g of fumed silica (Cab-o-sil M-5, Cabot Corporation) was added to the mixture and stirred for 1 more hour. The homogenous mixture was then transferred to Teflon-lined autoclaves (Parr, 43 ml) and heated at 160 °C for 6 days with 75 rpm rotation. The solid product was then vacuum filtered, washed with de-ionized water and dried at 80 °C for 12 h. The as-made product was then calcined at 560 °C for 8 hours using a heating ramp of 3 °C min^{-1} . The resulting zeolite is designated H^+ -[B]-SSZ-13.

NH_4^+ -ZSM-5 was obtained following the synthesis and ion exchange procedures given in Yun et al.¹⁶⁷

2.2.1.1 NH_4^+ Exchange

NH_4^+ -SSZ-13 was obtained by exchanging 1 g of calcined Na/H-SSZ-13 (Si/Al = 6) in 500 ml 0.2 M NH_4NO_3 (Sigma Aldrich, >99%) solution. The suspension was stirred for 3 hours at a temperature of 80 °C for ion exchange and then the zeolite was filtered, washed with 500 ml de-ionized water and dried at a temperature of 80 °C in air for 4 h. This exchange procedure was repeated three times.

2.2.1.2 Na^+ Exchange

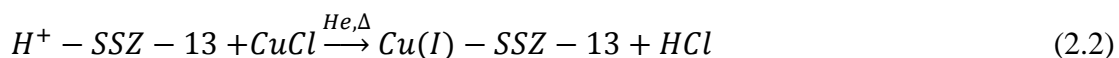
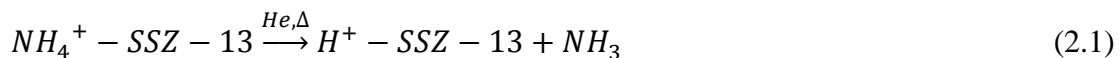
NH_4^+ -SSZ-13 was exchanged with Na^+ in 500 ml of a 0.1 M NaNO_3 (Sigma Aldrich >99%)/ de-ionized water solution at a temperature of 80 °C for 3 hours to obtain Na-SSZ-13. The samples were vacuum filtered and washed with de-ionized water as described in NH_4^+ exchange. Na-SSZ-13 samples (Si/Al = 6 and Si/Al = 12)

were tested for hydrogen adsorption capacities and compared to Cu(I)-SSZ-13 samples.

2.2.1.3 Solid State Cu(I)Cl Exchange

Cu(I) exchange of NH_4^+ -SSZ-13 was performed via solid state CuCl exchange of H^+ -SSZ-13 in a quartz flow reactor (Figure 2.1). NH_4^+ ion exchange performed for as-prepared Na/H-SSZ-13 (Si/Al = 6) sample as explained above. Ion exchanged NH_4^+ -SSZ-13 was dried under vacuum ($<500 \mu\text{mHg}$) at $90 \text{ }^\circ\text{C}$ for 12 hours to ensure there is no water vapor entrapped inside the zeolite pores. After measuring the dry weight, dehydrated NH_4^+ -SSZ-13 (300– 400 mg) was placed inside the quartz flow reactor having 30 mm diameter and 210 mm length. The temperature of the system was increased to $560 \text{ }^\circ\text{C}$ with a heating rate of $2 \text{ }^\circ\text{C min}^{-1}$. To heat the reactor, Ceramic Radiant Full Cylinder heater from OMEGA (CRFC-26/120-A) and a temperature controller (Cole Parmer, Love controls 16A) were used. The ammonium groups of NH_4^+ -SSZ-13 were decomposed (Eq. 2.1) to give H^+ -SSZ-13 at $560 \text{ }^\circ\text{C}$ under $50 \text{ cm}^3 \text{ min}^{-1}$ helium (Keen Gas, 99.999% purity) flow for 10 hours. After cooling the sample to $100 \text{ }^\circ\text{C}$, the gas inlet and outlet of the reactor were sealed using close-ended Ultra-Torr vacuum fittings and the reactor was transferred to a dry argon glove box. A predetermined amount of CuCl (Sigma Aldrich, 97%), to give $\text{Cu(I)/H}^+ = 1$, was dried at a temperature of $80 \text{ }^\circ\text{C}$ under vacuum conditions ($<500 \mu\text{mHg}$) for 12 hours, and then mixed with the H^+ -SSZ-13 inside the glovebox using a mortar and pestle for 5 min. The resulting zeolite and CuCl mixture was placed back into the reactor and the reactor was transferred to the synthesis set-up and connected to helium flow without being exposed to oxygen or water vapor. The quartz reactor was heated initially to $300 \text{ }^\circ\text{C}$ with a heating rate of $2 \text{ }^\circ\text{C min}^{-1}$ and the temperature was maintained at $300 \text{ }^\circ\text{C}$ for

6 hours to allow Cu(I) exchange (Eq. 2.2.). Formed HCl vapor was carried out of the reactor with a continuous 50 cm³ min⁻¹ helium flow.



The height of the bed containing the zeolite and CuCl mixture in the reactor did not exceed 5 mm to ensure uniform exchange. After 6 h of CuCl exchange, the samples were further heated to a temperature of 550 °C (using a heating rate of 2 °C min⁻¹) for 10 h to remove excess CuCl from the sample. Cu(I)-ZSM-5 was also obtained starting from NH₄⁺-ZSM-5 using the method explained above. Cu-[B]-SSZ-13 sample was treated at 550 °C for 9 h. Another Cu(I)-SSZ-13 (Si/Al = 6) sample was Cu(I) exchanged at 560 °C for 8 h under 50 cm³ min⁻¹ He flow, then the temperature was increased to 750 °C at a heating rate of 1 °C min⁻¹ and kept at 750 °C for 9 h in order to further reduce the Cl content. The resulting Cu(I)-zeolite samples were transferred to the argon glovebox and stored there for further applications.

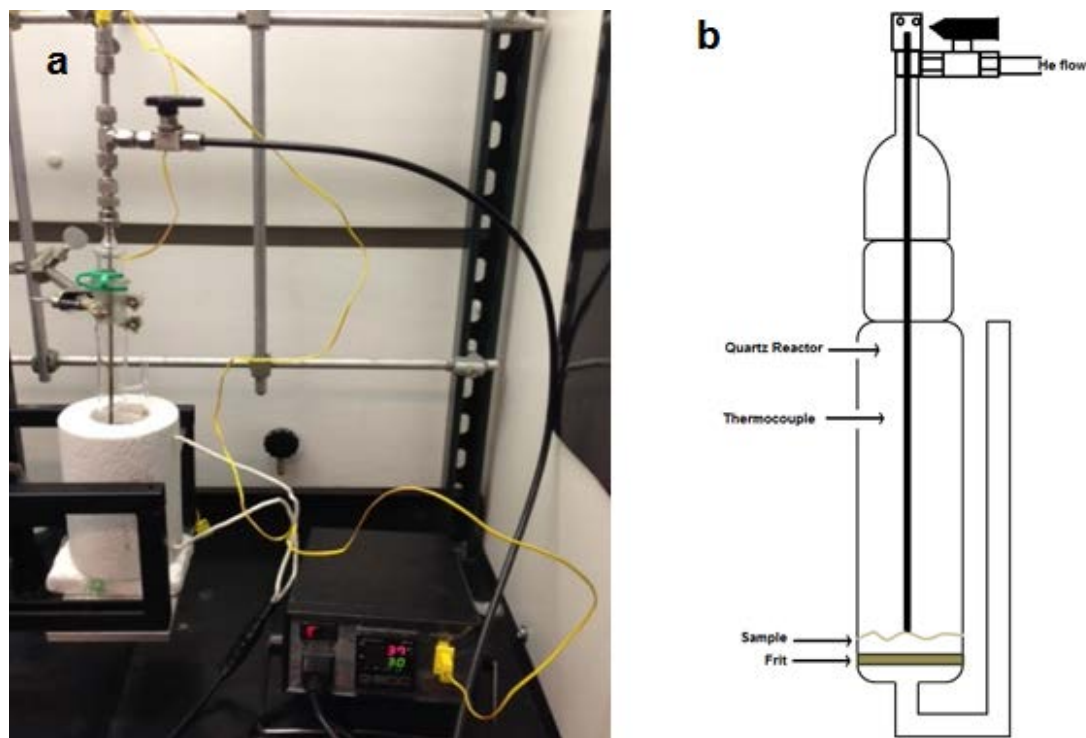


Figure 2.1: a) Solid State CuCl exchange set-up b) Schematic representation of the quartz reactor

2.2.1.4 Liquid Phase Cu(I) Exchange

1.1 g of H^+ -SSZ-13 (Si/Al = 12) sample was dehydrated under vacuum conditions at 300 °C for 6 h. Dehydrated sample was exchanged in 240 ml acetonitrile (Sigma Aldrich, 99.8%) solution containing 0.015 M CuCl (Sigma Aldrich, 97%) by stirring at 25 °C for 10 h. The solution was maintained O_2 free by purging $50 \text{ cm}^3 \text{ min}^{-1}$ N_2 (Keen Gas, 99.999%) through the acetonitrile solution using a bubbler. After the exchange was completed, the sample was filtered, washed with 250 ml methanol and dried at 80 °C for 12 h. The color of the sample after being exposed to air was white.

The residual acetonitrile was eliminated from the sample by oxidation of the sample. After the sample was pelleted and sieved (between 250 and 425 μm), it was

placed in a quartz reactor (ID = 7 mm) and was supported by quartz wool. A ceramic radiant full cylinder heater (Omega, CRFC-26/120-A) was used to heat the quartz tube. The furnace temperature was controlled using a thermocouple placed around the center of the quartz tube and an Omega CN/74000 temperature controller. The temperature was increased to 350 °C (using a heating rate of 10 °C min⁻¹) by flowing 50 cm³ min⁻¹ 10% O₂ balance He. The temperature was maintained at 350 °C for 4 h for complete oxidation of residual acetonitrile. The color of the sample was observed to be light blue color after the sample was exposed to air O₂ and humidity, indicating accessible Cu cations.

2.2.2 Analytical Methods

The samples that were exposed to air were characterized by Powder X-Ray Diffraction using a Phillips X'Pert diffractometer equipped with a Cu K α source ($\lambda = 1.5418 \text{ \AA}$). The diffractograms were obtained over the 2θ range of 5 to 50° using a step size of 0.01°. XRD patterns were also obtained by mixing 0.005 g of standard silicon powder with 0.02 g of zeolite. Measured diffractograms were corrected using Si (111) peak position of 28.465° at $\lambda = 1.5418 \text{ \AA}$ (Si lattice spacing: 5.4307 Å) and further analyzed using CelRef Unit-Cell Refinement software (developed by Jean Laugier and Bernard Bochu),¹⁶⁸ where unit cell parameters of a rhombohedral lattice system with a space group type of $R\bar{3}m$ were refined for sodium and copper exchanged zeolites.

The elemental compositions of samples are determined by Inductively Coupled Plasma Optical Emission Spectroscopy (ICP-OES) technique in Galbraith Laboratories, Knoxville, Tennessee. Compositions are also obtained by using Energy Dispersive X-ray spectra (EDX) with electrons supplied from JEOL JSM 7400F

electron microscope operating with an accelerating voltage of 15 kV and a current of 10 μ A.

Cu(I)-zeolites have been shown to bind nitrogen gas strongly even at room temperature (-80 kJ mol^{-1} for Cu(I)-ZSM-5).¹⁶⁹ Therefore, texture properties of the Cu(I)-exchanged zeolites were determined using argon (Keen Gas, 99.999% purity) adsorption at a temperature of $-196 \text{ }^\circ\text{C}$ with Micromeritics ASAP 2020 Surface Area and Porosity Analyzer. Na-SSZ-13 samples were characterized with nitrogen (Keen Gas, 99.999% purity) adsorption at $-196 \text{ }^\circ\text{C}$ after being dehydrated at a temperature of $350 \text{ }^\circ\text{C}$ for 6 hours under vacuum conditions ($500 \text{ } \mu\text{mHg}$). Cu(I) exchanged zeolites, on the other hand, were vacuum activated at a temperature of $425 \text{ }^\circ\text{C}$ for 6 hours. The free space volume was measured using helium (Keen Gas, 99.999% purity) before the analysis. The samples were evacuated (at $2 \text{ } \mu\text{mHg}$) at room temperature for 2 h in order to fully evacuate He from the pores prior to adsorption measurements. The temperature of the sample during adsorption and free space measurements was set to $-196 \text{ }^\circ\text{C}$ using a dewar filled with liquid nitrogen during analysis.

The micropore volume of the prepared samples was calculated using statistical thickness method (t-plot)¹⁷⁰ and Harkins and Jura¹⁷¹ thickness equation over the thickness range of 3.5 to 5 \AA (Eq. 2.3):

$$t(\text{\AA}) = \left(\frac{13.99}{0.034 - \log(P/P_0)} \right)^{0.5} \quad (2.3)$$

2.2.3 Hydrogen Adsorption Experiments

Hydrogen adsorption experiments were performed using ultra high purity grade (Keen Gas, 99.999%) dihydrogen and Micromeritics ASAP 2020 instrument. Na-SSZ-13 samples (powder, around 150 mg) were pretreated at $350 \text{ }^\circ\text{C}$ for 6 hours

prior to hydrogen adsorption in order to eliminate water vapor or other adsorbates. Cu(I) exchanged samples (powder, around 150 mg) were vacuum activated (500 μmHg) at 425 $^{\circ}\text{C}$ for 6 hours at the degas port of Micromeritics ASAP 2020 instrument. The sample tubes were backfilled with argon gas at room temperature after degassing was complete. After transferring the sample tubes to the analysis port, the zeolites were evacuated at a temperature of 425 $^{\circ}\text{C}$ for 15 min for complete desorption of argon. Evacuation at 2 μmHg continued for 45 more minutes at room temperature. Free space volume measurement and following 2 h evacuation at room temperature were performed as explained in pore volume characterization section. During adsorption experiments and free space measurements, temperature of the samples was controlled using liquid nitrogen (-196 $^{\circ}\text{C}$) filled dewar or using an ethylene glycol-water mixture bath. The temperature of the mixture was controlled using LAUDA Alpha RA 12 temperature controller by flowing the same mixture through a glass-jacketed beaker containing ethylene glycol-water mixture.

The hydrogen adsorption isotherms were obtained for a pressure range of 10–760 mmHg of hydrogen. The absolute hydrogen adsorption amounts were reported in mmol H_2 per gram of zeolite. The excess hydrogen adsorption amounts for tested samples were also calculated using Eq. 2.4:

$$q_{ex} = q - \rho_H V_a \quad (2.4)$$

where q_{ex} is the excess hydrogen adsorption amount ($\text{mmol H}_2 \text{ g}_{\text{zeolite}}^{-1}$), q is the absolute adsorption amount ($\text{mmol H}_2 \text{ g}_{\text{zeolite}}^{-1}$), ρ_H is the bulk density of hydrogen at adsorption pressure and temperature (0.03913 mmol cm^{-3} at 30 $^{\circ}\text{C}$ and 1 atm) and V_a is the pore volume of the adsorbent, which was determined experimentally.

Hydrogen adsorption isotherms (obtained at -196 °C) belonging to Cu(I)-SSZ-13 (Si/Al = 6) were fitted to Toth Adsorption Isotherm Model (Eq. 2.5), whereas, adsorption isotherms (obtained at 30 °C) belonging to Cu(I)-[B]-SSZ-13 were fitted to Sips Isotherm (Eq. 2.6) and a linear model for pressures higher than 0.2 atm (Eq. 2.7).

$$q = q_{max} \frac{KP}{(1+(KP)^t)^{1/t}} \quad (2.5)$$

$$q = q_{max} \frac{(K*P)^n}{1+(K*P)^n} \quad (2.6)$$

$$q = aP + b \quad (2.7)$$

where q is the total amount of H₂ adsorbed per gram of zeolite at the equilibrium pressure (P).

2.2.4 *In situ* FTIR Experiments

Fourier transform infrared spectra were obtained in collaboration with Dr. Silvia Bordiga. IR spectra were recorded using Nicolet 6700 FTIR Spectrometer equipped with a mercury cadmium telluride (MCT) cryodetector. 256 scans were collected for each spectrum with 1 cm⁻¹ resolution. Thin self-supporting wafers of zeolite samples were used in a transmission IR cell designed to allow *in vacuo* high temperature treatments, *in situ* gas dosage and low temperature measurements.

Adsorption of H₂ as the probe molecule on Cu(I)-SSZ-13 (Si/Al = 12) and Na-SSZ-13 (Si/Al = 12) samples was performed as follows. A zeolite wafer was prepared that has been hydrated at room conditions. Then the wafer has been evacuated at room temperature for 12 h prior to heating the sample to the temperature of 500 °C with a heating rate of 3 °C min⁻¹. The evacuation at this temperature continued for 3 h. After gradually cooling the sample to the temperature of -23 °C, 40 mbar of hydrogen was dosed to the cell. Spectra were collected at every 10 °C temperature drop after

reaching equilibrium. For Figure 2.8 inset, the spectra taken with the zeolite samples prior to the gas dosage was used as the background to be able to differentiate the perturbed H–H stretching bands more easily.

2.2.5 Diffuse Reflectance Infrared Fourier Transform Spectroscopy

Diffuse Reflectance Infrared Fourier Transform spectra (DRIFTS) of Cu(I)-SSZ-13 (Si/Al = 12) sample prepared by Cu(I) exchange in acetonitrile was obtained using a FTIR spectrometer (Nicolet Nexus 470) and a high temperature diffuse reflectance cell (Harrick, Praying Mantis). The spectrometer is equipped with an MCT-A (mercury cadmium telluride) detector and operated at resolution of 4 cm^{-1} .

Cu(I)-SSZ-13 (Si/Al = 12) sample prepared by CuCl exchange in acetonitrile was placed inside the sample holder of the diffuse reflectance cell and dehydrated at $450\text{ }^{\circ}\text{C}$ (with a heating rate of $5\text{ }^{\circ}\text{C min}^{-1}$) for 1 h by flowing $30\text{ cm}^3\text{ min}^{-1}$ He (Keen Gas, 99.999% purity). The spectra were collected during dehydration.

2.2.6 Powder Neutron Diffraction (PND) Experiments

Neutron Powder Diffraction (NPD) experiments were conducted on the high resolution diffractometer, BT1 at the National Institute of Standards and Technology Center for Neutron Research, Gaithersburg, MD. The wavelength was selected using a Ge(311) monochromator with an in-pile $60'$ collimator ($\lambda = 2.0787(2)\text{ \AA}$). Patterns were collected using 32 He detectors over the 2θ range of $1.3\text{--}166.3^{\circ}$ with 0.05° step size. Cu(I) SSZ-13 sample (Si/Al = 6, 0.891 g) was pretreated at $425\text{ }^{\circ}\text{C}$ for 6 hours and placed into a cylindrical Vanadium can in a dry helium box. The vanadium can was sealed with an Indium o- ring. The residual helium inside the vanadium can was removed using a turbo molecular pump prior to diffraction experiment. The

temperature of the sample was set to -263 °C and 27 °C using a closed cycle helium refrigerator.

H₂ adsorption onto pretreated sample was performed by calculating the precise amount of H₂ (H₂/ Cu = 0.5). H₂ was loaded at 27 °C and then cooled to -263 °C for diffraction experiment.

Rietveld refinement of the collected NPD data were performed using GSAS¹⁷² package along with EXPGUI (graphical user interface).¹⁷³ In Rietveld refinement of PND data, a hexagonal unit cell with the space group type $R\bar{3}m$ was used. Cu(II)-SSZ-13 (Si/Al = 12) NPD data was used as starting atomic coordinates for chabazite (CHA) framework.¹⁷⁴ After setting the experimental background manually, it was fitted using Shifted Chebyshev equation using 12 parameters. Peak profile terms (using pseudo-Voigt function with Finger-Cox-Jephcoat asymmetry) and unit cell parameters were fitted using Le Bail method. Atomic positions, occupancies and thermal displacement parameters (U_{iso}) were then fitted using Rietveld refinement and using soft constraints on tetrahedral bond lengths (T–O). The tetrahedral bond length (T–O) was set to 1.61 ± 0.03 with the restraint weight of 10. The occupancies of each framework and extra-framework atom have been refined without constraints for the diffraction data obtained with D₂ loading. Cu occupancies for bare Cu-SSZ-13 samples were then fixed to the refined values obtained from diffraction data with D₂ adsorption.

2.3 Results and Discussion

2.3.1 Material Characterization

Initial characterization of Na-SSZ-13 and Cu(I)-SSZ-13 samples by powder X-ray Diffraction showed that Cu(I)-SSZ-13 and Na-SSZ-13 zeolites are pure chabazite

with high crystallinity (Figure 2.2). The vapor phase exchange of CuCl and further treatment of the samples up to the temperature of 750 °C did not result in sample degradation. Refined rhombohedral unit cell parameters (a , α) for Na and Cu(I)-exchanged zeolites were given in Table 2.1. Na- and Cu(I)-SSZ-13 samples with Si/Al ratio of 6 have higher unit cell volumes (805 and 799 Å³ respectively) than the volumes of Na- and Cu(I)-SSZ-13 samples with Si/Al ratio of 12 (785 and 786 Å³ respectively) due to higher concentration of Al–O bonds in SSZ-13 (Si/Al = 6) ($d_{\text{Al-O}}$: 1.73 Å & $d_{\text{Si-O}}$: 1.61 Å).¹⁷⁵ Cu-[B]-SSZ-13 sample, on the other hand, has smaller unit cell volume (767 Å³) due to shorter B–O bonds ($d_{\text{B-O}}$: 1.51 Å)¹⁷⁶ than Si–O bonds.

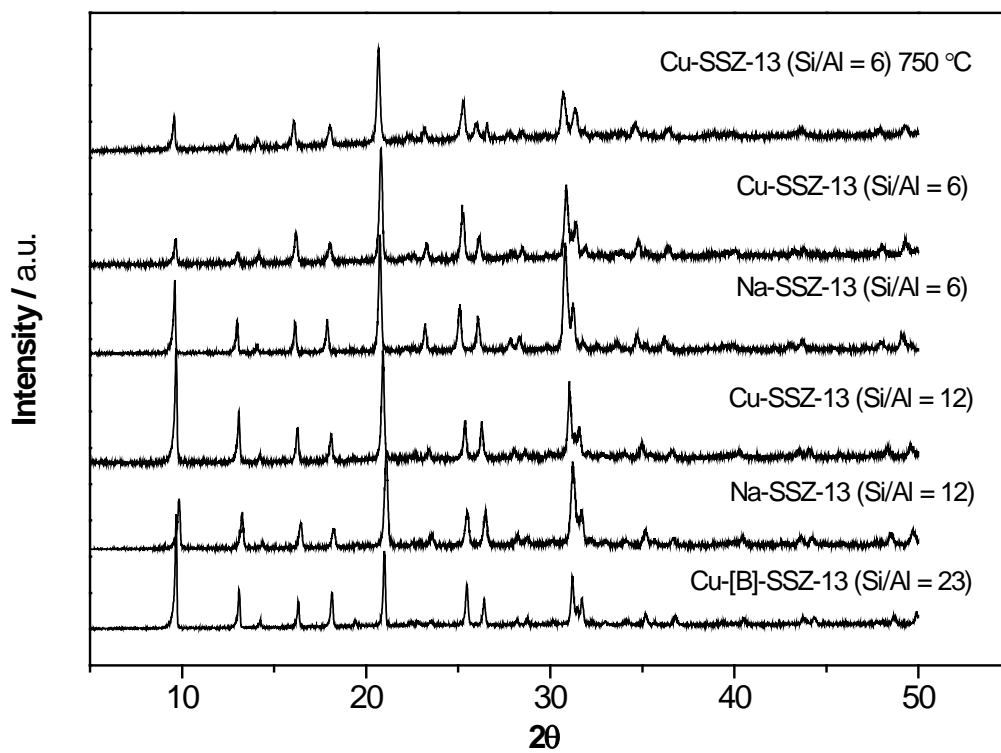


Figure 2.2: Powder XRD pattern of Na-SSZ-13 (Si/Al=6 & 12), Cu-SSZ-13 (Si/Al=6 & 12) and Cu-[B]-SSZ-13 samples, Cu K α , $\lambda = 1.5418 \text{ \AA}$

Table 2.1: Refined rhombohedral unit cell parameters ($R\bar{3}m$) for prepared Na- and Cu(I)-SSZ-13 zeolites using CelRef Unit-Cell refinement software¹⁶⁸

Sample	$a / \text{Å}$	α	Volume / Å^3
Cu(I)-[B]-SSZ-13	9.1804	94.33	766.7
Cu(I)-SSZ-13 (Si/Al = 12)	9.2588	94.41	786.3
Na-SSZ-13 (Si/Al = 12)	9.2528	94.36	784.9
Cu(I)-SSZ-13 (Si/Al = 6)	9.3089	94.49	798.8
Na-SSZ-13 (Si/Al = 6)	9.3279	94.24	804.6

Solid state Cu(I) exchange of SSZ-13 samples resulted in 97% and 98% Cu(I) exchange for Si/Al = 6 and Si/Al = 12 samples (Table 2.2), which is equivalent to 13.2 and 8.6 wt.% Cu concentration (2.07 mmol Cu g⁻¹ and 1.33 mmol Cu g⁻¹) respectively.

For all Cu(I) exchanged samples, ‘extra’ chlorine was observed in the final product. The reaction between the Brønsted acid sites of ZSM-5 and CuCl occurs at the temperature of 300 °C based on the observation of HCl vapor at that temperature.¹⁷⁷ There are some contradictory observations reported on the ‘excess’ CuCl residing within the zeolite. One hour heat treatment at the temperature of 500 °C after vapor phase exchange of CuCl with H-ZSM-5 having Si/Al = 90 was shown to remove most of the excess CuCl.¹⁷⁷ However, solid state CuCl exchanged ZSM-5 (Si/Al = 11) contains 0.48 Cl/Al even after 40 h heat treatment in helium at the temperature of 550 °C.⁵⁴ Sen et al. reported formation of chlorine ion tetrahedra inside the supercage and the sodalite cage of FAU coordinated to four copper cations that are either bonded to three oxygen atoms of 6 member ring or further connected to two framework oxygen atoms of 12 member ring by single crystal diffraction of vapor phase CuCl exchanged Na-Y.¹⁶² In our case, 10 h treatment at a temperature of 550 °C was insufficient to eliminate ‘extra’ CuCl that is occluded in the crystals. Increasing the treatment temperature to 750 °C for CuCl exchange of SSZ-13 (Si/Al = 6) resulted in a lower chlorine content, together with lower Cu(I) exchange (Table 2.2).

Calculated micropore volumes of samples were also given in Table 2.2. Lower concentration of Na in SSZ-13 (Si/Al = 12) zeolite results in a higher available pore volume for adsorption compared to Na-SSZ-13 (Si/Al = 6). For Cu(I) exchanged samples, extra chlorine content together with high Cu(I) concentration caused lower

micropore volumes than those of Na exchanged zeolites. Higher micropore volumes were observed when Cu content was lower as in Cu(I)-[B]-SSZ-13 sample.

Table 2.2: t-plot micropore volumes and chemical compositions of prepared Na- and Cu(I)- samples obtained from ICP-OES and EDX

Samples	Chemical Composition				M (Cu or Na) concentration / mmol M g ⁻¹	Micropore Volume / cm ³ g ⁻¹
	Si/Al or Si/B	Cu(I)/Al or Cu(I)/B	Na/Al	Cl/Al or Cl/B		
Cu(I)-SSZ-13 (Si/Al = 6)	5.8	0.97 ^a		0.16	2.07	0.182
Cu(I)-SSZ-13 (Si/Al = 6)-750°C	6.0	0.65 ^a		0.06	1.41	0.239
Cu(I)-[B]-SSZ-13	23.5	0.70 ^a		0.08	0.46	0.248
Na-SSZ-13 (Si/Al = 6) ^b	4.8±0.8		0.94±0.12		2.54	0.233
Cu(I)-SSZ-13 (Si/Al = 12) ^b	10.2±0.7	0.98±0.14 ^a		0.34±0.06	1.33	0.183
Na-SSZ-13 (Si/Al = 12) ^b	9.1±0.7		0.76±0.08		1.22	0.265

a: Cu/Al (or Cu/B) ratios were calculated by subtracting Cl/Al (or Cl/B) ratio from total Cu/Al (or Cu/B) ratio assuming presence of occluded CuCl

b: Determined by using EDX with an accelerating voltage of 15 kV and a current of 10 μA

2.3.2 H₂ Adsorption Isotherms

Hydrogen adsorption isotherms belonging to Cu(I)- and Na- SSZ-13 samples are given in Figure 2.3 and 2.4. At 30 °C and -196 °C; Cu(I)-SSZ-13 and Na-SSZ-13 zeolites with Si/Al = 6 showed better hydrogen adsorption capacity on per gram basis than Cu(I)-SSZ-13 and Na-SSZ-13 zeolites having Si/Al = 12 due to higher concentrations of Na and Cu(I) cations. When the hydrogen adsorption capacities per mol of Cu cation is calculated, Si/Al = 6 and Si/Al = 12 have similar capacities at

similar conditions (0.097 versus 0.085, Table 2.3). At 30 °C, Cu(I)-[B]-SSZ-13 sample showed remarkable hydrogen adsorption capacity both per gram basis and per mol of Cu, reaching 0.05 wt.% H₂ adsorption capacity at 1 atm H₂ pressure.

H₂ adsorption capacities of metal organic frameworks and other potential hydrogen adsorbents are often not reported at room temperature and at atmospheric pressure. Instead, adsorption capacities at higher pressures are reported to compensate for the low adsorption enthalpy values (-4– -12 kJ mol⁻¹) observed on metal organic frameworks.¹⁷⁸ Hydrogen adsorption capacities at room temperature and 1 atm hydrogen pressure for the metal organic frameworks reported in Table 2.3 are calculated here by extrapolating the experimental data reported for higher pressures. Cu(I)-SSZ-13 (Si/Al = 6), Cu(I)-SSZ-13 (Si/Al = 6)- 750 °C, and Cu(I)-[B]-SSZ-13 samples showed total and excess H₂ adsorption capacities (per gram basis) that are higher than Cu(I)-ZSM-5 and triple that of IRMOF-8 at 1 atm (Table 2.3).

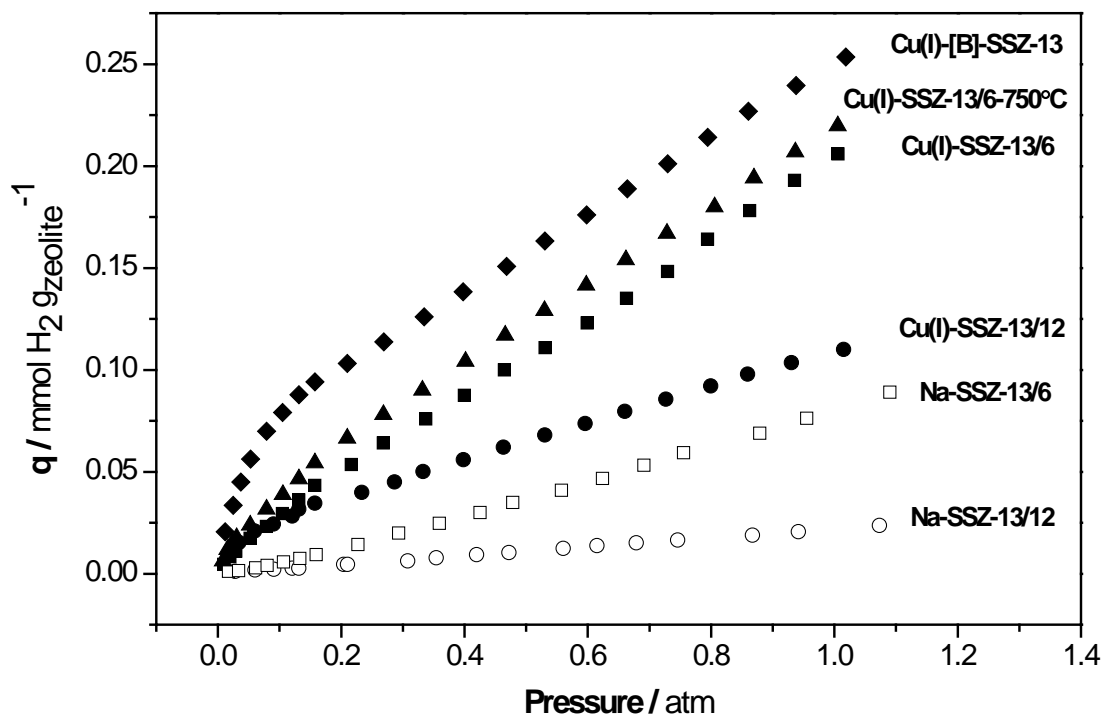


Figure 2.3: Hydrogen adsorption isotherms for Na- and Cu(I)-samples at 30 °C. Sample names are given in M-SSZ-13/xx format, where M represents the cation type and xx represents the Si/Al ratio.

At 30 °C, all samples except Cu(I)-[B]-SSZ-13 showed linear adsorption trend at lower pressures similar to Henry's law isotherm. After 0.3 atm hydrogen pressures, the isotherms could be fitted to Toth adsorption isotherm model (Eq. 2.5) which accounts for the surface heterogeneity. Cu(I)-[B]-SSZ-13, on the other hand, followed Sips adsorption model (Eq. 2.6) up to pressures of 0.2 atm and then showed a linear adsorption model, indicative of heterogeneous hydrogen adsorption sites at very low concentrations.

Table 2.3: Total and excess hydrogen adsorption amounts per gram of adsorbent and per cm³ of pore volume at the equilibrium pressure of 1 atm and temperature of 30 °C

Adsorbent	Total Adsorption / mmol H ₂ g ⁻¹	Excess Adsorption / mmol H ₂ g ⁻¹	Micropore Volume / cm ³ g ⁻¹	Excess Adsorption / mol H ₂ mol Cu ⁻¹	Excess Adsorption / mmol H ₂ cm ⁻³	Ref
Cu(I)-[B]-SSZ-13	0.250	0.240	0.248	0.522	0.968	^a
Cu(I)-SSZ-13	0.232	0.223	0.239	0.158	0.933	^a
(Si/Al=6)-750 °C						
Cu(I)-SSZ-13 (Si/Al=6)	0.208	0.201	0.182	0.097	1.104	^a
Na(I)-SSZ-13 (Si/Al=6)	0.077	0.068	0.233	0.027	0.292	^a
Cu(I)-SSZ-13 (Si/Al=12)-CH ₃ CN	0.228					^a
Cu(I)-SSZ-13 (Si/Al=12)	0.120	0.113	0.183	0.085	0.617	^a
Na(I)-SSZ-13 (Si/Al=12)	0.0220	0.012	0.265	0.010	0.045	^a
Cu(I)-ZSM-5 (Si/Al=12)	0.185	0.181	0.113	0.190	1.602	^a
Cu(I)-ZSM-5 (Si/Al=22) ^b	0.201					133
MOF-177 monolith ^c		0.039	1.920		0.020	179
IRMOF-8 ^c		0.063	0.640		0.098	125
MOF-5 ^c		0.0265	1.695		0.016	158
Fe-BTT ^c		0.0295	0.715		0.041	180

a: Adsorption at 1 atm and 30 °C, this work

b: Adsorption at 1 atm and 20 °C extrapolated to 1 atm using the isotherm starting at higher pressure values

c: Adsorption at 1 atm and 25 °C, extrapolated to 1 atm using the isotherm starting at higher pressure values

Hydrogen adsorption isotherms at 20 °C, 30 °C, and 40 °C have been obtained on Cu(I)-SSZ-13 (Si/Al = 6) sample and fitted to Toth adsorption model for pressures higher than 0.3 atm (Appendix A.1.1). Then, the isosteric heat of hydrogen adsorption has been calculated using Clausius- Clapeyron equation at constant hydrogen loadings (0.08–0.13 mmol H₂ g⁻¹, 0.04 –0.07 H₂/Cu(I), Figure 2.5). The calculated isosteric heat of adsorption on Cu(I)-SSZ-13 (Si/Al = 6) was found to be between 20 and 23 kJ mol H₂⁻¹. This adsorption enthalpy is in excellent agreement with the optimal hydrogen adsorption enthalpy value that was calculated to be in the range of -22 – -25 kJ mol⁻¹

for hydrogen adsorption (at loading pressure of 30 bar) and desorption (exhaust pressure of 1.5 bar) at ambient temperature.¹³⁸

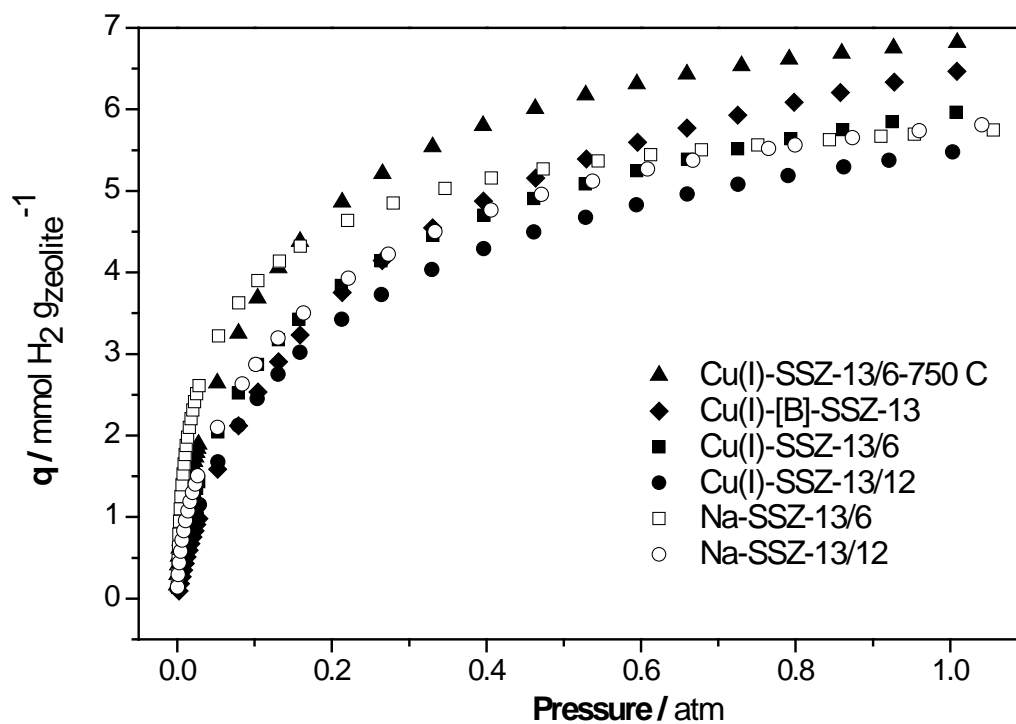


Figure 2.4: Hydrogen adsorption isotherms for Na- and Cu(I)-samples at -196 °C. Sample names are given in M-SSZ-13/xx format, where M represents the cation type and xx represents the Si/Al ratio.

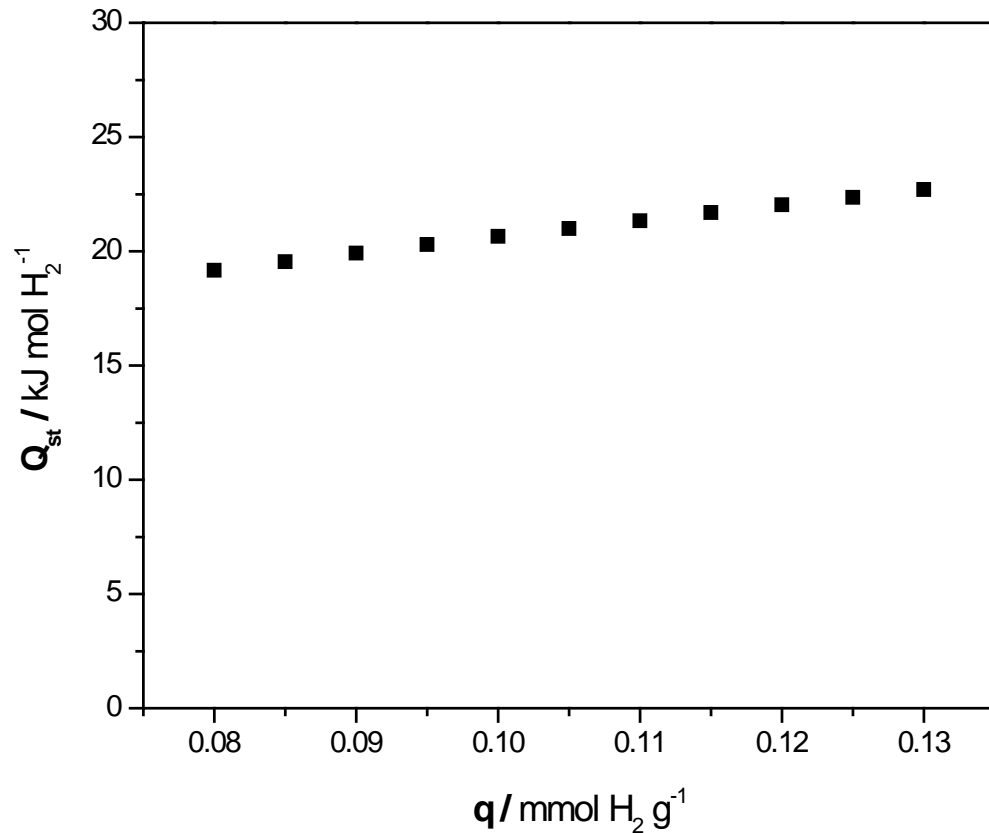


Figure 2.5: Calculated isosteric heat of adsorption versus adsorbed hydrogen amounts on Cu(I)-SSZ-13 (Si/Al = 6) for the temperature range between 20 °C and 40 °C

Hydrogen adsorption isotherms at 30 °C, 40 °C and 50 °C were also obtained on Cu(I)-[B]-SSZ-13 to calculate the isosteric heat of hydrogen adsorption. The adsorption isotherms have been fitted using Sips model (Eq. 2.6) and a linear model (Eq. 2.7) as explained above. Isotheres have been obtained using these models, from which isosteric heat of adsorption has been calculated (Appendix A.1.2). Figure 2.6

shows the changes in the heat of adsorption at constant hydrogen loadings between 0.02 and 0.17 mmol H₂ g⁻¹ (0.04–0.37 H₂/Cu(I)). The adsorption enthalpy values are found to be between 20 kJ mol⁻¹ and 50 kJ mol⁻¹, which explain much higher hydrogen adsorption capacity of Cu(I)-[B]-SSZ-13 sample at 30 °C.

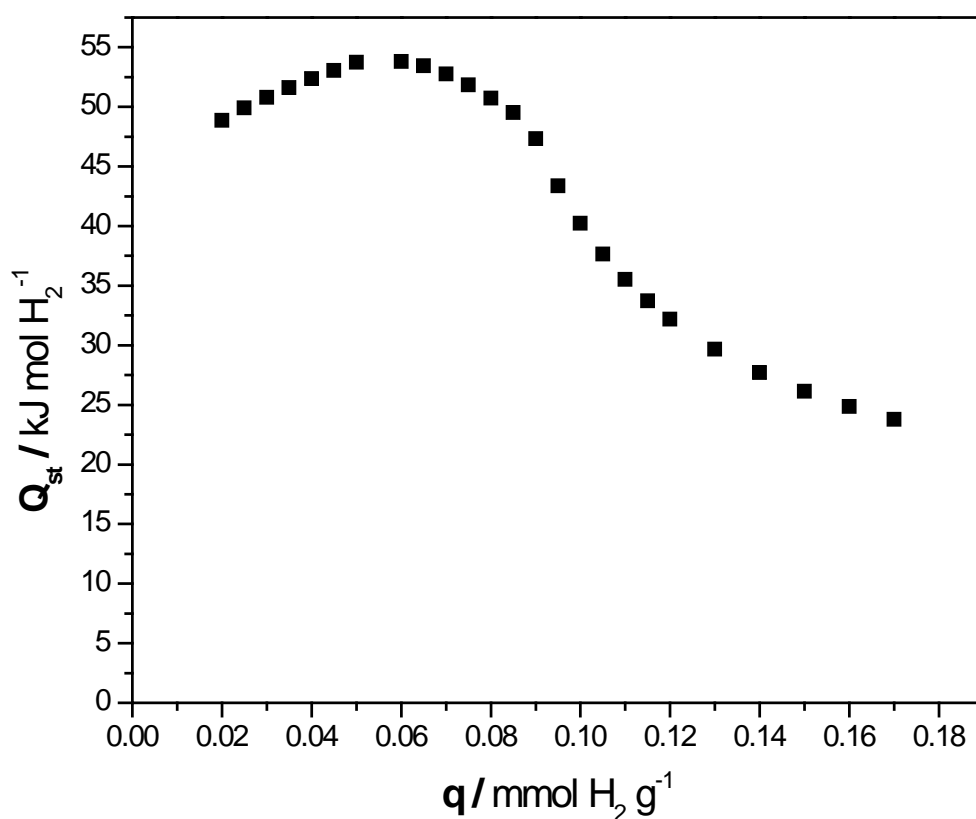


Figure 2.6: Calculated isosteric heat of adsorption versus adsorbed hydrogen amounts on Cu(I)-[B]-SSZ-13 for the temperature range between 30 °C and 50 °C

At the temperature of -196 °C, Na-SSZ-13 samples (Si/Al = 6 and Si/Al = 12) adsorbed more hydrogen molecules than Cu(I) exchanged samples especially at lower pressure regions (Figure 2.4). The hydrogen adsorption isotherms were fitted to Toth adsorption isotherm model in order to get information on kinetics of adsorption. The calculated higher Henry's constant values ($\text{mmol H}_2 \text{ g}^{-1} \text{ atm}^{-1}$) for Na-SSZ-13 zeolites indicate higher adsorption capacity and kinetics for Na-SSZ-13 samples than those for Cu(I)-SSZ-13 samples (Table A.4) at -196 °C per g of zeolite basis.

Total hydrogen adsorption capacity for Cu(I)-SSZ-13 (Si/Al = 6)-750 °C sample and Cu(I)-[B]-SSZ-13 sample exceeded that of Na-SSZ-13 (Si/Al = 6) sample at higher hydrogen pressures. At 1 atm of H_2 pressure, mmol H_2 adsorbed per mmol Cu content values are 4.8 and 14.10 for Cu(I)-SSZ-13 (Si/Al = 6)-750 °C and Cu(I)-[B]-SSZ-13 samples respectively, which indicates interaction of hydrogen molecules with zeolite pores. Higher micropore volumes (0.239 and $0.248 \text{ cm}^3 \text{ g}^{-1}$, Table 2.2) of these samples can explain higher adsorption capacities when compared to Cu(I)-SSZ-13 (Si/Al = 6) sample, which has smaller micropore volume ($0.182 \text{ cm}^3 \text{ g}^{-1}$, Table 2.2).

2.3.3 *In situ* FTIR Experiments

IR spectra of *in vacuo* heat treated (at the temperature of 500 °C) Cu(I)- and Na- exchanged samples in the OH stretching region ($3000 - 3800 \text{ cm}^{-1}$) are compared with Cu-SSZ-13 (Si/Al = 12, Cu/Al = 0.44) prepared by copper (II) acetate exchange¹⁵⁵ in Figure 2.7. Absence of the bands at 3610 cm^{-1} and 3597 cm^{-1} (denoted as d and e in Figure 2.7), which were assigned to the Brønsted acid sites,^{155,181} indicates a near complete exchange of the Brønsted acid sites with Na and Cu(I) cations for CuCl and NaNO_3 exchanged SSZ-13 (Si/Al = 12) samples.

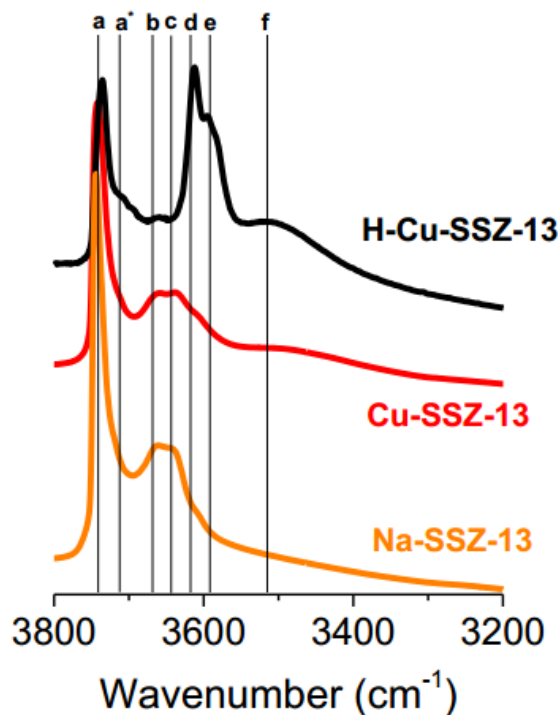


Figure 2.7: IR spectra in the OH region for samples Cu-SSZ-13 (Si/Al = 12, Cu/Al = 0.44, copper (II) acetate exchanged), Cu(I)-SSZ-13 (Si/Al = 12, Cu/Al = 0.98, CuCl exchanged) and Na-SSZ-13 (Si/Al = 12, Na/Al = 0.76) denoted as H-Cu-SSZ-13, Cu-SSZ-13 and Na-SSZ-13 respectively. The bands indicated by letters are; a & a*: external and internal silanol groups, b & c: hydroxyl groups of extra-framework aluminum, d & e: high frequency and low frequency Brønsted acid sites, f: highly defective silanol nests

Bands in the 3645– 3670 cm⁻¹ region are observed for both Cu(I)- and Na-SSZ-13 sample. It is reasonable to assign these bands to extra-framework Al–OH groups, which could be formed by the static air heat treatment of the samples at the temperature of 560 °C during preparation.¹⁸²

Free hydrogen $\nu(\text{HH})$ mode is active only in Raman scattering, therefore any band appearing in IR spectroscopy is associated with stretching frequencies of a H–H bond perturbed by the hydrogen adsorption process. A hydrogen molecule perturbed

by the external electric field imposed by a Cu(I) cation shows $\nu(\text{HH})$ stretching bands at 3136 and 3415 cm^{-1} at $-23\text{ }^\circ\text{C}$ (Figure 2.8). As the temperature is decreased, the intensity of the band at 3415 cm^{-1} increases more than the intensity increase of the band at 3136 cm^{-1} . Additional bands at 3220 and 3265 cm^{-1} were also observed with isobaric temperature reductions. The bathochromic shift in H–H stretching frequencies for the bands at 3136 and 3415 cm^{-1} ($\Delta\nu_{\text{HH}} = -1025$ and -746 cm^{-1} with respect to 4161 cm^{-1} (free hydrogen molecule Raman frequency)) is comparable to the bathochromic shift observed with Cu(I)-ZSM-5 ($\Delta\nu_{\text{HH}} = -1079$ and -861 cm^{-1}),¹³³ indicating similar strong $\text{H}_2\text{-Cu(I)}$ interactions.

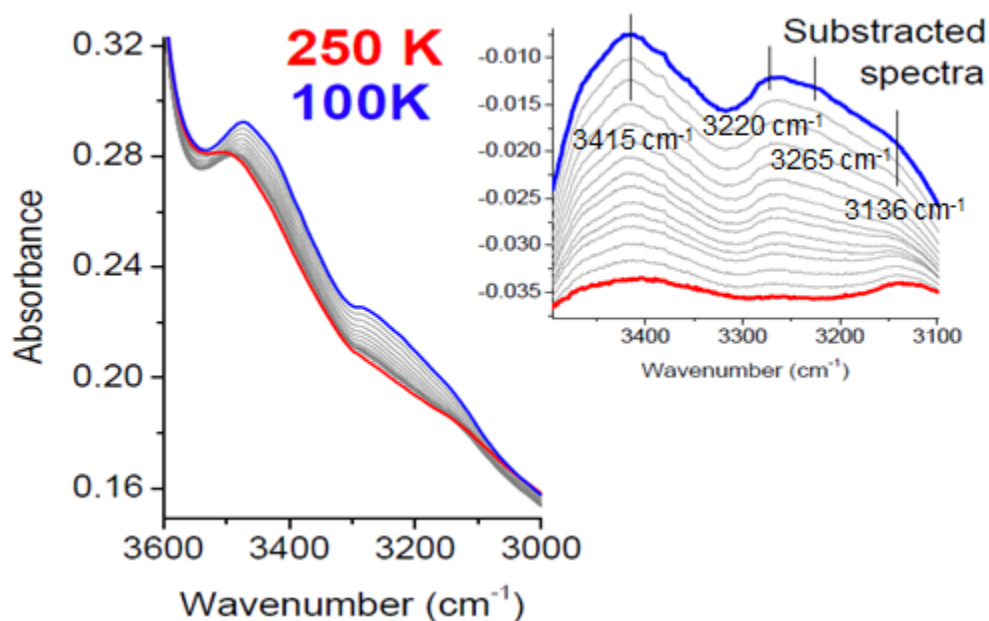


Figure 2.8: IR spectra of Cu(I)-SSZ-13 (Si/Al = 12, Cu/Al = 0.98) in equilibrium with 40 mbar H_2 at decreasing temperature from $-23\text{ }^\circ\text{C}$ (250 K) to $-173\text{ }^\circ\text{C}$ (100 K), sample was pre-treated *in vacuo* at $500\text{ }^\circ\text{C}$ for 3 h

The bathochromic shifts in the $\nu(\text{HH})$ mode has been related to the formation of $[\text{Cu}^+(\eta^2\text{-H}_2)]$ moiety (a transition metal dihydrogen complex¹³¹ with Cu) upon adsorption.¹³³ The energetics of Cu(I) cation and H₂ interaction in chabazite framework (Si/Al = 11) by periodic *ab initio* simulations with Hartree–Fock and the hybrid B3LYP Hamiltonians was reported by Solans-Monfort et al.¹³⁹ They reported B3LYP bathochromic harmonic H₂ frequency shifts ($\Delta\nu_{\text{HH}}$) of -847 and -957 cm⁻¹ for adsorption by Cu(I) cations found at the window of the 6MR and at the window of 8MR. The shifts observed with Cu(I)-SSZ-13 (Si/Al = 12) ($\Delta\nu_{\text{HH}} = -746$ and -1025 cm⁻¹) are very close to these values, which indicates adsorption at both sites.

Experimental hydrogen adsorption on CuCl exchanged ZSM-5 (Si/Al = 90) zeolite showed a band with $\nu(\text{HH}) = 3222$ cm⁻¹ in the same report from Solans-Monfort et al.¹³⁹, and that band was assigned to CuCl/H₂ adducts based on $\nu(\text{HH})$ value of 3222 cm⁻¹ observed for $[\text{Cu}(\eta^2\text{-H}_2)\text{Cl}]$ in an argon matrix.¹⁸³ In our case, bands observed at 3220 and 3265 cm⁻¹ could be interpreted as the interaction between hydrogen and occluded CuCl species (Table 2.2) even though the interaction at -23 °C seems to be minor compared to -173 °C.

As the temperature was further decreased to -258 °C (15 K), increased adsorbed hydrogen amount resulted in the interaction of hydrogen with external silanols and hydroxyl groups of extra-framework aluminum with observed $\nu(\text{HH})$ values of 4135 and 4110 cm⁻¹ respectively (Figure 2.9). The $\nu(\text{OH})$ shifts of -20 and -25 cm⁻¹ for external silanols and extra-framework Al OH groups supports the interaction of these sites with hydrogen at -258 °C (15 K) (Figure 2.9). Additional $\nu(\text{HH})$ band at 4128 cm⁻¹ could be related to 4130 cm⁻¹ band observed with H₂ adsorbed on H-SSZ-13 (Si/Al = 11.6) and H-CHA (Si/Al = 2.1) zeolites at -258 °C (15

K) which was assigned to the liquid like H₂ inside the zeolite cages interacting with walls of the zeolite.¹⁸⁴ The high frequency (HF) and low frequency (LF) Brønsted acid sites are known to result in $\nu(\text{HH})$ values of 4109 and 4090 cm⁻¹ respectively for hydrogen adsorbed on H-SSZ-13 (Si/Al = 11.6) at -258 °C (15 K).¹⁸⁴ The absence of these bands on Cu(I)-SSZ-13 (Si/Al=12) also confirms full exchange of Brønsted acid sites with Cu(I) cation.

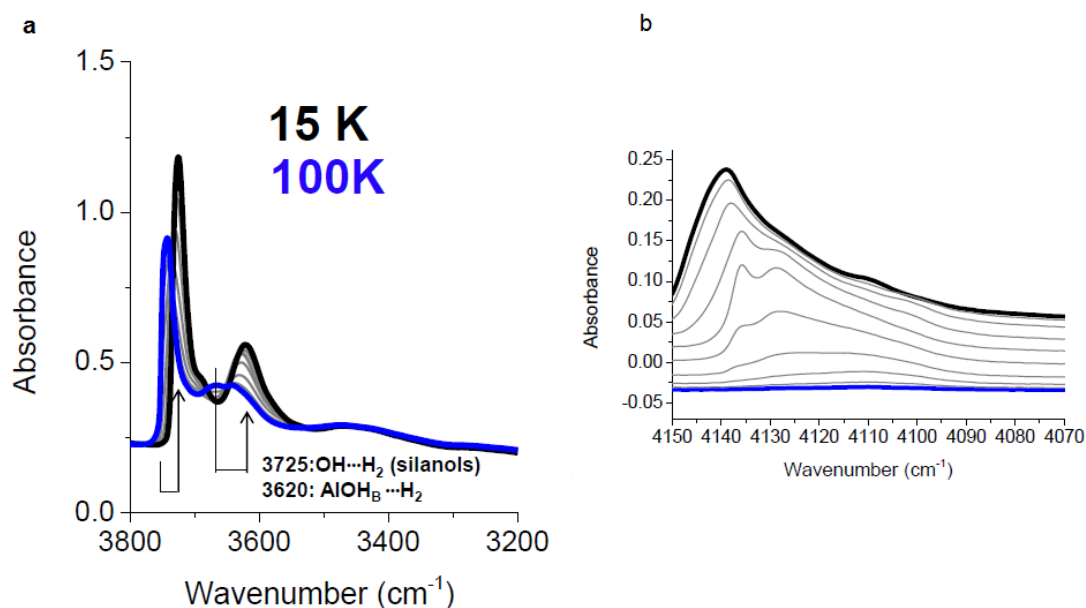


Figure 2.9: IR spectra of Cu(I)-SSZ-13 (Si/Al = 12, Cu/Al = 0.98) in equilibrium with 40 mbar H₂ at decreasing temperature from -173 °C (100 K) to -258 °C (15 K). a. OH region b. H-H region. Sample was pre-treated *in vacuo* at 500 °C for 3 h

Hydrogen adsorption on Na-SSZ-13 (Si/Al = 12) zeolite resulted in $\nu(\text{HH})$ values of 4110, 4121 and 4135 cm⁻¹ as temperature was decreased from -173 °C (100 K) to -258 °C (15 K) with 40 mbar H₂ dosing at -23 °C (250 K) (Figure 2.10). H-H

stretching frequencies of 4135 and 4110 cm^{-1} were previously assigned to the hydrogen interacting with external silanols and hydroxyl groups of extra-framework aluminum respectively for Cu(I)-SSZ-13 zeolite. Observed shifts in hydroxyl groups support the interaction of hydrogen with external silanols and hydroxyls of extra-framework aluminum species (Figure 2.10,a).

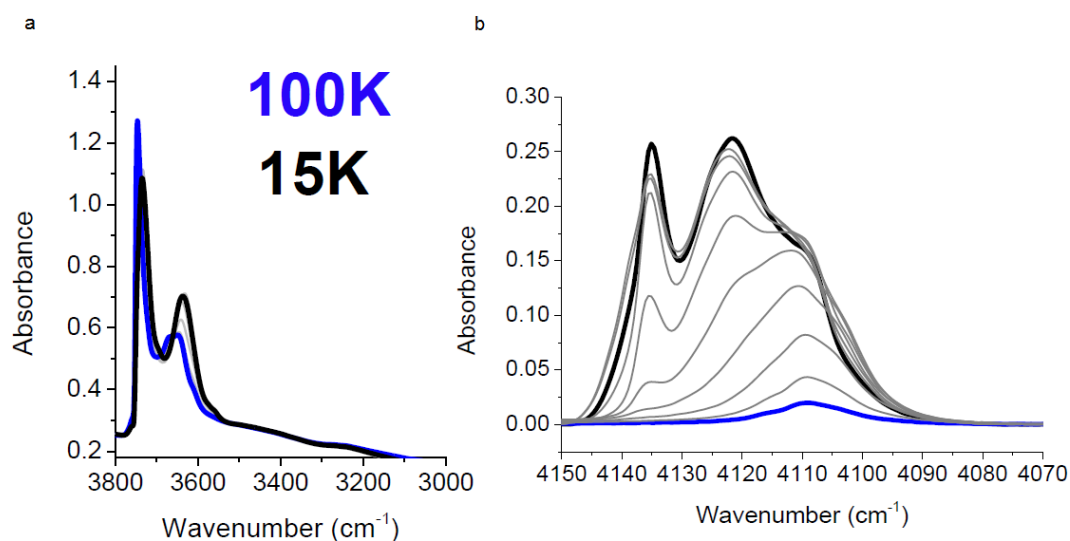


Figure 2.10: IR spectra of Na-SSZ-13 (Si/Al = 12, Na/Al = 0.76) in equilibrium with 40 mbar H_2 at decreasing temperature from $-173\text{ }^\circ\text{C}$ (100 K) to $-258\text{ }^\circ\text{C}$ (15 K). a: OH region, b: HH region. Sample was pre-treated *in vacuo* at $500\text{ }^\circ\text{C}$ for 3 h

The band with $\nu(\text{HH})$ of 4121 cm^{-1} ($\Delta\nu_{\text{HH}} = -40\text{ cm}^{-1}$) is assigned to hydrogen interacting with Na^+ Lewis acid site at the window of the 6MR of CHA which is close to $\nu(\text{HH})$ value of 4125 cm^{-1} assigned for hydrogen interaction with Na located in the window of 6MR of the sodalite cage of FAU.¹⁸⁵ No strong perturbation of the hydrogen molecule by Na-SSZ-13 (Si/Al = 12) was observed at $-23\text{ }^\circ\text{C}$ (250 K)

(absence of ν_{HH} bands at 3000 – 3400 cm^{-1} region) in accordance with the volumetric adsorption data obtained at 30 °C (Figure 2.3).

2.3.4 Powder Neutron Diffraction (PND) Experiments

Possible cation locations on CHA framework have been reported to be: i) at the center of the d6MR (Site I), ii) at the window of the 6MR (Site II), iii) near the corner of the 4MR (Site III) and at the window of the 8MR (Site III').¹⁸⁶

We investigated Cu(I) cation location and unit cell parameters of Cu(I)-SSZ-13 (Si/Al = 6) with neutron powder diffraction experiments conducted at -263 °C (10 K, see Table A.5 for refined atomic parameters) and at 27 °C (300 K, Table A.6) under vacuum conditions and with adsorbed D₂ (Table A.7). Two Cu locations were refined for Cu(I)-SSZ-13 (Si/Al = 6) sample at these conditions. At -263 °C (10 K), one copper was at the Site II (Cu1), centered between three O1 atoms with a mean distance of 2.180(5) Å and another copper cation was at Site III' (Cu2, Figure 2.11) with Cu1/Cu2 ratio of 1.24. At this temperature, Cu1 was found 0.05 Å away from the plane of O1 atoms in the *c* axis of the hexagonal unit cell. The occupation of Site II by Cu cation is supported by the perturbation of O1 atom with the longest T–O distance being the T–O1 distance, and the T–O1–T angle being the smallest T–O–T angle (Table 2.4). The second Cu(I) site is found on the window of 8MR (Site III') (Cu2) with Cu2–O2 distance of 2.13 Å (Table 2.4), close to the theoretical distance of 2.06 Å calculated for the second most preferable (stable) location of copper cation using B3LYP periodic calculations.¹³⁹

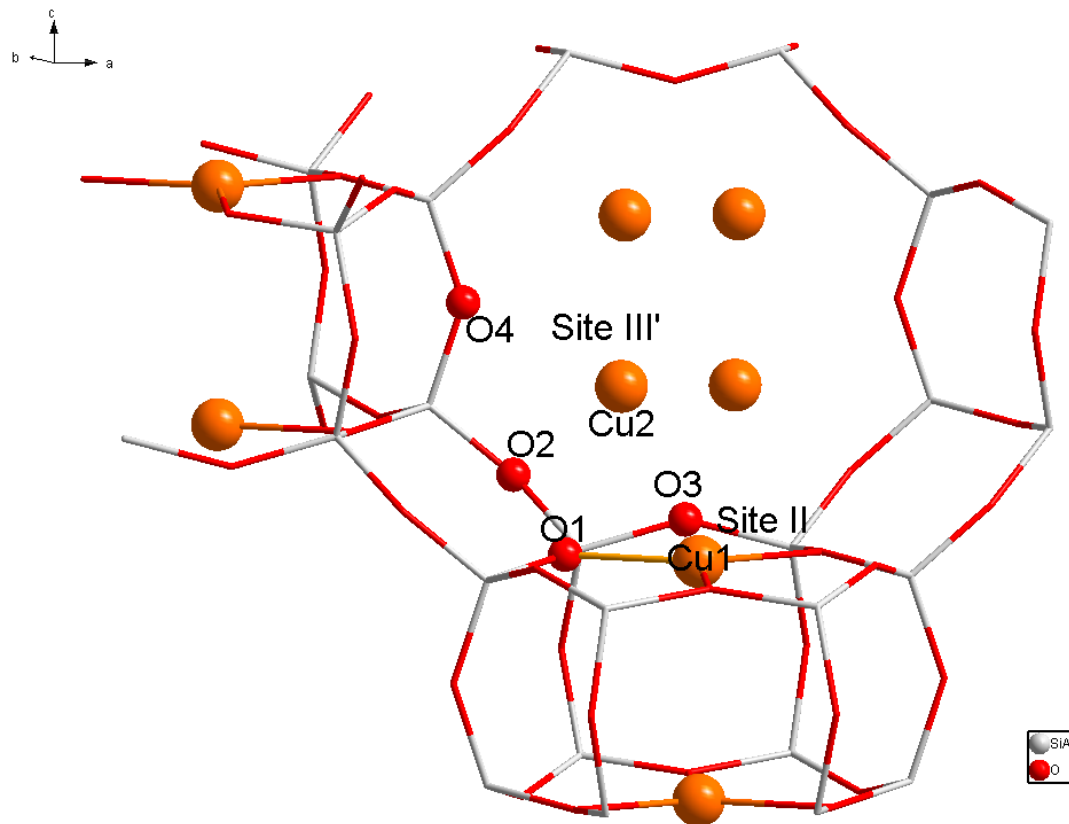


Figure 2.11: Representation of Cu(I)-SSZ-13 (Si/Al = 6) with two copper position: Cu1 at Site II and Cu2 at Site III'

At 27 °C, a 10.8 Å³ of decrease in the unit cell volume (negative thermal expansion) was observed with refined cell parameters of $a = 13.6054(5)$ Å and $c = 15.0170(9)$ Å (Table A.6). At this temperature, positions of Cu(I) cation at Site II and four oxygen atoms were best refined with anisotropic Debye-Waller factors. By using anisotropic factors, the Cu(I)-O1 distance was found 2.198(6) Å with 0.15 Å displacement from the O(1) plane (in contrast to 0.05 Å found at -263 °C). Cu2–O2 and Cu2–O4 distances are refined to 2.26(3) Å and 2.31(8) Å (Table 2.4), longer at 27 °C than at -263 °C. These more exposed locations of Cu(I) cations (migrated towards

chabazite cage) at Site III' and anisotropic movement of Cu1 at Site II with increased kinetic energy could explain the improved adsorption properties of Cu(I)-SSZ-13 sample at 30 °C when compared to -196 °C.

Table 2.4: Bond distances and T–O–T angles obtained via Rietveld Refinement of PND data of bare Cu(I)-SSZ-13 (Si/Al = 6, Cu₅Al_{5.14}Si_{30.86}O₇₂) at -263 °C (10 K) and 27 °C (300 K), and PND data obtained at -263 °C with D₂ loading at 27 °C (300 K), $R\bar{3}m$

	Bare, -263 °C (10 K)	D₂ loading, -263 °C	Bare, 27 °C (300 K)
Bond	Distance / Å	Distance / Å	Distance / Å
T–O1	1.660(5)	1.645(4)	1.634(4)
T–O2	1.604(5)	1.602(4)	1.616(4)
T–O3	1.619(6)	1.621(4)	1.610(4)
T–O4	1.600(5)	1.617(4)	1.607(4)
<T–O>	1.621	1.621	1.617
Cu1–O1	2.180(5)	2.211(5)	2.198(6)
Cu2–O2	2.13(6)	2.29(6)	2.26(3)
Cu2–O4			2.31(8)
Cu1–D1		2.5(1)	
Cu2–D2		2.2(1)	
Cu3–D3		2.35(19)	
Angle	Degrees	Degrees	Degrees
T–O1–T	140.7	142.8	142.6
T–O2–T	159.4	157.5	158.7
T–O3–T	148.3	147.9	147.9
T–O4–T	144.1	143.6	142.7
<T–O–T>	148.1	148.0	148.0

Hydrogen-Cu(I) interactions are further investigated by loading D₂ on Cu(I)-SSZ-13 at 27 °C. Two different Cu(I) locations near Site II are observed from neutron diffraction data obtained at -263 °C. One site (Cu1) was at the same level with O1

atoms (at the 6MR level) and one site (Cu3) was 1.31 Å away from the 6MR window. This unexpected migration of Cu3 cations from Site II can be related to the strong interaction of Cu(I) with deuterium, resulting in Cu3–D3 bonds with a refined distance of 2.3(2) Å. Even stronger interaction between D₂ and Cu(I) cations is observed between D2 and Cu2 (at 8MR window, Site III') with Cu2–D2 distance of 2.2(1) Å (Table 2.4). This stronger interaction of D₂ with Cu(I) at 8MR is in agreement with theoretically estimated binding energy of hydrogen molecule at Site III' when compared to Site II (56 kJ mol⁻¹ versus 13 kJ mol⁻¹).¹³⁹ Refined Cu–D distances in this work are comparable to 2.23(5) Å found for Co₂(*m*-dobdc) material with calculated isosteric heat of adsorption of 11.5 kJ mol⁻¹.¹⁵⁹

Strong hydrogen binding to the copper cation at Site III' was calculated to result in bathochromic shift in $\nu(\text{HH})$ of -957 cm⁻¹.¹³⁹ The observed shift of -1025 cm⁻¹ on Cu(I)-SSZ-13 (Si/Al = 12) sample at -23 °C (Figure 2.8) could, therefore, be correlated to this second preferred site of Cu(I) at the 8MR, whereas smaller shift by -746 cm⁻¹ could be resulted from interaction of H₂ with Cu(I) at Site II (Cu3).

Accessibility of the extra framework cation to the hydrogen molecule is as important as Cu(I) distribution for hydrogen adsorption capacities. In this study, the majority of the copper cation for Cu(I)-SSZ-13 (Si/Al = 6) zeolite was found to be located at Site II. At -263 °C center of the Cu(I) cation at Site (II) was found 0.05 Å away from the O1 plane with the Cu–O distance of 2.180(5) Å. Considering 1.35 Å Shannon radii of oxygen atom and 0.6 Å radii of Cu(I) cation, there is a high probability that the majority of Cu(I) cations are shielded by O atom at low temperatures. Na, on the other hand, having a Shannon radii of 1.02 Å, was located vertically 0.85 Å away from O(1) atom plane.¹⁸⁷ With this position of Na, hydrogen

can freely interact with Na cation at Site II, which explains higher hydrogen adsorption capacities of Na-SSZ-13 when compared to Cu(I)-SSZ-13 at -196 °C (Figure 2.4).

Anisotropic movement of Cu(I) cation at Site II (along [001] direction) with the increase in temperature to 27 °C allowed stronger interaction of Cu(I) and deuterium at 27 °C, which resulted in guest-induced Cu(I) migration (1.31 Å) at Site II. Guest induced cation migration is not an unfamiliar phenomena for Cu(I)-containing zeolites such as Cu(I)-Y.¹⁶³ Palomino et al. reported displacement of Cu(I) cations up to 0.975 Å in the presence of CO at -193 °C. Shang et al. suggested that the degree of guest induced migration is related to the electronic quadrupole moments and polarizability of the guest molecules that could increase the cation-guest molecule interaction.¹⁸⁸ In our case, reported formation of Cu–H₂ complexes renders hydrogen a potential ‘strong’ guest molecule especially at high enough temperatures even though dihydrogen has negligible quadrupole moment, which explains high dihydrogen adsorption capacities of Cu(I)-SSZ-13 zeolites at 30 °C (Figure 2.3).

2.3.5 Liquid Phase Cu(I) Exchange

Cu(I)-SSZ-13 (Si/Al = 12) sample was prepared by exchanging Cu(I) in O₂ free acetonitrile with the purpose of obtaining Cl-free Cu(I)- samples. Cu(I) is effectively solvated by acetonitrile (with CuCl solubility of 0.13 g_{CuCl} g_{CH₃CN}⁻¹ at 18 °C), which makes acetonitrile a great solvent for Cu(I) exchange. EDX and ICP results confirmed successful Cu(I) exchange without any Cl residual inside the pores (Table 2.5), unlike solid state CuCl exchange, which resulted in Cl impurities (Table 2.2). The crystal structure is preserved after Cu(I) exchange and the oxidative treatment at 450 °C (Figure A.4). The Cu content of the sample showed differences using EDX and

ICP analysis, indicating inhomogeneous Cu(I) exchange, which could result from diffusion limitations of plausible Cu(I)(CH₃CN)₄ complexes.

Table 2.5: Chemical composition of Cu(I)-SSZ-13 (Si/Al = 12) prepared by exchanging Cu(I) in acetonitrile, composition obtained by ICP-OES and EDX analysis

Technique	Chemical Composition			Cu concentration / mmol Cu g ⁻¹
	Si/Al	Cu(I)/Al	Cl/Al	
ICP-OES	12.0	0.42	-	0.52
EDX	11.4±0.42	0.88±0.09	-	1.10

After the Cu(I) exchange, the sample has been analyzed using DRIFT. After dehydration of sample at 450 °C for 1 h by flowing 30 cm³ min⁻¹ He, CH₃ and CN related vibrations were observed at 2937 cm⁻¹ and 2292 cm⁻¹ together with a vibration at 2157 cm⁻¹, which is close to reported Cu(I)- bound C–O vibration at 2155 cm⁻¹.¹⁵⁵ Acetonitrile was observed to be preserved on the zeolite surface even after evacuation at 500 µmHg for 8 h at 425 °C.

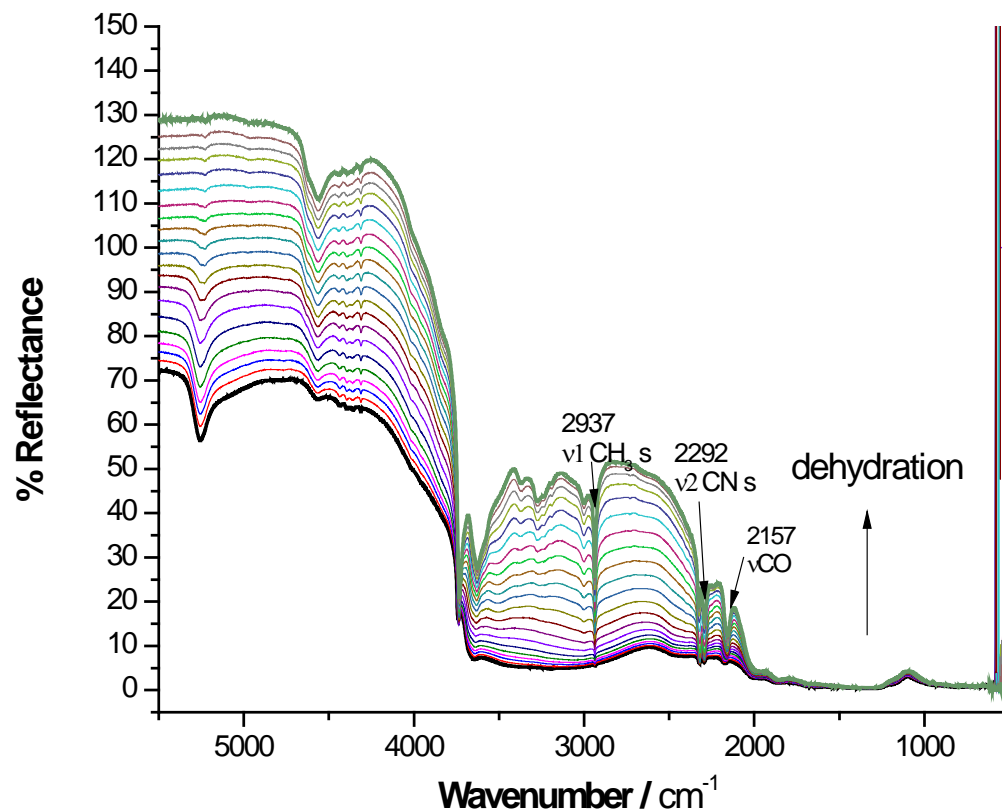


Figure 2.12: DRIFT spectra of Cu(I)-SSZ-13 (Si/Al = 12) sample prepared by Cu(I) exchange in acetonitrile as temperature was increased from 25 °C (black, hydrated sample) to 450 °C (green, dehydrated sample)

An oxidation and subsequent reduction procedure has been developed to use Cu-SSZ-13 samples prepared by Cu(I) exchange in acetonitrile for H₂ adsorption. The conditions required to oxidize residual acetonitrile, and to reduce Cu(II) into Cu(I) are obtained from O₂ TPR, CO TPR and CO TPD experiments. The sample was oxidized at 350 °C (at a heating rate of 10 °C min⁻¹) for 4 h using 50 cm³ min⁻¹ 10% O₂ balance

He flow. After cooling down to 25 °C, the temperature was raised to 300 °C (with a heating rate of 10 °C min⁻¹) and maintained at 300 °C for 2 h by flowing 50 cm³ min⁻¹ 10% CO (Matheson, 99.999%) balance He. Then CO was desorbed at 350 °C for 2 h using 45 cm³ min⁻¹ He flow.

After this procedure, the sample was re-hydrated in air, and dehydrated inside the DRIFTS cell by repeating the same procedure. Figure 2.13 shows the dehydration of Cu(I)-SSZ-13 (Si/Al = 12) sample, resulting in acetonitrile free sample with vibrations at 3600 cm⁻¹ and 3576 cm⁻¹ confirming presence of Brønsted acid sites due to un-exchanged H⁺ sites.

After the oxidation and reduction steps, the sample was transferred to a Micromeritics sample container in an Argon glove box, and tested for H₂ adsorption as described in section 2.2.3 without being exposed to O₂ or water vapor. At 30 °C and 1 atm, Cu(I)-SSZ-13 (Si/Al = 12)-CH₃CN sample adsorbed 0.228 mmol H₂ g_{zeolite}⁻¹ (0.44 H₂/Cu), which is nearly double of H₂ adsorption capacity of Cu(I)-SSZ-13 (Si/Al = 12) sample prepared by CuCl solid state exchange (0.120 mmol H₂ g_{zeolite}⁻¹ (0.09 H₂/Cu) Table 2.3), indicating the potential for the liquid phase Cu(I) exchanged SSZ-13 samples.

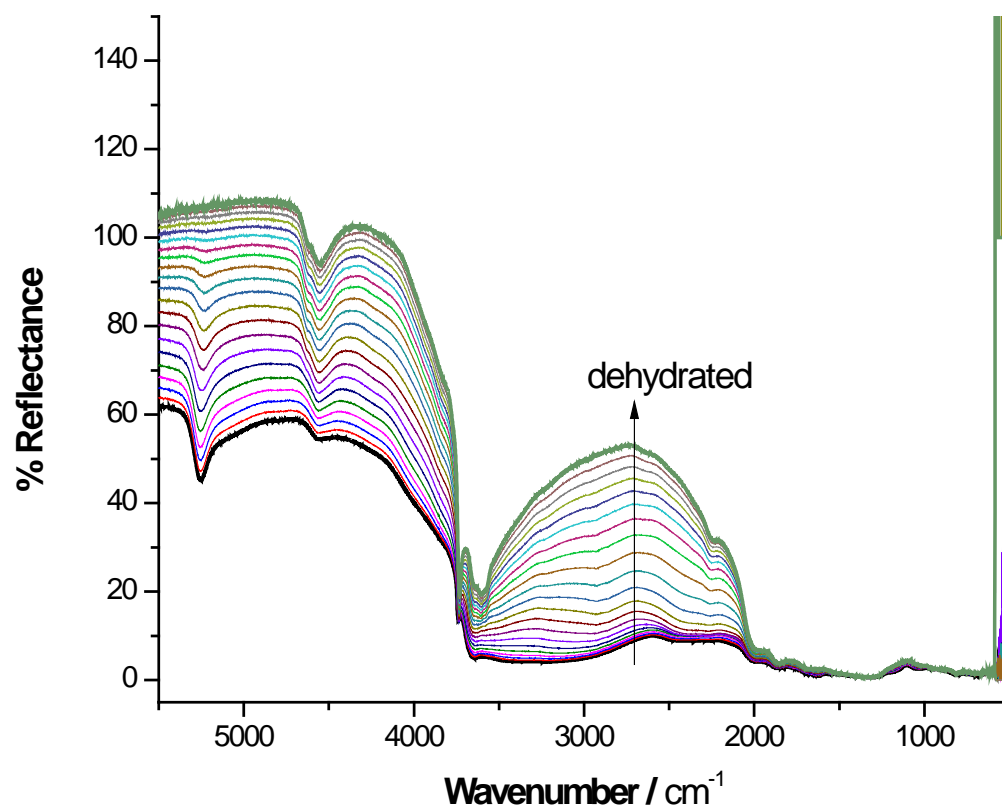


Figure 2.13: DRIFT spectra of Cu(I)-SSZ-13 (Si/Al = 12) sample prepared by Cu(I) exchange in acetonitrile and oxidized at 350 °C for 4 h. The spectra was taken as temperature was increased from 25 °C (black, hydrated sample) to 450 °C (green, dehydrated sample)

2.4 Conclusion

Cu(I)-SSZ-13 samples prepared by solid state CuCl exchange was found to adsorb three times the amount of hydrogen adsorbed by MOFs at 30 °C and 1 atm. H₂/Cu ratios reached 0.5 (0.05 wt.%) at 1 atm hydrogen pressure by Cu(I)-[B]-SSZ-13 sample having isosteric heat of H₂ adsorption between 50 and 20 kJ mol⁻¹. Cu(I)-SSZ-

13 (Si/Al = 6) sample, on the other hand, showed isosteric heat of adsorption around 20 kJ mol^{-1} , which is considered optimum for hydrogen adsorption on cation exchanged zeolites.¹³⁸

Solid state Cu(I)Cl exchange on SSZ-13 resulted in Cu(I) cations on two different sites, which showed bathochromic H–H bond stretching frequency shifts by 1025 cm^{-1} and 746 cm^{-1} at $-23 \text{ }^\circ\text{C}$ that are in very good agreement with theoretically calculated shifts.¹³⁹ Na-SSZ-13 zeolite, on the other hand, resulted in a bathochromic shift of 40 cm^{-1} in agreement with the hydrogen adsorption capacity of this sample at $30 \text{ }^\circ\text{C}$.

PND experiments conducted for Cu(I)-SSZ-13 (Si/Al = 6) showed two Cu(I) locations: one at the window of the 6MR and one at the window of the 8MR. Strong hydrogen interactions with Cu(I) cations are confirmed by deuterium adsorption at $27 \text{ }^\circ\text{C}$, which resulted in Cu–D distances as short as $2.2(1) \text{ \AA}$.

At lower temperatures ($-263 \text{ }^\circ\text{C}$) Cu(I) cations were found to be shielded by electrons of the framework oxygen atoms with Cu–O_{framework} distances of $2.180(5) \text{ \AA}$, which results in lower hydrogen adsorption capacities than Na-SSZ-13 at $-196 \text{ }^\circ\text{C}$.

Finally, chlorine free Cu(I)-SSZ-13 samples were prepared by CuCl exchange in acetonitrile solution. Hydrogen adsorption capacities per Cu(I) cation was found to be 5 times that of solid state CuCl exchanged samples, even though Cu(I) exchange in acetonitrile was found to be not homogenous through the crystals.

Chapter 3

DIRECT METHANE CONVERSION TO METHANOL ON Cu- EXCHANGED SMALL-PORE ZEOLITES

3.1 Introduction

The direct and selective conversion of methane to methanol is an extremely challenging, yet economically very desirable reaction. The challenge of activating the very stable methane at moderate temperatures by avoiding formation of CO and CO₂ can be overcome only by using very selective catalysts. Selective FeO¹¹⁵ and Cu_xO_y^{114,117,120} sites that can convert methane to methanol at moderate conditions have been identified on Fe- and Cu- exchanged zeolites.

Fe- exchanged zeolites show methane activation at temperatures as low as room temperature,¹⁰⁹ however the need for the pre-treatment of Fe- exchanges samples with an inert gas at temperatures as high as 900 °C and the requirement of N₂O to create active (FeO)_α sites¹¹⁵ remain important disadvantages of Fe- exchanged zeolites. Cu- exchanged zeolites can activate methane at temperatures as low as 125 °C,⁵ and the active Cu_xO_y species can be formed at temperatures as low as 200 °C¹¹⁹ using O₂ treatment. The majority of the methanol formation investigations performed on Cu- exchanged zeolites have been concentrated on Cu-ZSM-5 and Cu-mordenite samples, which show methanol formation amounts ranging between 6 and 135 μmol CH₃OH g_{zeolite}⁻¹ depending on the details of the reaction procedure.^{5,69,70,113,114,119}

Methanol can be formed selectively on Cu- exchanged zeolites following a 3-step procedure: i) activation of Cu-zeolite in O₂ at temperatures between 200 °C and

450 °C, ii) Methane reaction at temperatures between 150 °C and 200 °C and iii) methanol extraction using solvent or steam at temperatures between 135 °C and 200 °C.

The active site forming upon O₂ treatment of Cu-ZSM-5 and Cu-mordenite has been identified as mono-(μ-oxo)dicopper(II),^{117,120} which has been associated with a characteristic ligand to metal charge transfer (LCMT) energy transition at 22,700 cm⁻¹ and resonance-enhanced Raman Cu–O vibrations at 456 and 870 cm⁻¹.¹¹⁷ In addition to this mono-(μ-oxo)dicopper(II) species, water-stable copper (II) oxide,¹¹⁸ as well as a trinuclear copper oxygen cluster, [Cu₃O₃]²⁺,¹¹⁴ have been suggested to be the active sites for Cu-mordenite, which could be the reason for observed higher specific methanol formation activity of Cu-mordenite at 200 °C when compared to Cu-ZSM-5, known to have only mono-(μ-oxo)dicopper(II) species as the active site.⁵ Interestingly, Cu-FER and Cu-*BEA samples also showed different methane activation properties, such as methane activation temperature, when compared to Cu-ZSM-5,⁵ which indicates the possibility of different Cu_xO_y active species forming on different frameworks, but all forming methanol at 200 °C.

In this chapter, we investigated Cu-exchanged SSZ-13, -SSZ-16 and -SSZ-39 samples for methanol formation at 200 °C following a similar procedure used in literature.⁷⁰ The results were compared to Cu-ZSM-5 and Cu-mordenite using the same procedure and the active sites forming on these frameworks were investigated using UV-vis and Raman spectroscopy.

3.2 Experimental

3.2.1 Zeolite Synthesis and Ion Exchange

SSZ-13 (Si/Al = 6) was synthesized hydrothermally by modifying the protocol reported elsewhere.¹⁶⁵ 16.45 g of de-ionized water, 10 g of sodium silicate solution (Sigma Aldrich, 26.5 wt.% SiO₂, 10.6 wt.% Na₂O) and 6.712 g of *N,N,N*-trimethyl-1-adamantanamonium hydroxide solution (TMAdaOH, Sachem Inc., 25 wt.%) were stirred at room temperature for 15 min to have a homogeneous mixture. Later, 1 g of Na-Y (Zeolyst, CBV100, Si/Al = 2.47) was added to the mixture and the mixture was stirred for 30 more minutes at room temperature. The homogenous white solution was then transferred to 43 ml Teflon-lined autoclave (Parr) and the autoclave was rotated at a rate of 45 rpm at 150 °C for 6 days. The solid product was recovered with vacuum filtration, washed with de-ionized water (250 ml for 1 g of zeolite) and dried at 80 °C for 3 h (in air, Fisher Scientific Isotemp Lab Oven). The as-made product was calcined in a 22 mm ID quartz tube with a 20 mm quartz frit (Chemglass, medium) with 80 cm³ min⁻¹ air (Keen Gas, total hydrocarbon < 0.1 ppm) flow in a Thermo Scientific Lindberg Blue M furnace. The temperature was held at 120 °C (with 5 °C min⁻¹ heating rate) for 2 h to dehydrate the zeolite and at 580 °C (using 5 °C min⁻¹ heating rate) for 6 h to calcine the structure directing agent. The resulting zeolite is designated Na/H-SSZ-13.

SSZ-13 (Si/Al =12) was synthesized as described in section 2.2.1. The as-made product was calcined at 580 °C (using 5 °C min⁻¹ heating rate) using the quartz tube described above for 6 h to obtain H⁺-SSZ-13 (Si/Al = 12).

SSZ-39 (Si/Al = 10) was synthesized using 20 wt.% tetramethyl piperidinium hydroxide as the surface directing agent. 6.69 g of tetramethyl piperidinium hydroxide

(Sachem, Inc., 20 wt.%,) was mixed with 17.67 g of deionized water, 12.84 g of sodium silicate solution (37.5 wt.%, PQ Corporation) and 1.026 g 1 M NaOH solution for 15 min, then 1.283 g NH₄-USY (Zeolyst CBV 712, Si/Al = 6) was added slowly to the mixture and the stirring was continued for 30 more min at room temperature. The synthesis gel was then transferred to 43 ml Teflon-lined autoclave (Parr) and heated at 150 °C for 7 days under rotation at a rate of 45 rpm. The zeolite crystals were then recovered using vacuum filtration and washed with 500 ml of deionized water. The as-made zeolite was calcined at 560 °C (with 5 °C min⁻¹ heating rate) for 8 h with 80 cm³ min⁻¹ air flow. The resulting zeolite is designated Na/H-SSZ-39.

SSZ-16 (Si/Al = 10) was synthesized hydrothermally using 1,3-Bis(1-adamantyl) imidazolium hydroxide solution¹⁸⁹ as the structure directing agent. 16.8 g of 20 wt.% 1,3-Bis(1-adamantyl) imidazolium hydroxide solution, 1 g of 1 N NaOH solution and 12.2 g of Banco “N” silicate (PQ corporation, ~28 wt.% SiO₂, 8.9 wt.% Na₂O) was stirred at room temperature for 15 min. Later, 1.25 g NH₄-USY (Zeolyst CBV 712, Si/Al = 6) was added slowly to the synthesis gel and stirred for an additional 1 h at room temperature. The synthesis gel was then transferred into 43 ml Teflon-lined autoclave (Parr) and heated at 150 °C for 7 days under rotation (45 rpm). The resulting crystals were recovered using a centrifuge (International Equipment Company, Centra MP4, 4000 rpm) for 6 min, washed with de-ionized water (200 ml for 1 g) three times and dried at 80 °C for 3 h (in air, Fisher Scientific Isotemp Lab Oven). The as-made zeolite was then calcined at 560 °C (using 5 °C min⁻¹ heating rate) for 8 h with 80 cm³ min⁻¹ air flow (Keen Gas, total hydrocarbon < 0.1 ppm) in a Thermo Scientific Lindberg Blue M 1 inch diameter tubular furnace. The resulting zeolite is designated Na/H-SSZ-16 (Si/Al = 10).

SSZ-16 (Si/Al = 6.5) was synthesized hydrothermally using a procedure similar to the one used for SSZ-16 (Si/Al = 10). 3.36 g of the structure directing agent hydroxide (20 wt.%) was mixed with 0.2 g of 1 N NaOH and 2.44 g of DI water. Then, 2.5 g of Banco “N” silicate (PQ corporation, ~28 wt.% SiO₂, 8.9 wt.% Na₂O) was added and stirred for about 15 minutes. Finally, 0.25 g of NH₄-Y (Zeolyst CBV500, Si/ Al = 2.47) as the aluminum source was added under stirring for another 15 minutes. The synthesis gel was then transferred into 43 ml Teflon-lined autoclave (Parr) and heated at 150 °C for 7 days under rotation with 45 rpm. The as-made zeolite was recovered, washed, dried, and then calcined as described for SSZ-16 (Si/Al = 10). The resulting zeolite is designated Na/H-SSZ-16 (Si/Al = 6.5).

Na-mordenite (Tricat, Si/Al = 5) and NH₄⁺-ZSM-5 (Zeolyst, CBV 2314, Si/Al = 11.5) were obtained from commercial sources.

3.2.1.1 Na⁺ Exchange

Na- exchange of the materials was performed by exchanging Na/H- or H-zeolites in 1 M NaNO₃/ de-ionized water solution at 80 °C for 3 h. After the ion exchange, the samples were washed with de-ionized water (250 ml for 1 g) and then vacuum filtered and dried at 80 °C for 3 h (in air, Fisher Scientific Isotemp Lab Oven). The ion exchange was repeated three times for zeolites that contained proton from the original synthesis and two times for the materials that contained sodium from the original synthesis. The Na-materials were calcined at 550 °C (using 5 °C min⁻¹ heating rate) for 2 h by flowing 80 cm³ min⁻¹ air before exchange with copper (II) acetate.

3.2.1.2 Cu(II) Exchange

Copper (II) ion-exchange was performed by exchanging the Na⁺ -form of the zeolites in copper (II) acetate aqueous solution at 25 °C. The volume of the solutions was kept constant at 200 ml while the amount of copper (II) acetate (Aldrich, 98 wt.%) was calculated to result in a corresponding Cu/Al ratio of 0.5 in the solution in the beginning of each exchange. The exchange was repeated twice or three times for some materials until Cu/Al ratio of 0.25 on the sample has been reached. Each exchange was performed at 25 °C for 12 h. After each exchange, the zeolites were separated by vacuum filtration and a sample from the filtrate, and the filtrate was stored for analysis using UV–vis spectroscopy. The amount of copper loaded on the material (Cu/Al ratio) was determined by measuring the disappearance of copper acetate from the ion-exchange solutions with UV–vis spectroscopy. The amount of materials and copper acetate used in the exchanges is provided in Table 3.1.

Table 3.1: Quantity of materials used in copper (II) ion exchanges and the resulting Cu/Al ratios determined by the UV-vis

Zeolite (Si/Al)	Volume of solution / ml	Mass of zeolite / g	Mass of copper (II) acetate / g	Number of times exchanged	Cu/Al from UV-vis
Na-SSZ-13 (6)	200	0.632	0.136	2	0.35
Na-SSZ-13 (12)	200	0.631	0.074	2	0.35
Na-SSZ-16 (6.5)	200	0.901	0.183	2	0.34
Na-SSZ-16 (10)	200	0.555	0.077	2	0.45
Na-SSZ-39 (10)	200	0.331	0.046	2	0.26
Na-mordenite (5)	200	2.00	0.476	1	0.34
Na-ZSM-5 (11.5)	200	2.00	0.235	1	0.34
Samples used in Raman Spectroscopy					
Na-SSZ-13 (12)	200	5.20	0.561	2	0.45
Na-SSZ-39 (10)	200	4.00	0.450	2	0.40
Na-mordenite (5)	200	4.51	1.20	2	0.33
Na-ZSM-5 (11.5)	200	4.51	0.603	2	0.41

3.2.2 Analytical Methods

The samples were analyzed by X-ray diffraction using a Philips X'Pert powder diffractometer with a Cu K α source ($\lambda = 1.5418 \text{ \AA}$) over the range of $2\theta = 5.0\text{--}50.0^\circ$ with a step size of 0.02° and scan rate of 2 s per step.

The elemental composition of samples was determined by measuring the initial and remaining Cu(II) acetate concentration in the exchange solution using UV-vis spectroscopy (JASCO, V-5500) over a range between 200 nm and 900 nm. The concentration of Cu(II) acetate remaining in the solution was calculated using a calibration curve (Eq. 3.1):

$$\text{Concentration (M)} = \frac{\text{Absorbance} + 0.0384}{26.759} \quad (3.1)$$

which was obtained from the collected absorption intensities for the $d \leftarrow d$ transition of Cu(II) ion at 776 nm for prepared Cu(II) acetate solutions with concentrations between 0.001 M and 0.02 M (see Appendix B.1).

The elemental composition of some of the Cu-exchanged materials was determined also by Inductively Coupled Plasma Optical Emission Spectroscopy (ICP-OES) technique in Galbraith Laboratories, Knoxville, Tennessee (Table 3.1).

3.2.3 Methane Conversion Reactions

Methane conversion reactions were performed in a quartz reactor (ID = 7 mm), in which 0.300 ± 0.005 g of samples were loaded and supported by quartz wool. A ceramic radiant full cylinder heater (Omega, CRFC-26/120-A) was used to heat the quartz tube. The furnace temperature was controlled using an Omega CN/74000 temperature controller and a thermocouple placed around the center of the quartz tube. Gas flows were controlled by mass flow controllers (Brooks Instrument). The water vapor partial pressure was controlled by flowing the gas stream through a Swagelok stainless steel cylinder filled with de-ionized water at 25 °C. The effluent stream was directed to a gas chromatograph (GC) (Agilent 6890), which was used for quantification of methanol. A Supel-Q PLOT column (Supelco, 30 m x 0.32 mm) was used for separation, and a flame ionization detector was used for quantification. The temperature of the GC oven was held constant at 80 °C and valve injections of 1 ml were taken every 3 min. The effluent stream was also monitored using a mass spectrometer (MS) (Pfeiffer OmniStar GSD 320).

The procedure used for conversion of methane to methanol consists of three steps: i) oxidative pre-treatment of the material, ii) admission of methane, and iii)

removal of methane from the gas stream and admission of steam. Pre-treatment of materials was performed by heating the samples to a temperature of 450 °C at a heating rate of 2 °C min⁻¹ by flowing 50 cm³ min⁻¹ O₂ and holding at 450 °C for 10 h. The furnace was then cooled to 60 °C, and the gas flow was changed to a mixture of 4 cm³ min⁻¹ of CH₄ (Matheson, 99.99%) and 50 cm³ min⁻¹ of N₂ (Keen Gas, 99.999%). The temperature was held at 60 °C for 20 min and then increased by 5 °C min⁻¹ to 200 °C and held for another 20 min. Methane was then removed from the gas stream and N₂ was diverted through a water-containing saturator while keeping the temperature of the sample at 200 °C. The effluent stream was analyzed using GC and MS when steam was introduced to the reactor. The procedure for copper (II) acetate exchanged samples is outlined in Figure 3.1.

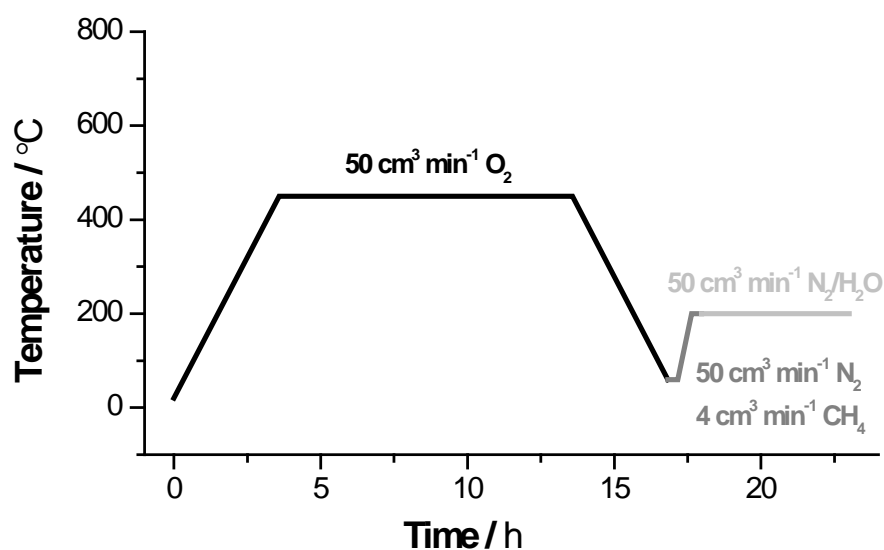


Figure 3.1: Temperature profile and gas flow rates used for conversion of methane to methanol on Cu(II) ion-exchanged samples

3.2.4 Diffuse Reflectance UV–vis Spectroscopy

A UV–vis spectrometer (JASCO, V-5500) equipped with an integrating sphere (JASCO ISV-469) was used to collect diffuse reflectance UV–vis spectra. About 120 mg of material was placed in a U-shaped optical quartz tube, which was connected to gas lines by Swagelok ultra-Torr vacuum fittings. The flow rates of gases were controlled using Brooks 5850e Series mass flow controllers and a 0154E control box. Before spectra were collected, the U-shaped tube was secured at the sample opening of the integrating sphere. The apparatus thus allowed for the material to be treated under gas flow at room temperature while continuously obtaining spectra, whereas spectra could not be measured while heat was applied. To treat the material at high temperature, the tube was separated from the integrating sphere and wrapped with heating tape and insulation. The temperature was controlled using a K-type thermocouple placed around the outside of the tube at the sample location, and a temperature controller (Watlow, Series 965). Baseline for the UV–vis spectra was obtained using barium sulfate (Sigma) packed inside the same quartz tube. UV–vis spectra were collected following various treatments.

O₂ treatment of the samples was performed as follows. The hydrated samples (exposed to air, ~120 mg) were heated to 450 °C at a heating rate of 5 °C min⁻¹ and held at 450 °C for 2 h under 20 cm³ min⁻¹ O₂ (Keen Gas, 99.997% purity) flow. Then the samples were cooled to 25 °C under O₂ flow. The tube was secured at the opening of the integrating sphere before collecting a spectrum at 25 °C with O₂ flow.

For spectra provided in Figure 3.4, O₂ treatment at 450 °C has been applied as described above. After cooling the sample to 25 °C with O₂ flow, several spectra were taken over and then the O₂ flow was stopped and propane (Matheson, 99.999%) was

admitted ($20 \text{ cm}^3 \text{ min}^{-1}$). Several spectra were taken over the course of time as indicated on Figure 3.4.

3.2.5 Raman Spectroscopy

Raman spectra were obtained in collaboration with Dr. Karl Booksh using a Bruker Senterra Raman microscope spectrometer with a CCD cooled to $-65 \text{ }^\circ\text{C}$.

Spectra were recorded at room temperature with excitation at 532 nm.

O₂ activation

Approximately 40 mg of Na-Cu-SSZ-39 (Si/Al = 10, Cu/Al = 0.48), Na-Cu-SSZ-13 (Si/Al = 12, Cu/Al = 0.47), Na-Cu-ZSM-5 (Si/Al = 11.5, Cu/Al = 0.53) and Na-Cu-mordenite (Si/Al = 5, Cu/Al = 0.33) samples were placed inside a Class A NMR Tube (Wilmad, 5 mm OD, 0.38 mm thickness) using a quartz wool to stabilize the samples. Samples were heated to $450 \text{ }^\circ\text{C}$ using a heating rate of $10 \text{ }^\circ\text{C min}^{-1}$, under flow of $40 \text{ cm}^3 \text{ min}^{-1}$ pure O_2 (Keen Gas, 99.997%). The temperature was then kept at $450 \text{ }^\circ\text{C}$ for 2 h with continuing O_2 flow. The NMR tube was then flame sealed with O_2 in it to preserve the formed Cu_xO_y species.

3.3 Results and Discussion

3.3.1 Material Characterization

Cu(II)-exchanged samples show high crystallinity with no additional phases (Figure 3.2). The elemental compositions of Cu(II) exchanged samples show Cu/Al ratios between 0.26 and 0.53 (Table 3.2). The UV-vis method applied here to calculate the exchanged Cu(II) amounts was found to be accurate when compared to ICP results (Table 3.2). The samples were exchanged to obtain Cu/Al ratios higher than 0.25 in order to ensure sufficient amounts of Cu(II) cations for methanol

formation. Cu/Al ratio of 0.25 was reported to correspond to the minimum copper concentration on Cu-ZSM-5 (1.5 wt.%) that show methanol production following a similar activation procedure to the one applied here.⁶⁸ Na content of the samples was also determined using ICP. Na/Al ratios for different samples were observed to be between 0.02 and 0.05.

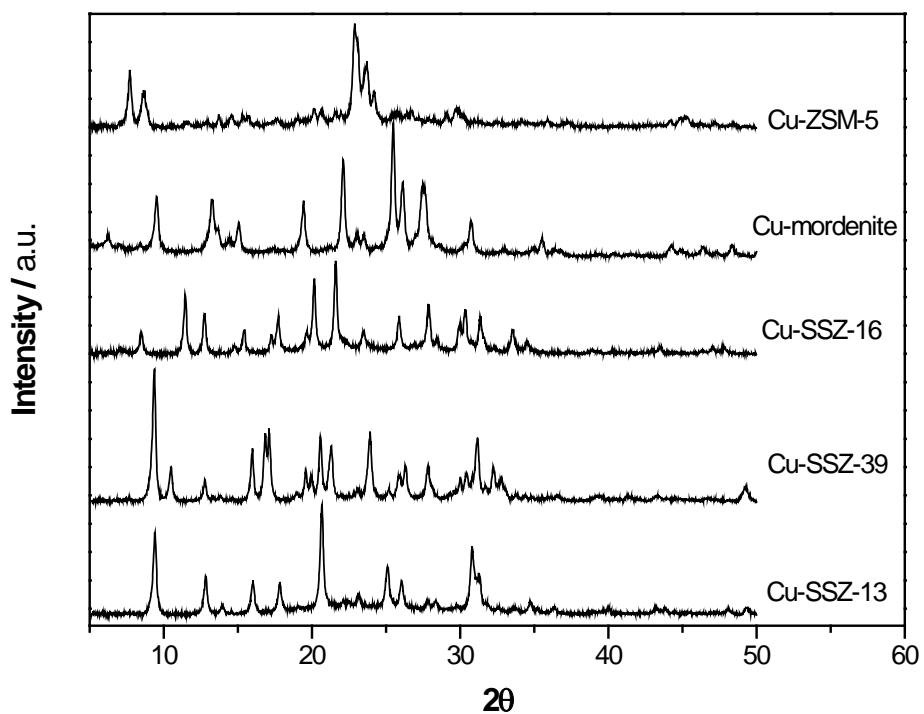


Figure 3.2: Powder XRD pattern of Cu-SSZ-13 (Si/Al = 12), Cu-SSZ-39 (Si/Al = 10), Cu-SSZ-16 (Si/Al = 6.5) Cu-mordenite, and Cu-ZSM-5 samples, Cu $K\alpha$, $\lambda = 1.5418 \text{ \AA}$

Table 3.2: Elemental compositions of the Cu-exchanged samples determined by UV-vis[†] and ICP

Zeolite (Si/Al)	Nominal Si/Al	Si/Al from ICP	Cu/Al from UV-vis	Cu/Al from ICP	Na/Al from ICP	Cu concentration / mmol Cu g ⁻¹
Na-SSZ-13	6	5.9	0.35	0.38	0.022	0.86
Na-SSZ-13	12		0.35			0.44
Na-SSZ-16	6.5		0.34			0.72
Na-SSZ-16	10		0.45			0.65
Na-SSZ-39	10		0.26			0.38
Na-mordenite	5		0.34			0.89
Na-ZSM-5	11.5		0.34			0.44
Samples used in Raman Spectroscopy:						
Na-SSZ-13	12	12.0	0.45	0.47	0.025	0.58
Na-SSZ-39	10	9.6	0.40	0.48	0.029	0.69
Na-mordenite	5		0.33			0.87
Na-ZSM-5	11.5	16	0.41	0.53	0.046	0.55

[†] Copper content calculated is described in section 3.2.2

3.3.2 Methanol Formation

Extraction of methanol following the O₂ pre-treatment and CH₄ admission to the system (3-step procedure as described above) was observed on Cu(II) exchanged samples over a period of 200 min (Figure B.2). The total amount of methanol produced per gram of zeolite and per Cu cation is given in Table 3.3.

Produced methanol amount per Cu basis on Cu-mordenite in this work (0.04) is comparable to 0.03 found by Alayon et al. on Cu-mordenite (Si/Al = 11, Cu/Al = 0.38)⁷⁰ using a very similar procedure (details of the different procedures are provided in Table 1.3). The procedures applied for methanol formation have an effect on the extracted methanol formation amounts. For instance, the liquid water/ acetonitrile extraction of methanol is believed to be an inefficient method. Groothaert et al.

reported 8.2 μmol of methanol per gram of Cu-ZSM-5 (Si/Al = 12, Cu/Al = 0.58) sample when extracted in liquid water, but observed 21.7 $\mu\text{mol g}^{-1}$ of CO_2 when heated in helium indicating inefficient organic removal from the surface by extraction in liquid water.⁵ Alayon et al., on the other hand, reported complete extraction of produced methanol from the surface by flowing steam at 200 °C, since they did not observe any additional CO_2 formation when the Cu-mordenite (Si/Al = 11, Cu/Al = 0.38) sample was heated in helium after methanol extraction.⁷⁰ The reason for observing higher methanol production on Cu-ZSM-5 here (16 $\mu\text{mol g}^{-1}$) when compared to the reported amounts (8.2 $\mu\text{mol g}^{-1}$)⁵ can be attributed to the more efficient steam extraction method.

Table 3.3: Methanol production amounts on Cu(II)- exchanged samples.

Zeolite	Pore Diameter / Å	Si/Al	Methanol / $\mu\text{mol}_{\text{CH}_3\text{OH}} \text{g}^{-1}$	Cu concentration mmol Cu g^{-1}	Methanol / Cu mol mol^{-1}
Na-SSZ-13	3.8	6	28	0.86	0.03
Na-SSZ-13	3.8	12	31	0.44	0.07
Na-SSZ-16	3.6	6.5	39	0.72	0.05
Na-SSZ-16	3.6	10	2	0.65	0.003
Na-SSZ-39	3.8	10	36	0.38	0.09
Na-mordenite	7	5	31	0.89	0.04
Na-ZSM-5	5.5	11.5	16	0.44	0.04

Another parameter that is observed to have an important effect on the produced methanol formation amounts is the CH_4 contact time. Grundner et al. reported that at least 30 min of CH_4 contact time with the zeolite is crucial for proper activation of methane molecule.¹¹⁴ Here, a procedure very similar to Alayon et al.⁷⁰ is applied, where CH_4 is activated for 20 min at 200 °C and methanol is extracted by purging

steam. With this method, small-pore zeolites: SSZ-13, SSZ-16 and SSZ-39 produced methanol per gram basis that are comparable and higher than Cu-mordenite and approximately double the amount Cu-ZSM-5 produced (Table 3.3). SSZ-13, SSZ-16 and SSZ-39 also showed higher activity per mol of Cu basis, reaching 0.09 mol CH₃OH mol Cu⁻¹ on Cu-SSZ-39. All samples produced CO₂ as the side product, however the concentration of CO₂ was significantly lower than the concentration of methanol in the effluent stream (1.6 μmol CO₂ g⁻¹ versus 31 μmol CH₃OH g⁻¹ on Cu-SSZ-13, Figure B.3).

The aluminum and copper concentration on zeolites have an important effect on the concentration of active Cu_xO_y species forming upon O₂ pre-treatment.⁶⁸ Here, different Si/Al ratio (6 versus 12) and different copper concentration (mol Cu per gram basis) of SSZ-13 are observed to result in similar methanol formation amounts per gram of zeolite (Table 3.3) and different methanol formation amount per copper, indicating the importance of Cu(II) distribution for different Si/Al ratios resulting in different fraction of Cu(II) that is active. A similar discussion is also valid for Cu-SSZ-16. While Si/Al ratio of 6.5 resulted in methanol formation comparable to SSZ-13 and SSZ-39, Si/Al ratio of 10 resulted in an insignificant amount of methanol formation despite having a larger Cu/Al ratio (Table 3.3).

The framework also has an important effect on the concentration and type of the active species. ZSM-5 (MFI) has interconnecting straight and sinusoidal channels with 10-member openings at the intersection, where the active mono-(μ-oxo)dicopper(II) species is suggested to form.¹¹⁷ In addition to the advantage provided by the alignment of the channels that increase the chance of having two (AlO_{4/2})⁻ sites in close proximity, MFI framework has typical micropore volumes (~0.17 cm³ g⁻¹)

that are nearly half of micropore volume of CHA framework ($\sim 0.30 \text{ cm}^3 \text{ g}^{-1}$), which locally increases the concentration of copper cations in the pores. Despite these mentioned advantages and similar Cu concentration, produced methanol amount was still lower on Cu-ZSM-5, suggesting the possibility of different active species on CHA, AFX and AEI frameworks. The structures and possible active species are evaluated in more detail in the next sections.

3.3.3 UV-vis Spectroscopy

UV-vis spectroscopy is used to analyze the speciation of Cu(II) cations in the samples upon O_2 treatment at $450 \text{ }^\circ\text{C}$. UV-vis spectroscopy is known to provide information about the coordination environment of the Cu(II) cations together with Cu_xO_y specific ligand to metal charge transfer energies that helps the identification of the active species. A characteristic band observed at $22,700 \text{ cm}^{-1}$ in literature is an example of LMCT energy of mono-(μ -oxo)dicopper(II) species that is formed on Cu-ZSM-5.¹¹⁷

The spectra of samples activated at $450 \text{ }^\circ\text{C}$ and kept in O_2 environment are given in Figure 3.3. The absorption bands observed between $12,000 \text{ cm}^{-1}$ and $20,000 \text{ cm}^{-1}$ are assigned to the $d \leftarrow d$ transitions of Cu(II) cations, which give information about the coordination geometry of Cu(II) cations through d orbital splitting energies. The $d \leftarrow d$ transitions of Cu-ZSM-5 was observed by a broad band centered at $14,000 \text{ cm}^{-1}$, which is in agreement with reported broad band at $13,500 \text{ cm}^{-1}$ for O_2 activated Cu-ZSM-5.¹⁵⁵ The broad feature of the band indicates distribution of Cu(II) cations at multiple sites. In fact, Mentzen et al. characterized 5 different Cu coordination on MFI framework.¹⁹⁰

Cu-mordenite, also showed one broad band centered at $13,500\text{ cm}^{-1}$. Two independent $d-d$ transitions were reported at $16,750\text{ cm}^{-1}$ and $13,600\text{ cm}^{-1}$ on Cu-mordenite and assigned to Cu(II) coordinated to single or two Al atoms respectively.¹⁹¹ Here, assignment of the band at $13,500\text{ cm}^{-1}$ to Cu(II) coordination to two Al atoms is in agreement with high Al concentration (Si/Al = 5) in mordenite.

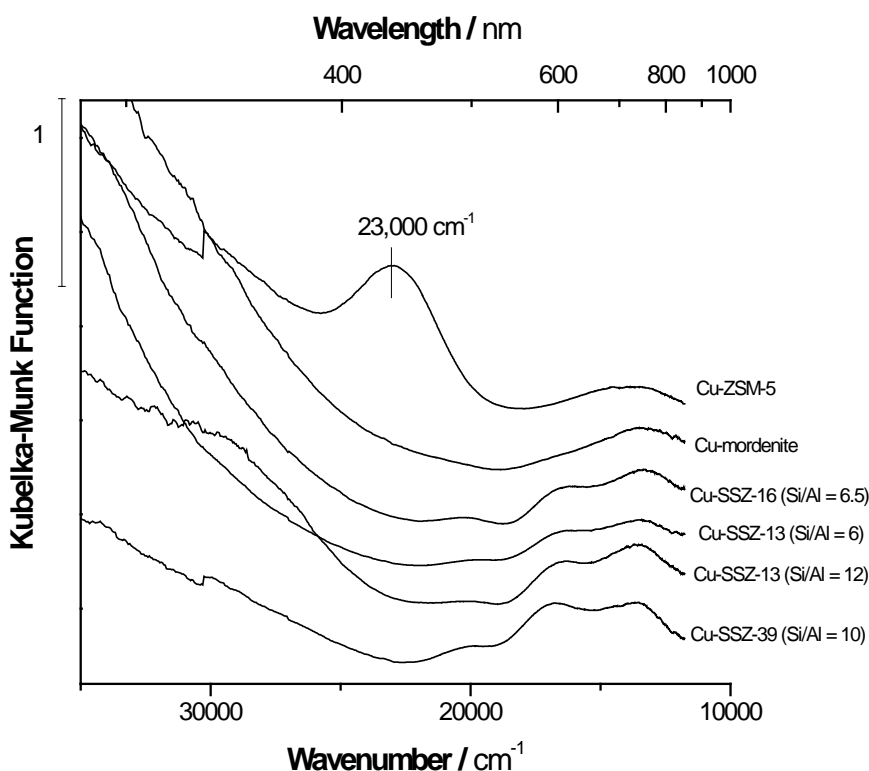


Figure 3.3: Diffuse reflectance UV-vis spectra of Cu-zeolites. Before the spectra were obtained, the samples were heated to $450\text{ }^{\circ}\text{C}$ in flowing O_2 , hold at $450\text{ }^{\circ}\text{C}$ for 2 h and cooled to $25\text{ }^{\circ}\text{C}$. Reproduced from Wulfers et al.⁷¹ with permission from the Royal Society of Chemistry

SSZ-13, SSZ-16 and SSZ-39 are small-pore zeolites because of the 8 member-ring openings between adjacent cages (pore diameters are given in Table 3.3). SSZ-16 and SSZ-39 are structurally similar to SSZ-13 since they share the same building units; i.e., double 6-member rings and 8MRs. Double 6-member rings have different stacking in different frameworks, resulting in *aft* and *gme* cages in SSZ-16¹⁹² and *per* cage (AEI cage) in SSZ-39¹⁹³ instead of *cha* cage in SSZ-13 (Figure 3.4).

Energetically, the most stable site for a bare Cu(II) cation is the window of the 6MR for SSZ-13¹⁵² and for frameworks having 6MRs.¹⁵³ On 6MR, bare Cu cation coordinates to framework oxygens in a distorted square planar geometry for two cases where two Al atoms are separated either by two Si atoms or a single Si atom on 6MR (Figure 1.4). Both cases cause the splitting of the d energy orbitals of Cu(II) with estimated $d_{x^2-y^2} \leftarrow d_{xy}$, $d_{x^2-y^2} \leftarrow d_{zx}, d_{yz}$ and $d_{x^2-y^2} \leftarrow d_{z^2}$ transition energies of $13,600\text{ cm}^{-1}$, $16,600\text{ cm}^{-1}$, $20,000\text{ cm}^{-1}$ and $10,900\text{ cm}^{-1}$, $13,600\text{ cm}^{-1}$, $16,600\text{ cm}^{-1}$ respectively.¹⁴²

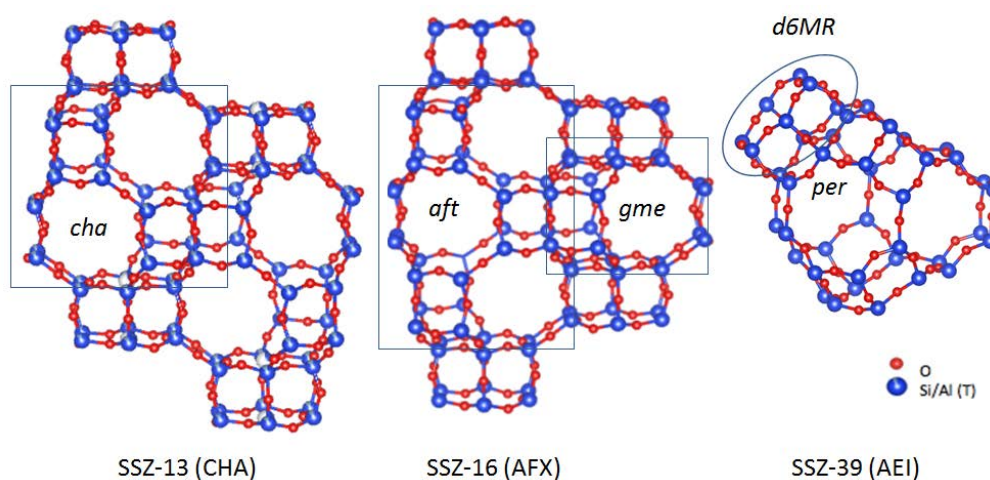


Figure 3.4: Schematic representation of SSZ-13 (CHA), SSZ-16 (AFX) and SSZ-39 (AEI)

The $d \leftarrow d$ transition energies observed for Cu-SSZ-13, -SSZ-16, -SSZ-39 (Table 3.4) between $13,400 \text{ cm}^{-1}$ and $20,300 \text{ cm}^{-1}$ are, therefore, in alignment with the assignment of these transitions to Cu(II) coordinated on 6MRs of these frameworks.

Table 3.4: $d \leftarrow d$ transitions of copper (II) ions in Cu-exchanged zeolites

Zeolite (Framework type)	Si/Al	$d \leftarrow d$ Transitions / cm^{-1}
ZSM-5 (MFI)	11.5	14,000
Mordenite (MOR)	5	13,500
SSZ-16 (AFX)	6.5	13,400, 16,200, 20,300
SSZ-13 (CHA)	6	13,500, 16,200, 19,700
SSZ-39 (AEI)	10	13,700, 16,750, 20,100

Transition observed in the region between $15,000 \text{ cm}^{-1}$ and $30,000 \text{ cm}^{-1}$ are characteristic for $\text{O}_{\text{bridge}} \rightarrow \text{Cu}$ charge transfer transitions in copper complexes.¹⁹⁴ The LCMT absorption band of a mono-(μ -oxo)dicopper(II) species is centered at $22,700 \text{ cm}^{-1}$ in numerous reports.^{5,68,69,117} Here, the band centered at $23,000 \text{ cm}^{-1}$ observed after O_2 activation of Cu-ZSM-5 is assigned to mono-(μ -oxo)dicopper(II) species based on these reports.

There were not any distinct transitions observed at the region between $15,000 \text{ cm}^{-1}$ and $30,000 \text{ cm}^{-1}$ following the activation of Cu-mordenite at $450 \text{ }^\circ\text{C}$ by O_2 . In literature, bands observed at $22,700 \text{ cm}^{-1}$,⁷⁰ and $22,200 \text{ cm}^{-1}$ (ref. ^{69,191}) on Cu-mordenite have been assigned to mono-(μ -oxo)dicopper(II) species following O_2 activation at $250 \text{ }^\circ\text{C}$ ¹⁹¹ and $450 \text{ }^\circ\text{C}$.^{69,70} Grundner et al., on the other hand, did not observe any band at $22,700 \text{ cm}^{-1}$ or $22,200 \text{ cm}^{-1}$ following O_2 activation of Cu-mordenite (Si/Al = 11) at $450 \text{ }^\circ\text{C}$ and suggested a trinuclear copper oxygen cluster,

$[\text{Cu}_3\text{O}_3]^{2+}$, as the active species forming on 8MR of mordenite.¹¹⁴ Shortly after, Vanelderen et al. reported a strong decrease of the absorption band intensity at 22,200 cm^{-1} when the O_2 treatment temperature is higher than 330 °C for Cu-mordenite (Si/Al = 5), showing irreversible instability of the species above 330 °C with absorption feature at 21,900 cm^{-1} . Here, the absence of the band at 22,200 cm^{-1} could also be related to the instability of mono-(μ -oxo)dicopper(II) species due to the high temperature (450 °C) O_2 treatment of Cu-mordenite.

Cu-SSZ-13, -SSZ-16, and -SSZ-39 samples also showed no discernible absorption bands between 20,000 cm^{-1} and 30,000 cm^{-1} , other than a shoulder at 30,000 cm^{-1} observed for Cu-SSZ-13 (Si/Al = 12, Cu/Al = 0.47). A similar shoulder at 29,000 cm^{-1} was previously reported for Cu-SSZ-13 (Si/Al = 13 Cu/Al= 0.44) and tentatively assigned to a μ -(η^2 : η^2) peroxo dicopper(II) complex,¹⁵⁵ while acknowledging the need for further characterization tools such as Raman spectroscopy.

Here, propane treatment at 25 °C is performed on O_2 activated samples to differentiate *reactive* species. The band at 22,900 cm^{-1} on Cu-ZSM-5 disappeared immediately upon interaction with propane at 25 °C (Figure 3.5) consistent with the high reactivity of mono-(μ -oxo)dicopper(II) species. On Cu-SSZ-13 (Si/Al = 6), no significant band intensity loss is observed after interaction of the activated sample with propane for 5 min except the broad intensity loss at the 35,000 –30,000 cm^{-1} region (Figure 3.5). After 40 min in propane flow, absorption intensity losses at 16,400 cm^{-1} and 13,900 cm^{-1} were also observed. There are spectroscopic findings for H_2O and CO formation on the Cu-ZSM-5 (Si/Al = 16) surface when an O_2 activated Cu-ZSM5 is contacted with propane at room temperature.¹⁹⁵ If a similar case is valid

on Cu-SSZ-13, contact of produced H₂O with bare Cu(II) cations could result in [CuOH]⁺ formation, decreasing the $d \leftarrow d$ transition intensities.

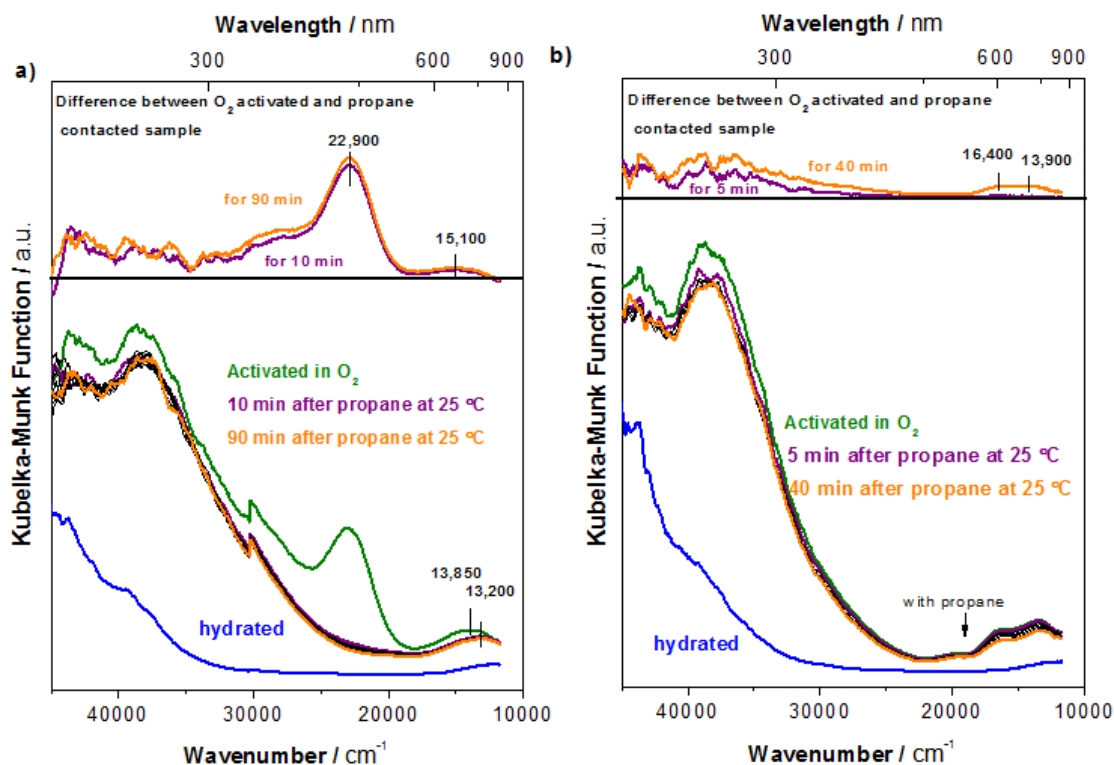


Figure 3.5: Diffuse reflectance UV-vis spectra of a) Cu-ZSM-5 and b) Cu-SSZ-13 (Si/Al = 6). The samples were heated to 450 °C in flowing O₂ for 2 h, cooled to 25 °C and the flow was diverted to propane. The difference between the spectra taken after propane treatment and O₂ treatment are shown as purple and orange lines and given above the measured spectra

Since UV-vis spectroscopy did not reveal any discernible bands following O₂ or propane treatments on Cu-SSZ-13, -SSZ-16 and -SSZ-39 samples, Raman spectra following O₂ treatment are taken on Cu-exchanged samples.

3.3.4 Raman Spectroscopy

Raman spectra of Cu-ZSM-5 (Si/Al = 16, Cu/Al = 0.53), Cu-mordenite (Si/Al = 5, Cu/Al = 0.33), Cu-SSZ-13 (Si/Al = 12, Cu/Al = 0.47), and Cu-SSZ-39 (Si/Al = 10, Cu/Al = 0.48) following O₂ treatment at 450 °C (for 2 h) has been compared to the hydrated states of the samples (hydrated by exposing the samples to air for 12 h) to reveal Cu–O vibrations belonging to the Cu_xO_y species in addition to the framework T–O–T vibrations (Figure 3.6–3.9, Table 3.5).

Cu-ZSM-5 showed Cu–O vibrations at 453 cm⁻¹, 600 cm⁻¹, and increased intensity at 803 cm⁻¹ in addition to the T–O–T bending vibrations at 294 cm⁻¹, 381 cm⁻¹ and 460 cm⁻¹ belonging to the 6MR, 5MR and 4MR, and symmetric T–O–T stretching vibration at 803 cm⁻¹.^{196,197}

Resonance-enhanced Raman vibrations at 456 cm⁻¹ and 870 cm⁻¹ are reported by Woertink et al. to belong to the symmetric and asymmetric Cu–O stretching vibrations of a mono–(μ–oxo)dicopper(II) species forming on Cu-ZSM-5 (Si/Al = 12, Cu/Al = 0.54).¹¹⁷ Observed Raman vibrations at 453 cm⁻¹ and increased band intensity at 803 cm⁻¹ can therefore be related to formed mono–(μ–oxo)dicopper(II) species.

Using an excitation wavelength of 532 nm for Raman spectra of Cu-ZSM-5 sample here revealed all possible vibrations of the sample including the framework vibrations, unlike the resonance-enhanced Raman spectra obtained by Woertink et al.¹¹⁷ The additional stretch at 600 cm⁻¹ could therefore belong to other Cu_xO_y species forming in Cu-ZSM-5 upon O₂ activation of the sample. One possible Cu_xO_y species could be a bis(μ–oxo)dicopper(III) species with reported characteristic Cu–O stretch at ~600 cm⁻¹.¹⁹⁸ Another possibility is the band belonging to a symmetric stretch of a mono–(μ–oxo)dicopper(II) species with an Cu–O–Cu angle of approximately 100° as calculated by Woertink et al.¹¹⁷ Raman spectra obtained after activation of the sample

by flowing $^{18}\text{O}_2$ are required for a definitive identification of the species with observed vibration at 600 cm^{-1} .

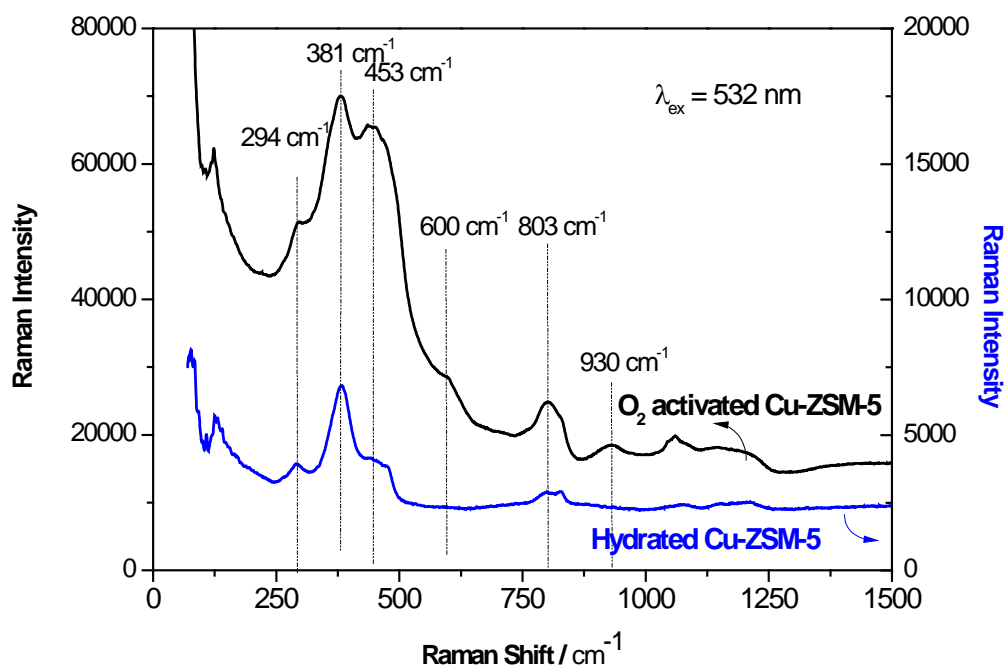


Figure 3.6: Raman spectra ($\lambda_{\text{ex}} = 532\text{ nm}$) of Cu-ZSM-5 (Si/Al = 16, Cu/Al = 0.53) activated in O_2 at $450\text{ }^\circ\text{C}$ for 2 h (black) and hydrated at room conditions (blue). Both spectra are taken at $25\text{ }^\circ\text{C}$

O_2 treated Cu-mordenite showed vibrations at 456 cm^{-1} , 569 cm^{-1} , 600 cm^{-1} (shoulder) and 760 cm^{-1} in addition to the framework vibrations observed at 400 cm^{-1} , 451 cm^{-1} , 465 cm^{-1} and 817 cm^{-1} , which are characteristic mordenite framework vibrations.¹⁹⁹ Vanelderren et al. reported two mono-(μ -oxo)dicopper(II) species forming on Cu-mordenite with symmetric and asymmetric Cu–O stretching vibrations at 465 cm^{-1} , 850 cm^{-1} , and at 450 cm^{-1} , 870 cm^{-1} respectively.¹²⁰ Here, we observe the

vibration at 456 cm^{-1} , which could be considered as the symmetric Cu–O stretching vibration of mono-(μ -oxo)dicopper(II) species, but we are missing the asymmetric Cu–O stretching vibrations expected between 850 cm^{-1} and 870 cm^{-1} . The additional vibrations observed at 569 cm^{-1} , 600 cm^{-1} and 760 cm^{-1} can belong to a mono-(μ -oxo)dicopper(II) species with an Cu–O–Cu angle between 100° and 129° ,¹¹⁷ however strong vibration intensity at 760 cm^{-1} could also suggest an O–O stretch as observed for a μ -(η^2 : η^2) peroxo dicopper(II) species.²⁰⁰ Isotope-sensitive vibrations determined by $^{18}\text{O}_2$ activation are also needed for identification of the Cu_xO_y species forming on Cu-mordenite.

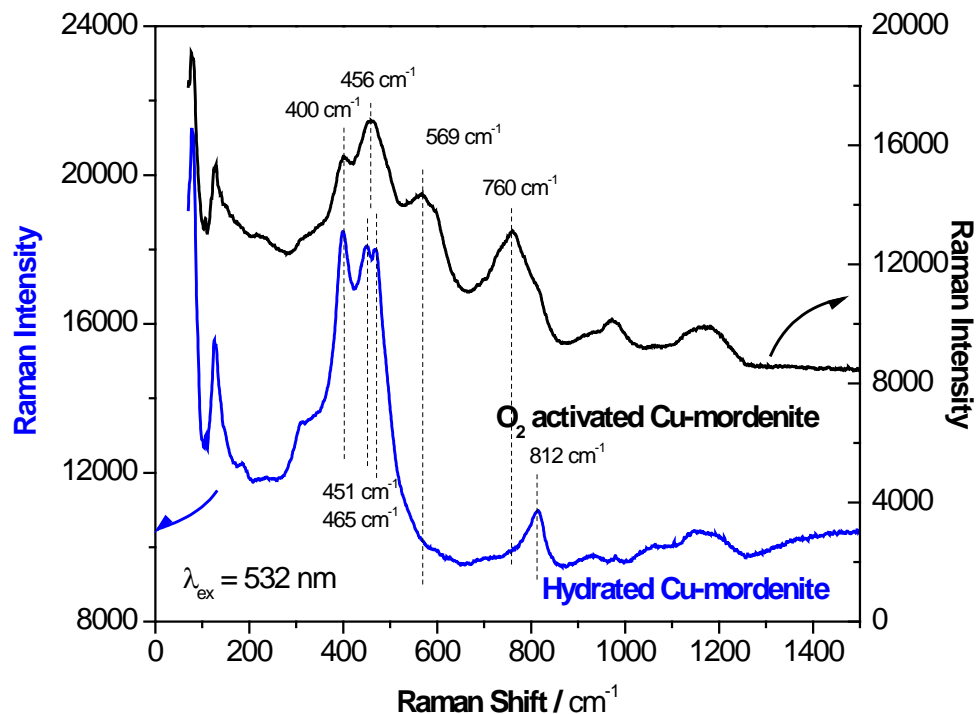


Figure 3.7: Raman spectra ($\lambda_{\text{ex}} = 532 \text{ nm}$) of Cu-mordenite (Si/Al = 5, Cu/Al = 0.33) activated in O_2 at $450 \text{ }^\circ\text{C}$ for 2 h (black) and hydrated at room conditions (blue). Both spectra are taken at $25 \text{ }^\circ\text{C}$

Cu-SSZ-13 and Cu-SSZ-39 showed similar vibrations for Raman spectra taken after O_2 treatment of the samples (Figure 3.8–3.9). The framework vibrations observed at 467 cm^{-1} and 487 cm^{-1} are assigned to the T–O–T bending vibrations of 4MRs,²⁰¹ for SSZ-13 and SSZ-39 samples. Additional to the framework vibrations, vibrations at 360 cm^{-1} , 511 cm^{-1} , 574 cm^{-1} , and 616 cm^{-1} were observed following O_2 activation of Cu-SSZ-13 at $450 \text{ }^\circ\text{C}$ (Figure 3.8). Guo et al. reported Cu–O vibrations at 350 cm^{-1} , 425 cm^{-1} , and 535 cm^{-1} following O_2 treatment of a Cu-SSZ-13 (Si/Al = 4.3, Cu/Al = 0.37) sample and assigned the vibration at 350 cm^{-1} to a mono-(μ -oxo)dicopper(II)

species with an Cu–O–Cu angle of 160° .²⁰¹ An additional band observed at 610 cm^{-1} , similar to what has been observed here on Cu-SSZ-13 (Si/Al = 12, Cu/Al = 0.47) has been assigned to a bis(μ -oxo)dicopper(III) complex by Guo et al.²⁰¹

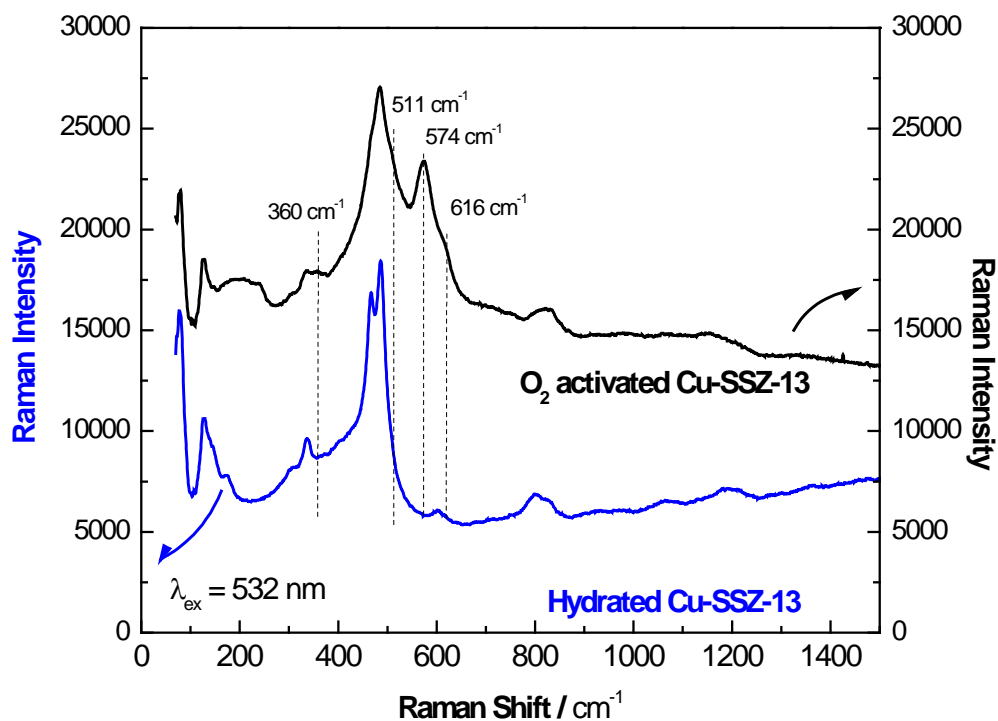


Figure 3.8: Raman spectra ($\lambda_{\text{ex}} = 532\text{ nm}$) of Cu-SSZ-13 (Si/Al = 12, Cu/Al = 0.47) activated in O₂ at 450 °C for 2 h (black) and hydrated at room conditions (blue). Both spectra are taken at 25 °C

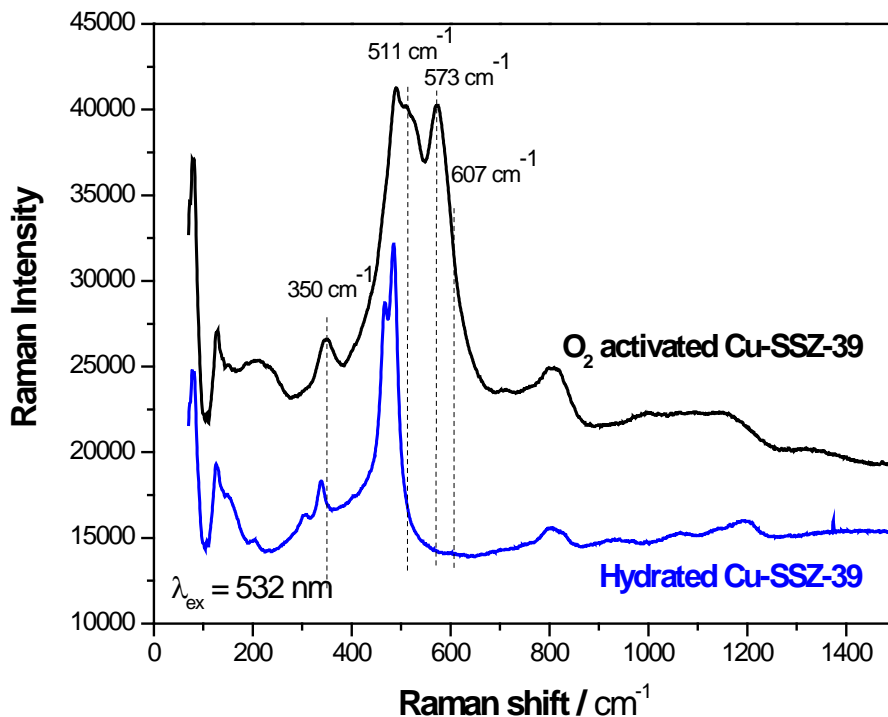


Figure 3.9: Raman spectra ($\lambda_{\text{ex}} = 532 \text{ nm}$) of Cu-SSZ-39 (Si/Al = 10, Cu/Al = 0.48) activated in O_2 at $450 \text{ }^\circ\text{C}$ for 2 h (black) and hydrated at room conditions (blue). Both spectra are taken at $25 \text{ }^\circ\text{C}$

In this chapter, we detected very similar Cu–O vibrations observed on Cu-SSZ-13 and Cu-SSZ-39 following O_2 treatment of the samples, different from the ones observed on Cu-ZSM-5 and Cu-mordenite (Table 3.5), indicating that different Cu_xO_y species are forming on the small-pore zeolites. Definite assignment of these bands requires more detailed investigation including $^{18}\text{O}_2$ isotope Raman experiments and theoretical investigations to support the identification of the Cu_xO_y species on Cu-exchanged small-pore zeolites. (The following chapter gives a complementary investigation for identification of Cu_xO_y species on Cu-SSZ-13.)

Table 3.5: Experimentally observed Raman vibrations on Cu- exchanged zeolites following O₂ treatment at 450 °C for 2 h

Zeolite (Framework type)	Si/Al	Cu/Al	Raman shifts / cm⁻¹
ZSM-5 (MFI)	16	0.53	453, 600, 803
Mordenite (MOR)	5	0.33	456, 569, 760
SSZ-13 (CHA)	12	0.47	360, 511, 574, 611
SSZ-39 (AEI)	10	0.48	350, 511, 573, 607

The Raman spectra following O₂ treatment of the samples indicate formation of Cu_xO_y species on Cu-SSZ-13 and Cu-SSZ-39 that are different than mono-(μ-oxo)dicopper(II) species. These Cu_xO_y species forming on Cu-exchanged small pore zeolites are observed to activate methane also at 200 °C and produce methanol with high selectivity and activity that is higher than Cu-ZSM-5 and Cu-mordenite.

3.4 Conclusion

Cu(II) exchanged small-pore zeolites (-SSZ-13, -SSZ-16, and -SSZ-39) are shown to produce methanol from methane and water using a cyclic process containing 3-steps. Methanol formation selectivity as high as 95% is observed on Cu- exchanged small-pore zeolites. The amount of methanol produced per gram of small-pore zeolites reaching to 39 μmol g⁻¹, is shown to be greater when compared to Cu-mordenite and more than two times of that on Cu-ZSM-5.

The active species responsible for methanol formation on Cu-ZSM-5 was reported to be a bent mono-(μ-oxo)dicopper(II) species ([Cu-O-Cu]²⁺) that can activate methane at temperatures as low as 125 °C⁶⁹ with an activation energy of 15.7 kcal mol⁻¹.¹¹⁷ Here, no evidence of a mono-(μ-oxo)dicopper(II) species is found from the UV-vis spectra of Cu-SSZ-13, -SSZ-16, or -SSZ-39 samples following O₂ activation at 450 °C. Instead, an LCMT band at 30,000 cm⁻¹ is observed on Cu-SSZ-

13 (Si/Al = 12), indicative of a non-framework Cu–O bond that is stable at high temperatures.

Raman spectra of O₂ activated samples confirmed formation of Cu_xO_y species on Cu- exchanged small-pore zeolites with additional vibrations observed at 360 cm⁻¹, 511 cm⁻¹, 574 cm⁻¹ and 611 cm⁻¹ on Cu-SSZ-13. The similarity of framework vibration and Cu–O vibration frequencies confirms the similarity of Cu_xO_y species forming on Cu-SSZ-13, Cu-SSZ-16 and Cu-SSZ-39. In the next chapter, Cu-SSZ-13 is further characterized to identify the active Cu_xO_y species forming on Cu(II) exchanged small-pore zeolites.

Chapter 4

Cu_xO_y CLUSTERS ON Cu-SSZ-13 AND Cu-SSZ-39

4.1 Introduction

Cu-exchanged zeolites are promising heterogeneous catalysts for a variety of reactions including N_2O , NO decomposition and hydroxylation of benzene to phenol.¹⁴⁹ Among the Cu-exchanged zeolites, Cu-SSZ-13 has attracted special interest in catalysis due to its remarkable activity and selectivity for low temperature selective catalytic reduction (SCR) of NO_x by NH_3 ^{65,67} and due to its high-temperature hydrothermal stability.¹⁴³ In the previous chapter, we showed that copper exchanged small-pore zeolites including Cu-SSZ-13 can produce methanol from methane at 200 °C with higher yields than Cu-ZSM-5 and Cu-mordenite when a 3-step cyclic process is applied.⁷¹ The formation of reactive Cu_xO_y species on the metal-exchanged zeolites is imperative for selective methanol formation, a property which is difficult to achieve via steady-state heterogeneous catalysis.⁷⁸ For Cu-exchanged ZSM-5 and mordenite, active species has been suggested to be a mono-(μ -oxo)dicopper(II) complex, $[\text{Cu}-\text{O}-\text{Cu}]^{2+}$ ^{70,117,120,191}, which activates methane at 200 °C. When the O_2 activated small-pore zeolites are characterized using UV-vis and Raman spectroscopy, the features belonging to the active Cu_xO_y species differ from CuZSM-5 and Cu-mordenite, indicating formation of different Cu_xO_y species.

Identification of the composition and structure of these Cu_xO_y species is critical to elucidate the mechanism of methanol production on small-pore zeolites and to design materials with increased active site concentrations. Among small-pore

zeolites, Cu-SSZ-13, have been previously characterized following O₂ activation to better understand its SCR activity.^{142,143,148,151,155,156,202–208} The possibility of Cu_xO_y clusters have been suggested in some of these reports,^{142,206,209,210} in addition to reported bare Cu cations or [CuOH]⁺ moieties following dehydration, but the identity of Cu_xO_y clusters forming on Cu-SSZ-13 has never been revealed.

In this chapter, we have conducted an experimental and theoretical investigation of copper(II) acetate exchanged -SSZ-13 (Si/Al = 12) and -SSZ-39 (Si/Al = 10) to identify the structure and understand properties of these reactive species. The investigation included *in situ* Powder X-ray Diffraction (PXRD), UV–vis spectroscopy and Raman spectroscopy following sample oxidation at 450 °C.

4.2 Methods

4.2.1 Zeolite Synthesis and Ion Exchange

SSZ-13 (Si/Al = 5 and 12) and SSZ-39 (Si/Al = 10) samples were synthesized as described in Chapter 3.

4.2.1.1 Cu(II) exchange

The Cu(II) ion-exchange was performed to the H-form of the zeolite samples. To obtain the H⁺-forms, Na/H-SSZ-13 (Si/Al = 5) sample was firstly exchanged in 0.2 M 500 ml NH₄NO₃ (Sigma-Aldrich, >99%) /de-ionized water solution at 80 °C for 3 h. This ion exchange process was repeated three times to ensure complete ion exchange to the NH₄⁺- form. After each exchange, the zeolites were vacuum filtered, washed with de-ionized water (200 ml for 1 g) and dried at 80 °C for 3 h. NH₄⁺-form of the zeolites were then dehydrated at 120 °C (using a 5 °C min⁻¹ heating rate) for 2 h

and the ammonium groups were decomposed at 560 °C (5 °C min⁻¹ heating rate) for 8 h with 80 cm³ min⁻¹ air flow to obtain H⁺-form of the zeolites.

Cu(II) ion-exchanges were performed as described in Chapter 3. A calculated amount of Cu(II) acetate was added to 500 ml of de-ionized water to have a starting Cu(II) concentration corresponding to Cu/Al = 0.5. It was adjusted to 0.1 and 0.2 for resulting H-Cu-SSZ-13 (Si/Al =12, Cu/Al = 0.02 and Cu/Al = 0.13) samples. The amounts of Cu(II) acetate and zeolites are given in Table 4.1. H⁺- zeolites were then added to the solution and stirred for 12 h at 25 °C. Some samples have been exchanged twice to ensure Cu/Al ratio larger than 0.25. The amount of copper acetate remaining in solution after ion-exchange was calculated using UV–vis absorbance intensities of the filtrate solutions, which was then used to calculate the extent of Cu(II) exchange on the sample. After the Cu(II) exchange, the samples were filtrated, washed with de-ionized water and dried as described in Chapter 3. The zeolites were then calcined at 550 °C (using a heating rate of 5 °C min⁻¹) for 4 h to remove any residual acetate. Na-Cu-SSZ-13 (Si/Al = 12) and Na-Cu-SSZ-39 samples were exchanged as described in Chapter 3.

Table 4.1: Quantity of materials used in copper (II) ion exchanges and the resulting Cu/Al ratios determined by UV–vis

Zeolite (Si/Al)	Volume of solution / ml	Mass of zeolite / g	Mass of copper (II) acetate / g	Number of times exchanged	Cu/Al from UV–vis
H-SSZ-13 (5)	500	5.00	1.285	2*	0.40
H-SSZ-13 (12)	500	15.00	1.780	2*	0.41
H-SSZ-13 (12)	50	0.9	0.06	1	0.13
H-SSZ-13 (12)	50	1	0.024	1	0.02

* Cu(II) concentration in the solution is set to correspond to one fourth of the Al content of the zeolite in the beginning of the second exchange.

4.2.2 Analytical Methods

The samples were analyzed by X-ray diffraction using a Philips X'Pert powder diffractometer with a Cu K α source ($\lambda = 1.5418 \text{ \AA}$) over the range of $2\theta = 5.0\text{--}50.0^\circ$ with a step size of 0.02° and scan rate of 2 second per step.

The elemental composition of samples was determined by Inductively Coupled Plasma Optical Emission Spectroscopy (ICP-OES) technique in Galbraith Laboratories, Knoxville, Tennessee.

The textural properties of the samples were determined using N₂ adsorption at -196°C (Micromeritics Triflex apparatus). The materials were dehydrated under vacuum at a temperature of 300°C for 10 h before N₂ adsorption (Keen Gas, 99.999% purity). The free space volume was measured using helium (Keen Gas, 99.999% purity) before the analysis. Evacuation (at $2 \mu\text{mHg}$) at room temperature followed the free space measurements prior to adsorption measurements. The temperature of the sample during adsorption and free space measurements was set to -196°C using a dewar filled with liquid nitrogen during analysis. The micropore volume of the prepared samples was calculated using statistical thickness method (t-plot¹⁷⁰) and Harkins and Jura¹⁷¹ thickness equation over the thickness range of 3.5 to 5 \AA (Eq. 4.1).

$$t(\text{\AA}) = \left(\frac{13.99}{0.034 - \log(P/P_0)} \right)^{0.5} \quad (4.1)$$

4.2.3 Synchrotron Powder X-ray Diffraction Experiments

Variable temperature powder X-ray diffraction data was collected at beamline 17-BM-B in Advanced Photon Source (APS), Argonne National Laboratory, IL, using a monochromatic beam of wavelength 0.75009 \AA . Diffraction images were recorded on an amorphous Si based area detector placed 250 mm away from the sample. The beam center, sample to detector distance, detector tilt angle and tilt plane rotation

angle was calibrated using LaB₆ (NIST SRM 660a). The hydrated samples (around 20 mg) were loaded in a glass capillary (Mark Rohrchen) with an outer diameter of 1 mm and a wall thickness of 1/100 mm. The glass capillary was connected to a flow furnace system whose details were reported elsewhere.²¹¹ Cu-SSZ-13 (Si/Al = 12, Cu/Al = 0.4) was heated to 500 °C at a heating rate of 9 °C min⁻¹ under 5 cm³ min⁻¹ O₂ (Ultrahigh purity) flow then cooled down to 50 °C under same 5 cm³ min⁻¹ O₂ flow by turning the heater off. Diffraction patterns were collected continuously during heating and cooling of the sample.

XRD data were analyzed using the Rietveld method using GSAS package¹⁷² along with EXPGUI (graphical user interface).¹⁷³ In Rietveld refinement of XRD data, a hexagonal unit cell with the space group type $R\bar{3}m$ was used. Cu(II)-SSZ-13 (Si/Al = 12) powder neutron diffraction data was used as starting atomic coordinates for CHA.¹⁷⁴

4.2.4 Diffuse Reflectance UV–vis Spectroscopy

Diffuse reflectance UV–vis spectra were collected using a UV–vis spectrometer (JASCO, V-5500) and a set-up that allowed gas flow during spectra collection as described in Chapter 3. Baseline for the UV–vis spectra was obtained using barium sulfate (Sigma).

For O₂ treatment at 450 °C, the hydrated samples (exposed to air O₂ and humidity) were heated to 450 °C at a heating rate of 5 °C min⁻¹ and held at 450 °C for 2 h under 20 cm³ min⁻¹ O₂ (Keen Gas, 99.997% purity) flow. The samples were then cooled to 25 °C and a spectrum was taken at 25 °C. H-Cu-SSZ-13 (Si/Al = 12, Cu/Al = 0.4) sample was heated back to 200 °C with 20 cm³ min⁻¹ O₂ flow, then the flow was switched to 20 cm³ min⁻¹ CH₄ flow (Matheson, 99.99%). After 2 h at 200 °C, the

sample was cooled to 25 °C and a spectrum was taken at 25 °C with continuous CH₄ flow.

For the He treatment at 450 °C, the hydrated samples were heated to 450 °C using a heating rate of 5 °C min⁻¹ and held at 450 °C for 4 h under 20 cm³ min⁻¹ He (Keen Gas, 99.999% purity) flow. After cooling to 25 °C, a spectrum was obtained.

For CO treatment, the hydrated samples were heated to 450 °C using a heating rate of 5 °C min⁻¹ and held at 450 °C for 1 h under 20 cm³ min⁻¹ He (Keen Gas, 99.999% purity) flow and cooled to 350 °C under He flow. Then the gas was switched to 20 cm³ min⁻¹ 5% CO (Matheson, 99.999%) balance He flow at 350 °C for 1 h for reduction of the sample to Cu(I). Then the gas was switched back to 20 cm³ min⁻¹ He for 1 h for desorption of CO from the samples. After cooling to 25 °C in He flow, a spectrum was obtained. Then 5 cm³ min⁻¹ O₂ flow was added to the preexisting He flow and another spectrum was obtained at 25 °C.

4.2.5 *In situ* Raman Spectroscopy of H-Cu-SSZ-13

Raman spectra of H-Cu-SSZ-13 (Si/Al = 12, Cu/Al = 0.4) were obtained in Argonne National Laboratory, IL in collaboration with Dr. Hacksung Kim. The spectra were obtained flowing O₂ or He (100 cm³ min⁻¹) at room temperature unless otherwise indicated. The excitation wavelength of 267 nm for mid-UV Raman measurements was provided by the third harmonic generation output of an 800 nm laser line from a 4 kHz repetition rate, nanosecond pulsed, wavelength-tunable Ti:Sapphire laser (Coherent, Indigo-S). Excitation at a wavelength of 458 nm for visible Raman measurements was obtained using a wavelength-tunable Ar ion laser (Melles Griot). To avoid laser-induced sample degradation during the data collection, all the laser power delivered to the sample was kept very low (<1 mW). Also, a

fluidized bed reactor that is a combined use of a shaker and a heat sink by flowing oxygen or helium was employed.²¹² A collimated laser light was focused on the sample, and then the scattered light was refocused by using a 90° off-axis ellipsoidal reflector with the backscattering geometry onto a triple-grating spectrometer (Princeton Instruments, Trivista 555) where Rayleigh light is filtered out and stray light is significantly suppressed. The Raman light was collected by a liquid N₂-cooled UV-enhanced CCD detector. Cyclohexane, chloroform, and trichloroethylene were used as a frequency standard for calibration of Raman shifts. The accuracy of the Raman shifts is estimated to be $\pm 1 \text{ cm}^{-1}$.

The procedures of ¹⁶O₂ treatment at 450°C are the same as described in ‘UV–vis spectroscopy’ (See above). For ¹⁸O₂ treatment at 450°C, pure ¹⁸O₂ gas (Aldrich, 99%) was introduced into the sample and flowed through a closed circulatory system that includes a recirculation pump, a mass flowmeter, and two moisture traps. The gas flow rate in the closed circulatory system was kept at 60 cm³ min⁻¹. The sample was heated and cooled to room temperature and the moisture generated from the heated sample was trapped into the moisture traps.

4.2.6 Raman Spectroscopy of Na-Cu-SSZ-13 and Na-Cu-SSZ-39

Raman spectra of He treated Na-Cu-SSZ-13 (Si/Al =12, Cu/Al = 0.47) and Na-Cu-SSZ-39 (Si/Al = 10, Cu/Al = 0.48) were obtained using a Bruker Senterra Raman microscope in collaboration with Dr. Karl Booksh as described in Chapter 3.

Approximately 40 mg of Na-Cu-SSZ-13 (Si/Al =12, Cu/Al = 0.47) and Na-Cu-SSZ-39 (Si/Al = 10, Cu/Al = 0.48) were placed inside a Class A NMR Tube (Wilma, 5 mm OD, 0.38 mm thickness) using quartz wool to stabilize the samples. Samples were heated to 450 °C at a heating rate of 10 °C min⁻¹, under 40 cm³ min⁻¹ He (Keen Gas,

99.999%) flow. The temperature was then kept at 450 °C for 4 h with continuing He flow. The NMR tube was then flame sealed with He for spectra measurement.

4.2.7 Methane Conversion

The hydrated samples (0.300 ± 0.005 g and particle size between 40–60 mesh) were tested for methanol formation as described in Chapter 3. The reaction procedure for O₂ and He treatments were as follows:

O₂ treatment at 450 °C: The hydrated copper containing samples were first activated in 50 cm³ min⁻¹ O₂ (Keen Gas, 99.997% purity) flow at 450 °C for 7 h using a heating rate of 5 °C min⁻¹. After cooling the sample to 50 °C in 80 min with 50 cm³ min⁻¹ O₂ flow, the flow was switched to 35 cm³ min⁻¹ CH₄ (Matheson, 99.99%) and the temperature was kept at 50 °C for 20 min. Then, the temperature was increased to 200 °C at a heating rate of 5 °C min⁻¹ and the flow was switched to He, which was diverted through a water-containing saturator kept at 25 °C for methanol extraction. The water vapor pressure was 3.2 kPa in He flow.

He treatment at 450 °C: The hydrated copper containing samples were first dehydrated in 50 cm³ min⁻¹ He (Keen Gas, 99.990% purity) flow at 450 °C for 4 h using a heating rate of 5 °C min⁻¹. After cooling the sample to 50 °C in 80 min using 50 cm³ min⁻¹ He flow, the flow was switched to 35 cm³ min⁻¹ CH₄ (Matheson, 99.99%) flow and the temperature was kept at 50 °C for 20 min. The temperature was then increased to 200 °C at a heating rate of 5 °C min⁻¹ and the flow was switched to He, which was diverted through a water-containing saturator for methanol extraction as described above.

4.3 Results and Discussion

4.3.1 Material Characterization

Cu(II)- exchanged samples show high crystallinity with no additional phases (Figure 4.1).

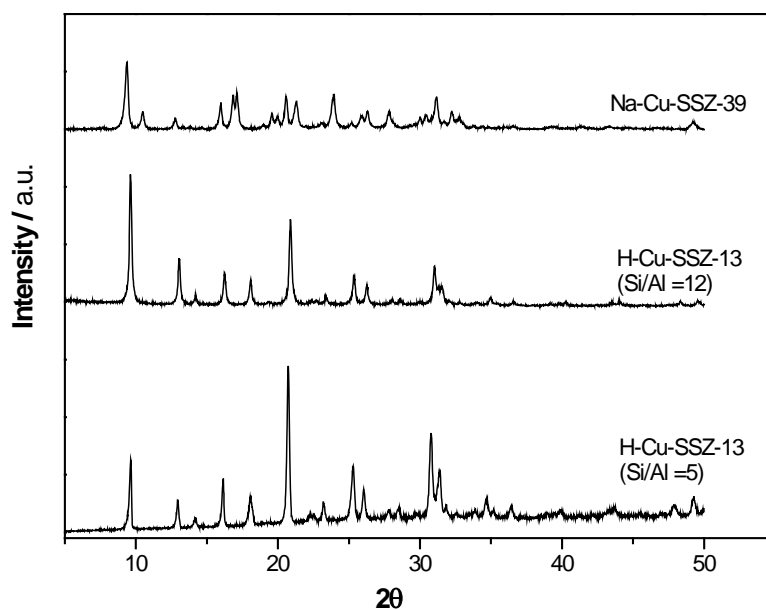


Figure 4.1: Powder XRD pattern of H-Cu-SSZ-13 (Si/Al = 5, Cu/Al = 0.39), H-Cu-SSZ-13 (Si/Al = 12, Cu/Al = 0.40) and Na-Cu-SSZ-39 (Si/Al = 10), Cu $K\alpha$, $\lambda = 1.5418 \text{ \AA}$

The elemental analysis and the measured micropore volumes of the Cu(II) exchanged samples are given in Table 4.2. The Cu/Al ratios calculated using the UV-vis method (described in section 4.2.1) are found to be in good agreement with the ratios found by ICP-OES. The Cu(II) -exchange of -SSZ-13 (Si/Al = 5 and Si/Al =

12) samples with final Cu/Al ratios of 0.39 and 0.4 resulted in 0.017 and 0.025 cm³ g⁻¹ decrease in micropore volume of the samples, which indicates accessibility of the micropores.

Table 4.2: Elemental analysis of copper(II) acetate-exchanged samples calculated from UV-vis and from ICP-OES. t-plot micropore volumes of H⁺- form and Cu(II) exchanged samples are measured with N₂ adsorption at -196 °C

Zeolite (Si/Al)	Si/Al from ICP	Cu/Al from UV-vis	Cu/Al from ICP	Cu content / mmol Cu g ⁻¹	Na/Al from ICP	Micropore Volume / cm ³ g ⁻¹
H-SSZ-13 (5)						0.278
H-Cu-SSZ-13 (5)	5.0	0.40	0.39	1.04		0.261
H-SSZ-13 (12)						0.301
H-Cu-SSZ-13 (12)	11.7	0.41	0.40	0.50		0.276
H-Cu-SSZ-13 (12)		0.13		0.16		
H-Cu-SSZ-13 (12)		0.02		0.03		
Na-Cu-SSZ-13 (12)	11.9	0.45	0.47	0.58	0.025	
Na-Cu-SSZ-39 (10)	9.6	0.40	0.48	0.72	0.029	

4.3.2 Synchrotron Powder X-ray Diffraction Experiments

The oxidation state of Cu cation and Cu_xO_y formation depend on the ‘history’ of the sample including treatment conditions such as the temperature and treatment gas composition.^{117,148,156} In this section we discuss Cu coordination and location on hydrated and high temperature (450 °C) O₂ treated Cu-SSZ-13 (Si/Al = 5 and 12) — kept in an O₂ atmosphere during cooling to 50 °C. Cu coordination at 50 °C following high temperature O₂ treatment is important because it is the temperature at which the sample is contacted with methane for methanol formation.

The evolution of Cu-SSZ-13 (Si/Al = 12, Cu/Al = 0.4 and Si/Al = 5 and Cu/Al = 0.39) upon O₂ treatment was monitored using variable temperature synchrotron PXRD. When the Cu-SSZ-13 (Si/Al = 12, Cu/Al = 0.4) sample is hydrated at 30 °C, 18% of Cu(II) cations in Cu-SSZ-13 (Si/Al = 12, Cu/Al = 0.4) were found near 6MR and 82% were near the 8MR. The hydrated copper cations were found away from the framework oxygen atoms and close to the center of the chabazite cage with Cu-O_{H₂O} distances of 1.97(4) Å and 2.06(7) Å (Table 4.3), which are in agreement with the value of 1.93 Å fitted to EXAFS data of hydrated Cu-SSZ-13 (Si/Al = 15, Cu/Al = 0.44).¹⁵⁶ Extra-framework oxygen atom to total copper ratio was refined to 6.18. An O/Cu value higher than 6 may suggest presence of hydrated Cu(II) cations in both octahedral Cu(II)(H₂O)₆²⁺ form²¹³ and in hydrolyzed [Cu(II)(H₂O)₆(OH)]⁺ form. Cu(II)(H₂O)₆²⁺ and [Cu(II)(H₂O)₆(OH)]⁺ complexes are suggested by Borfecchia et al.¹⁴⁸ and Paolucci et al.¹⁵⁶ for Cu(II) cations exchanged near two and one (AlO_{4/2})⁻ sites respectively. Refined atomic coordinates and occupancies can be found in Table C.1.

Upon heating to 450 °C in O₂, a 0.07 Å decrease in unit cell parameter *a* and a 0.08 Å increase in unit cell parameter *c* resulted in a 10 Å³ decrease in the unit cell volume (Figure C.1). The decrease in the unit cell volume with increasing temperature—a negative thermal expansion—is common in chabazite-type materials.^{143,214} However, when the temperature of the system was decreased back to 50 °C under flowing O₂, the unit cell parameters did not return to the starting hydrated values (Figure C.1). This hysteresis in the changes in the unit cell parameters can be related to the water ligand loss and consequent Cu ion migrations to the 6 and 8MRs as observed from the PXRD data collected after cooling of the sample to 50 °C.

Table 4.3: Cu distribution and bond distances obtained by Rietveld analysis of PXRD data of $H_{0.3}Cu_{1.2}Al_{2.7}Si_{33.3}O_{72}$ and $H_{1.2}Cu_{2.4}Al_6Si_{30}O_{72}$ (APS, 17-BM-B, $\lambda = 0.75009 \text{ \AA}$, Trigonal, R-3m)[†]

Cu-SSZ-13 (Si/Al = 12, Cu/Al = 0.4) 30 °C, hydrated		Cu %	Bond	Distance (Å)
Cu at 6MR		18	Cu1– O1 _(fw) *3	2.87(5)
			Cu1– O6 _(H2O)	2.06(7)
Cu at 8MR		82	Cu2– O3 _(fw)	3.05(3)
			Cu2– O5 _(H2O)	1.97(4)
	<i>a</i> / Å	13.5805(1)		
	<i>c</i> / Å	14.6748(2)		
	<i>V</i> / Å ³	2343.89(4)		
	χ^2	8.099		
	R _p / %	1.68		
	wR _p / %	2.24		
Cu-SSZ-13 (Si/Al = 12, Cu/Al = 0.4) 50 °C, O ₂ activated		Cu %	Bond	Distance (Å)
Cu at 6MR		23	Cu1– O1 _(fw) *3	2.293(4)
Cu at 8MR		47 (Total)		
		26	Cu2– O2 _(fw)	2.20(4)
			Cu2– O3 _(fw)	2.74(4)
			Cu2– O4 _(fw)	2.09(4)
		21	Cu3– O2 _(fw) *2	2.76(3)
			Cu3– O3 _(fw)	2.22(6)
	<i>a</i> / Å	13.5494(2)		
	<i>c</i> / Å	14.7720(2)		
	<i>V</i> / Å ³	2348.59(8)		
	χ^2	2.610		
	R _p / %	1.51		
	wR _p / %	1.99		
Cu-SSZ-13 (Si/Al = 5, Cu/Al = 0.39) 50 °C, O ₂ activated		Cu %	Bond	Distance (Å)
Cu at 6MR		80 (Total)		
		67	Cu1– O1 _(fw) *3	2.16(1)
		13	Cu4– O1 _(fw) *2	1.96(4)
			Cu4– O3 _(fw)	2.0(2)
Cu at 8MR		12	Cu3– O3 _(fw)	2.6(1)
			Cu3– O2 _(fw)	2.96(2)
Cu at 4MR		8	Cu2– O1 _(fw)	1.92(1)
			Cu2– O2 _(fw)	1.896(7)
	<i>a</i> / Å	13.4932(5)		
	<i>c</i> / Å	15.1027(7)		
	<i>V</i> / Å ³	2381.3(2)		
	χ^2	4.211		
	R _p / %	2.52		
	wR _p / %	3.59		

[†] See Figure 4.2 to identify different Cu positions on Cu-SSZ-13 (Si/Al = 12, Cu/Al = 0.4) and Figure 4.3 for Cu-SSZ-13 (Si/Al = 5, Cu/Al = 0.39)

At 50 °C, dehydrated Cu cations near 6 MR (Cu1) were coordinated to three oxygen atoms on the 6MR (Figure 4.2) with Cu–O_{fw} distances of 2.293(4) Å. (Table 4.3, Table C.2). Cu on the symmetry axis of the 6MR has been often reported for SSZ-13 with different Si/Al ratios using XRD,^{143,151,154,174} where higher occupations were observed with higher Al content.¹⁴³ However, using Extended X-ray Absorption Fine Structure Analysis (EXAFS) and Electron Paramagnetic Resonance (EPR) spectroscopy, it has been shown that Cu(II) coordinates to 4 framework oxygen atoms in a distorted square planar fashion on the plane of 6MR (Figure 1.4).^{142,148,150,151} This site, with two Al atoms on the 6MR, is favorable for bare Cu(II) cations^{152,154} when compared to the Cu sites on 8MR having two Al atoms (more favorable by 54–71 kJ mol⁻¹)¹⁵². [CuOH]⁺ species, on the other hand, were reported to be present on Cu-SSZ-13 after O₂ treatment¹⁴⁸ and was reported to be more favorable on 8MR.^{148,154}

The fraction of Cu on 6MR (Cu1) increased from 0.18 to 0.23 upon dehydration, indicating Cu migration from 8 MR to 6MR. This migration could be due to loss of OH ions as well as H₂O ligands after dehydration (see Figure 4.14) since bare Cu cations are favored at 6MR when compared to 8MR either in Cu(II) or in Cu(I) state.¹⁵² The refined fraction of Cu cations on 6MR, 0.23, is in close agreement with the refined value of 0.2 for Cu occupation at 6MR on Cu-SSZ-13 (Si/Al = 15.5, Cu/Al = 0.45) reported before.¹⁵⁴

Two Cu(II) sites were found near 8MR: Cu2 (26%) with Cu– O_{fw}(framework) distances of 2.09(4) Å and 2.20(4) Å and Cu3 (21%) further away from the framework oxygen atoms (Table 4.3, Figure 4.2). Cu– O_{fw} distances for Cu cations at 8MR are larger than optimized Cu– O_{fw} distances for bare Cu(II) with 2 Al or for [CuOH]⁺

species on 8MR ($\text{Cu}-\text{O}_{\text{fw}}$ between 1.93 and 2.03 Å)¹⁴⁸ indicating the existence of other Cu_xO_y species on 8MR.

It was not possible to refine the positions of extra-framework oxygen atoms due to the distribution of copper cation positions and the lower form factor of oxygen (compared to copper cations); 8.02 $e \text{ atom}^{-1}$ for O and 29.3 $e \text{ atom}^{-1}$ for Cu at 16.5 keV).²¹⁵

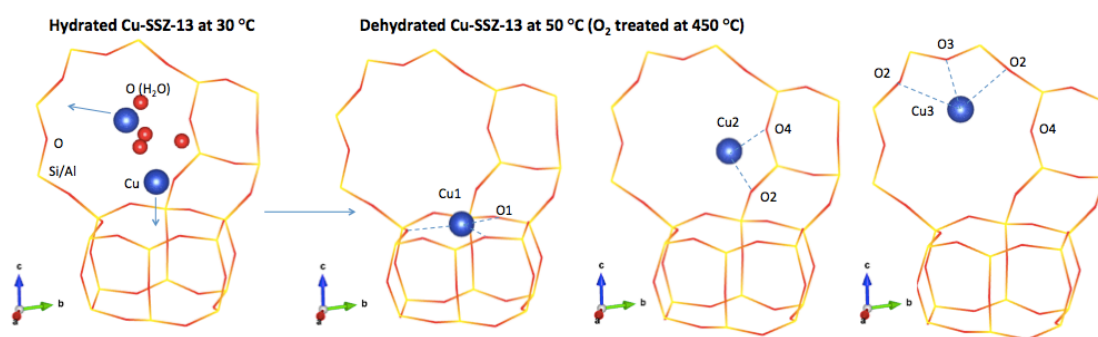


Figure 4.2: Schematic of d6MR and 8MR of hydrated and dehydrated Cu-SSZ-13 (Si/Al = 12, Cu/Al = 0.4) at 30 °C refined in space group $R-3m$ (No.166). For illustration purposes, all extra-framework atoms are represented in the same cage on left. The three refined Cu sites found after O_2 treatment at 450 °C are given on right.

O_2 treatment of Cu-SSZ-13 (Si/Al = 5, Cu/Al = 0.39) at 450 °C followed by cooling to 50 °C led to 80% of the Cu(II) cations near the 6MR; 67% (Cu1) at the center of the 6 MR (as on Cu-SSZ-13 (Si/Al = 12)), and 13% (Cu4) slightly off center towards O3, with two 1.96(4) Å $\text{Cu}-\text{O}_{\text{fw}}$ bonds (Cu4–O1) and one 2.0(2) Å (Cu4–O3) bond (Table 4.3, Table C.3). Only 12% of copper is found near 8 MR (Cu3) and 8% (Cu2) is found above the 4MR with $\text{Cu}-\text{O}_{\text{fw}}$ distances of 1.92(1) Å and 1.896(7) Å (Table 4.3, Figure 4.3).

Dehydrated Cu-SSZ-13/5 at 50 °C (O₂ treated at 450 °C)

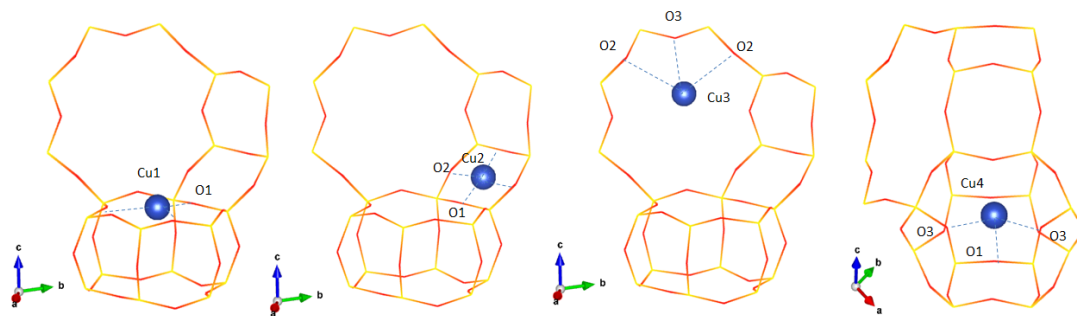


Figure 4.3: Schematic of d6MR and 8MR of dehydrated Cu-SSZ-13 (Si/Al = 5, Cu/Al = 0.39) refined in space group *R-3m* (No.166). Figures display the four refined Cu sites found after O₂ treatment at 450 °C. Atomic parameters can be found in Table S2.3.

Cu(II) location and coordination in SSZ-13 has been investigated by several methods including XRD.^{143,151,154,204} Si/Al ratios were observed to have an effect on Cu distribution.^{205,206} The Cu(II) sites were exclusively coordinated to the window of the 6MR when Si/Al was 6,¹⁴³ whereas, Cu(II) coordination to the 8MR window were mainly observed with higher Si/Al ratios (80% of Cu(II) on 8MR with Si/Al of 15.5).¹⁵⁴ Here, we show that there is a major difference in Cu distribution on SSZ-13 samples having Si/Al ratios of 5 and 12. The difference in Cu site distribution on the two SSZ-13 samples can be attributed to Al contents of the samples. Higher Al content results in a higher fraction of 6MRs having two Al atoms.²⁰⁵ With more 6MRs having two Al atoms, more (bare) Cu(II) cations occupy this energetically favorable site as observed on Cu-SSZ-13 (Si/Al = 5). Bates et al.²⁰⁵ calculated the maximum achievable Cu/Al ratio for the Cu associated with two Al atoms on the 6MR to be 0.23 and 0.11 for Si/Al = 5 and 12 respectively;²⁰⁵ from our Rietveld refinements Cu occupation on 6 MR results in a Cu/Al = 0.26 for Si/Al = 5 and Cu/Al = 0.09 for Si/Al = 12, in very good agreement with these estimates.²⁰⁵

4.3.3 Diffuse Reflectance UV–vis Spectroscopy

Spectroscopy and crystallography are the most frequently used methods that reveal the structures of the oxidized Cu(II) centers in biology.²¹⁶ UV–vis spectroscopy helps to establish the LMCT transition absorption bands of Cu_xO_y species as a function of concentration and attenuation factor of the species.⁶⁸ The activity of the mono-(μ -oxo)dicopper(II) species ($[\text{Cu}-\text{O}-\text{Cu}]^{2+}$) for methanol formation has been monitored on Cu-ZSM-5 and Cu-mordenite following the change in the intensity of the LMCT band at $22,700\text{ cm}^{-1}$.^{5,117,120} In Chapter 3, it was noted that unlike Cu-ZSM-5; Cu-SSZ-13, -SSZ-16 and -SSZ-39 did not show discernible LMCT bands in the $20,000\text{--}30,000\text{ cm}^{-1}$ region other than a shoulder at $30,000\text{ cm}^{-1}$ observed on Cu-SSZ-13 (Si/Al = 12, Cu/Al = 0.47). Here Cu-SSZ-13 samples with different Si/Al and Cu/Al ratios have been investigated using DR UV–vis spectroscopy following O_2 treatment of the samples at $450\text{ }^\circ\text{C}$.

The shoulders observed at $30,000\text{ cm}^{-1}$ and $35,000\text{ cm}^{-1}$ on Cu-SSZ-13 (Si/Al = 12, Cu/Al = 0.4) are more pronounced when compared to SSZ-13 (Si/Al = 5, Cu/Al = 0.39), which have more than twice the Cu concentration of Si/Al = 12 (Table 4.2), indicating the importance of Si/Al ratio and Cu distribution on Cu_xO_y formation. Increasing Cu(II)/Al ratio on SSZ-13 (Si/Al = 12) resulted in increased absorption intensity between $30,000\text{ cm}^{-1}$ and $35,000\text{ cm}^{-1}$ indicating higher concentration of Cu_xO_y sites. The bands at $13,600\text{ cm}^{-1}$, $16,500\text{ cm}^{-1}$ and $19,700\text{ cm}^{-1}$ also showed increased intensity with increasing Cu/Al ratio (Figure 4.4).

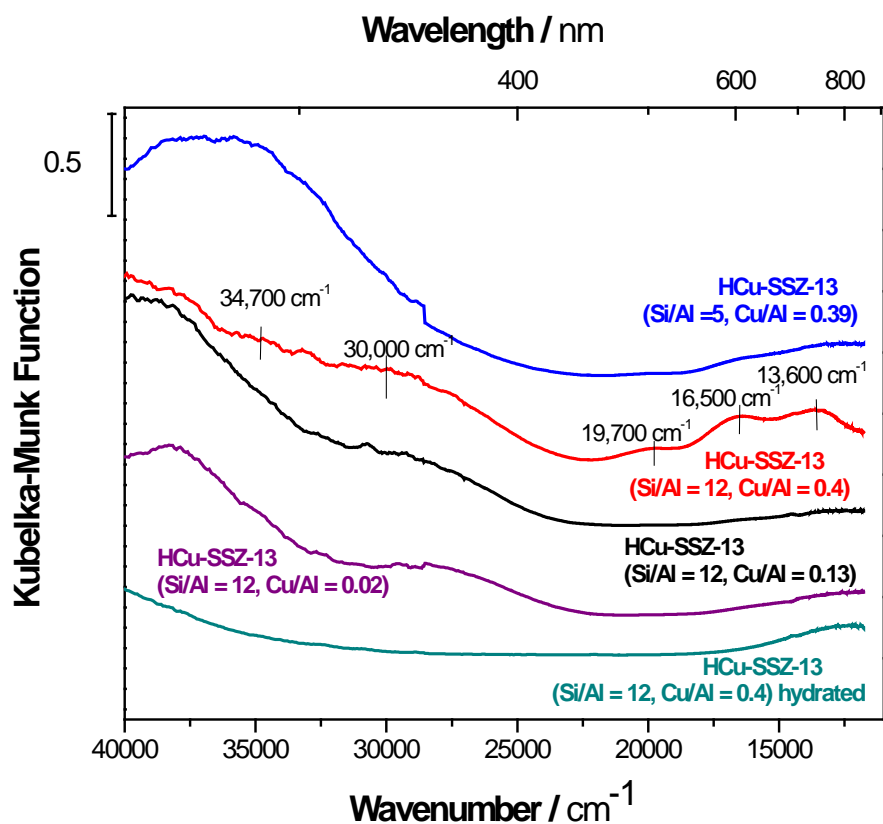


Figure 4.4: DR UV-vis absorption spectra of Cu-SSZ-13 samples in hydrated form and after O₂ treatment at 450 °C for 2 h. Before the spectra were collected, the temperature was reduced to room temperature under O₂ flow.

The bands at 13,600 cm⁻¹, 16,600 cm⁻¹, 20,000 cm⁻¹ and 10,900 cm⁻¹, 13,600 cm⁻¹, 16,600 cm⁻¹ have been assigned to $d_{x^2-y^2} \leftarrow d_{xy}$, $d_{x^2-y^2} \leftarrow d_{zx}$, d_{yz} and $d_{x^2-y^2} \leftarrow d_{z^2}$ transition energies belonging to Cu(II) coordination to 6MR with two Al atoms at third-nearest-neighbors (-Al-O-(Si-O)₂-Al-, site B in Figure 1.4, site A1 using notation by Godiksen et al.¹⁴²) and at second-nearest-neighbor position (-Al-O-(Si-O)-Al-, site A in Figure 1.4, site A2 using Godiksen notation.¹⁴²) respectively. For Cu-SSZ-13 (Si/Al = 14, Cu/Al = 0.44), 11% of Cu(II) cations were found at site

A1 and another 10% were found at site A2 by EPR, giving a total of 21% of Cu(II) EPR active cations (corresponding to a Cu/Al ratio of 0.09) residing at 6MR.¹⁴² This Cu distribution is in agreement with our PXRD results for Cu-SSZ-13 (Si/Al= 12, Cu/Al = 0.4) giving Cu/Al = 0.09 for Cu(II) at 6MR. Furthermore, assignment of equal concentration of site A1 and A2 is reasonable with Cu-SSZ-13 (Si/Al= 12, Cu/Al = 0.4) based on observed equal intensity of 16,600 cm⁻¹ and 13,600 cm⁻¹. But there are spectral features that require further explanation if this assignment is encompassing of all possibilities. For instance, absence of bands at 16,600 cm⁻¹ and 20,000 cm⁻¹ on Si/Al = 12 samples with lower Cu concentrations (Cu/Al = 0.13 and Cu/Al = 0.02), indicates exclusive occupancy of site A2; two Al atoms at second-nearest-neighbor position (-Al-O-(Si-O)-Al-) —according to the assignment by Godiksen et al.¹⁴² The presence of two Al atoms at second-nearest-neighbor position can be confirmed by the band at -102 ppm from ²⁹Si NMR spectra of SSZ-13 (Si/Al =12) sample indicating Si(2Al) coordination (Figure C.2), however thermodynamic favorability of site A1 where two Al atoms are at third nearest neighbors is theoretically shown over site A2 by 19 to 22 kJ mol⁻¹,^{152,156} which would indicate preferential occupation of site A1 before A2. Similarly, a higher occupation of site A1 with assigned UV-vis bands at 16,600 cm⁻¹ and 20,000 cm⁻¹ was expected for Cu-SSZ-13 (Si/Al = 5, Cu/Al = 0.39) sample, which showed Si(1Al)/Si(2Al) ratio of 2.2 (Figure C.4) from ²⁹Si NMR spectra.

PXRD results showed 77% of Cu(II) cations on 8MR of Cu-SSZ-13 (Si/Al = 12, Cu/Al = 0.4), whereas that percentage for the Si/Al = 5 sample is found as 12% suggesting that the pronounced bands at 30,000 cm⁻¹ and 35,000 cm⁻¹ on Cu-SSZ-13 (Si/Al = 12, Cu/Al = 0.4) to belong to Cu_xO_y species with Cu(II) at 8MR (Figure 4.4).

Moreover, evolution of the bands at $30,000\text{ cm}^{-1}$, $19,500\text{ cm}^{-1}$ and $16,750\text{ cm}^{-1}$ with increased temperature (Figure 4.5) could be interpreted as energy activated formation of a Cu_xO_y species, where the origin of the bands at $19,500\text{ cm}^{-1}$ and $16,750\text{ cm}^{-1}$ are still debatable. One possibility is that they belong to Cu_xO_y species since similar transition energies at $19,083\text{ cm}^{-1}$ and $16,260\text{ cm}^{-1}$ are reported for trans- μ -1,2-peroxo dicopper(II) species.²¹⁷ Or, formation of Cu_xO_y species with increased temperature could be accompanied by an increased bare Cu(II) cation concentration at 6MR (and therefore the intensity of the bands at $20,000\text{ cm}^{-1}$ and $16,600\text{ cm}^{-1}$ following the assignment by Godiksen et al.),¹⁴² which would also explain the increase in EPR intensity as temperature is increased from $250\text{ }^\circ\text{C}$ to $400\text{ }^\circ\text{C}$.¹⁴²

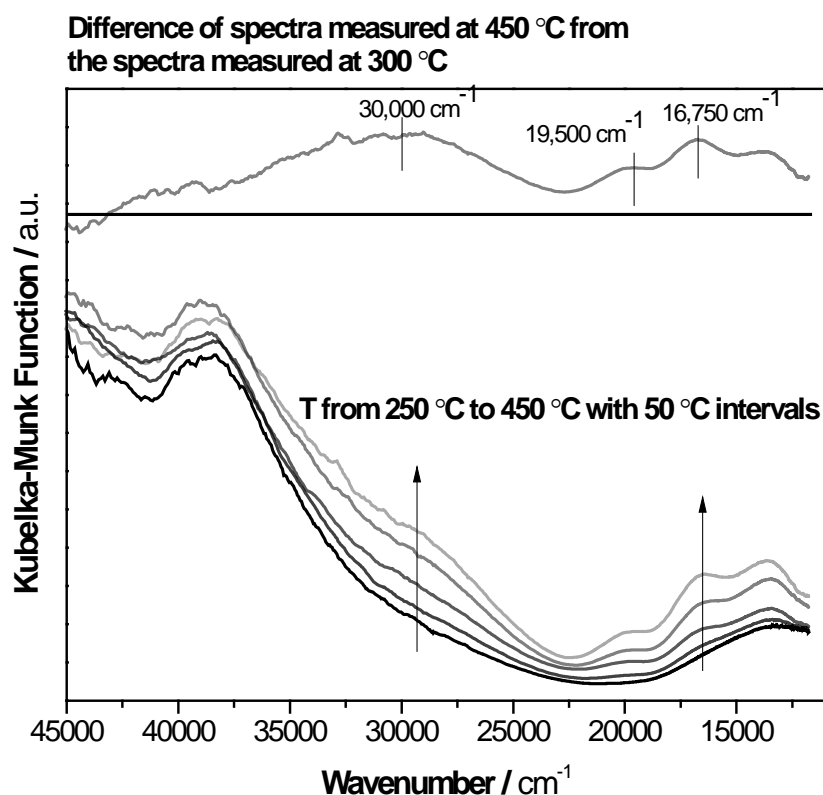


Figure 4.5: DR UV-vis absorption spectra of Cu-SSZ-13 (Si/Al = 12, Cu/Al = 0.4) after O₂ treatment at 250 °C, 300 °C, 350 °C, 400 °C and 450 °C. Before the spectra were collected, the temperature was reduced to room temperature under O₂ flow. The difference between the spectra taken at 450 °C and 300 °C is given above the measured spectra.

The higher amount of methanol formation on Cu-SSZ-13 (Si/Al = 12, Cu/Al = 0.35, 0.07 methanol/Cu) when compared to that of Cu-SSZ-13 (Si/Al = 6, Cu/Al = 0.35, 0.03 methanol/Cu) (see Chapter 3) suggests higher concentration of reactive Cu_xO_y species on Cu-SSZ-13 (Si/Al = 12, Cu/Al 0.4). Therefore, O₂ treated Cu-SSZ-13 (Si/Al = 12, Cu/Al 0.4) was contacted with methane at 200 °C to reveal the characteristic absorption energies of reactive Cu_xO_y species based on intensity

losses/changes. Reduction of absorption intensities from a broad band centered at $29,500\text{ cm}^{-1}$ (and shoulders at $35,000\text{ cm}^{-1}$ and $22,200\text{ cm}^{-1}$) upon CH_4 admission (Figure 4.6) indicates that the reactive species have absorption features at $22,200\text{ cm}^{-1}$, $29,500\text{ cm}^{-1}$ and $35,000\text{ cm}^{-1}$. Interestingly, no absorption losses at the bands at $13,600\text{ cm}^{-1}$, $16,600\text{ cm}^{-1}$, $20,000\text{ cm}^{-1}$ were observed, supporting the assignment of these bands to bare Cu(II) cations.

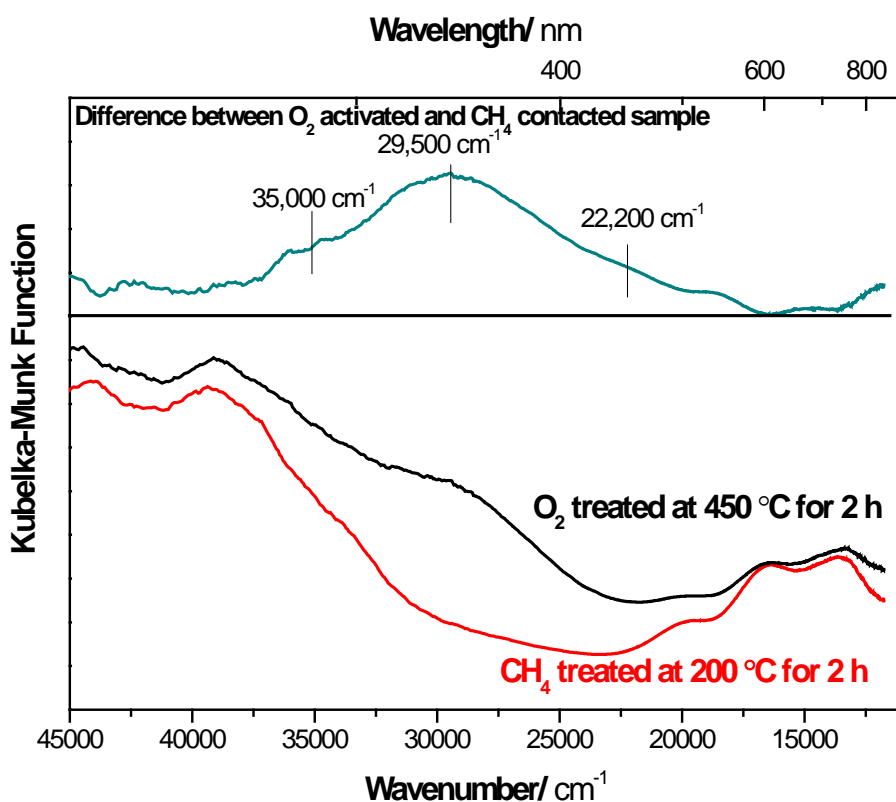


Figure 4.6: DR UV-vis absorption spectra of Cu-SSZ-13 (Si/Al = 12, Cu/Al = 0.4) after O_2 treatment at $450\text{ }^\circ\text{C}$ 2 h, and subsequent CH_4 treatment at $200\text{ }^\circ\text{C}$ for 2h. Before the spectra were collected, the temperature was reduced to room temperature under O_2 or CH_4 flow. The difference between the O_2 and CH_4 treated spectra is given above the measured spectra.

4.3.4 *In situ* Raman Spectroscopy of H-Cu-SSZ-13

Raman spectra of O₂ treated H-Cu-SSZ-13 (Si/Al = 12, Cu/Al = 0.4) were measured using an excitation wavelength of 458 nm (Figure 4.7). The bands at 467 cm⁻¹ and 487 cm⁻¹ are assigned to the T-O-T bending vibrations in the zeolite 4MR as deduced from the literature²⁰¹ and from density functional theory (DFT) calculations performed here (see below).

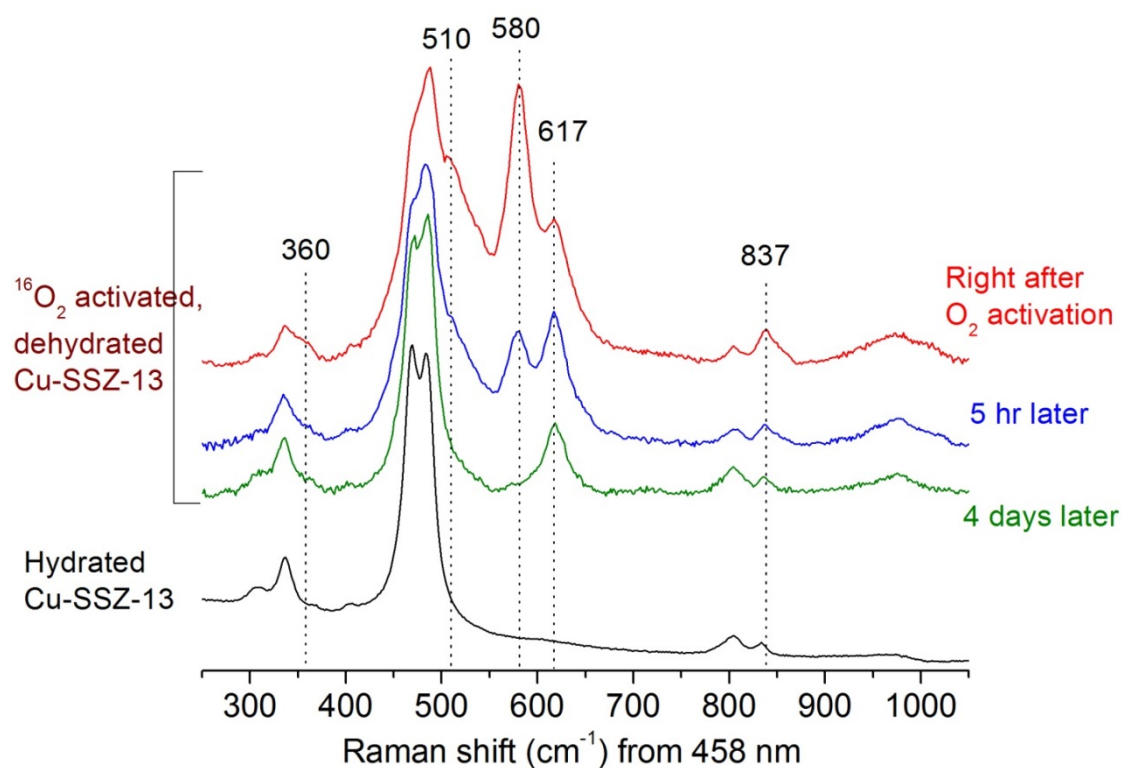
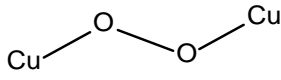
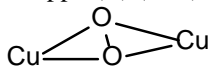
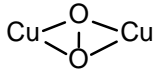
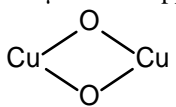
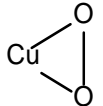


Figure 4.7: *In situ* Raman spectra of O₂ activated (at 450 °C for 2 h) H-Cu-SSZ-13 (Si/Al = 12, Cu/Al = 0.4). Blue and green spectra are taken after indicated time spent in pure O₂ environment. Hydrated H-Cu-SSZ-13 is given for comparison (black)

The O₂ activated sample showed five new bands at 360 cm⁻¹, 510 cm⁻¹, 580 cm⁻¹, 617 cm⁻¹ and 837 cm⁻¹ when compared to the hydrated sample. The vibrations at 360, 510, 580 and 837 cm⁻¹ disappeared after 4 days at room temperature in O₂, showing instability of some of the Cu_xO_y species; the band at 617 cm⁻¹ maintains a constant intensity suggesting other species that are stable. The decrease in intensity of these four bands over time could be due to a small amount of H₂O leaking into the system despite the continuous O₂ flow and presence of moisture traps, or due to time instability of the species. In either case, the simultaneous disappearance of the bands might suggest that these vibrations belong to the same species. This group of four vibrations is in fact in excellent agreement with trans-μ-1,2-peroxo dicopper(II) species (Table 4.4) where 360 cm⁻¹ is assigned to the bending vibration of Cu–O bond ($\delta_{\text{Cu-O}}$), 510 cm⁻¹ and 580 cm⁻¹ are assigned to the stretching vibrations of Cu–O bond ($\nu_{\text{Cu-O}}$) and 837 cm⁻¹ is assigned to the O–O stretching vibration ($\nu_{\text{O-O}}$) of peroxide.

¹⁸O isotope experiments were performed by treating the dehydrated H-Cu-SSZ-13 (Si/Al = 12, Cu/Al = 0.4) at 450 °C in ¹⁸O₂ flow for 13 h and then keeping it under ¹⁸O₂ loop flow for nearly 4 days. The spectra reveal a 24 cm⁻¹ shift for the band at 617 cm⁻¹ (Figure 4.8). The observed frequency at 617 cm⁻¹ and the degree of oxygen isotope shift of $\Delta(^{18}\text{O}_2) = 24 \text{ cm}^{-1}$ are in good agreement with those of the totally symmetric breathing mode (A_g with D_{2h} and C_{2h} symmetry in the Cu₂O₂ diamond core)¹⁹⁸ for bis(μ-oxo)dicopper(III) species with a Cu–O–Cu angle around 101°²¹⁸ (Table 4.4). Similarly, a band at 610 cm⁻¹ was previously observed on Cu-SSZ-13 (Si/Al = 4.3 and Cu/Al = 0.36) and assigned to a bis(μ-oxo)dicopper(III) complex by Guo et al.²⁰¹

Table 4.4: Mononuclear and binuclear Cu_xO_y complexes mentioned in the literature and in this work and their spectroscopic features

Cu_xO_y species	$\lambda_{\text{max}} / \text{cm}^{-1}$, ($\epsilon / \text{M}^{-1}\text{cm}^{-1}$)	rR vibrations ($\Delta^{18}\text{O}_2$) / cm^{-1}	This work / cm^{-1} , $\lambda_{\text{ex}} = 532 \text{ nm}$	This work / cm^{-1} , $\lambda_{\text{ex}} = 458 \text{ nm}$
Trans- μ -1,2-peroxo dicopper(II)	22,989 (1700) 19,083 (11,300) 16,260 (5,800)	$\nu_{\text{Cu-O}} = 561$ (26) $\nu_{\text{O-O}} = 832$ (44) ²¹⁷	$\nu_{\text{Cu-O}} = 511$, 574 $\delta_{\text{Cu-O}} = 360$, 240, 213 $\nu_{\text{O-O}} = 836$	$\nu_{\text{Cu-O}} = 510$, 580 $\delta_{\text{Cu-O}} = 360$, $\nu_{\text{O-O}} = 837$
				
μ - $\eta^2:\eta^2$ -peroxo dicopper(II) (bent)	18,200 (1000) 20,400–23,800 (5,000) 27,800 (20,000)	$\nu_{\text{Cu-Cu}} = 297$ $\nu_{\text{O-O}} = 750$ (41) ²¹⁹		
				
μ - $\eta^2:\eta^2$ -peroxo dicopper(II) (planar)	17,100–19,800 (1000) 27,300–29,600 (20,000)	$\nu_{\text{Cu-Cu}} = 284$ $\nu_{\text{O-O}} = 763$ (40) ²⁰⁰		
				
Bis- μ -oxo dicopper(III)	22,300–25,000 (13,000– 28,000) 30,800–32,700 (11,000– 21,000)	$\nu_{\text{Cu-O}} = 609$ (23) ¹⁹⁸	616	617 ($\Delta^{18}\text{O}_2 = 24$)
				
η^2 -Superoxo dicopper (II)	10,200 (<400) 14,300 (<400) 22,100 (<400) 26,100 (<400)	$\nu_{\text{Cu-O}} = 554$ (20) $\nu_{\text{O-O}} = 1043$ (59) ²²⁰		
				

Giordanino et al.¹⁵⁵ have previously suggested a side-on μ -($\eta^2:\eta^2$) peroxo dicopper(II) species which shows a characteristic UV-vis absorption and Raman band²⁰⁰ at $29,000 \text{ cm}^{-1}$ and at $\sim 763 \text{ cm}^{-1}$, respectively. While our UV-vis spectra shows a characteristic side-on peroxide absorption band at $29,000 \text{ cm}^{-1}$, Raman spectral position at 837 cm^{-1} indicates an end-on peroxide rather than a side-on.

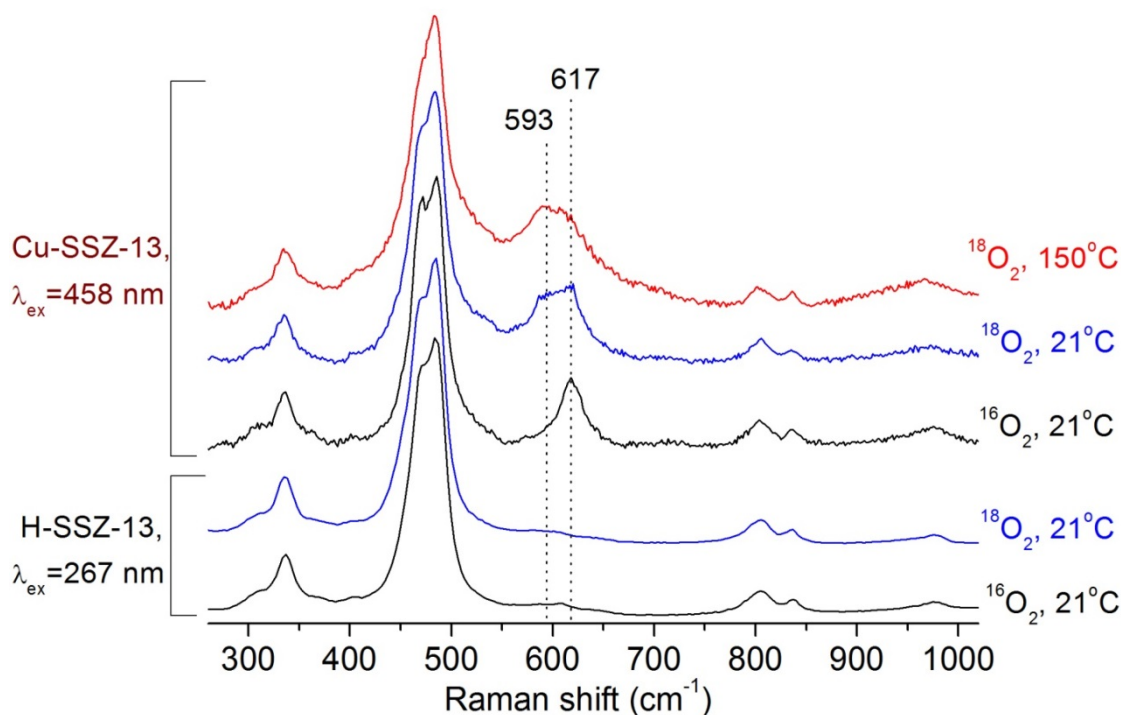


Figure 4.8: Comparison of *in situ* $^{18}\text{O}_2$ and $^{16}\text{O}_2$ activated Raman spectra of H-Cu-SSZ-13 (Si/Al = 12, Cu/Al = 0.4) and H-SSZ-13/12. $^{18}\text{O}_2$ activation was performed at 450 °C for 13 h before cooling the samples to 150 °C and 21 °C for spectra measurement (red and blue) and $^{16}\text{O}_2$ activation was performed at 450 °C for 2 h before cooling the samples to 21 °C (black)

4.3.5 Theoretical Calculations

In the literature several $\text{Cu}_x\text{O}_y\text{H}_z$ species including trans- μ -1,2-peroxo dicopper(II), bis(μ -oxo)dicopper(III), $[\text{CuOCu}]^{2+}$ and $[\text{CuOH}]^+$, have been suggested to form on Cu- exchanged zeolites.^{148,206,221} Their spectroscopic features are displayed in Table 4.4. However, it can be expected that these features and the relative stability vary with their local environment and therefore the zeolite support.

To elucidate the stability and spectroscopic features of $\text{Cu}_x\text{O}_y\text{H}_z$ species in SSZ-13 we modeled a series of different sites within the framework of the material in collaboration with Dr. Florian Goeltl. The different possibilities included the

stoichiometries displayed in Table 4.4, different positions within the framework as well as different anchoring points, consisting of activated O atoms (O atoms closest to framework Al), silanol defects and normal framework O atoms. We also included a $[\text{CuOH}]^+$ site in the eight-ring, which is the most common site at the encountered Si/Al ratios.

To compare the stabilities of the sites we calculated the chemical potential of the Cu atoms (μ^{Cu}) as:

$$\mu^{\text{Cu}}(T, P^{O_2} / P_0) = \frac{1}{x} \left(G^{\text{Cu}_x\text{O}_y\text{H}_z\text{Vzeo}} - G^{\text{zeo}+\text{H}_x} - \frac{z-x}{2} G^{\text{H}_2\text{O}} - \frac{y-z+x}{2} G^{O_2} \right) \quad (4.1)$$

where G denotes the temperature and pressure corrected Gibbs Free Energies of the species in the superscript. Using this approach for the characterization we find the $[\text{CuOH}]^+$ site to be the most stable under the characterization conditions (i.e. room temperature and vacuum). However, three other sites lead to a μ^{Cu} close enough to be present in the system. Starting with the most stable one, these three sites are a Cu_2O_2 site bridging an eight- and a six-ring, a Cu_2O site located in the eight ring, both anchored on Al atoms, and a Cu_2O_2 site located in the eight-ring, anchored on one silanol defect and on activated framework Os. The relative μ^{Cu} s and structures are displayed in Figure 4.9.

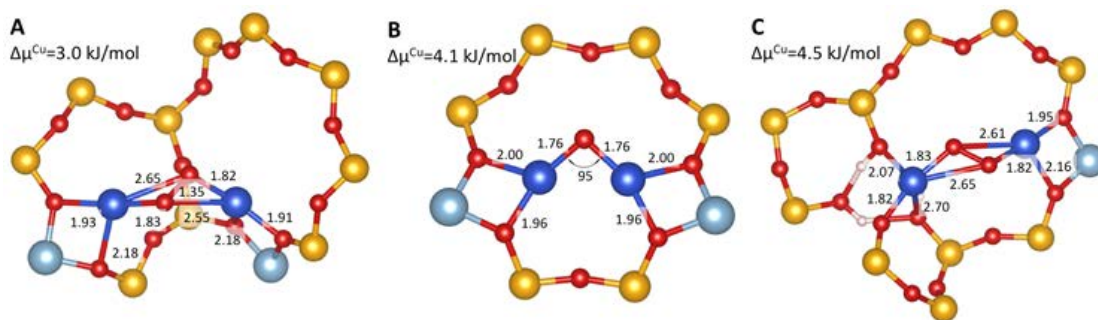


Figure 4.9: The three different structures with μ^{Cu} within 5 kJ mol^{-1} of a $[\text{CuOH}]^+$ site in the zeolite. Si atoms are displayed in yellow, O in red, Cu atoms in blue, Al atoms in silver and H atoms in white. The bond distances are given in units of Å.

Species designated as **A** is a trans- μ -1,2-peroxo dicopper(II) species with Cu–Cu distance of 3.98 \AA and Cu–O(extra-framework) distances of 1.82 and 1.83 \AA , which are close to $4.359(1) \text{ \AA}$ and $1.852(5) \text{ \AA}$ found for trans- μ -1,2-peroxo dicopper(II) species forming in biological systems.²²² Furthermore, the optimized Cu–O_{framework} distances of 1.91 \AA and 2.18 \AA are in very good agreement with Cu2–O2 and Cu2–O4 distances of $2.09(4) \text{ \AA}$ and $2.20(4) \text{ \AA}$ refined for Cu2 site near 8MR (Figure 4.2) on Cu-SSZ-13 (Si/Al = 12, Cu/Al = 0.4) using PXRD (Table 4.3). This agreement of Cu–O_{framework} distances motivates us to assign Cu2 site (Figure 4.2) to the Cu cation of trans- μ -1,2-peroxo dicopper(II) species that is coordinated to the 8MR. Based on this assignment, one can estimate a trans- μ -1,2-peroxo dicopper(II) species concentration of 23% on Cu-SSZ-13 (Si/Al = 12, Cu/Al = 0.4) (Table 4.3).

Site **B** is a mono-(μ -oxo)dicopper(II) species with a Cu–Cu distance of 2.60 \AA , Cu–O distance of 1.76 \AA and with a Cu–O–Cu angle of 95° . These values of Cu–Cu distance and Cu–O–Cu angle are typical for bis(μ -oxo)dicopper(III) species with Cu–Cu distances between 2.73 \AA and 2.88 \AA ²¹⁸ and Cu–O–Cu angle of 101° .²¹⁸ It is

not easy to differentiate mono-(μ -oxo)dicopper(II) species and bis(μ -oxo)dicopper(III) species using Raman or X-ray absorption spectroscopy¹²¹ due to their similar configuration. However, DFT calculations show that within the zeolite confinement, bis(μ -oxo)dicopper(III) species is not the most stable species as it is in homogenous phase.^{121,223,224} Vilella et al. have in fact suggested trans- μ -1,2-peroxo dicopper(II) species to be the most stable configuration for zeolites with 10 MR and 12 MR, such as MFI and MOR, having Al–Al distances around 8 Å, and suggested a cis- μ -1,2-peroxo dicopper(II) species to be the most stable for 8MR of CHA. However, for CHA, it is not reasonable to limit the calculations to 8MR since due to the high Si/Al ratio; it is more likely to have two Al atoms not on the same 8MR but one at 8MR and one at 6MR. In our calculations we considered all possible Al distributions, and as a result we have found the most stable species as given in Figure 4.9.

The last species is again a trans- μ -1,2-peroxo dicopper(II) species forming on one Al atom and one silanol defect with a Cu–Cu distance of 4.13 Å and Cu–O distances of 1.82 Å and 1.83 Å. The defect sites could result from dealumination of the zeolite upon calcination or activation, as observed from the octahedrally coordinated Al atoms using the ²⁷Al NMR (Figure C.3).

We also calculated vibrational spectra for these sites. Unfortunately, identifying Raman active vibrations in this case is not straightforward. Raman activity is determined by a change in polarizability of the system with respect to the given vibration, but doing so for a system containing as many vibrations as this one would be very time consuming. We, therefore, focus on identifying the stretching vibrations of the Cu-O bonds, which are known to be Raman active. We then assign the Raman

intensity of this vibration as the amplitude of the stretch. Furthermore we calculated optical absorption spectra for the three sites using TDHF and both spectroscopies are displayed in Figure 4.10.

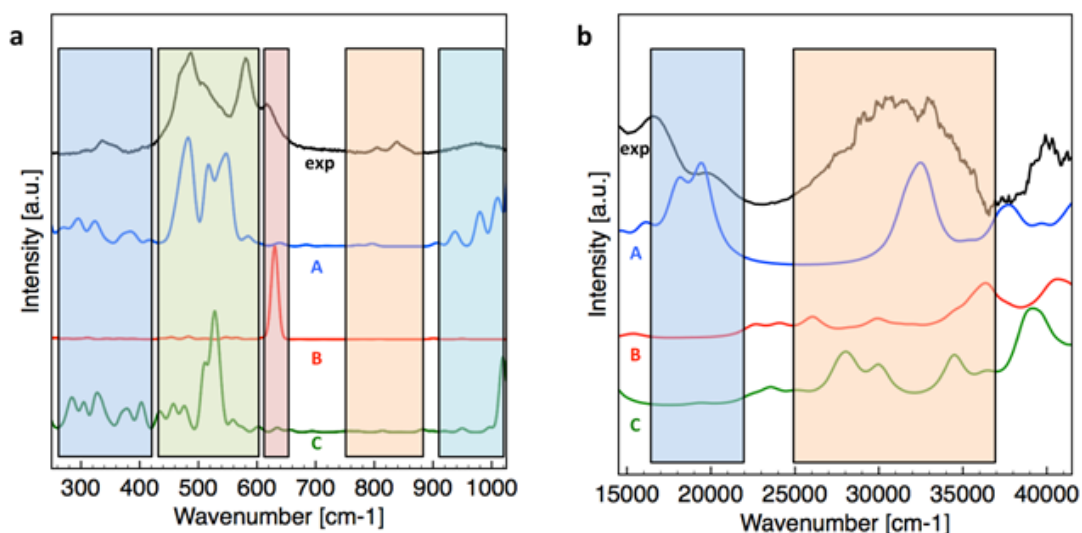


Figure 4.10: Comparison of experimental and calculated (a) Raman and (b) UV-vis spectra belonging to A, B, and C species (notations are given in Figure 4.9). The experimental Raman spectrum of Cu-SSZ-13 (Si/Al = 12, Cu/Al = 0.4) is given as black line on the left figure. On the right, the difference between the spectra of O₂ activated Cu-SSZ-13, Si/Al = 12, Cu/Al = 0.4 and Cu/Al = 0.02 is given in black and denoted as ‘exp’.

Based on the results from the stretching vibration predictions, we can say that all three species are present on Cu-SSZ-13 sample under the given conditions. According to the calculations, the experimentally observed vibrations at 476 cm⁻¹, 510 cm⁻¹ and 580 cm⁻¹ belong to two trans- μ -1,2-peroxo dicopper(II) species (**A** and **C** in Figure 4.9), whereas the vibration at 617 cm⁻¹ could be assigned to the mono-(μ -oxo)dicopper(II) species with a Cu–O–Cu angle of 95° (**B** in Figure 4.9).

The UV–vis absorption spectra predictions suggest the trans- μ -1,2-peroxo dicopper(II) species (**A**) have LMCT transition absorptions between 16,000 cm^{-1} and 20,000 cm^{-1} that is most probably overlapped by the $d \leftarrow d$ transitions of bare Cu(II) cations. The LCMT transitions of **A**, **B** and **C** species observed between 22,000 cm^{-1} and 35,000 cm^{-1} suggest involvement all three species in methane activation based on the broad absorption loss observed between 22,200 cm^{-1} and 35,000 cm^{-1} upon methane contact of Cu-SSZ-13 (Figure 4.6).

4.3.6 Effect of He Activation

He activation of Na-Cu-SSZ-13 (Si/Al = 12, Cu/Al = 0.4) and Na-Cu-SSZ-39 (Si/Al = 10, Cu/Al = 0.48) showed similar spectroscopic features when compared to O_2 activation, indicating formation of the same Cu_xO_y species by He treatment. The similarity of the spectroscopic features belonging to Cu-SSZ-13 and Cu-SSZ-39 samples is not surprising due to the structural similarity between the two frameworks, however the resemblance of the spectra of the samples treated with O_2 or He is surprising when compared to Cu-ZSM-5, on which mono-(μ -oxo)dicopper(II) species is shown to decompose when treated at 450–500 $^\circ\text{C}$ by He.^{69,117}

The UV–vis spectra of O_2 - and He -treated Na-Cu-SSZ-13 (Si/Al = 12, Cu/Al = 0.4) and Na-Cu-SSZ-39 (Si/Al = 10, Cu/Al = 0.48) (Figure 4.11) display three bands in the 13,000–20,000 cm^{-1} region indicating the presence of Cu(II) cations regardless of the treatment gas. He treatment of Cu-SSZ-13 is known to result in *auto-reduction* of the sample up to some extent.¹⁴⁸ The *auto-reduction* is reported to proceed by homolytic loss of OH ligands of Cu(II) cations that are coordinated near single $\text{AlO}_{4/2}^-$ units at temperatures higher than 300 $^\circ\text{C}$ in an inert atmosphere.^{148,156} The bare Cu(II) cations on the 6MR, on the other hand, cannot be readily *auto-reduced*. Theoretical

calculations performed by Paolucci et al. showed possible reduction of Cu(II) cation to Cu(I) cation together with formation of an additional Brønsted acid site at temperatures as high as 500 °C.¹⁵⁶ Therefore, at temperatures lower than 500 °C, it is expected to see the same concentration of Cu(II) cations on the 6MR.

It was noticed that the absorption band intensity in the 25,000–35,000 cm^{-1} region, which was related to the reactive species (Figure 4.6), was slightly more pronounced for O₂ treated than He treated samples.

He activated samples were investigated also using Raman spectroscopy and compared to the O₂ treated samples (Figure 4.12). Observed Raman bands following O₂ treatment of Na-Cu-SSZ-13 (Si/Al = 12) were very similar to H-Cu-SSZ-13 (Figure 4.7) confirming the negligible effect of Na content on Na-Cu-SSZ-13. Bands at 511 cm^{-1} , 574 cm^{-1} and 616 cm^{-1} were observed following both O₂ and He treatment for Na-Cu-SSZ-13 where intensities of bands at 511 cm^{-1} and 574 cm^{-1} were lower after He treatment (Figure 4.12).

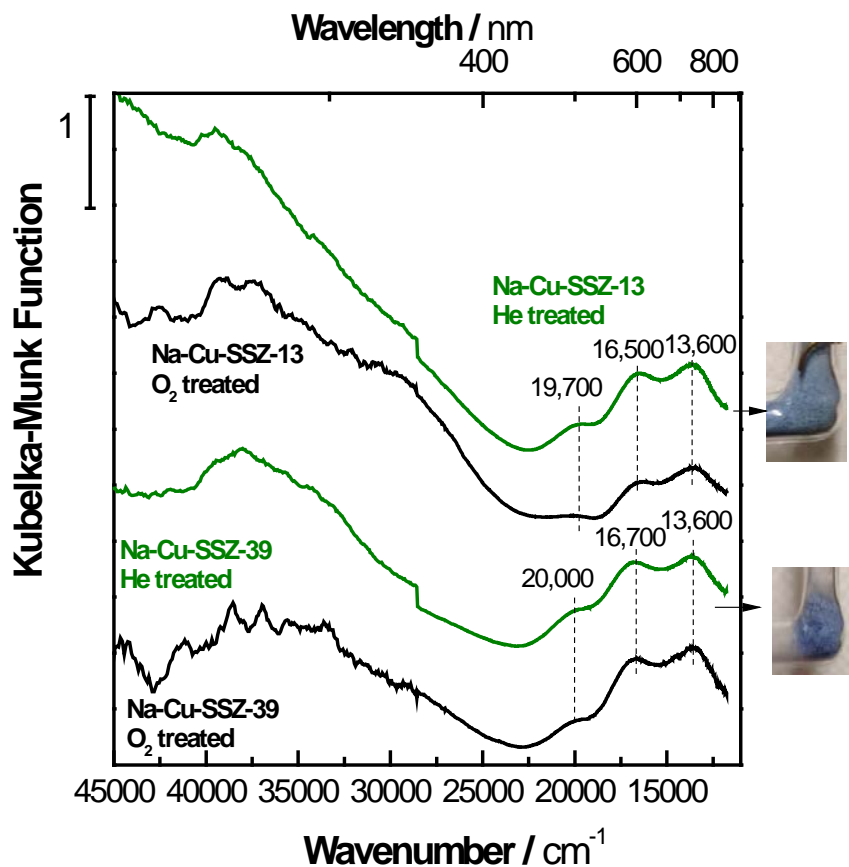


Figure 4.11: DR UV-vis spectra of Na-Cu-SSZ-13 (Si/Al = 12, Cu/Al = 0.47) and Na-Cu-SSZ-39 (Si/Al = 10, Cu/Al = 0.48) samples after O₂ and He treatment at 450 °C.

Na-Cu-SSZ-39 also shows three major bands at 511 cm⁻¹, 573 cm⁻¹ and 607 cm⁻¹, where the first two are also less intense after He treatment (Figure 4.12). Considering the assignment of these bands to trans-μ-1,2-peroxo dicopper(II) species, one could infer that both He and O₂ treatment result in formation of trans-μ-1,2-peroxo dicopper(II) species and mono-(μ-oxo)dicopper(II) species, but O₂ treatment results in a higher concentration of trans-μ-1,2-peroxo dicopper(II) species.

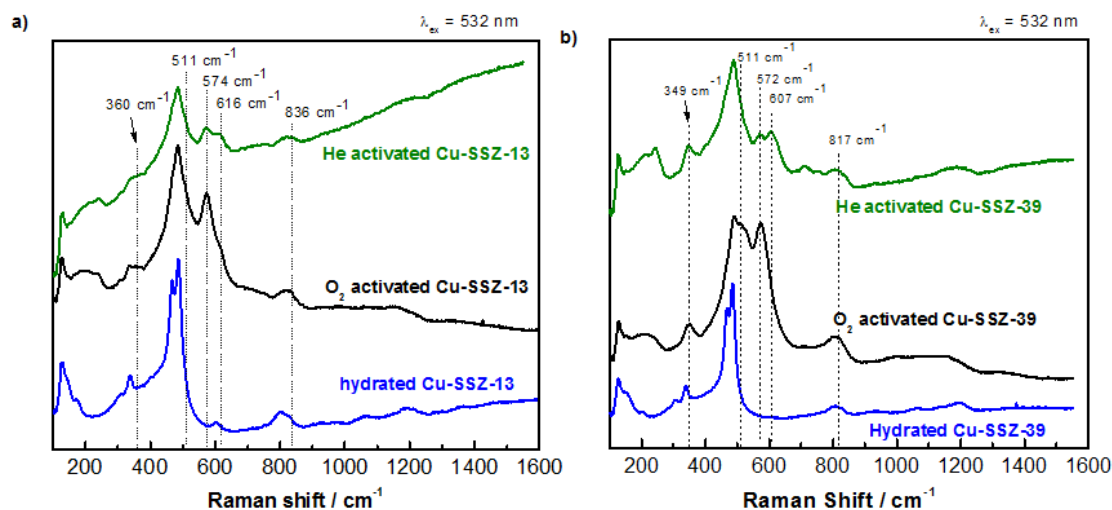


Figure 4.12: a) Raman spectra ($\lambda_{ex} = 532 \text{ nm}$) of hydrated (blue), O₂ treated at 450 °C (black) and He treated at 450 °C (green) Na-Cu-SSZ-13 (Si/Al = 12, Cu/Al = 0.47). b) Raman spectra ($\lambda_{ex} = 532 \text{ nm}$) of hydrated (blue), O₂ treated at 450 °C (black) and He treated at 450 °C (green) Na-Cu-SSZ-39 (Si/Al = 10, Cu/Al = 0.48)

When methanol production amounts were tested following He activation at 450 °C, Na-Cu-SSZ-13 and Na-Cu-SSZ-39 samples produced methanol in significant but lower quantities when compared to the O₂ pre-treatment (Table 4.5). The differences in methanol production amounts for O₂ and He treatment were 0.032 CH₃OH/Cu for Na-Cu-SSZ-13 and 0.009 CH₃OH/Cu for Na-Cu-SSZ-39.

Table 4.5: Amount of methanol produced by Na-Cu-SSZ-13 (Si/Al = 12, Cu/Al = 0.47) and Na-Cu-SSZ-39 (Si/Al = 10, Cu/Al = 0.48) using O₂ or He treatments (Experimental details are given in section 4.2.7)

Sample	O ₂ pre-treatment at 450 °C		He pre-treatment at 450 °C	
	Methanol (μmol g ⁻¹)	Methanol/Cu	Methanol (μmol g ⁻¹)	Methanol/Cu
Na-Cu-SSZ-13	28.1	0.050	10	0.018
Na-Cu-SSZ-39	22.7	0.035	18.5	0.026

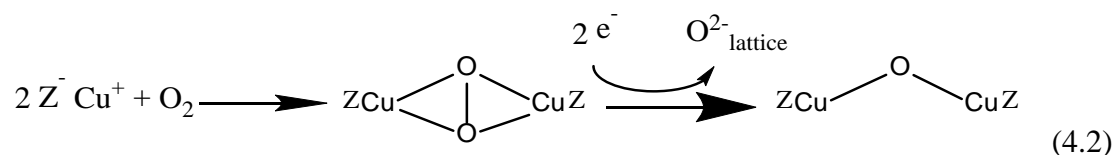
4.3.7 Precursor for Cu₂O₂ and Cu₂O species on Cu-SSZ-13

The precursor of the active site is investigated here using UV-vis spectroscopy where Cu(I)-SSZ-13 (Si/Al = 12, Cu/Al = 0.4) is exposed to O₂ at 25 °C. A similar procedure was applied to Cu-ZSM-5 to identify the precursor to methanol forming mono-(μ-oxo)dicopper(II) species.¹¹² While Cu-ZSM-5 is known to *auto-reduce* to Cu(I)-ZSM-5 easily,^{33,225} Cu-SSZ-13 partially reduces to Cu(I) depending on the ‘reducing’ conditions such as in vacuum^{155,203} or He flow.^{142,148} Therefore, dehydrated samples are first treated in a 5% CO/He mixture at 350 °C for 1 h to reduce to Cu(I)-SSZ-13 (see experimental section for details). After desorbing the chemisorbed and physisorbed CO again at 350 °C in He flow, the temperature was decreased to 25 °C for measurement of a reference spectrum. The color of the sample following the CO treatment is white, indicating Cu(I) state, even though some *d*←*d* transitions were still observed (red, Figure 4.13). The flow was then switched to 20% O₂/He at 25 °C and another spectrum was measured (blue, Figure 4.13). Figure 4.13 shows a rapid change in the UV-vis spectral features before and after O₂ admission for Cu-SSZ-13. A broad band was immediately observed after O₂ admission with a maximum intensity at 27,800 cm⁻¹. The band at 27,800 cm⁻¹ could be interpreted as a peroxo to Cu(II) charge transfer band for μ-(η²:η²) peroxo dicopper(II) species (see Table 4.4);^{219,226} however

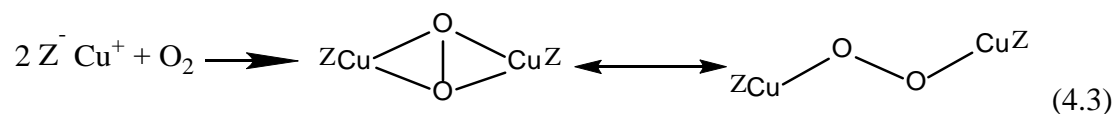
additional spectroscopic information is required to confirm the identification of this species.

When H-Cu-SSZ-13 was further heated to 450 °C by continuing O₂ flow, the spectrum resembled to the spectra obtained after O₂ treatment of the hydrated sample at 450 °C (Figure C.6) indicating transformation of a possible μ-(η²:η²) peroxo dicopper(II) species into trans-μ-1,2-peroxo dicopper(II) species and mono-(μ-oxo)dicopper(II) species upon heat treatment at 450 °C.

Transformation of μ-(η²:η²) peroxo dicopper(II) species into mono-(μ-oxo)dicopper(II) species has been reported to occur by 2e⁻ transfer from the spectator Cu(I) cations on Cu-ZSM-5 (Eq 4.2).¹¹²



The transformation of μ-(η²:η²) peroxo dicopper(II) species into trans-μ-1,2-peroxo dicopper(II) species (Eq. 4.3) is thermodynamically possible at elevated temperatures. CuO₂Cu species formation on zeolites has been investigated using density functional theory by Goodman et al., also on copper exchanged zeolites,²²⁷ and an energy difference of 12 kcal mol⁻¹ has been found between μ-(η²:η²) peroxo dicopper(II) and trans-μ-1,2-peroxo dicopper(II) species, μ-(η²:η²) peroxo dicopper(II) species being more stable. This transformation would also require some mobility of the Cu(II) ions, which is possible at temperatures as high as 450 °C.



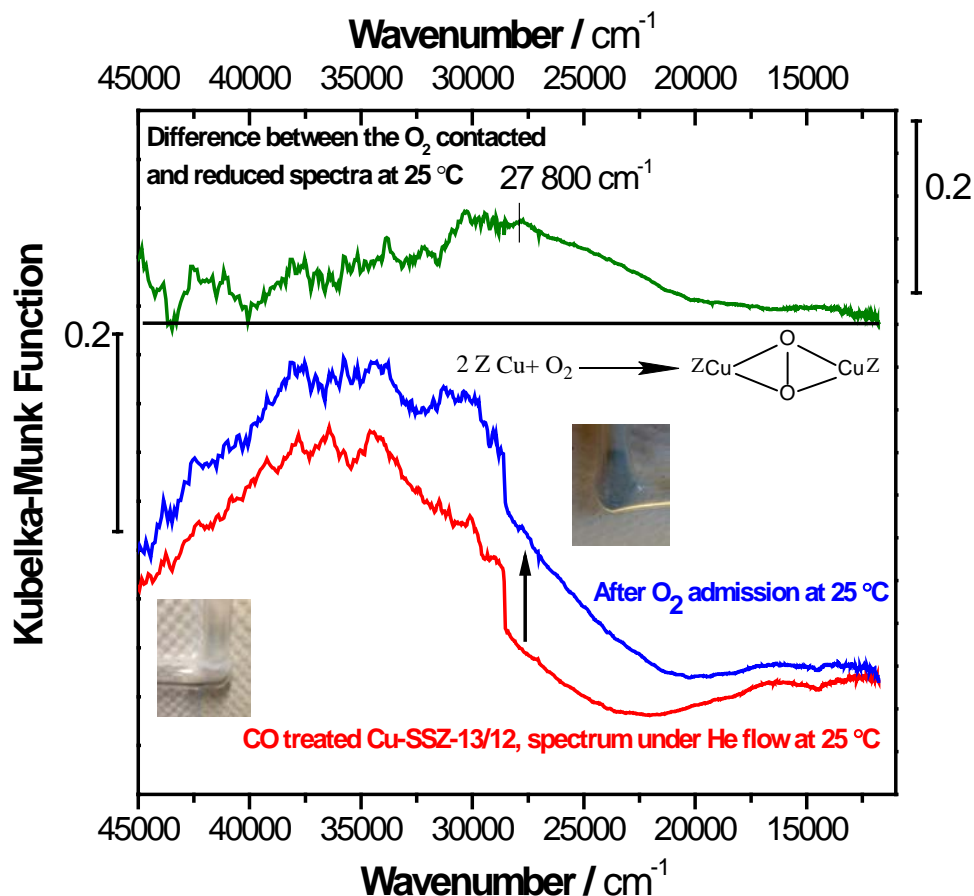


Figure 4.13: DR UV-vis spectra before (red spectrum) and after (blue spectrum) O_2 admission for Cu(I)-SSZ-13 (Si/Al = 12, Cu/Al = 0.4). Green line is the difference of the blue and red spectra showing the additional absorption features formed after O_2 exposure at 25 °C. The feature observed at $28,500\text{ cm}^{-1}$ was caused by a lamp switch in the spectrometer

4.3.8 Dehydration Mechanisms and O_2 Free Route to Cu_2O_2 and Cu_2O species

The final state of Cu cations on SSZ-13 is determined not only by Al and Cu content of the zeolite as also mentioned in this chapter, but also by treatment conditions such gas atmosphere, temperatures, treatment time and even zeolite synthesis methods.^{142,148,203,204} Therefore, it is essential to keep in mind the differences

in Si/Al ratios Cu/Al ratios, and treatment conditions while discussing nature of Cu cations on Cu-SSZ-13. There are, however, some commonly accepted mechanisms for dehydration and oxidation of Cu-SSZ-13. The dehydration mechanism includes Cu cations that are coordinated near single or two $(\text{AlO}_{4/2})^-$ units. Most recently, the dehydration mechanism for Cu-SSZ-13 (Si/Al = 13) has been suggested to follow water dissociation during dehydration for some of the Cu(II) cations coordinated near two $(\text{AlO}_{4/2})^-$ units $[\text{Cu}(\text{II})(\text{H}_2\text{O})_n]^{2+}$ resulting in one Brønsted acid site and one $[\text{CuOH}]^+$ site. Further heating is reported to lead to bare Cu(II) cations near 6 MR,¹⁴⁸ which explains the higher concentration of EPR-active bare Cu(II) cations at 400 °C when compared to 250 °C.¹⁴² Another explanation is made by Paolucci et al. for dehydration of $[\text{Cu}(\text{II})(\text{H}_2\text{O})_n]^{2+}$ species near two $(\text{AlO}_{4/2})^-$ units (that are mostly at 6MR) using theoretical calculations.¹⁵⁶ They have proposed single water ligand attached to Cu(II) at 6MR at temperatures between 200 °C and 350 °C, and at temperatures higher than 350 °C, the final water ligand is lost to have bare Cu(II) at the 6MR (Figure 4.14).

The remaining Cu(II) cations, balanced with single $(\text{AlO}_{4/2})^-$ unit upon ion exchange, $[\text{Cu}(\text{II})(\text{H}_2\text{O})_n(\text{OH})]^+$, preserve the $[\text{CuOH}]^+$ form by removal of water ligands. O_2 treatments at temperatures higher than 250 °C^{148,204} have been suggested to preserve some $[\text{CuOH}]^+$ species,¹⁴⁸ whereas He treatment or vacuum treatment has been suggested to result in Cu(I) cations by loss of (OH) ligands by homolytic dissociation of the OH group.^{148,155} The findings from Borfecchia et al.¹⁴⁸ and Paolucci et al.¹⁵⁶ have been summarized in Figure 4.14, which shows the complexity of the dehydration on Cu-SSZ-13.

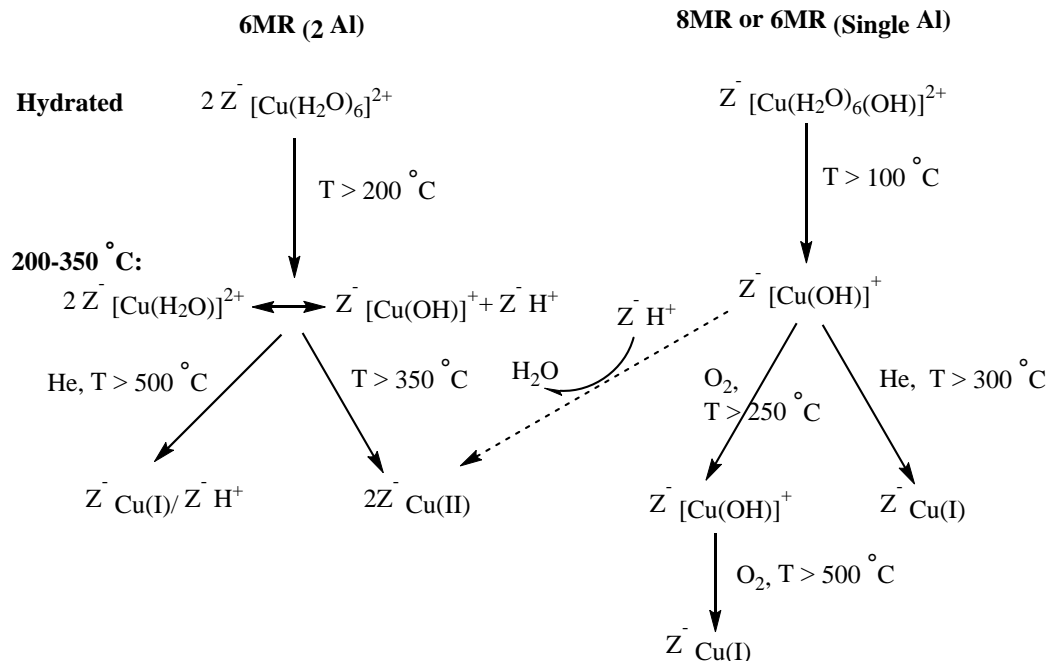


Figure 4.14: Chemical scheme of dehydration on Cu-SSZ-13 as summarized from Borfecchia et al.¹⁴⁸ and Paolucci et al.¹⁵⁶ The dashed arrow shows the suggested Cu(II) migration mechanism from 8MR to 6MR as observed by PXRD here.

Based on our Rietveld refinement on hydrated Cu-SSZ-13 (Si/Al = 12, Cu/Al = 0.4) sample, we have shown that there are both $[Cu(II)(H_2O)_6]^{2+}$ and $[Cu(II)(H_2O)_6(OH)]^+$ species present on 6MR and 8MR respectively (18% and 82% distribution, Table 4.3), in excellent agreement with theoretical calculations provided by Paolucci et al.¹⁵⁶ And by thermal treatment at 450 °C in O₂, 5% increase of 6MR site occupation is observed here, indicating migration of Cu(II) from 8MR to 6MR most probably by reaction of OH group from $[Cu(II)(OH)]^+$ with a close by Brønsted acid site during dehydration.

While the theory given in Figure 4.14 is consistent with most experimental findings, there are some important details that require further explanation. For

instance, the destination of lost OH ligands that play an important role in dehydration is unknown. In addition, there are non-intuitive findings such as O₂ treatment of Cu-SSZ-13 samples has been reported to result in Cu(I) cations both on Si/Al = 6²⁰⁴ and 13²⁰³ at 400 °C (by XAS). This is explained by Paolucci et al. using theory by showing thermodynamic favorability of Cu(I) sites forming by (OH) loss under O₂ atmosphere at temperatures higher than 500 °C.¹⁵⁶

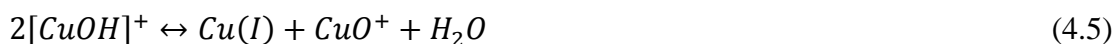
In this chapter we showed evidence for Cu₂O₂ and Cu₂O species formation following O₂ or He treatment at 450 °C. Cu_xO_y moieties on SSZ-13 has been discussed by several groups^{142,206,209,210} for high copper concentrations. However, besides the EPR results indicating Cu_xO_y species,^{142,210} there have not been enough experimental evidence for such species in literature. We show that Cu₂O coordinates to 8MR with two Al and Cu₂O₂ balanced by two (AlO_{4/2})⁻ units; one Cu located on a 6MR and second at an adjacent 8MR with Al–Al distance of 7.43 Å. This optimized distance is in very good agreement with the theoretical 8 Å Al–Al distance Vilella et al. reported for the most stable Cu₂O₂ structures on 10 MR and 12 MR.²²¹ For this optimized Cu₂O₂ structure on SSZ-13, two Al atoms are found on different d6MRs, and not on the same 8MR, which makes this structure more likely on SSZ-13 samples with high Si/Al ratios.

The mechanism for Cu₂O₂ and Cu₂O formation by O₂ treatment of the hydrated Cu-SSZ-13 is yet to be determined. But partial *auto-reduction* of Cu(II)-SSZ-13 to Cu(I)-SSZ-13 in O₂ environment, as observed by Giordanino et al.²⁰³ and Kwak et al.²⁰⁴, leads us to consider a route involving the small fraction of Cu(I)-SSZ-13, from [CuOH]⁺ sites as observed in Figure 4.14 for higher temperatures, and O₂

resulting in trans- μ -1,2-peroxo dicopper(II) and mono-(μ -oxo)dicopper(II) species (see Eq. 4.2 and 4.3).

The most revealing results are found from He activation of Cu-SSZ-13 and Cu-SSZ-39. He treatment at 450 °C results in spectral features that are in agreement with Cu_2O_2 and Cu_2O formation, similar to O_2 treatment. Interestingly, formation of Cu_xO_y on Cu-SSZ-13 (Si/Al = 14) after He treatment has also been suggested based on increased EPR signal intensity of Cu-SSZ-13 by hydration of He treated sample.¹⁴² The absence of O_2 in these He treatments¹ (yet resulting in Cu_2O_2 and Cu_2O species), indicates a source of extra-framework oxygen atoms that has to be either H_2O molecules or OH^- ligands (Figure 4.14).¹⁴⁸

A possible route for Cu_2O formation can be considered to be condensation of $[\text{CuOH}]^+$ species into $[\text{Cu}-\text{O}-\text{Cu}]^{2+}$ species, proposed as an intermediate for *auto-reduction* to Cu(I) (Eq. 4.4).²²⁵ Another route for Cu_2O_2 formation could be based on $[\text{CuO}]^+$ formation by hydroxyl radical loss from $[\text{CuOH}]^+$ species (Eq. 4.5). These type of dehydration mechanisms (Eq. 4.4 and 4.5) have been suggested for Cu(II)-exchanged ZSM-5 with low Al concentrations or over-exchanged Cu-zeolites, which have $[\text{Cu(II)(H}_2\text{O)}_n(\text{OH})]^+$ type of cations after ion exchange.²²⁸



¹ In order to account for the plausible O_2 contaminant in 99.999 % purity He gas, we repeated He treatment of Cu-SSZ-13 (Si/Al = 12, Cu/Al = 0.4) sample by addition of a O_2 purifier (ZPure Glass Oxygen Purifier, Chromatography Research Supplies) in the He line, and obtained UV-vis spectra of the sample which showed the features at $30,000 \text{ cm}^{-1}$ that are related to the Cu_2O_2 sites (Figure C.7).

The putative CuO^+ intermediate has been theoretically shown to carry methane oxidation to methanol reaction in an energetically downhill pathway,²²⁹ however a stable CuO^+ species has never been experimentally detected on zeolites. One theoretical investigation of CuO^+ species on Cu-ZSM-5 showed energetically favored self-organization of two CuO^+ species in close proximity into $\text{Cu}_2\text{O}_2^{2+}$ species (Eq.4.6, $\text{Cu}_2\text{O}_2^{2+}$ species 165 to 188 kJ mol^{-1} more stable) with the distance between two framework Al atoms up to 8.72 Å,²³⁰ which is in really good agreement with what we have found for optimized trans- μ -1,2-peroxo dicopper(II) species (site A, Figure 4.9).

For the formation of trans- μ -1,2-peroxo dicopper(II) species, one can start with two $[\text{CuOH}]^+$ sites on different 8MRs, which can either *auto-reduce* to two Cu(I) sites and form Cu_2O_2 sites (Eq. 4.3), or form Cu_2O_2 from four different $[\text{CuOH}]^+$ sites following Eq. 4.5 and 4.6. Similarly, for the formation of mono-(μ -oxo)dicopper(II) species, one either needs two Cu(I) sites obtained by *auto-reduction* of $[\text{CuOH}]^+$ sites at 8MR (by O_2 treatment at 450 °C, Figure 4.14) and form Cu_2O following Eq. 4.2. Or more simply Cu_2O forms from condensation of two close by $[\text{CuOH}]^+$ sites (Eq. 4.4) in either presence or absence of O_2 .

All suggested routes are based on $[\text{CuOH}]^+$ sites, which are experimentally shown to exist on Cu-SSZ-13 at mild temperatures (250 °C)¹⁴⁸ either as exchanged at 8MR, or by water ligand dissociation at 6MR (Figure 4.14). We propose that instead of having only $[\text{CuOH}]^+$ sites after heat treatment at 450 °C, Cu_2O_2 and Cu_2O species form by loss of OH ligands depending on the locations of $[\text{CuOH}]^+$ sites and mobility of Cu species at elevated temperature (450 °C).

4.3.9 Reactivity of Cu_2O_2 species

Nature's metalloenzymes containing iron or copper show remarkable methane oxidation selectivity and activity at ambient conditions.^{79,231} Elucidating the copper active site for the particulate MMO (pMMO) is crucial to understanding the oxidation mechanism, however the copper-oxo species has not been structurally determined yet because of the difficulty of isolating the active site. The iron active sites in soluble MMO (sMMO), in contrast, has been identified to be a bis(μ -oxo) diiron center.^{80-82,104} In analogy to the sMMO, the site for pMMO has been suggested to be a bis(μ -oxo) dicopper center⁹⁸⁻¹⁰⁰ (based on XAS indicating a Cu-Cu distance of 2.5–2.7 Å⁹⁷). Furthermore, DFT studies suggest a transformation of a plausible μ -(η^1 : η^2) peroxo Cu(I)Cu(II) or μ -(η^2 : η^2) peroxo dicopper(II) species into bis(μ -oxo) Cu(II)Cu(III) species for the active dicopper site.⁹⁸ Most recently, (μ -oxo)(μ -hydroxo) Cu(II) Cu(III) species has been theoretically shown to be more reactive when compared to bis(μ -oxo) Cu(II)Cu(III) species.¹⁰²

On copper exchanged zeolites, we observe the analogues of these active sites as trans- μ -1,2-peroxo dicopper(II) species and mono-(μ -oxo)dicopper(II) species. The UV-vis band intensity losses at 22,200 cm^{-1} , 29,500 cm^{-1} and 35,000 cm^{-1} upon CH_4 treatment of O_2 activated Cu-SSZ-13 (Figure 4.6) and the theory shows that both trans- μ -1,2-peroxo dicopper(II) species and mono-(μ -oxo)dicopper(II) species have potential for activating methane at 200 °C.

Mono-(μ -oxo)dicopper(II) species was shown to activate methane by its induced $\text{Cu}^{\text{I}}\text{-O}^{\cdot-}\text{-Cu}^{\text{II}}$ transition state which abstracts H^+ from methane to result in $[\text{Cu}(\text{OH})\text{-Cu}]^{2+}$ formation.¹¹⁷ Trans- μ -1,2-peroxo dicopper(II) species can also be considered to be electrophilic based on the O_2^{2-} , but in literature, interconversion between trans- μ -1,2-peroxo dicopper(II) and bis(μ -oxo)dicopper(III) species has been

suggested to be effective in activating methane by the electrophilic nature of the bis(μ -oxo)dicopper(III) species together with nucleophilicity of trans- μ -1,2-peroxo dicopper(II) species.²³² Similarly, an equilibrium between trans- μ -1,2-peroxo dicopper(II) species and bis(μ -oxo)dicopper(III) species within the small-pore zeolites at elevated temperatures could explain methane activation at 200 °C.

4.4 Conclusion

Formation of trans- μ -1,2-peroxo dicopper(II) species and mono-(μ -oxo)dicopper(II) species are shown on Cu-SSZ-13 (Si/Al = 12, Cu/Al = 0.4) and Cu-SSZ-39 (Si/Al = 10, Cu/Al = 0.48) using PXRD, UV-vis and Raman spectroscopy following O₂ or He treatment at 450 °C. The thermodynamically optimized Cu₂O and Cu₂O₂ structures have at least one Cu cation on the 8MR of Cu-SSZ-13; this emphasizes the importance of the Cu cation distribution and Si/Al ratio for Cu_xO_y formation for zeolites having 6MRs. The findings from PXRD experiments indicate higher concentration of bare Cu(II) sites on 6MR of Cu-SSZ-13 Si/Al = 5, which has higher Al content when compared to Si/Al = 12. These bare Cu(II) sites that are balanced by two (AlO_{4/2})⁻ units are considered to be inactive for methanol formation. Higher concentration of Cu cations on the 8MR on Si/Al = 12 sample, on the other hand, is believed to result in higher concentration of active species that result in methanol per copper ratios that is more than double when compared to that of Si/Al = 5 sample (see Chapter 3).

The suggested Cu₂O₂ and Cu₂O formation mechanisms starting from hydrated forms of zeolites involve [CuOH]⁺ sites that are balanced by single (AlO_{4/2})⁻ units, which are observed with higher Si/Al ratios. Even though higher Si/Al ratios are expected to result in a higher Cu(II) occupation near single (AlO_{4/2})⁻ sites, one should

consider the probability of having another single $(\text{AlO}_{4/2})^-$ site in proximity of the 8MR (the optimum Al–Al distance for trans- μ -1,2-peroxo dicopper(II) species is given to be 8 Å by Vilella et al.).²²¹ For one single $(\text{AlO}_{4/2})^-$ site present on a 6MR, there are nine 6MR that have tetrahedral sites shared with three 8 MRs adjacent to the first 6MR. Hence statistically, the lowest Al concentration for a dicopper species to form should account for two Al atoms on total of 10 6MRs, which makes the highest possible Si/Al ratio as 29. One should also keep in mind that, the Cu concentration per gram of zeolite would decrease with higher Si/Al ratios, which would result in lower methanol formation yields per gram of zeolite. Very similar methanol formation amounts found by Si/Al = 5 and Si/Al = 12 (Table 3.3) confirms this argument, indicating the Si/Al ratio of 12 could be the optimum for highest methanol production per gram of zeolite.

The trans- μ -1,2-peroxo dicopper(II) and mono- $(\mu$ -oxo)dicopper(II) species on Cu-SSZ-13 showed spectroscopic features including LMCT transitions in the 22,200 cm^{-1} and 35,000 cm^{-1} region and Cu–O vibrations at 360, 510, 580, 617 and 837 cm^{-1} . The Cu–O vibration at 617 cm^{-1} ($\Delta^{18}\text{O} = 24 \text{ cm}^{-1}$) is assigned to stretching vibration of an thermodynamically favored mono- $(\mu$ -oxo)dicopper(II) species with an Cu–O–Cu angle of 95°, which resembles the diamond structure of a bis(μ -oxo)dicopper(III) species. Both the trans- μ -1,2-peroxo dicopper(II) and mono- $(\mu$ -oxo)dicopper(II) species are suggested to take part in methane activation at 200 °C.

Chapter 5

CATALYTIC METHANOL FORMATION ON Cu-SSZ-13

5.1 Introduction

A cost effective, small-scale process for natural gas conversion to liquid fuels is needed for upgrading natural gas at remote locations since existing methane-to-liquid fuels technology is economical only at large-scales. One-step partial oxidation of methane to methanol meets these requirements, but obtaining high selectivity to the desired products, methanol and formaldehyde, is very challenging. Oxidation reactions involving C–H bond homolysis from methane via heterogeneous catalysis (at high temperature, $T > 500\text{ }^{\circ}\text{C}$) result either in low selectivity or low conversions²³³ due to facile activation of the C–H bonds of the products, leading to fast over oxidation to CO and CO₂.^{77,78}

Methanol selectivity higher than 95% can be achieved on Cu- or Fe-exchanged zeolites using a 3-step cyclic process that has been investigated in Chapter 3 and Chapter 4 of this thesis. The reason for the frequent application of this 3-step process is the required temperature difference between high temperature ($450\text{ }^{\circ}\text{C}$) O₂ activation to create active Cu_xO_y sites in high concentration, and low temperature ($200\text{ }^{\circ}\text{C}$) for the methane reaction in order to prevent CO₂ formation.^{70,113} *Isothermal* step-wise methanol formation at $150\text{ }^{\circ}\text{C}$ and $200\text{ }^{\circ}\text{C}$ has been reported using NO¹¹³ or O₂¹¹⁹ as the oxidant, but the reported methanol production amounts — $0.63\text{ }\mu\text{mol CH}_3\text{OH g}_{\text{zeolite}}^{-1}$ (on Cu-ZSM-5, Si/Al = 12, Cu/Al = 0.31, following 0.5 bar CH₄ activation for 1 h)¹¹³ and $5.4\text{ }\mu\text{mol CH}_3\text{OH g}_{\text{zeolite}}^{-1}$ (on Cu-mordenite, Si/Al = 6, Cu/Al = 0.35,

following 1 bar CH₄ activation for 30 min)¹¹⁹— were much lower than the methanol formation amounts obtained by O₂ activation performed at 450 °C —8.1 μmol CH₃OH g_{zeolite}⁻¹ on Cu-ZSM-5⁵ and 45.3 μmol CH₃OH g_{zeolite}⁻¹ on Cu-mordenite.¹¹⁹ High CH₄ pressure increases methanol production amounts on Cu-mordenite, resulting in methanol production as high as 103.3 μmol CH₃OH g_{zeolite}⁻¹ at 36 bar CH₄ pressure.¹¹⁹ Higher methanol production amounts, reaching 7 mmol CH₃OH g_{zeolite}⁻¹, were reported by Hammond et al. in aqueous batch media using H₂O₂, (in 30 bar of CH₄) on Cu/Fe-ZSM-5 with methanol selectivity of 85%.²³¹

At ambient pressures, catalytic methanol production with Fe-ZSM-5 was obtained by co-feeding nitrous oxide, methane and steam at 275 °C, reaching a methanol selectivity of 62%.¹¹⁶ The main disadvantage of using Fe-zeolites is that Fe-ZSM-5 needs to be activated at 900 °C in He (to create active divalent Fe cations)¹¹⁵ before the start of the catalytic process.

We have investigated the methane partial oxidation reaction using N₂O on Cu-SSZ-13 (CHA framework type), and report catalytic methanol production on Cu exchanged zeolites at ambient pressures by co-feeding methane, nitrous oxide and steam in gas phase at temperatures between 250 °C and 300 °C. This is achieved without the need for high-temperature pre-treatments of the sample. We have investigated the effect of methane and N₂O and steam partial pressures on methanol selectivity as well as comparing O₂ and N₂O as oxidants.

5.2 Experimental

5.2.1 Zeolite Synthesis and Ion Exchange

Cu-SSZ-13 (Si/Al = 12, Cu/Al = 0.4) was synthesized and ion exchanged as described in Chapter 4.

Na-Mordenite (Si/Al = 5) was purchased from Tricat (TZM 1011). 5 g of Na-Mordenite was ion exchanged in 500 ml of 0.2 M NH_4NO_3 (Sigma-Aldrich, >99%) / de-ionized water solution at 80 °C for 3 h with rigorous stirring. This ion exchange process was repeated three times to ensure complete ion exchange to NH_4^- form. After each exchange, the zeolite was vacuum filtered, washed with de-ionized water (200 ml for 1 g) and dried at 80 °C for 3 h.

NH_4^- -ZSM-5 (Si/Al = 11.5) was purchased from Zeolyst (CBV 2314). NH_4^- form of ZSM-5 and Mordenite were dehydrated at 120 °C (with 5 °C min^{-1} heating rate) for 2 h and the ammonium groups were decomposed at 560 °C (with 5 °C min^{-1} heating rate) for 8 h with 80 $\text{cm}^3 \text{min}^{-1}$ air flow to obtain H^+ -form of the zeolites before performing Cu(II) exchange.

Copper (II) ion-exchange was performed by exchanging H-form of the zeolites in an aqueous copper (II) acetate (Aldrich, 98% purity) solution at 25 °C for 12 h. Volume of the solution was kept at 500 ml and the amount of copper (II) acetate varied depending of the mass of the zeolite and targeted Cu/Al ratio. Cu-ZSM-5 was exchanged only once with starting Cu(II)/Al of 1 in the solution. Cu-Mordenite was exchanged twice with starting Cu(II) solutions containing Cu/Al of 1. After stirring the zeolites in Cu(II) acetate solutions for 12 h, the zeolites were separated by vacuum filtration and a sample from the filtrate was kept for Cu quantification using UV-vis spectroscopy. The amount of Cu(II) left after ion-exchange was calculated using UV-

vis absorbance intensities of the filtrate solutions. The extent of Cu(II) exchange of the zeolite (Cu/Al) is then calculated using disappeared Cu(II) concentration from the solution.

5.2.2 Methane Conversion Experiments

5.2.2.1 Equipment

The hydrated samples (0.300 ± 0.005 g and particle size between 40–60 mesh) were tested for methanol formation using a reactor system described in Chapter 3. Methanol was analyzed using a gas chromatograph (GC) (Agilent 7890A) with a flame ionization detector and a HP-PLOT Q column (Agilent19091P-Q04, 30 m x 0.32 mm x 0.02 mm). For the cyclic process experiments, a different GC (Agilent 6890) with Supel-Q PLOT column (Supelco, 30 m x 0.32 mm) was used for methanol quantification. CO and CO₂ were analyzed using a thermal conductivity detector of Agilent 7890A with a HayeSep Q column (Agilent G3591-81121, 12 ft 1/8" 2 mm). The temperature of the oven was set to 140 °C (inlet port was set to 200 °C and detector temperatures were set to 250 °C) and valve injections of 1 ml volume were taken every 10 min with a split ratio of 15:1. The effluent stream was also monitored on-line with a mass spectrometer (Pfeiffer OmniStar GSD 320). Quantification of produced CO for reactions involving O₂ was performed using the calibration of $m/z = 28$ signal for CO since CO and O₂ peaks overlapped in TCD chromatograms (See Appendix D.1 for CH₃OH, CO and CO₂ calibrations).

5.2.2.2 3-Step Cyclic Procedure

Hydrated Cu-SSZ-13 was first activated in $50 \text{ cm}^3 \text{ min}^{-1}$ O₂ (Keen Gas, 99.997% purity) flow or $5 \text{ cm}^3 \text{ min}^{-1}$ N₂O (Keen Gas, medical purity) and $50 \text{ cm}^3 \text{ min}^{-1}$

¹ He flow at a temperature of 200, 300 or 450 °C for 2 h with a heating rate of 5 °C min⁻¹. After cooling the sample to 200 °C (cooling rate of 5 °C min⁻¹) with continuing O₂ or N₂O/He flow, the gas was switched to 35 cm³ min⁻¹ CH₄ (Matheson, 99.99%) flow and the temperature was maintained at 200 °C for 1 h. After 1 h, the gas was switched to 50 cm³ min⁻¹ He flow, which was diverted through a water-containing saturator kept at 25 °C (water vapor pressure of 3.2 kPa), while keeping the temperature of the sample at 200 °C. Extracted methanol was then analyzed with a GC as explained above.

5.2.2.3 Catalysis Experiments

Hydrated Cu- zeolites were saturated at 20 °C by 120 cm³ min⁻¹ CH₄/N₂O/He/H₂O flow with a specific composition for 15 min. The feed mixture containing CH₄/N₂O/He is diverted through a water-containing saturator kept at 25 °C unless stated otherwise. Temperature of the samples was increased to the desired reaction temperatures at a heating rate of 5 °C min⁻¹. The system was kept at the reaction temperature for 3 h as samples were analyzed each 10 min using GC. To investigate the effect of water vapor partial pressure, the water-containing saturator was placed in a water bath thermostat (LAUDA Alpha RA 8) where the bath temperature was kept at 60 °C (water vapor pressure of 19.9 kPa).

The selectivity for CH₃OH, CO or CO₂ was calculated using Eq. 5.1.

$$\text{Selectivity of X(\%)} = \frac{\text{X production rate } (\mu\text{mol X g}^{-1}\text{h}^{-1}) * 100}{\text{Total product production rate } (\mu\text{mol (CH}_3\text{OH+ CO+ CO}_2\text{) g}^{-1}\text{h}^{-1})} \quad (5.1)$$

5.2.3 Diffuse Reflectance UV–vis Spectroscopy

Diffuse reflectance UV–vis spectra were collected using a UV–vis spectrometer (JASCO, V-5500) and a in-house prepared set-up that allowed gas flow

during spectra collection as described in Chapter 3. The reference for the UV–vis spectra was obtained using barium sulfate (Sigma).

UV–vis spectra were collected following O₂ or N₂O/He pre-treatments at 270 °C. The hydrated samples (exposed to air) were heated to 270 °C with a heating rate of 5 °C min⁻¹ and kept at that temperature for 2 h under 20 cm³ min⁻¹ O₂ or 20 cm³ min⁻¹ 30% N₂O (balance He) flows. The samples were then cooled to 25 °C with continuing flow and a spectrum was taken at 25 °C.

In a different experiment, Cu-SSZ-13 was treated with 30% N₂O flow as explained above. After taking a spectrum at 25 °C with continuing 30% N₂O flow, the sample was heated back to 270 °C with 5 °C min⁻¹ heating rate then the flow was switched to 20 cm³ min⁻¹ 30% CH₄. After holding the temperature at 270 °C for 1 h, the sample was cooled to 25 °C for measuring another spectrum.

5.3 Results and Discussion

5.3.1 Material Characterization

The elemental analysis of the Cu(II) exchanged samples are given in Table 5.1. Similar Cu/Al ratios on Cu exchanged samples resulted in approximately double Cu concentration on Cu-mordenite (0.94 mmol Cu g⁻¹) when compared to Cu-SSZ-13 and Cu-ZSM-5. Cu(II)- exchanged samples show high crystallinity with no additional phases (Figure 5.1). Powder XRD pattern of Cu-SSZ-13 is given in Chapter 4.

Table 5.1: Elemental analysis of copper(II)acetate exchanged samples[†]

Zeolite	Nominal Si/Al	Cu/Al from UV-vis	Cu concentration / mmol Cu g ⁻¹
H-Cu-SSZ-13	12	0.40	0.50
H-Cu-ZSM-5	11.5	0.44	0.57
H-Cu-mordenite	5	0.36	0.94

[†] Copper content calculated is described in section 5.2.

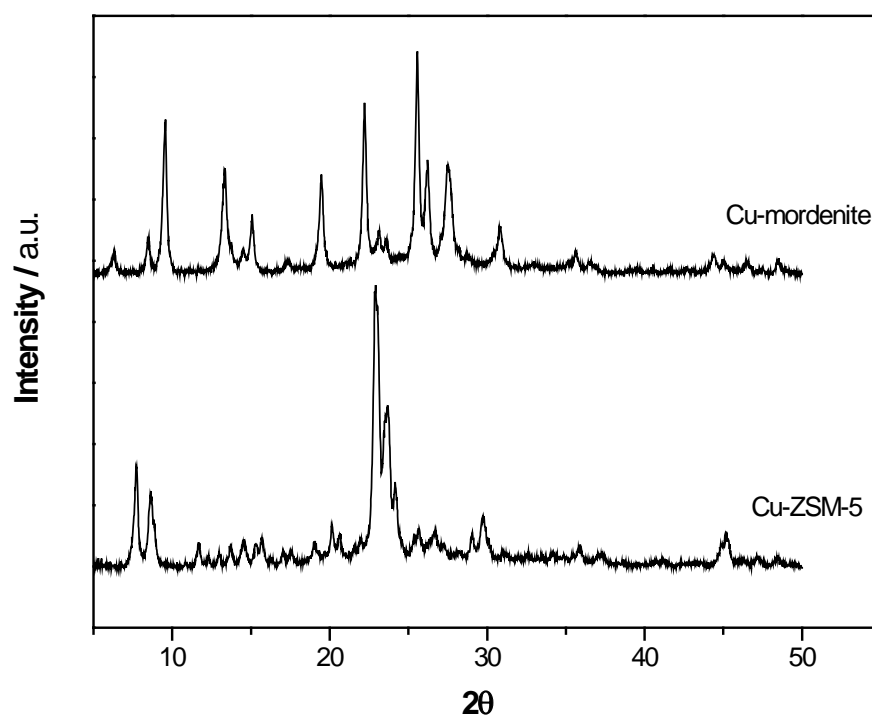


Figure 5.1: Powder XRD pattern of Cu-ZSM-5 (Si/Al = 11.5), Cu-mordenite (Si/Al = 5), Cu K α , $\lambda = 1.5418 \text{ \AA}$

5.3.2 3-step Cyclic Methanol Production: Effect of N₂O

Initially methanol production using the 3-step process with either N₂O or O₂ was compared for pre-oxidation at 200 °C, 300 °C and 450 °C (Cu-SSZ-13: Si/Al = 12, Cu/Al = 0.4). Larger quantities of methanol were observed at 200 °C and 300 °C by N₂O pre-oxidation than by O₂ pre-oxidation (see Table 5.2). The increased methanol formation amounts could be interpreted as higher concentration of active species forming by N₂O treatment at lower temperatures when compared to O₂ activation. Note that the 13 μmol CH₃OH g_{zeolite}⁻¹ of *isothermal* methanol production at 200 °C using the N₂O pre-treatment is much higher than the 0.63 μmol CH₃OH g_{zeolite}⁻¹ formed *isothermally* with NO at 150 °C on Cu-ZSM-5¹¹³ or the 5.4 μmol CH₃OH g_{zeolite}⁻¹ observed with O₂ *isothermally* at 200 °C on Cu-mordenite (Si/Al = 6, Cu/Al = 0.35).¹¹⁹

At temperatures higher than 350 °C, catalytic decomposition of N₂O to O₂ and N₂ was observed on Cu-SSZ-13 (see Figure D.4); this is in agreement with N₂O decomposition temperature on Cu-ZSM-5.³² This side reaction occurring at temperatures above 350 °C is possibly the reason why smaller quantities of methanol were observed with N₂O than with O₂ at 450 °C.

Table 5.2: Methanol production on Cu-SSZ-13 (Si/Al = 12) using N₂O or O₂ as oxidant[†]

Oxidation Temperature / °C	Oxidant	CH ₃ OH formation / μmol CH ₃ OH g ⁻¹
200	10% N ₂ O/He	13
	O ₂	10
300	10% N ₂ O/He	29
	O ₂	25
450	10% N ₂ O/He	35
	O ₂	45

[†] After treatment by O₂ or N₂O at indicated temperatures for 2 h, the sample was treated with CH₄ at 200 °C for 1 h followed by steam extraction of methanol at 200 °C

5.3.3 Catalytic Methanol Production

Catalytic experiments were conducted in the temperature range of 200–300 °C, to avoid N₂O decomposition into O₂, using a gas composition consisting of 30% methane, 30% nitrous oxide and 3% steam (balance He, see Table 5.3). Methanol was not observed below 250 °C within the detection limits of the FID, but note that this could be due to insufficient thermal energy to desorb methanol from the surface at 250 °C, as Parfenov et al.¹¹⁶ have suggested for Fe-ZSM-5. Above 250 °C, steady state methanol production rates were observed over Cu-SSZ-13 without any deactivation for the duration of the measurements (the maximum time-on-stream was 23 hours, see Figure D.5). Methanol, CO and CO₂ were observed as the products of the catalytic methane oxidation with methanol selectivity between 20% and 27% for temperatures between 250 °C and 265 °C. As temperature increased, CO and CO₂ formation rates increased faster than the methanol production rate, resulting in an increased turnover frequency but lower methanol selectivity (Table 5.3).

The need for copper for methanol production was confirmed by testing H-SSZ-13 (Si/Al = 12) at 270 °C. The methanol production rate of 2 $\mu\text{mol g}_{\text{cat}}^{-1} \text{h}^{-1}$ is found using H-SSZ-13, which is much smaller than 28 $\mu\text{mol g}_{\text{cat}}^{-1} \text{h}^{-1}$ methanol production rate observed on Cu-SSZ-13.

Table 5.3: Catalytic CH_3OH and CO_x production rates and selectivity values^a

Sample	Temperature / °C	CH_3OH rate / $\mu\text{mol CH}_3\text{OH g}^{-1} \text{h}^{-1}$	CO rate / $\mu\text{mol CO g}^{-1} \text{h}^{-1}$	CO_2 rate / $\mu\text{mol CO}_2 \text{ g}^{-1} \text{h}^{-1}$	CH_3OH Sel. / %	CO Sel. / %	CO_2 Sel. / %	TOF ^d / h^{-1}
Cu-SSZ-13	250	12	34	4	24	68	8	0.10
Cu-SSZ-13	260	19	42	8	27	61	12	0.14
Cu-SSZ-13	265	22	66	15	21	64	15	0.21
Cu-SSZ-13	270	28	124	22	16	72	12	0.35
Cu-SSZ-13	275	34	208	54	12	70	18	0.60
Cu-SSZ-13	300	55	1794	527	2	76	22	4.80
Cu-SSZ-13	300 ^b	49	262	83	13	66	21	0.79
Cu-SSZ-13	270 ^c	12	49	370	3	11	86	0.87
Cu-SSZ-13	300 ^c	9	55	290	1	12	87	0.72
Cu-mordenite	270	10	28	3	24	70	6	0.05
Cu-ZSM-5	270	6	1632	503	0.3	76.2	23.5	3.80

^a: Reaction conditions: 0.300±0.005 g catalyst weight; feed 30% CH_4 , 30% N_2O , 3% H_2O balance helium (30.4 kPa CH_4 , 30.4 kPa N_2O , 3.2 kPa H_2O , 37.3 kPa He); flow rate: 120 $\text{cm}^3 \text{min}^{-1}$, WHSV = 19,650 $\text{g}_{\text{feed}} \text{g}_{\text{cat}}^{-1} \text{h}^{-1}$

^b: Same conditions with ^a except 20% H_2O instead of 3% H_2O

^c: Same conditions with ^a, 30% O_2 instead of 30% N_2O

^d: Mole of total oxidation products/ mole of Cu^{2+} /h

Narsimhan et al. recently reported catalytic methanol production on Cu-ZSM-5 by flowing methane (98.1 kPa), water vapor (3.2 kPa) and 0.0025 kPa O_2 at 210 °C with 0.88 $\mu\text{mol g}_{\text{cat}}^{-1} \text{h}^{-1}$ methanol production rate and ~70% methanol selectivity.²³⁴ The observed high methanol selectivity is probably related to the low methanol production and methane conversion rates at 210 °C, as we also have observed higher

selectivity at lower temperatures. At higher temperatures, our results agree with the results of Narsimhan et al. —Cu-SSZ-13 (Si/Al = 15, Cu/Al = 0.55) is reported to produce methanol at a rate of $16.1 \mu\text{mol g}_{\text{cat}}^{-1} \text{h}^{-1}$ at $260 \text{ }^\circ\text{C}$ (with feed gas composition of 88% CH_4 / 0.087% O_2 / 3% H_2O),²³⁴ whereas we obtained $19 \mu\text{mol g}_{\text{cat}}^{-1} \text{h}^{-1}$ methanol production rate on Cu-SSZ-13 (Si/Al = 12, Cu/Al = 0.4) using 30% CH_4 / 30% N_2O / 3% H_2O feed gas at $260 \text{ }^\circ\text{C}$ (Table 5.3). Comparison of the methanol selectivity for the two feed gas conditions is not possible since these data were not reported by Narsimhan et al.²³⁴

Cu-SSZ-13 is a superior catalyst for steady state methanol production at the performed reaction conditions ($270 \text{ }^\circ\text{C}$, 30% CH_4 , 30% N_2O , 3% H_2O balance helium) when compared to Cu-ZSM-5 and Cu-mordenite at comparable Cu/Al ratios (Cu-SSZ-13 Si/Al = 12, Cu/Al = 0.4, Cu-mordenite Si/Al = 5, Cu/Al = 0.38, Cu-ZSM-5 Si/Al = 11.5, Cu/Al = 0.44). While higher selectivity toward methanol was observed on Cu-mordenite at $270 \text{ }^\circ\text{C}$, methanol production rates were lower when compared to Cu-SSZ-13 ($10 \mu\text{mol CH}_3\text{OH g}_{\text{zeolite}}^{-1} \text{h}^{-1}$ versus $28 \mu\text{mol CH}_3\text{OH g}_{\text{zeolite}}^{-1} \text{h}^{-1}$ on Cu-SSZ-13) despite higher Cu concentration on Cu-mordenite ($0.94 \text{ mmol Cu g}^{-1}$ versus $0.50 \text{ mmol Cu g}^{-1}$ for Cu-SSZ-13). Cu-ZSM-5 showed very low methanol selectivity (0.3% at $270 \text{ }^\circ\text{C}$) in contrast to the selective methanol formation via the cyclic process using an N_2O activation step at $200 \text{ }^\circ\text{C}$.¹¹⁷

The activation energy for methanol production on Cu-SSZ-13 was calculated for temperatures between $250 \text{ }^\circ\text{C}$ and $270 \text{ }^\circ\text{C}$ to be $142 \pm 30 \text{ kJ mol}^{-1}$ (see Figure 5.2). The activation energy for methanol production on Cu-SSZ-13, Cu-mordenite and Cu-ZSM-5 have been reported as $100 \pm 2.1 \text{ kJ mol}^{-1}$, $149 \pm 2 \text{ kJ mol}^{-1}$ and $80 \pm 2 \text{ kJ mol}^{-1}$, respectively, by Narsimhan et al. (using methanol production rate obtained from a feed

gas composition of 88% CH₄/ 0.087% O₂/ 3% H₂O),²³⁴ with no dependence of methanol production rate on O₂ but a first order dependence on CH₄ involving a kinetically relevant C–H abstraction step.

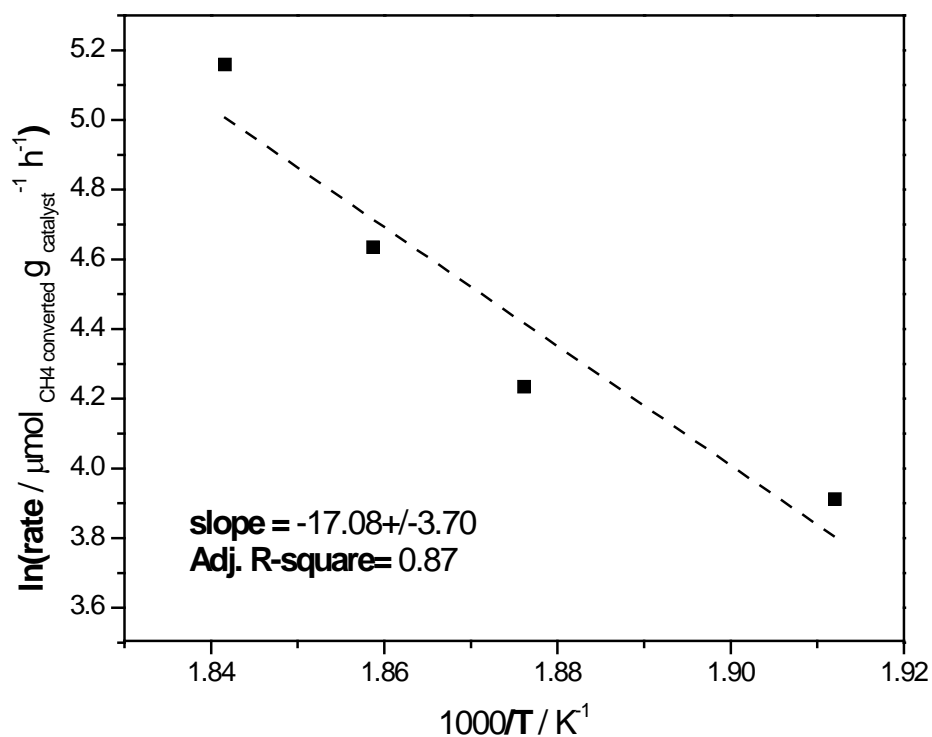


Figure 5.2: Arrhenius plot of methane oxidation rate ($\mu\text{mol}_{\text{CH}_4 \text{ converted}} \text{g}_{\text{zeolite}}^{-1} \text{h}^{-1}$) of Cu-SSZ-13 at the temperature range of 250–270 °C. The feed gas mixture for these experiments was: 30% CH₄: 30% N₂O: 3% H₂O balance He at ambient pressure, flow rate 120 cm³ min⁻¹, WHSV = 19,650 g_{feed} g_{cat}⁻¹ h⁻¹

We have investigated the effect of CH₄ and N₂O partial pressure on methane oxidation rates at 270 °C using the rate expression given in Eq. 5.2. Changes in CH₄ partial pressure showed no effect on methane oxidation rate between the pressures of 20.2 kPa and 40.5 kPa at 270 °C with a calculated rate order of $\alpha = -0.08 \pm 0.05$ (see Figure 5.3). The methane oxidation rate increased to 1.26 mol_{CH₄ converted} mol_{Cu}⁻¹ h⁻¹ when CH₄ partial pressure was increased to 50.7 kPa (Table D.4). On the other hand, when the effect of methane partial pressure has been investigated on methanol production rate, a rate order of 1.1 ± 0.1 (Figure D.7) was observed for methane pressures up to 40.5 kPa. This value is similar to CH₄ order observed for methanol production rate on Cu-ZSM-5 with O₂ as the oxidant.²³⁴

$$r_{CH_4} = -k_{app} P_{CH_4}^\alpha P_{N_2O}^\beta \quad (5.2)$$

The increasing effect of CH₄ partial pressure on methanol formation has been reported by Tomkins et al., where 36 bar CH₄ resulted in 103.3 μmol CH₃OH g_{zeolite}⁻¹ methanol formation using the cyclic procedure as compared to 45.3 μmol CH₃OH g_{zeolite}⁻¹ obtained at 1 bar CH₄ pressure.¹¹⁹ Xu et al. also observed high catalytic methanol production rate on Fe-Cu-ZSM-5 (193 μmol CH₃OH g_{zeolite}⁻¹ h⁻¹, with 77% methanol selectivity) when 20 bar methane pressure is used at 50 °C (using H₂O₂ as the oxidant).²³⁵ In our experiments, we observed an increase in methanol production rates to 57 μmol CH₃OH g_{zeolite}⁻¹ h⁻¹ as the methane partial pressure was increased to 50.7 kPa. Methanol selectivity increased to 20% from 9% as the pressure was increased from 20.3 kPa to 40.5 kPa, and then dropped back to 9% as the methane pressure was further increased to 50.7 kPa (Table D.4).

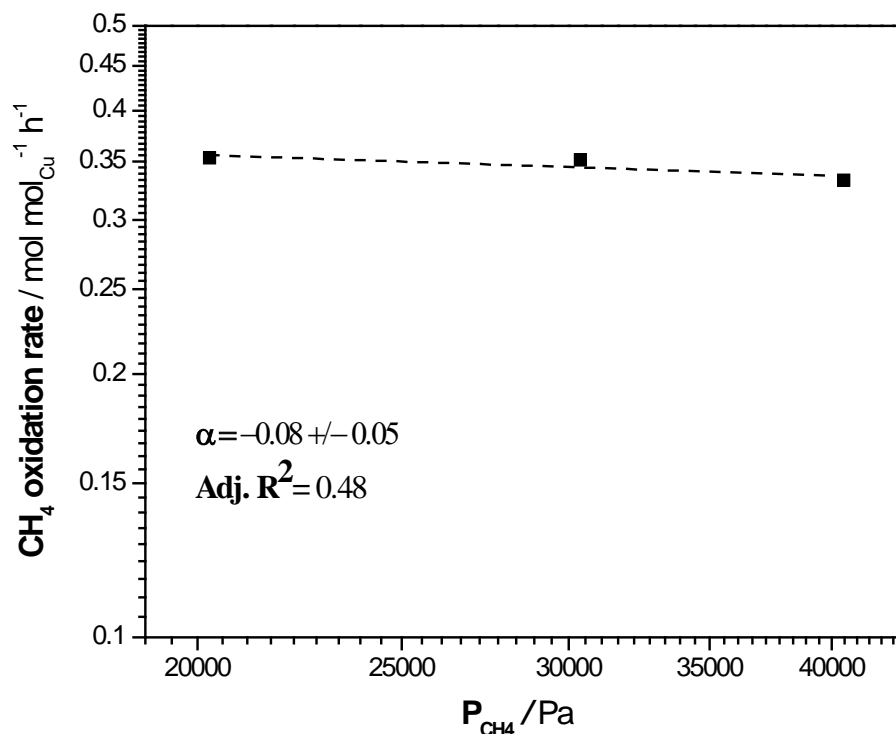


Figure 5.3: log-log plot of methane oxidation rate versus partial pressure of CH_4 (between 20265 Pa and 40530 Pa) at 270 °C on Cu-SSZ-13 (feed gas composition: 20– 40% CH_4 , 30% N_2O , 3% H_2O , balance He; flow rate: $120 \text{ cm}^3 \text{ min}^{-1}$)

A N_2O rate order of $\beta = 0.26 \pm 0.06$ (Figure 5.4), was observed for methane oxidation reaction, whereas the partial pressure of N_2O was observed to have no effect on methanol production rates, which resulted in decreased methanol selectivity with increased N_2O pressure (Table D.5). Methanol selectivity of 26% was obtained at 3 kPa N_2O pressure without any significant decrease in methanol formation rate ($27 \mu\text{mol CH}_3\text{OH g}_{\text{zeolite}}^{-1} \text{h}^{-1}$) when compared to 30.4 kPa N_2O pressure. The lack of N_2O pressure dependence of methanol formation rates suggests an opportunity to use lower

N₂O concentrations to achieve higher methanol selectivity without much impact on methanol production rate.

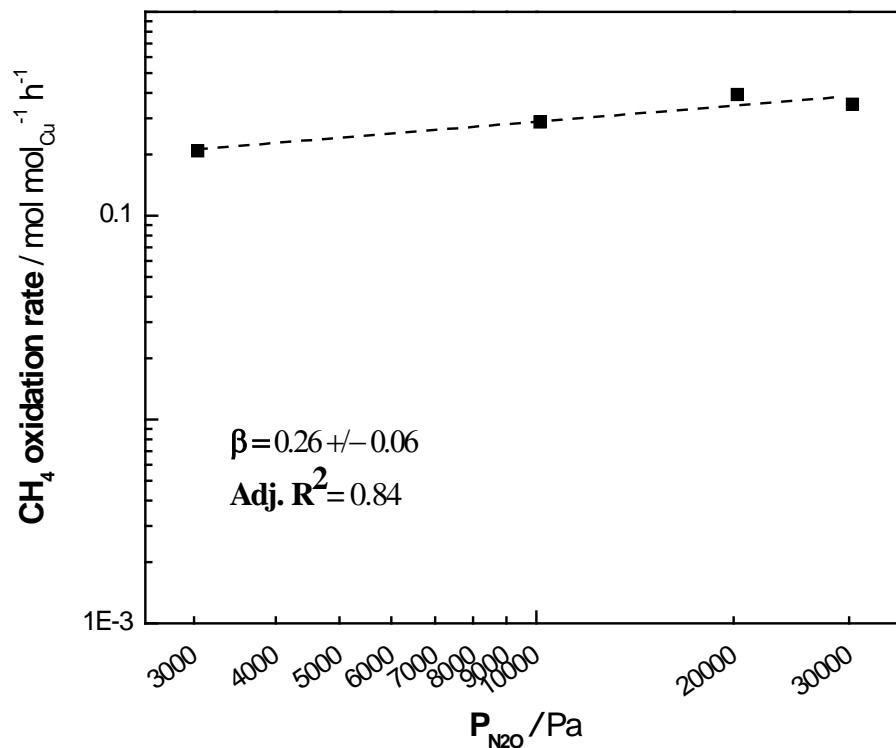


Figure 5.4: log-log plot of methanol formation rate versus partial pressure of N₂O (between 3040 Pa and 30400 Pa) at 270 °C on Cu-SSZ-13 (feed gas composition: 30% CH₄, 3– 30% N₂O, 3% H₂O, balance He; flow rate: 120 cm³ min⁻¹)

The effect of water partial pressure on methanol formation rate and methanol selectivity was investigated at 300 °C (Table 5.3). Methanol was produced with a selectivity of 2% at a water vapor partial pressure of 0.03 atm (3.2 kPa) in the feed

gas, but when the water partial pressure was increased to 19.9 kPa (by increasing the saturator temperature to 60 °C), methanol formation rate decreased only by 11%. At the same time, CO and CO₂ formation were suppressed, resulting in an increased in methanol selectivity of 13% (Table 5.3). The increasing effect of water vapor pressure on methanol selectivity was also reported for Fe-ZSM-5, and was ascribed to the suppressed coke formation with increasing water content rather than suppressed CO and CO₂ production. Decreased CO and CO₂ formation rates here indicate an inhibition effect of H₂O on sites responsible for over-oxidation.

Cu-SSZ-13 was also investigated for catalytic methane conversion using O₂ at 270 °C and 300 °C (Table 5.3). Within this temperature range methanol selectivity did not exceed 3% due to formation of CO and CO₂. The high selectivity toward CO₂ within this temperature range contrasts the high selectivity towards CO when N₂O is utilized as the oxidant. Higher selectivity towards CO (when compared to CO₂) was also reported on Fe-ZSM-5 using N₂O as the oxidant.¹¹⁶ Parfenov et al. suggested [Fe^{III}-O•]²⁺ sites as the active sites for catalytic methanol production as well as for the cyclic methanol production.¹¹⁶ Similarly for Cu-SSZ-13, different copper centers containing one or two extra-framework oxygen atoms could be the reason for higher CO or CO₂ selectivity observed here.

To summarize, steady-state methanol formation was observed on Cu-SSZ-13 with higher methanol production rates per gram basis when compared to Cu-mordenite and Cu-ZSM-5 (having similar or higher copper concentrations) at 270 °C. An activation energy of 142 kJ mol⁻¹ was measured for methane activation at temperatures between 250 °C and 270 °C. The investigation of methane, N₂O and water effect on

methanol production and selectivity imply potential for higher methanol selectivity when lower N₂O and higher CH₄ and water vapor pressure are used.

5.3.4 Diffuse Reflectance UV–vis Spectroscopy

The active site for catalytic methanol formation is affected by the presence of water and thus steam affects methanol production. N₂O and heat treatment of Cu-ZSM-5¹¹⁷ and Cu-mordenite¹²⁰ result in mono-(μ-oxo)dicopper(II) formation. However, steam in the feed gas could result in a different water-stable active site as suggested by Alayon et al. for Cu-mordenite.¹¹⁸ Recently, Yumura et al. suggested water stable (HO–Cu–O–Cu–OH) and (HO–Cu–OH–Cu–O) sites that can theoretically cleave C–H bond of methane more effectively (with C–H bond activation barrier of 43.9 and 33 kJ mol⁻¹) than mono-(μ-oxo)dicopper(II) species.²³⁶ Mono-(μ-oxo)dicopper(II) species activates methane via H-atom abstraction with an activation energy of 65.6 kJ mol⁻¹ on Cu-ZSM-5¹¹⁷ and 61.4 and 46.4 kJ mol⁻¹ on Cu-mordenite.¹²⁰ These kind of oxo-hydroxo species are also suggested as active sites for Fe-ZSM-5 created in presence of H₂O₂.²³¹ Keeping in mind that steam could make different active sites, we investigated the effect of O₂ and N₂O on Cu-SSZ-13 that resulted in major differences in methanol, CO and CO₂ selectivity.

Diffuse reflectance UV–vis spectra of Cu-SSZ-13 treated with 30% N₂O (balance He) were compared to the spectra obtained after O₂ treatment at 270 °C (Figure 5.5). N₂O and O₂ clearly have different effects on the samples as O₂ treated samples are dark blue, whereas N₂O treated samples are pale green. The band at 38,800 cm⁻¹ in both spectra is assigned to the LMCT from the framework oxygen atoms to Cu²⁺ upon dehydration.¹⁵⁵ The absorption bands at 19,900 cm⁻¹ and 16,600 cm⁻¹, which have been assigned to the *d*←*d* transitions of bare Cu²⁺ on the 6MR,^{142,155}

could only be seen after O₂ treatment, whereas weaker absorption features at 23,100 cm⁻¹ and 21,000 cm⁻¹ are present only after N₂O treatment.

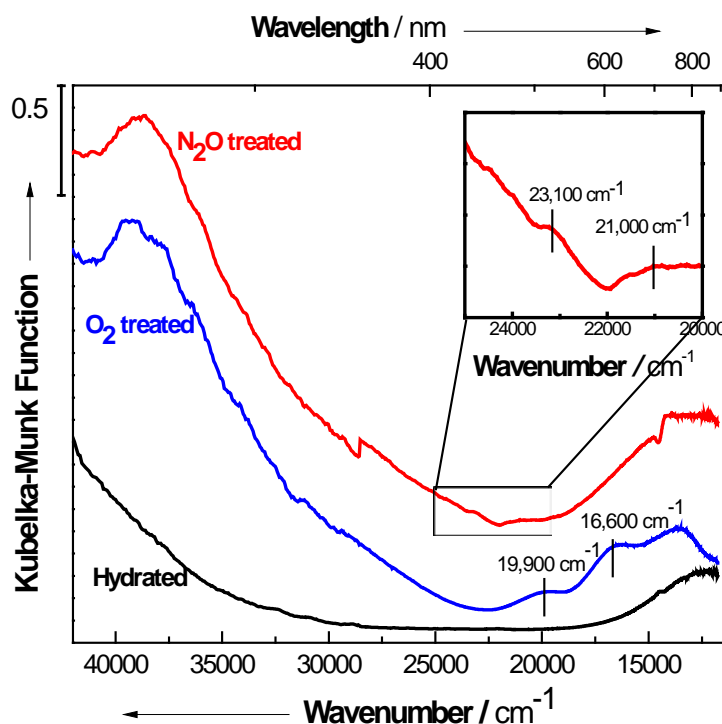


Figure 5.5: Diffuse reflectance UV-vis spectra of Cu-SSZ-13 (Si/Al = 12) after O₂ or 30% N₂O/He treatment at 270 °C. The spectrum of hydrated Cu-SSZ-13 is provided for comparison. Before each spectrum was collected, the quartz sample holder was cooled to room temperature with continuing N₂O/He flow. The spike at 28,500 cm⁻¹ is an artifact caused by a lamp switch in the spectrometer.

Similar bands are observed at 23,100 cm⁻¹ and 21,000 cm⁻¹ on Cu-mordenite, and at 22,800 cm⁻¹ and 21,200 cm⁻¹ on Cu-ZSM-5 following N₂O treatments (Figure 5.6). Electronic transitions at 23,100 cm⁻¹ and 21,900 cm⁻¹ have been assigned to oxo

→ Cu(II) LMCT for two mono-(μ -oxo)dicopper(II) species on different sites, both near 8 member rings of Cu-mordenite.¹²⁰ It is possible that mono-(μ -oxo)dicopper(II) species form near 8 member rings of SSZ-13, similar to mordenite. Differences in electronic transition energies and methanol selectivity on Cu-ZSM-5 could be due to lattice effect of MFI framework since mono-(μ -oxo)dicopper(II) species has been suggested to form near 10 member channels of ZSM-5 but not in CHA.¹¹⁷

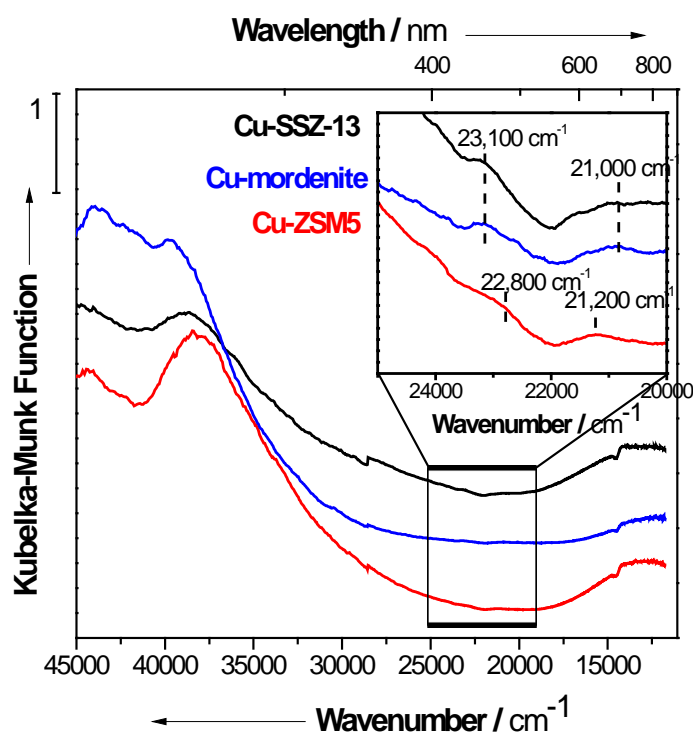


Figure 5.6: Diffuse reflectance UV-vis spectra of Cu-SSZ-13 (Si/Al = 12), Cu-mordenite (Si/Al = 5) and Cu-ZSM-5 (Si/Al = 11.5) following 30% N₂O/He treatment at 270 °C. Before each spectrum was collected, the quartz sample holder was cooled to room temperature with continuing N₂O/He flow. The spike at 28,500 cm⁻¹ is an artifact caused by a lamp switch in the spectrometer.

Another important feature for the reactive species forming on Cu-SSZ-13 is the reduction of the electronic transition in the 25,000–30,000 cm^{-1} region in addition to the reduction of the bands at 23,100 cm^{-1} and 21,000 cm^{-1} when N_2O treated Cu-SSZ-13 is contacted with CH_4 (30%) at 270 °C (see Figure D.8). We tentatively suggest that a mono-(μ -oxo)dicopper(II) species is the dominant species formed with N_2O over Cu-SSZ-13, whereas following O_2 treatment (at 450 °C), trans- μ -1,2-peroxo dicopper(II) species and mono-(μ -oxo)dicopper(II) species formed (see Chapter 4). The difference species with either mono or dioxygen contents could explain different selectivity towards CO and CO_2 in presence N_2O or O_2 , although further investigations are needed to confirm this hypothesis.

5.4 Conclusion

This report demonstrates catalytic methanol production at temperatures between 250 °C and 300 °C on Cu-SSZ-13 using N_2O as the oxidant. N_2O has been shown to cause higher methanol selectivity when compared to O_2 in methane oxidation reactions. Lower methanol selectivity was observed at high methane conversion, with increasing temperature or N_2O pressures. The low selectivity for higher methane conversion is consistent with the well-known yield limitations of alkane oxidation reactions constrained by homolysis of C–H bonds (“hot” approach) as suggested by Labinger.⁷⁷ In these alkane oxidation reactions, the reaction rate constant for over-oxidation of the desired selective oxidation product is considered to be always larger than the rate constant of the selective oxidation, resulting in lower yields with higher conversions.

The higher methanol selectivity and higher methanol production rates with higher CH_4 partial pressure up to 40.5 kPa and higher methanol selectivity with lower

N₂O pressures without an impact on the methanol production rate implied potential for higher methanol formation rates and selectivity with methane pressure of 40.5 kPa and N₂O pressure lower than 3 kPa. Furthermore, water vapor pressure of 19.9 kPa results in increased methanol selectivity without a significant decrease in methanol production rate (when compared to water vapor pressure of 3.2 kPa).

While the reactive site remains to be identified, the higher methanol formation rates found on Cu-SSZ-13, when compared to medium pore Cu-ZSM-5 and Cu-mordenite, suggest that there is potential for other copper exchanged small-pore zeolites like SSZ-16 and SSZ-39.

Chapter 6

SUMMARY AND OUTLOOK

6.1 Summary

Cu- exchanged zeolites are promising materials for a variety of environmentally important reactions including NO_x reduction and decomposition,^{27,28,30,31,33} and selective oxidation reactions such as one-step hydroxylation of benzene to phenol⁴²⁻⁴⁴ and direct methane oxidation to methanol.^{5,68,69} In addition to the tunable properties of zeolites such as acidity, pore shape and diameter that can be used to control reactant and product selectivity, Cu-exchanged zeolites provide additional catalytic features due to the redox properties of the Cu cation, which are important especially in selective catalytic reduction of NO_x with NH₃.^{65,208} In recent years, Cu- exchanged ZSM-5 and mordenite were shown to produce methanol from methane using a 3-step cyclic process, which involves reactive Cu_xO_y cluster formation, methane activation and methanol extraction steps.^{5,68,70} Application of this 3-step process yields methanol in high selectivity, which is very difficult to achieve via steady-state heterogenous catalysis.⁷⁸ The selectivity is partly due to Cu_xO_y active sites, which can be considered biomimetic to copper-oxygen clusters in methane monooxygenase enzymes, clusters that can selectively convert methane to methanol at ambient conditions.¹⁰³

Catalytic activity on transition metal exchanged zeolites depends on the coordination of the cation since the framework oxygen atoms act as the ligands affecting the electronic properties of the cation, which also provides strong orbital

interactions between the guest molecules and the cation. One important example is Kubas-type dihydrogen complex formation between H_2 and Cu(I) cations on Cu(I) exchanged zeolites.^{133,136} This kind of orbital interactions result in hydrogen adsorption enthalpies between -73 and -39 kJ mol H_2^{-1} on Cu(I)-ZSM-5,¹³⁵ values greater than the optimal absolute hydrogen adsorption enthalpy value (-22 – -25 kJ mol H_2^{-1}) calculated for a loading pressure of 30 bar and desorption pressure of 1.5 bar at ambient temperature.¹³⁸

In this thesis, Cu-SSZ-13 and related chabazite-type framework structures have been investigated in hydrogen adsorption and direct methane conversion to methanol. Cu-ZSM-5 and Cu-mordenite zeolites are the more frequently investigated materials for these applications due to their commercial availability. Cu-ZSM-5 and Cu-mordenite are medium (5.6 Å) and large (7 Å) pore zeolites that have three-dimensional and one-dimension pore channels, to which Cu cation coordinates in many different geometries. Cu-SSZ-13 differs from Cu-ZSM-5 and Cu-mordenite by having small-pores (with 8 member ring openings having a diameter of 3.8 Å) and cavities, and due to these properties it is hydrothermally more stable¹⁴³ than Cu-ZSM5 and Cu-mordenite. Furthermore, Cu-SSZ-13 shows excellent activity and selectivity for SCR of NO_x with NH_3 .⁶⁵

In Chapter 2, we have investigated solid state CuCl exchanged Cu(I)-SSZ-13 and Cu(I)-[B]-SSZ-13 for hydrogen adsorption capacity at ambient temperature and pressure and found:

- Cu(I)-SSZ-13 and Cu(I)-[B]-SSZ-13 adsorbed H_2 at 1 atm and 30 °C with a mole per gram capacity that is more than triple the amount achieved on IRMOF-8.

- The excess hydrogen adsorption capacity of the best sample, Cu(I)-[B]-SSZ-13 reached 0.52 mol H₂ mol Cu⁻¹ (0.24 mmol H₂ g⁻¹) at 1 atm and 30 °C, which is more than two times per mol H₂ per mol of Cu capacity of Cu(I)-ZSM-5.
- Cu(I)-SSZ-13 (Si/Al = 6) showed isosteric heat of adsorption around 20 kJ mol⁻¹, which is considered optimum for hydrogen adsorption on cation exchanged zeolites. Cu(I)-[B]-SSZ-13 showed slightly higher isosteric heat of adsorption (between 50 and 20 kJ mol⁻¹).
- The relatively strong hydrogen interaction on Cu(I)-SSZ-13 has been shown by bathochromic H–H bond stretching frequency shifts by 1025 cm⁻¹ and 746 cm⁻¹ and by refined Cu–D distances as short as 2.2(1) Å (using powder neutron diffraction with deuterium adsorption).

In addition to solid-state CuCl exchange, which resulted in excess CuCl inside the pores, a liquid Cu(I) exchange method has been developed that resulted in chlorine free Cu(I)-SSZ-13. The H₂ adsorption capacity (on per gram and per Cu basis) of the samples prepared using this method doubled the amount obtained on solid-state CuCl exchanged SSZ-13.

In Chapter 3, we have introduced Cu-exchanged small-pore zeolites including Cu-SSZ-13, Cu-SSZ-16 and Cu-SSZ-39 in selective methanol formation field. The main findings include the following:

- Cu-SSZ-13, Cu-SSZ-16 and Cu-SSZ-39 showed higher selective methanol formation amounts when compared to Cu-ZSM-5 and Cu-mordenite. The methanol amount per gram of zeolite reached 39 μmol g⁻¹ on Cu-SSZ-16 (Si/Al = 6.5) and mole of methanol per mole of Cu reached 0.09 on Cu-SSZ-39.
- The characteristics of a bent mono-(μ-oxo)dicopper(II) species ([Cu–O–Cu]²⁺) were easily observed on Cu-ZSM-5 using UV–vis and Raman spectroscopy. Presence of mono-(μ-oxo)dicopper(II) species was also confirmed by its observed reaction with propane at 25 °C as a band at 22,900 cm⁻¹ disappeared upon contacting of O₂ activated Cu-ZSM-5 with propane at 25 °C.

- Cu-SSZ-13 and Cu-SSZ-39 showed similar framework and Cu_xO_y vibrations. The similarity of the observed vibrations indicated the similar building structures such as 6MR and 8MRs and similar coordination geometry of the Cu cations to these building structures. The additional vibrations observed at 360, 511, 574 and 611 cm^{-1} upon O_2 activation at $450\text{ }^\circ\text{C}$ indicated formation of Cu_xO_y species, even though it was difficult to detect them using UV-vis spectroscopy.

In Chapter 4, more elaborate investigation was performed to identify the Cu_xO_y species forming on Cu-SSZ-13 and Cu-SSZ-39. A complementary approach was applied using *in situ* synchrotron powder X-ray diffraction, UV-vis and Raman spectroscopy and theoretical calculations. As a result of the thorough investigation the following are found:

- Trans- μ -1,2-peroxo dicopper(II), $[\text{Cu}_2\text{O}_2]^{2+}$, and mono-(μ -oxo)dicopper(II), $[\text{Cu}_2\text{O}]^{2+}$, species were observed to form on Cu-SSZ-13 and Cu-SSZ-39 upon O_2 or He activation at $450\text{ }^\circ\text{C}$. The optimum distance between the two Cu atoms for the trans- μ -1,2-peroxo dicopper(II) species were found to be between 3.98 \AA and 4.13 \AA , which requires two corresponding $[\text{AlO}_{4/2}]^-$ units to be in different 8MRs. Mono-(μ -oxo)dicopper(II) species are formed on the 8MR plane with a Cu-O-Cu of 95° , that showed different Cu-O vibrations than mono-(μ -oxo)dicopper(II) species formed on Cu-ZSM-5 due to the difference in Cu-O-Cu angle.
- Different Si/Al ratios of Cu-SSZ-13 showed different Cu distribution among 6MR and 8MR sites that resulted in different concentration of the active Cu_2O_2 and Cu_2O species. Higher Si/Al ratios were observed to result in lower concentrations of $[\text{AlO}_{4/2}]^-$ units, and therefore higher concentration of $[\text{Cu}(\text{II})(\text{H}_2\text{O})_6(\text{OH})]^+$ complexes that are believed to play an important role in Cu_2O_2 and Cu_2O formation. The Si/Al ratio of 12 is suggested to be optimum when methanol formation per gram of zeolite is considered.
- μ -(η^2 : η^2) peroxo dicopper(II) species is shown to be the precursor for trans- μ -1,2-peroxo dicopper(II) and mono-(μ -oxo)dicopper(II) species when the reduced Cu(I)-SSZ-13 sample is contacted with O_2 . Transformation of μ -(η^2 : η^2) peroxo dicopper(II) species into trans- μ -1,2-peroxo dicopper(II) and mono-(μ -oxo)dicopper(II)

species is suggested by increased kinetic energy. Trans- μ -1,2-peroxo dicopper(II) and mono-(μ -oxo)dicopper(II) species are also suggested to form from hydrated Cu-SSZ-13 sample via dehydration and condensation of $[\text{CuOH}]^+$ complexes.

- The intensity decrease of the absorption bands at $22,200\text{ cm}^{-1}$, $29,500\text{ cm}^{-1}$ and $35,000\text{ cm}^{-1}$ upon CH_4 interaction of O_2 activated Cu-SSZ-13 indicated methane activation at $200\text{ }^\circ\text{C}$ by both trans- μ -1,2-peroxo dicopper(II) and mono-(μ -oxo)dicopper(II) species.

In Chapter 5, catalytic direct methanol production is investigated at temperatures between $250\text{ }^\circ\text{C}$ and $300\text{ }^\circ\text{C}$ by flowing methane, N_2O and steam on Cu-SSZ-13. Steady-state methanol formation was observed with methanol production rates that are the highest among the Cu-exchanged zeolites. The effect of methane, N_2O and water has also been investigated. The main findings are as follows:

- Cu-SSZ-13 showed steady-state methanol formation rates reaching $28\text{ }\mu\text{mol CH}_3\text{OH g}^{-1}\text{ h}^{-1}$ (at $270\text{ }^\circ\text{C}$) and methanol selectivity of 16 %. The methanol selectivity increased with lower methane conversions at lower temperatures, lower N_2O partial pressures and higher water vapor partial pressures.
- Methane was observed to increase both methanol formation rate and methanol selectivity as its pressure has been increased from 20.3 kPa to 40.5 kPa . The methanol selectivity dropped when methane partial pressure was further increased to 50.7 kPa .
- Utilization of N_2O resulted in higher methanol selectivity when compared to O_2 environment. O_2 and N_2O treatment of the samples resulted in different UV-vis characteristic absorptions.

This thesis introduced Cu-exchanged small-pore zeolites, especially Cu-SSZ-13, in the fields of molecular hydrogen adsorption and direct methane conversion to methanol. Experimental evidence presented here show that these zeolites are more efficient than commercially available ZSM-5 and mordenite in both fields due to the different framework topology and Cu coordination. This thesis provides an opportunity to improve molecular hydrogen adsorption and methane oxidation

properties of Cu- exchanged zeolites based on the atomic-level information presented here.

6.2 Outlook

Cu-SSZ-13 is proven to be efficient in molecular hydrogen and direct methane conversion fields in this work. The main disadvantage of SSZ-13 is the expensive structure directing agent (*N,N,N*-trimethyl-1-adamantanammonium hydroxide) that limits its wide application. This can be overcome by using more economical structure directing agents such as copper tetraethylenepentamine^{201,237} or choline chloride.²³⁸ These new synthesis protocols could especially be applied in molecular hydrogen adsorption, where higher concentration of copper cations would increase the H₂ adsorption capacity per gram of zeolite basis.

In Chapter 2, the most effective Cu(I)- exchanged zeolite for H₂ adsorption was shown to be Cu(I)-[B]-SSZ-13 that has a Si/B ratio of 23. Higher H₂ adsorption capacities could be achieved by increasing B and therefore Cu content of these zeolites. The other points that could be improved in Chapter 2 include following:

- Solid-state CuCl exchange resulted in excess CuCl content inside the pores. Cu(I) exchange that results in chlorine free samples has been achieved here by dissolving CuCl in acetonitrile. However, the Cu(I) distribution was not homogeneous. Other methods that would result in chlorine free samples with Cu(I)/Al ratios reaching 1 are required to be investigated. One possibility could be using ammonia as Cu(I) ligands as investigated by Schwan et al.²³⁹
- At lower temperatures (-263 °C) Cu(I) cations were found to be shielded by electrons of the framework oxygen atoms when coordinated at 6MR. Other small-pore frameworks including 8MRs and excluding 6MRs could be explored for better H₂ adsorption capacity at cryogenic conditions.

In Chapter 3, SSZ-16 has shown significant direct methanol formation activity with a Si/Al ratio of 6.5, whereas Si/Al ratio of 10 resulted in negligible methanol formation. The differences between the different Si/Al ratios could be investigated by Raman spectroscopy that would elucidate corresponding active/ inactive Cu_xO_y species forming on Cu-SSZ-16.

In Chapter 3 and 4, the Cu_2O_2 and Cu_2O species forming by O_2 and He treatments on Cu-SSZ-13 and Cu-SSZ-39 has been revealed in addition to the inactive bare Cu(II) cations that have high concentrations when there are more 6MRs with two Al atoms. The suggestions to increase selective methanol formation amount on Cu-exchanged zeolites include the following:

- Different framework types having 8MRs but not d6MRs could be tested for higher Cu_2O_2 and Cu_2O concentrations. Some framework types could be: ABW, FER, MER, PHI, THO, among which FER would be a more reasonable option with higher Al content (Si/Al = 5) compared to others.
- Since $[\text{CuOH}]^+$ complexes are shown to play an important role in active site formation, higher Si/Al ratios of small-pore zeolites should be investigated that would result in higher concentration of $[\text{Cu(II)(H}_2\text{O)}_6(\text{OH})]^+$ complexes after aqueous ion exchange.
- Cu_2O_2 and Cu_2O formation could be enhanced using a route starting from Cu(I)- form of the zeolites, which would involve either CO pre-treatment or NO and NH_3 pre-treatment.¹⁵⁶

In Chapter 5, it was shown that catalytic methanol formation is possible on Cu-SSZ-13 between temperatures of 250 °C and 300 °C, using a mixture of methane, N_2O and steam. Higher methanol formation rates obtained on Cu-SSZ-13 when compared to Cu-mordenite and Cu-ZSM-5 indicated potential for other small-pore zeolites such as SSZ-39 and SSZ-16. The methanol selectivity was lower when compared to the 3-

step cyclic process mentioned in Chapter 3 and 4. Some findings from Chapter 5 could be used to further increase the methanol selectivity such as:

- High water vapor partial pressure (> 20 kPa)
- Methane partial pressure at 40.5 kPa
- Low N_2O partial pressure (< 3 kPa)

Another way of increasing methanol selectivity could be utilization of small-pore zeolites with mesopores. Mesoporous zeolites are known for decreasing the diffusion path length of the reactants and therefore increasing the product selectivity.²⁴⁰ Mesoporous CHA has already been reported in literature for its improved stability for methanol-to-olefin reaction.²⁴¹

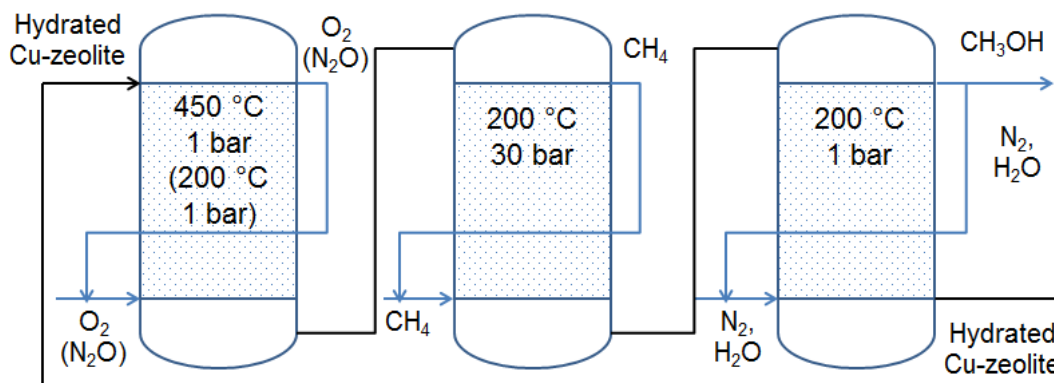


Figure 6.1: Schematic representation of fluidized bed reactors in series for selective methanol production using Cu- exchanged zeolites.

As an alternative to co-feeding methane, N_2O and steam, three fluidized bed reactors could be used in series as depicted in Figure 6.1. Air could be utilized for formation of Cu_xO_y active species in the first step, however the required temperature

for reasonable methanol yields would be higher when compared to utilization of N_2O , which can activate Cu- exchanged small pore zeolites at temperatures as low as 200 °C.

REFERENCES

- (1) Monthly Energy Review May 2016
http://www.eia.gov/totalenergy/data/monthly/pdf/sec2_3.pdf (accessed Jun 20, 2016).
- (2) Higher calorific values for some common fuels
http://www.engineeringtoolbox.com/fuels-higher-calorific-values-d_169.html
(accessed Jun 20, 2006).
- (3) USDRIVE. *Target Explanation Document: Onboard Hydrogen Storage for Light-Duty Fuel Cell Vehicles*; 2015.
- (4) da Silva, M. J. *Fuel Process. Technol.* **2016**, *145*, 42–61.
- (5) Groothaert, M. H.; Smeets, P. J.; Sels, B. F.; Jacobs, P. A.; Schoonheydt, R. A. *J. Am. Chem. Soc.* **2005**, *127*, 1394–1395.
- (6) Vogt, E. T. C.; Whiting, G. T.; Dutta Chowdhury, A.; Weckhuysen, B. M. *Zeolites and Zeotypes for Oil and Gas Conversion*, 1st ed.; Elsevier Inc., 2015; Vol. 58.
- (7) US Geological Survey. *Mineral Commodity Summaries 2015*.
- (8) Milton, R. M. Molecular Sieve Adsorbents. US2882243, 1959.
- (9) Milton, R. M. Molecular Sieve Adsorbents. US2882244, 1959.
- (10) Kerr, G. T. *Inorg. Chem.* **1966**, *5* (9), 1537–1539.
- (11) International Zeolite Association. Database of Zeolite Structures
<http://www.iza-structure.org/databases/> (accessed Jul 4, 2016).
- (12) Sun, J.; Bonneau, C.; Cantín, Á.; Corma, A.; Díaz-Cabañas, M. J.; Moliner, M.; Zhang, D.; Li, M.; Zou, X. *Nature* **2009**, *458* (7242), 1154–1157.
- (13) Davis, M. E. *Ind. Eng. Chem. Res.* **1991**, *30* (May), 1675–1683.
- (14) Weitkamp, J. *Solid State Ionics* **2000**, *131* (1), 175–188.

- (15) Loewenstein, W. *Am. Mineral.* **1956**, *39*, 92–96.
- (16) Bell, A. T. In *Catalysis by Unique Metal Ion Structures in solid Matrices*; Centi, G., Wichterlová, B., Bell, A. T., Eds.; Kluwer Academic Publishers: Dordrecht, The Netherlands, 2001; pp 55–57.
- (17) Shan, J. H.; Liu, X. Q.; Sun, L. B.; Cui, R. *Energy and Fuels* **2008**, *22* (6), 3955–3959.
- (18) Stephenson, M. J.; Holmes, S. M.; Dryfe, R. A. W. *Angew. Chemie Int. Ed.* **2005**, *44* (20), 3075–3078.
- (19) Vermeiren, W.; Gilson, J. P. *Top. Catal.* **2009**, *52* (9), 1131–1161.
- (20) Corma, A. *Catal. Letters* **1993**, *22* (1-2), 33–52.
- (21) Rahimi, N.; Karimzadeh, R. *Appl. Catal. A Gen.* **2011**, *398* (1-2), 1–17.
- (22) Perego, C.; Ingallina, P. *Catal. Today* **2002**, *73* (1-2), 3–22.
- (23) Marcilly, C. *Oil Gas Sci. Technol.* **2001**, *56* (5), 499–514.
- (24) Jones, A. J.; Carr, R. T.; Zones, S. I.; Iglesia, E. *J. Catal.* **2014**, *312*, 58–68.
- (25) Vogt, E. T. C.; Whiting, G. T.; Dutta Chowdhury, A.; Weckhuysen, B. M. *Zeolites and Zeotypes for Oil and Gas Conversion*, 1st ed.; Elsevier Inc., 2015; Vol. 58.
- (26) Iwamoto, M.; Yokoo, S.; Sakai, K.; Kagawa, S. *J. Chem. Soc. Faraday Trans. 1* **1981**, *77* (7), 1629.
- (27) Iwamoto, M.; Furukawa, H.; Mine, Y.; Uemura, F.; Mikuriya, S.; Kagawa, S. *J. Chem. Soc. Chem. Commun.* **1986**, No. 16, 1272.
- (28) Iwamoto, M.; Iwamoto, M.; Yahiro, H.; Yahiro, H.; Tanda, K.; Tanda, K.; Mizuno, N.; Mizuno, N.; Mine, Y.; Mine, Y.; Kagawat, S.; Kagawat, S. *J. Phys. Chem.* **1991**, No. 7, 3727–3730.
- (29) Li, Y.; Armor, J. N. *Appl. Catal. B Environ.* **1992**, *1*, L21–L29.
- (30) Kapteijn, F.; Marban, G.; Rodriguez-Mirasol, J.; Moulijn, J. A. *J. Catal.* **1997**, *167*, 256–265.
- (31) Smeets, P. J.; Groothaert, M. H.; van Teeffelen, R. M.; Leeman, H.; Hensen, E. J. M.; Schoonheydt, R. A. *J. Catal.* **2007**, *245* (2), 358–368.

- (32) Smeets, P. J.; Sels, B. F.; van Teeffelen, R. M.; Leeman, H.; Hensen, E. J. M.; Schoonheydt, R. A. *J. Catal.* **2008**, *256*, 183–191.
- (33) Groothaert, M. H.; van Bokhoven, J. A.; Andrea, A.; Weckhuysen, B. M.; Schoonheydt, R. A. *J. Am. Chem. Soc.* **2003**, *125*, 7629–7640.
- (34) Groothaert, M. H.; Lievens, K.; Leeman, H.; Weckhuysen, B. M.; Schoonheydt, R. A. *J. Catal.* **2003**, *220*, 500–512.
- (35) Groothaert, M. H.; Lievens, K.; Van Bokhoven, J. A.; Battiston, A. A.; Weckhuysen, B. M.; Pierloot, K.; Schoonheydt, R. A. *ChemPhysChem* **2003**, *4*, 626–630.
- (36) Seiyama, T. *J. Catal.* **1977**, *48* (1-3), 1–7.
- (37) Centi, G.; Nigro, C.; Perathoner, S.; Stella, G. *Catal. Today* **1993**, *17* (1-2), 159–166.
- (38) Komatsu, T.; Nunokawa, M.; Moon, I. S.; Takahara, T.; Namba, S.; Yashima, T. *J. Catal.* **1994**, *148*, 427–437.
- (39) Sullivan, J. A.; Cunningham, J.; Morris, M. A.; Keneavey, K. *Appl. Catal. B, Environ.* **1995**, *7* (95), 137–151.
- (40) Salker, A. V.; Weisweiler, W. *Appl. Catal. A Gen.* **2000**, *203* (2), 221–229.
- (41) Baik, J. H.; Yim, S. D.; Nam, I.-S.; Mok, Y. S.; Lee, J.-H.; Cho, B. K.; Oh, S. H. *Top. Catal.* **2004**, *30/31* (x), 37–41.
- (42) Rahkamaa-Tolonen, K.; Maunula, T.; Lomma, M.; Huuhtanen, M.; Keiski, R. L. *Catal. Today* **2005**, *100* (3-4), 217–222.
- (43) Sjövall, H.; Olsson, L.; Fridell, E.; Blint, R. J. *Appl. Catal. B Environ.* **2006**, *64*, 180–188.
- (44) Brandenberger, S.; Kröcher, O.; Tissler, A.; Althoff, R. *Catal. Rev.* **2008**, *50* (4), 492–531.
- (45) Grossale, A.; Nova, I.; Tronconi, E.; Chatterjee, D.; Weibel, M. *Top. Catal.* **2009**, *52* (13-20), 1837–1841.
- (46) Kwak, J. H.; Tran, D.; Burton, S. D.; Szanyi, J.; Lee, J. H.; Peden, C. H. F. *J. Catal.* **2012**, *287* (3), 203–209.
- (47) Yamanaka, H.; Hamada, R.; Nibuta, H.; Nishiyama, S.; Tsuruya, S. *J. Mol.*

- Catal. A-Chemical* **2002**, *178*, 89–95.
- (48) Hamada, R.; Shibata, Y.; Nishiyama, S.; Tsuruya, S. *Phys. Chem. Chem. Phys.* **2003**, *5* (5), 956–965.
- (49) Kubacka, A.; Wang, Z.; Sulikowski, B.; Cores Corberan, V. *J. Catal.* **2007**, *250*, 184–189.
- (50) Ene, A. B.; Archipov, T.; Roduner, E. *J. Phys. Chem. C* **2010**, *114* (34), 14571–14578.
- (51) Ene, A. B.; Archipov, T.; Roduner, E. *J. Phys. Chem. C* **2011**, *115* (9), 3688–3694.
- (52) Anderson, S. A.; Root, T. W. *J. Catal.* **2003**, *217*, 396–405.
- (53) Anderson, S. A.; Root, T. W. *J. Mol. Catal. A Chem.* **2004**, *220*, 247–255.
- (54) Zhang, Y.; Drake, I. J.; Briggs, D. N.; Bell, A. T. *J. Catal.* **2006**, *244* (2), 219–229.
- (55) Zhang, Y.; Briggs, D. N.; de Smit, E.; Bell, A. T. *J. Catal.* **2007**, *251*, 443–452.
- (56) Zhang, Y.; Bell, A. T. *J. Catal.* **2008**, *255*, 153–161.
- (57) Wang, H.; Huang, L.; Holmberg, B. A.; Yan, Y. *Chem. Commun.* **2002**, No. 16, 1708–1709.
- (58) White, J. C.; Dutta, P. K.; Shqau, K.; Verweij, H. *Langmuir* **2010**, *26* (12), 10287–10293.
- (59) Liu, Q.; Pham, T.; Porosoff, M. D.; Lobo, R. F. *ChemSusChem* **2012**, *5* (11), 2237–2242.
- (60) Akhtar, F.; Liu, Q.; Hedin, N.; Bergström, L. *Energy Environ. Sci.* **2012**, *5* (6), 7664.
- (61) Abu-Zied, B. M. *Microporous Mesoporous Mater.* **2011**, *139* (1-3), 59–66.
- (62) Rutkowska, M.; Piwowarska, Z.; Micek, E.; Chmielarz, L. *Microporous Mesoporous Mater.* **2015**, *209*, 54–65.
- (63) De La Torre, U.; Pereda-Ayo, B.; González-Velasco, J. R. *Chem. Eng. J.* **2012**, *207-208*, 10–17.

- (64) Mihai, O.; Widyastuti, C. R.; Andonova, S.; Kamasamudram, K.; Li, J.; Joshi, S. Y.; Currier, N. W.; Yezerets, A.; Olsson, L. *J. Catal.* **2014**, *311*, 170–181.
- (65) Kwak, J. H.; Tonkyn, R. G.; Kim, D. H.; Szanyi, J.; Peden, C. H. F. *J. Catal.* **2010**, *275* (2), 187–190.
- (66) Kwak, J. H.; Tran, D.; Szanyi, J.; Peden, C. H. F.; Lee, J. H. *Catal. Letters* **2012**, *142* (3), 295–301.
- (67) Bull, I.; Koermer, G. S.; Moini, A.; Unverricht, S. CATALYSTS, SYSTEMS AND METHODS UTILIZING NON-ZEOLITIC METAL-CONTAINING MOLECULAR SIEVES HAVING THE CHA CRYSTAL STRUCTURE. US 2009/0196812, 2009.
- (68) Beznis, N. V.; Weckhuysen, B. M.; Bitter, J. H. *Catal. Letters* **2010**, *138*, 14–22.
- (69) Smeets, P. J.; Groothaert, M. H.; Schoonheydt, R. A. *Catal. Today* **2005**, *110*, 303–309.
- (70) Alayon, E. M.; Nachtegaal, M.; Ranocchiari, M.; van Bokhoven, J. A. *Chem. Commun.* **2012**, *48*, 404.
- (71) Wulfers, M. J.; Teketel, S.; Ipek, B.; Lobo, R. F. *Chem. Commun.* **2015**, *51*, 4447–4450.
- (72) King, S. T. *Catal. Today* **1997**, *33*, 173–182.
- (73) Anderson, S. A.; Manthata, S.; Root, T. W. *Appl. Catal. A Gen.* **2005**, *280* (2), 117–124.
- (74) Iwamoto, M.; Hamada, H. *Catal. Today* **1991**, *10*, 57–71.
- (75) Li, J.; Chang, H.; Ma, L.; Hao, J.; Yang, R. T. *Catal. Today* **2011**, *175* (1), 147–156.
- (76) Hammond, C.; Conrad, S.; Hermans, I. *ChemSusChem* **2012**, *5* (9), 1668–1686.
- (77) Labinger, J. A. *J. Mol. Catal. A Chem.* **2004**, *220* (1), 27–35.
- (78) Otsuka, K.; Wang, Y. *Appl. Catal. A Gen.* **2001**, *222*, 145–161.
- (79) Colby, J.; Stirling, D. I.; Dalton, H. *Biochem. J.* **1977**, *165* (2), 395–402.
- (80) Merckx, M.; Kopp, D. A.; Sazinsky, M. H.; Blazyk, J. L.; Muandlller, J.;

- Lippard, S. J. *Angew. Chemie - Int. Ed.* **2001**, *40*, 2782–2807.
- (81) Shu, L.; Nesheim, J. C.; Kauffmann, K.; Münck, E.; Lipscomb, J. D.; Que, L. *Science (80-.)*. **1997**, *275*, 515–518.
- (82) Banerjee, R.; Proshlyakov, Y.; Lipscomb, J. D.; Proshlyakov, D. A. *Nature* **2015**, *518* (7539), 431–434.
- (83) Spencer, N. D. *J. Catal.* **1988**, *109*, 187–197.
- (84) de Lucas, A.; Valverde, J. L.; Canizares, P.; Rodriguez, L. *Appl. Catal. A-Gen.* **1999**, *184*, 143–152.
- (85) Parmaliana, A.; Frusteri, F.; Mezzapica, A.; Scurrrell, M. S.; Giordano, N. **1993**, 751–753.
- (86) Berndt, H.; Martin, A.; Bruckner, A.; Schreier, E.; Muller, D.; Kosslick, H.; Wolf, G.-U.; Lucke, B. *J. Catal.* **2000**, *191* (2), 384–400.
- (87) Alptekin, G. O.; Herring, A. M.; Williamson, D. L.; Ohno, T. R.; McCormick, R. L. *J. Catal.* **1999**, *112*, 104–112.
- (88) Otsuka, K.; Hatano, M. *Chem. Lett.* **1992**, 2397–2400.
- (89) Weng, T.; Wolf, E. E. *Appl. Catal. A Gen.* **1993**, *96*, 383–396.
- (90) Sojka, Z.; Herman, R. G.; Klier, K. *J. Chem. Soc. Chem. Commun.* **1991**, No. 3, 185–186.
- (91) Hargreaves, J. S. J.; Hutchings, G. J.; Joyner, R. W.; Taylor, S. H. *Chem. Commun.* **1996**, No. 4, 523.
- (92) Walker, G. S.; Lapszewicz, J. A.; Foulds, G. A. *Catal. Today* **1994**, *21* (2-3), 519–526.
- (93) Burch, R.; Squire, G. D.; Tsang, S. C. *J. Chem. Soc. Faraday Trans. 1 Phys. Chem. Condens. Phases* **1989**, *85* (10), 3561.
- (94) Foulds, G. A.; Gray, B. F.; Miller, S. A.; Walker, G. S. *Ind. Eng. Chem. Res.* **1993**, *32* (5), 780–787.
- (95) Chun, J. W.; Anthony, R. G. *Ind. Eng. Chem. Res.* **1993**, *32* (2), 259–263.
- (96) Culpepper, M. A.; Cutsail III, G. E.; Gunderson, W. A.; Hoffman, B. M.; Rosenzweig, A. C. *J. Am. Chem. Soc.* **2014**, *136*, 11767–11775.

- (97) Lieberman, R. L.; Kondapalli, K. C.; Shrestha, D. B.; Hakemian, A. S.; Smith, S. M.; Telser, J.; Kuzelka, J.; Gupta, R.; Borovik, A. S.; Lippard, S. J.; Hoffman, B. M.; Rosenzweig, A. C.; Stemmler, T. L. *Inorg. Chem.* **2006**, *45* (20), 8372–8381.
- (98) Shiota, Y.; Yoshizawa, K. *Inorg. Chem.* **2009**, *48* (3), 838–845.
- (99) Citek, C.; Lin, B.; Phelps, T. E.; Wasinger, E. C.; Stack, T. D. P. *J. Am. Chem. Soc.* **2014**, *136*, 14405–14408.
- (100) Citek, C.; Herres-Pawlis, S.; Stack, T. D. P. *Acc. Chem. Res.* **2015**, *48* (8), 2424–2433.
- (101) Culpepper, M. A.; Cutsail, G. E.; Hoffman, B. M.; Rosenzweig, A. C. *J. Am. Chem. Soc.* **2012**, *134*, 7640–7643.
- (102) Shiota, Y.; Juhász, G.; Yoshizawa, K. *Inorg. Chem.* **2013**, *52* (14), 7907–7917.
- (103) Sazinsky, M. H.; Lippard, S. J. In *Sustaining Life on Planet Earth: Metalloenzymes Mastering Dioxygen and Other Chewy Gases*; Springer International Publishing, 2015; pp 205–256.
- (104) Sirajuddin, S.; Rosenzweig, A. C. *Biochemistry* **2015**, *54* (14), 2283–2294.
- (105) Sobolev, V. I.; Dubkov, K. A.; Panna, O. V.; Panov, G. I. *Catal. Today* **1995**, *24* (3), 251–252.
- (106) Panov, G. I.; Sobolev, V. I.; Dubkov, K. A.; Parmon, V. N.; Ovanesyan, N. S.; Shilov, A. E.; Shteinman, A. A. *React. Kinet. Catal. Lett.* **1997**, *61* (2), 251–258.
- (107) Dubkov, K. A.; Sobolev, V. I.; Talsi, E. P.; Rodkin, M. A.; Watkins, N. H.; Shteinman, A. A.; Panov, G. I. *J. Mol. Catal. A Chem.* **1997**, *123* (97), 155–161.
- (108) Wood, B. R.; Reimer, J. A.; Bell, A. T.; Janicke, M. T.; Ott, K. C. *J. Catal.* **2004**, *225* (2), 300–306.
- (109) Starokon, E. V.; Parfenov, M. V.; Pirutko, L. V.; Abornev, S. I.; Panov, G. I. *J. Phys. Chem. C* **2011**, *115*, 2155–2161.
- (110) Beznis, N. V.; Weckhuysen, B. M.; Bitter, J. H. *Catal. Letters* **2010**, *136*, 52–56.
- (111) Beznis, N. V.; Van Laak, A. N. C.; Weckhuysen, B. M.; Bitter, J. H.

Microporous Mesoporous Mater. **2011**, *138* (1-3), 176–183.

- (112) Smeets, P. J.; Hadt, R. G.; Woertink, J. S.; Vanelderen, P.; Schoonheydt, R. A.; Sels, B. F.; Solomon, E. I. *J. Am. Chem. Soc.* **2010**, *132*, 14736–14738.
- (113) Sheppard, T.; Hamill, C. D.; Goguet, A.; Rooney, D. W.; Thompson, J. M. *Chem. Commun.* **2014**, *50* (75), 11053–11055.
- (114) Grundner, S.; Markovits, M. A. C.; Li, G.; Tromp, M.; Pidko, E. A.; Hensen, E. J. M.; Jentys, A.; Sanchez-Sanchez, M.; Lercher, J. A. *Nat. Commun.* **2015**, *6*, 7546.
- (115) Panov, G. I.; Dubkov, K. A.; Starokon, E. V. *Catal. Today* **2006**, *117* (1-3), 148–155.
- (116) Parfenov, M. V.; Starokon, E. V.; Pirutko, L. V.; Panov, G. I. *J. Catal.* **2014**, *318*, 14–21.
- (117) Woertink, J. S.; Smeets, P. J.; Groothaert, M. H.; Vance, M. A.; Sels, B. F.; Schoonheydt, R. A.; Solomon, E. I. *Proc. Natl. Acad. Sci. U. S. A.* **2009**, *106*, 18908–18913.
- (118) Alayon, E. M. C.; Nachtegaal, M.; Bodi, A.; Van Bokhoven, J. A. *ACS Catal.* **2014**, *4*, 16–22.
- (119) Tomkins, P.; Mansouri, A.; Bozbag, S. E.; Krumeich, F.; Park, M. B.; Alayon, E. M. C.; Ranocchiari, M.; van Bokhoven, J. A. *Angew. Chemie Int. Ed.* **2016**, *55*, 5467–5471.
- (120) Vanelderen, P.; Snyder, B. E. R.; Tsai, M.-L.; Hadt, R. G.; Vancauwenbergh, J.; Coussens, O.; Schoonheydt, R. A.; Sels, B. F.; Solomon, E. I. *J. Am. Chem. Soc.* **2015**, *137*, 6383–6392.
- (121) Alayon, E. M. C.; Nachtegaal, M.; Bodi, A.; Ranocchiari, M.; van Bokhoven, J. *Phys. Chem. Chem. Phys.* **2015**, *4*, 1166–1169.
- (122) Broom, D. P.; Webb, C. J.; Hurst, K. E.; Parilla, P. A.; Gennett, T.; Brown, C. M.; Zacharia, R.; Tylanakis, E.; Klontzas, E.; Froudakis, G. E.; Steriotis, T. A.; Trikalitis, P. N.; Anton, D. L.; Hardy, B.; Tamburello, D.; Corgnale, C.; van Hassel, B. A.; Cossement, D.; Chahine, R.; Hirscher, M. *Appl. Phys. A* **2016**, *122* (3), 151.
- (123) Texier-Mandoki, N.; Dentzer, J.; Piquero, T.; Saadallah, S.; David, P.; Vix-Guterl, C. *Carbon N. Y.* **2004**, *42*, 2744–2747.

- (124) Furukawa, H.; Ko, N.; Go, Y. B.; Aratani, N.; Choi, S. B.; Choi, E.; Yazaydin, A. O.; Snurr, R. Q.; O’Keeffe, M.; Kim, J.; Yaghi, O. M. *Science* (80-.). **2010**, 329 (5990), 424–428.
- (125) Ardelean, O.; Blanita, G.; Borodi, G.; Mihet, M.; Coros, M.; Lupu, D. *Int. J. Hydrogen Energy* **2012**, 37 (9), 7378–7384.
- (126) Vitillo, J. G.; Regli, L.; Chavan, S.; Ricchiardi, G.; Spoto, G.; Dietzel, P. D. C.; Bordiga, S.; Zecchina, A. *J. Am. Chem. Soc.* **2008**, 130 (26), 8386–8396.
- (127) Firlej, L.; Pfeifer, P.; Kuchta, B. *Adv. Mater.* **2013**, 25 (41), 5971–5974.
- (128) Lochan, R. C.; Head-Gordon, M. *Phys. Chem. Chem. Phys.* **2006**, 8, 1357–1370.
- (129) Frost, H.; Düren, T.; Snurr, R. Q. *J. Phys. Chem. B* **2006**, 110, 9565–9570.
- (130) Otero Areán, C.; Turnes Palomino, G.; Llop Carayol, M. R. *Appl. Surf. Sci.* **2007**, 253, 5701–5704.
- (131) Kubas, G. J. *Acc. Chem. Res.* **1988**, 21, 120–128.
- (132) Kubas, G. J. *Catal. Letters* **2005**, 104, 79–101.
- (133) Kazansky, V. B.; Pidko, E. A. *Catal. Today* **2005**, 110 (3-4), 281–293.
- (134) Serykh, A. I.; Kazansky, V. B. *Phys. Chem. Chem. Phys.* **2004**, 6, 5250.
- (135) Georgiev, P. A.; Albinati, A.; Eckert, J. *Chem. Phys. Lett.* **2007**, 449 (1-3), 182–185.
- (136) Georgiev, P. A.; Albinati, A.; Mojet, B. L.; Ollivier, J.; Eckert, J. *J. Am. Chem. Soc.* **2007**, 129 (26), 8086–8087.
- (137) Ramirez-Cuesta, A. J.; Mitchell, P. C. H. *Catal. Today* **2007**, 120, 368–373.
- (138) Garrone, E.; Bonelli, B.; Otero Areán, C. *Chem. Phys. Lett.* **2008**, 456, 68–70.
- (139) Solans-Monfort, X.; Branchadell, V.; Sodupe, M.; Zicovich-Wilson, C. M.; Gribov, E.; Spoto, G.; Busco, C.; Ugliengo, P. *J. Phys. Chem. B* **2004**, 108, 8278–8286.
- (140) Kozyra, P.; Świetek, M.; Datka, J.; Broclawik, E. *J. Comput. Chem. Japan* **2013**, 12 (1), 30–37.

- (141) Hereijgers, B. P. C.; Bleken, F.; Nilsen, M. H.; Svelle, S.; Lillerud, K. P.; Bjørgen, M.; Weckhuysen, B. M.; Olsbye, U. *J. Catal.* **2009**, *264* (1), 77–87.
- (142) Godiksen, A.; Stappen, F. N.; Vennestrøm, P. N. R.; Giordanino, F.; Rasmussen, S. B.; Lundegaard, L. F.; Mossin, S. *J. Phys. Chem. C* **2014**, *118* (40), 23126–23138.
- (143) Fickel, D. W.; Lobo, R. F. *J. Phys. Chem. C* **2010**, *114*, 1633–1640.
- (144) Schoonheydt, R. A.; Vandamme, L. J.; Jacobs, P. A.; Uytterhoeven, J. B. *J. Catal.* **1976**, *43* (1-3), 292–303.
- (145) Zecchina, A.; Bordiga, S.; Turnes Palomino, G.; Scarano, D.; Lamberti, C.; Salvalaggio, M. *J. Phys. Chem. B* **1999**, *103*, 3833–3844.
- (146) Kuroda, Y.; Yagi, K.; Horiguchi, N.; Yoshikawa, Y.; Kumashiro, R.; Nagao, M. *Phys. Chem. Chem. Phys.* **2003**, *5* (x), 3318.
- (147) Zhang, Y.; Drake, I. J.; Bell, A. T. *Chem. Mater.* **2006**, *18* (25), 2347–2356.
- (148) Borfecchia, E.; Lomachenko, K. A.; Giordanino, F.; Falsig, H.; Beato, P.; Soldatov, A. V.; Bordiga, S.; Lamberti, C. *Chem. Sci.* **2015**, *6*, 548–563.
- (149) Vanelderen, P.; Vancauwenbergh, J.; Sels, B. F.; Schoonheydt, R. A. *Coord. Chem. Rev.* **2013**, *257* (2), 483–494.
- (150) Korhonen, S. T.; Fickel, D. W.; Lobo, R. F.; Weckhuysen, B. M.; Beale, A. M. *Chem. Commun. (Camb)*. **2011**, *47*, 800–802.
- (151) Deka, U.; Juhin, A.; Eilertsen, E. A.; Emerich, H.; Green, M. A.; Korhonen, S. T.; Weckhuysen, B. M.; Beale, A. M. *J. Phys. Chem. C* **2012**, *116*, 4809–4818.
- (152) Göltl, F.; Bulo, R. E.; Hafner, J.; Sautet, P. *J. Phys. Chem. Lett.* **2013**, *4*, 2244–2249.
- (153) Groothaert, M. H.; Schoonheydt, R. A.; Delabie, A.; Pierloot, K. In *Catalysis by Unique Metal Ion Structures in solid Matrices*; Centi, G., Wichterlová, B., Bell, A. T., Eds.; Kluwer Academic Publishers: Dordrecht, 2000; pp 205–219.
- (154) Andersen, C. W.; Bremholm, M.; Vennestrøm, P. N. R.; Blichfeld, A. B.; Lundegaard, L. F.; Iversen, B. B. *IUCrJ* **2014**, *1*, 382–386.
- (155) Giordanino, F.; Vennestrøm, P. N. R.; Lundegaard, L. F.; Stappen, F. N.; Mossin, S.; Beato, P.; Bordiga, S.; Lamberti, C. *Dalt. Trans.* **2013**, *42*, 12741–12761.

- (156) Paolucci, C.; Parekh, A. A.; Khurana, I.; Di Iorio, J. R.; Li, H.; Albarracin Caballero, J. D.; Shih, A. J.; Anggara, T.; Delgass, W. N.; Miller, J. T.; Ribeiro, F. H.; Gounder, R.; Schneider, W. F. *J. Am. Chem. Soc.* **2016**, *138* (18), 6028–6048.
- (157) Satyapal, S. (Department of E. *2015 Annual Progress Report*; 2015.
- (158) Kaye, S. S.; Dailly, A.; Yaghi, O. M.; Long, J. R. *J. Am. Chem. Soc.* **2007**, *129*, 14176–14177.
- (159) Kapelewski, M. T.; Geier, S. J.; Hudson, M. R.; Stück, D.; Mason, J. A.; Nelson, J. N.; Xiao, D. J.; Hulvey, Z.; Gilmour, E.; FitzGerald, S. A.; Head-Gordon, M.; Brown, C. M.; Long, J. R. *J. Am. Chem. Soc.* **2014**, *136* (34), 12119–12129.
- (160) Drake, I. J.; Zhang, Y.; Briggs, D.; Lim, B.; Chau, T.; Bell, A. T. *J. Phys. Chem. B* **2006**, *110*, 11654–11664.
- (161) Guidry, T. F.; Price, G. L. *J. Catal.* **1999**, *181*, 16–27.
- (162) Sen, D.; Kim, C. W.; Heo, N. H.; Seff, K. *Microporous Mesoporous Mater.* **2014**, *185* (3), 16–25.
- (163) Turnes Palomino, G.; Bordiga, S.; Zecchina, A.; Marra, G. L.; Lamberti, C. *J. Phys. Chem. B* **2000**, *104*, 8641–8651.
- (164) Li, Z.; Xie, K.; Slade, R. C. T. *Appl. Catal. A Gen.* **2001**, *209*, 107–115.
- (165) Pham, T. D.; Liu, Q.; Lobo, R. F. *Langmuir* **2013**, *29* (2), 832–839.
- (166) Regli, L.; Bordiga, S.; Lamberti, C.; Lillerud, K. P.; Zones, S. I.; Zecchina, A. *J. Phys. Chem. C* **2007**, *111* (7), 2992–2999.
- (167) Yun, J. H.; Lobo, R. F. *Microporous Mesoporous Mater.* **2012**, *155*, 82–89.
- (168) Laugier, J.; Bochu, B. CELREF Unit-Cell refinement software
<http://www.ccp14.ac.uk/tutorial/lmgp/celref.htm>.
- (169) Itadani, A.; Sugiyama, H.; Tanaka, M.; Mori, T.; Nagao, M.; Kuroda, Y. *J. Phys. Chem. C* **2007**, *111*, 16701–16705.
- (170) Lippens, B. C.; Linsen, B. G.; Boer de, J. H. *J. Catal.* **1964**, *3*, 32–37.
- (171) Harkins, W. D.; Jura, G. *J. Amer. Chem. Soc.* **1944**, *66* (8), 1366–1373.

- (172) Larson, A. C.; Von Dreele, R. B. Los Alamos National Laboratory, 1994; pp 86–748.
- (173) Toby, B. H. *J. Appl. Crystallogr.* **2001**, *34*, 210–213.
- (174) Hudson, M. R.; Queen, W. L.; Mason, J. A.; Fickel, D. W.; Lobo, R. F.; Brown, C. M. *J. Am. Chem. Soc.* **2012**, *134*, 1970–1973.
- (175) Kapko, V.; Dawson, C.; Treacy, M. M. J.; Thorpe, M. F. *Phys. Chem. Chem. Phys.* **2010**, *12* (30), 8531–8541.
- (176) Valerio, G.; Ple´vert, J.; Goursot, A.; di Renzo, F. *Phys. Chem. Chem. Phys.* **2000**, *2* (5), 1091–1094.
- (177) Spoto, G.; Zecchina, A.; Bordiga, S.; Ricchiardi, G.; Martra, G.; Leofanti, G.; Petrini, G. *Appl. Catal. B, Environ.* **1994**, *3* (2-3), 151–172.
- (178) Sculley, J.; Yuan, D.; Zhou, H.-C. *Energy Environ. Sci.* **2011**, *4*, 2721.
- (179) Zacharia, R.; Cossement, D.; Lafi, L.; Chahine, R. *J. Mater. Chem.* **2010**, *20*, 2145.
- (180) Sumida, K.; Horike, S.; Kaye, S. S.; Herm, Z. R.; Queen, W. L.; Brown, C. M.; Grandjean, F.; Long, G. J.; Dailly, A.; Long, J. R. *Chem. Sci.* **2010**, *1*, 184.
- (181) Smith, L. J.; Davidson, A.; Cheetham, A. K. *Catal. Letters* **1997**, *49* (3/4), 143–146.
- (182) Kustov, L. M.; Kazanskii, V. B.; Beran, S.; Kubelkova, L.; Jiru, P. *J. Phys. Chem.* **1987**, *91* (20), 5247–5251.
- (183) Plitt, H. S.; Bar, M. R.; Ahlrichs, R.; Schnoekel, H. *Angew. Chem. Int. Ed. Engl.* **1991**, *30* (7), 832–834.
- (184) Regli, L.; Zecchina, A.; Vitillo, J. G.; Cocina, D.; Spoto, G.; Lamberti, C.; Lillerud, K. P.; Olsbye, U.; Bordiga, S. *Phys. Chem. Chem. Phys.* **2005**, *7*, 3197–3203.
- (185) Bordiga, S.; Garrone, E.; Lamberti, C.; Zecchina, A.; Arean, C. O.; Kazansky, V. B.; Kustov, L. M. *J. Chem. Soc. Faraday Trans.* **1994**, *90* (21), 3367.
- (186) Smith, L. J.; Eckert, H.; Cheetham, A. K. *J. Am. Chem. Soc.* **2000**, *122* (11), 1700–1708.
- (187) Pham, T. D.; Hudson, M. R.; Brown, C. M.; Lobo, R. F. *ChemSusChem* **2014**, *7*

- (11), 3031–3038.
- (188) Shang, J.; Li, G.; Singh, R.; Gu, Q.; Nairn, K. M.; Bastow, T. J.; Medhekar, N.; Doherty, C. M.; Hill, A. J.; Liu, J. Z.; Webley, P. A. *J. Am. Chem. Soc.* **2012**, *134*, 19246–19253.
- (189) Archer, R. H.; Zones, S. I.; Davis, M. E. *Microporous Mesoporous Mater.* **2010**, *130* (1-3), 255–265.
- (190) Mentzen, B. F.; Bergeret, G. *J. Phys. Chem. C* **2007**, *111*, 12512–12516.
- (191) Vanelderen, P.; Vancauwenbergh, J.; Tsai, M. L.; Hadt, R. G.; Solomon, E. I.; Schoonheydt, R. A.; Sels, B. F. *ChemPhysChem* **2014**, *15*, 91–99.
- (192) Lobo, R.; Zones, S.; Medrud, R. *Chem. Mater.* **1996**, *4756* (96), 2409–2411.
- (193) Anurova, N. A.; Blatov, V. A.; Ilyushin, G. D.; Proserpio, D. M. *J. Phys. Chem. C* **2010**, *114* (22), 10160–10170.
- (194) Solomon, E. I.; Ginsbach, J. W.; Heppner, D. E.; Kieber-Emmons, M. T.; Kjaergaard, C. H.; Smeets, P. J.; Tian, L.; Woertink, J. S. *Faraday Discuss.* **2011**, *148*, 11–39; discussion 97–108.
- (195) Centi, G.; Galli, A.; Perathoner, S. *J. Chem. Soc. Faraday Trans.* **1996**, *92* (24), 5129.
- (196) Bauer, F.; Geidel, E.; Peuker, C.; Pilz, W. *Zeolites* **1996**, *17*, 278–282.
- (197) Fan, F.; Sun, K.; Feng, Z.; Xia, H.; Han, B.; Lian, Y.; Ying, P.; Li, C. *Chem. - A Eur. J.* **2009**, *15* (13), 3268–3276.
- (198) Henson, M. J.; Mukherjee, P.; Root, D. E.; Stack, T. D. P.; Solomon, E. I. *J. Am. Chem. Soc.* **1999**, No. 121, 10332–10345.
- (199) Twu, J.; Dutta, P. K.; Kresge, C. T. *J. Phys. Chem.* **1991**, *95* (4), 5267–5271.
- (200) Baldwin, M. J.; Root, D. E.; Pate, J. E.; Fujisawa, K.; Kitajima, N.; Solomon, E. I. *J. Am. Chem. Soc.* **1992**, *114* (9), 10421–10431.
- (201) Guo, Q.; Fan, F.; Ligthart, D. A. J. M.; Li, G.; Feng, Z.; Hensen, E. J. M.; Li, C. *ChemCatChem* **2014**, *6* (2), 634–639.
- (202) McEwen, J. S.; Anggara, T.; Schneider, W. F.; Kispersky, V. F.; Miller, J. T.; Delgass, W. N.; Ribeiro, F. H. *Catal. Today* **2012**, *184* (1), 129–144.

- (203) Giordanino, F.; Borfecchia, E.; Lomachenko, K. A.; Lazzarini, A.; Agostini, G.; Gallo, E.; Soldatov, A. V.; Beato, P.; Bordiga, S.; Lamberti, C. *J. Phys. Chem. Lett.* **2014**, *5*, 1552–1559.
- (204) Kwak, J. H.; Varga, T.; Peden, C. H. F.; Gao, F.; Hanson, J. C.; Szanyi, J. J. *Catal.* **2014**, *314*, 83–93.
- (205) Bates, S. A.; Verma, A. A.; Paolucci, C.; Parekh, A. A.; Anggara, T.; Yezerets, A.; Schneider, W. F.; Miller, J. T.; Delgass, W. N.; Ribeiro, F. H. *J. Catal.* **2014**, *312*, 87–97.
- (206) Verma, A. A.; Bates, S. A.; Anggara, T.; Paolucci, C.; Parekh, A. A.; Kamasamudram, K.; Yezerets, A.; Miller, J. T.; Delgass, W. N.; Schneider, W. F.; Ribeiro, F. H. *J. Catal.* **2014**, *312*, 179–190.
- (207) Paolucci, C.; Verma, A. A.; Bates, S. A.; Kispersky, V. F.; Miller, J. T.; Gounder, R.; Delgass, W. N.; Ribeiro, F. H.; Schneider, W. F. *Angew. Chemie Int. Ed.* **2014**, *53*, 11828–11833.
- (208) Janssens, T. V. W.; Falsig, H.; Lundegaard, L. F.; Vennestrøm, P. N. R.; Rasmussen, S. B.; Moses, P. G.; Giordanino, F.; Borfecchia, E.; Lomachenko, K. A.; Lamberti, C.; Bordiga, S.; Godiksen, A.; Mossin, S.; Beato, P. *ACS Catal.* **2015**, *5* (5), 2832–2845.
- (209) Gao, F.; Walter, E. D.; Kollar, M.; Wang, Y.; Szanyi, J.; Peden, C. H. F. *J. Catal.* **2014**, *319*, 1–14.
- (210) Gao, F.; Walter, E. D.; Karp, E. M.; Luo, J.; Tonkyn, R. G.; Kwak, J. H.; Szanyi, J.; Peden, C. H. F. *J. Catal.* **2013**, *300*, 20–29.
- (211) Chupas, P. J.; Chapman, K. W.; Kurtz, C.; Hanson, J. C.; Lee, P. L.; Grey, C. P. *J. Appl. Crystallogr.* **2008**, *41*, 822–824.
- (212) Kim, H.; Kosuda, K. M.; Van Duyne, R. P.; Stair, P. C. *Chem. Soc. Rev.* **2010**, *39* (12), 4820–4844.
- (213) Fulton, J. L.; Hoffmann, M. M.; Darab, J. G.; Palmer, B. J.; Stern, E. A. *J. Phys. Chem. A* **2000**, *104* (49), 11651–11663.
- (214) Cruciani, G. *J. Phys. Chem. Solids* **2006**, *67* (9-10), 1973–1994.
- (215) NIST. FFAST: X-ray form factor, Attenuation and Scattering Tables <http://physics.nist.gov/PhysRefData/FFast/html/form.html> (accessed Jun 20, 2006).

- (216) Solomon, E. I.; Heppner, D. E.; Johnston, E. M.; Ginsbach, J. W.; Cirera, J.; Qayyum, M.; Kieber-Emmons, M. T.; Kjaergaard, C. H.; Hadt, R. G.; Tian, L. *Chem. Rev.* **2014**, *114* (7), 3659–3853.
- (217) Baldwin, M. J.; Ross, P. K.; Pate, J. E.; Tyeklar, Z.; Karlin, K. D.; Solomon, E. I. *J. Am. Chem. Soc.* **1991**, *113*, 8671–8679.
- (218) Mahapatra, S.; Halfen, J. A.; Wilkinson, E. C.; Pan, G.; Wang, X.; Young, V. G.; Cramer, C. J.; Que, L.; Tolman, W. B. *J. Am. Chem. Soc.* **1996**, *118* (46), 11555–11574.
- (219) Pidcock, E.; Obias, H. V.; Abe, M.; Liang, H. C.; Karlin, K. D.; Solomon, E. I. *J. Am. Chem. Soc.* **1999**, *121* (I), 1299–1308.
- (220) Chen, P.; Root, D. E.; Campochiaro, C.; Fujisawa, K.; Solomon, E. I. *J. Am. Chem. Soc.* **2003**, *125* (22), 466–474.
- (221) Vilella, L.; Studt, F. *Eur. J. Inorg. Chem.* **2016**, *2016* (10), 1514–1520.
- (222) Jacobson, R. R.; Tyeklar, Z.; Farooq, A.; Karlin, K. D.; Liu, S.; Zubieta, J. J. ... **1988**, *110* (11), 3690–3692.
- (223) Conde, A.; Vilella, L.; Balcells, D.; Díaz-Requejo, M. M.; Lledós, A.; Pérez, P. *J. J. Am. Chem. Soc.* **2013**, *135*, 3887–3896.
- (224) Yumura, T.; Takeuchi, M.; Kobayashi, H.; Kuroda, Y. *Inorg. Chem.* **2009**, *48* (2), 508–517.
- (225) Turnes Palomino, G.; Fisticaro, P.; Bordiga, S.; Zecchina, A.; Giamello, E.; Lamberti, C. *J. Phys. Chem. B* **2000**, *104* (2), 4064–4073.
- (226) Holland, P. L.; Tolman, W. B. *Coord. Chem. Rev.* **1999**, *192*, 855–869.
- (227) Goodman, B. R.; Schneider, W. F.; Hass, K. C.; Adams, J. B. *Catal. Letters* **1998**, *56*, 183–188.
- (228) Larsen, S. C.; Aylor, A.; Bell, A. T.; Reimer, J. A. *J. Phys. Chem.* **1994**, *98* (44), 11533–11540.
- (229) Shiota, Y.; Yoshizawa, K. *J. Am. Chem. Soc.* **2000**, *122* (16), 12317–12326.
- (230) Pidko, E. A.; Hensen, E. J. M.; van Santen, R. A. *Proc. R. Soc. A Math. Phys. Eng. Sci.* **2012**, *468*, 2070–2086.
- (231) Hammond, C.; Forde, M. M.; Ab Rahim, M. H.; Thetford, A.; He, Q.; Jenkins,

- R. L.; Dimitratos, N.; Lopez-Sanchez, J. A.; Dummer, N. F.; Murphy, D. M.; Carley, A. F.; Taylor, S. H.; Willock, D. J.; Stangland, E. E.; Kang, J.; Hagen, H.; Kiely, C. J.; Hutchings, G. J. *Angew. Chemie - Int. Ed.* **2012**, *51*, 5129–5133.
- (232) Kieber-Emmons, M. T.; Ginsbach, J. W.; Wick, P. K.; Lucas, H. R.; Helton, M. E.; Lucchese, B.; Suzuki, M.; Zuberbuhler, A. D.; Karlin, K. D.; Solomon, E. I. *Angew. Chemie - Int. Ed.* **2014**, *53*, 4935–4939.
- (233) Holmen, A. *Catal. Today* **2009**, *142* (0920), 2–8.
- (234) Narsimhan, K.; Iyoki, K.; Dinh, K.; Román-Leshkov, Y. *ACS Cent. Sci.* **2016**, acscentsci.6b00139.
- (235) Xu, J.; Armstrong, R. D.; Shaw, G.; Dummer, N. F.; Freakley, S. J.; Taylor, S. H.; Hutchings, G. J. *Catal. Today* **2016**, *270*, 93–100.
- (236) Yumura, T.; Hirose, Y.; Wakasugi, T.; Kuroda, Y.; Kobayashi, H. *ACS Catal.* **2016**, *6* (4), 2487–2495.
- (237) Ren, L.; Zhu, L.; Yang, C.; Chen, Y.; Sun, Q.; Zhang, H.; Li, C.; Nawaz, F.; Meng, X.; Xiao, F.-S. *Chem. Commun.* **2011**, *47* (35), 9789–9791.
- (238) Xu, R.; Zhang, R.; Liu, N.; Chen, B.; Zhang Qiao, S. *ChemCatChem* **2015**, *7* (23), 3842–3847.
- (239) Shwan, S.; Skoglundh, M.; Lundegaard, L. F.; Tiruvalam, R. R.; Janssens, T. V. W.; Carlsson, A.; Vennestrøm, P. N. R. *ACS Catal.* **2015**, *5* (1), 16–19.
- (240) Chen, L.-H.; Li, X.-Y.; Rooke, J. C.; Zhang, Y.-H.; Yang, X.-Y.; Tang, Y.; Xiao, F.-S.; Su, B.-L. *J. Mater. Chem.* **2012**, *22* (34), 17381.
- (241) Wu, L.; Degirmenci, V.; Magusin, P. C. M. M.; Szyja, B. M.; Hensen, E. J. M. *Chem. Commun.* **2012**, *48* (76), 9492.

Appendix A

H₂ ADSORPTION ON Cu(I)- EXCHANGED SAMPLES

A.1 Isothermic Heat of Adsorption Calculations for Cu(I)-exchanged samples

A.1.1 Cu(I)-SSZ-13 (Si/Al = 6) Sample

H₂ adsorption isotherms at 20 °C, 30 °C, and 40 °C are fitted to Toth Adsorption Isotherm model for pressures higher than 0.3 atm (Figure A.1). Fitted model parameters can be found in Table A.1.

The isothermic heat of hydrogen adsorption was calculated using Clausius-Clapeyron equation (Eq. A.1) at constant hydrogen loadings (0.08-0.13 mmol H₂ g⁻¹).

$$\ln P = \frac{\Delta H_{ads}}{R} \frac{1}{T} + C \quad (\text{A.1})$$

The corresponding pressure values at 20 °C, 30 °C, and 40 °C for determined hydrogen loadings (0.08–0.13 mmol H₂ g⁻¹) were calculated from the Toth adsorption isotherm with fitted model parameters (Table A.1). Then, the heat of adsorption was calculated by performing least square fitting of the isostere (at each hydrogen loading) with a straight line (Figure A.2).

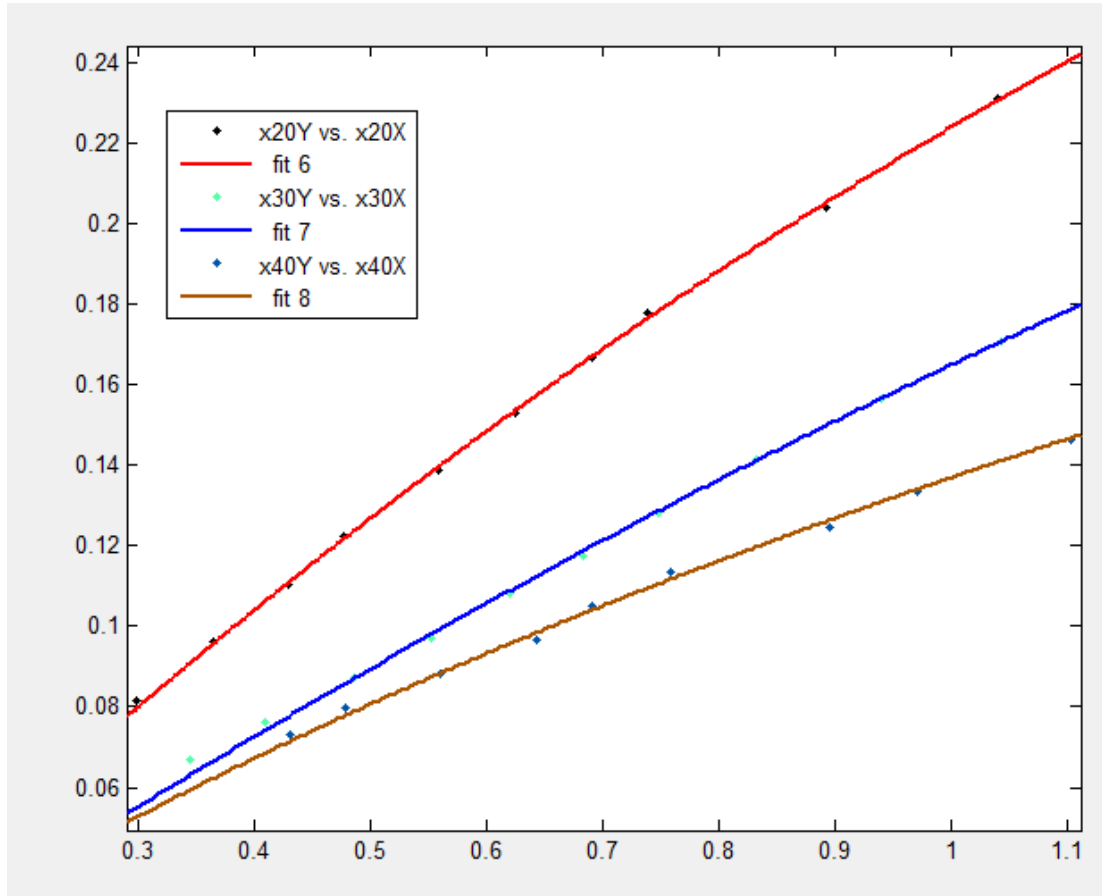


Figure A.1: Toth Isotherm Model Fitting of the hydrogen adsorption isotherms obtained experimentally at 20, 30 and 40 °C on Cu(I)-SSZ-13 (Si/Al = 6) sample. Y axis represents H₂ adsorption capacity, mmol H₂ g_{zeolite}⁻¹, X axis represents H₂ pressure, atm.

Table A.1: Toth Adsorption Isotherm Model ($q = q_{max} \left(\frac{KP}{(1+(KP)^t)} \right)^{1/t}$) parameters found by fitting Cu(I)-SSZ-13 (Si/Al = 6) hydrogen adsorption isotherm data at a temperature range of 20 °C and 40 °C

Temperature / °C	q_{max} / mmol H ₂ g ⁻¹	K / mmol H ₂ g ⁻¹ atm ⁻¹	t
20	0.7244	0.3913	1.196
30	0.6234	0.3041	1.334
40	0.8259	0.2657	0.7033

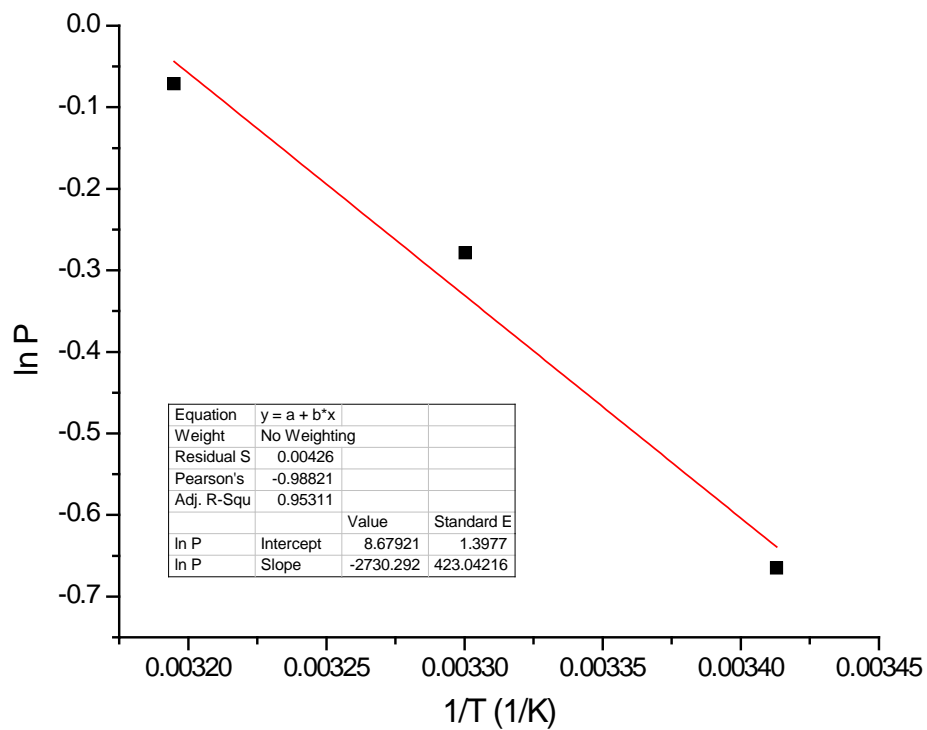


Figure A.2: 0.13 mmol H₂ g⁻¹ isostere least square fitting with a straight line

A.1.2 Cu(I)-[B]-SSZ-13 Sample

H₂ adsorption isotherms at 30 °C, 40 °C, and 50 °C are fitted to Sips

Adsorption Isotherm model for pressures lower than 0.2 atm and to a linear model for pressures higher than 0.2 atm (Figure A.3). Fitted model parameters can be found in Table A.2 and Table A.3.

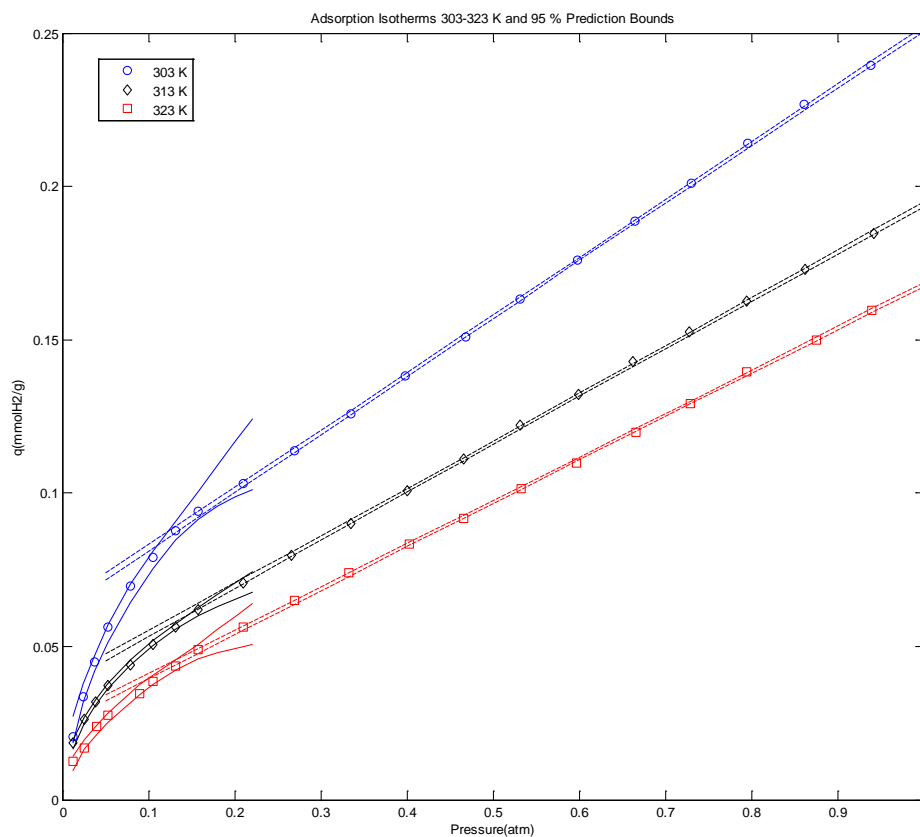


Figure A.3: Hydrogen adsorption experimental data and 95% prediction intervals for the fitted Sips adsorption model for low pressure region (0–0.2 atm) and 95% prediction intervals for the linear model for high pressure region (0.2–1 atm)

Table A.2: Sips Model fitting $q = q_{max} \frac{(K*P)^n}{1+(K*P)^n}$, for pressure region: 0–0.2 atm
 R^2 :0.9955, 0.9988, 0.9944

Temperature / °C	q_{max} / mmol H ₂ g ⁻¹	K / atm ⁻¹	n
30	0.4243	0.9118	0.6334
40	0.3637	0.3156	0.5316
50	0.3419	0.3181	0.6029

Table A.3: Linear Model fitting $q = aP + b$ for pressure region: 0.2-1atm,
 R^2 :0.9997, 0.9997, 0.9997

Temperature / °C	a	b
30	0.1883±0.002	0.0634±0.001
40	0.1557±0.0018	0.0386±0.0012
50	0.1419±0.0017	0.0262±0.001

The isosteric heat of hydrogen adsorption was calculated using Clausius-Clapeyron equation at constant hydrogen loading values evaluated at three different regions. For low q amounts (0.02– 0.05 mmol H₂ g⁻¹), Sips model with the parameters given in Table A.2 were used to calculate for corresponding P values. For medium q region (0.06–0.09 mmolH₂ g⁻¹), Sips Model for 30 °C and Linear Model for 40 °C and 50 °C was used. For high H₂ loadings (0.09–0.17 mmol H₂ g⁻¹), Linear models for all temperature isotherms were used.

A.2 Fitting of H₂ Adsorption Isotherms at -196 °C

The isotherms obtained at -196 °C are fitted to Toth adsorption model (Table A.4).

Table A.4: Henry's constant ($q_{\max} * K$ - mmol H₂ g⁻¹ atm⁻¹) and other equation parameters found by fitting hydrogen adsorption isotherm data to Toth Model ($q = q_{\max} \frac{KP}{(1+(KP)t)^{1/t}}$)

	$q_{\max} / \text{mmol H}_2 \text{ g}^{-1}$	K / atm^{-1}	$q_{\max} * K / \text{mmol H}_2 \text{ g}^{-1} \text{ atm}^{-1}$	t
Cu(I)-SSZ-13 (Si/Al = 6)	8.845	21.82	193	0.488
Na-SSZ-13 (Si/Al = 6)	7.545	133.9	1009	0.428
Cu(I)-SSZ-13 (Si/Al = 12)	10.35	11.62	120	0.464
Na-SSZ-13 (Si/Al = 12)	10.51	25.25	265	0.401
Cu(I)-SSZ-13 (Si/Al = 6)- 750 °C	10.02	21.98	220.2	0.5096
Cu(I)-[B]-SSZ-13	9.274	5.151	47.77	0.7272

A.3 Powder Neutron Diffraction (PND) Experiments

Table A.5: Atomic Parameters from Rietveld refinement of Cu(I)-SSZ-13 (Si/Al = 6, Cu₅Al_{5.14}Si_{30.86}O₇₂) PND data at -263 °C (10 K) [NCNR, BT-1](Trigonal, R-3m, Goodness of fit parameters $\chi^2 = 1.092$, $R_p = 4.57\%$, $wR_p = 5.58\%$, $\lambda = 2.0787(2)$ Å, $a = 13.6192(5)$ Å, $c = 15.0540(8)$ Å, $V = 2418.2(1)$ Å³)

	x/a	y/b	z/c	Occu- pancy	$U_{iso} / \text{Å}^2$	Multipli- city
Si	0.0003(5)	0.2292(4)	0.1011(4)	0.860	0.005(1)	36
Al	0.0003(5)	0.2292(4)	0.1011(4)	0.140	0.005(1)	36
O1	0.9076(2)	0.0924(2)	0.1144(4)	1	0.028(2)	18
O2	0.9691(4)	0.3025(4)	0.1667	1	0.013(1)	18
O3	0.1222(2)	0.2444(4)	0.1280(4)	1	0.026(2)	18
O4	0	0.2653(4)	0	1	0.025(2)	18
Cu1	0	0	0.118(1)	0.349	0.009(6)	6
Cu2	0.299(5)	0.082(5)	0.581(5)	0.047	0.02(2)	36

Table A.6: Atomic Parameters from Rietveld refinement of Cu(I)-SSZ-13 (Si/Al = 6, $\text{Cu}_5\text{Al}_{5.14}\text{Si}_{30.86}\text{O}_{72}$) PND data at 27 °C (300 K) [NCNR, BT-1](Trigonal, R-3m, Goodness of fit parameters $\chi^2 = 0.9949$, $R_p = 4.58\%$, $wR_p = 5.56\%$, $\lambda = 2.0787(2)$ Å, $a = 13.6054(5)$ Å, $c = 15.0170(9)$ Å, $V = 2407.3(2)$ Å³)

	x/a	y/b	z/c	Occu- pancy	$U_{\text{iso}}/U_{\text{ani}} /$ Å ²	Multipli- city
Si	0.0000(4)	0.2274(3)	0.1014(3)	0.860	0.007(1)	36
Al	0.0000(4)	0.2274(3)	0.1014(3)	0.140	0.007(1)	36
O1	0.9069(2)	0.0930(2)	0.1143(5)	1	0.05021	18
O2	0.9690(4)	0.3024(4)	0.1667	1	0.02726	18
O3	0.1227(2)	0.2453(5)	0.1275(5)	1	0.03329	18
O4	0	0.2652(4)	0	1	0.0324	18
Cu1	0	0	0.124(2)	0.349	0.05104	6
Cu2	0.291(7)	0.062(6)	0.606(5)	0.047	0.09(3)	36
	U_{11}	U_{12}	U_{13}	U_{22}	U_{23}	U_{33}
O1	0.034(4)	0.011(4)	-0.015(3)	0.034(4)	0.015(3)	0.075(7)
O2	0.036(4)	0.027(4)	0.003(2)	0.036(4)	-0.003(2)	0.022(4)
O3	0.014(3)	0.023(3)	-0.009(2)	0.045(5)	-0.017(5)	0.051(6)
O4	0.051(5)	0.025(6)	0.006(4)	0.026(3)	0.003(2)	0.029(4)
Cu1	0.012(9)	0.006(5)	0	0.012(9)	0	0.13(3)

Table A.7: Atomic Parameters from Rietveld refinement of Cu(I)-SSZ-13 (Si/Al = 6, $\text{Cu}_5\text{Al}_{5.14}\text{Si}_{30.86}\text{O}_{72}$) PND data obtained at -263 °C (10 K) with D₂ loading at 27 °C (300 K) [NCNR, BT-1](Trigonal, R-3m, Goodness of fit parameters $\chi^2 = 1.065$, $R_p = 4.33\%$, $wR_p = 5.41\%$, $\lambda = 2.0787(2)$ Å, $a = 13.6230(5)$ Å, $c = 15.0347(98)$ Å, $V = 2416.4(2)$ Å³)

	x/a	y/b	z/c	Occu- pancy	$U_{\text{iso}} / \text{Å}^2$	Multipli city
Si	0.0001(4)	0.2288(3)	0.1022(3)	0.860	0.0033	36
Al	0.0001(4)	0.2288(3)	0.1022(3)	0.140	0.0033	36
O1	0.9063(2)	0.0937(2)	0.1153(4)	1	0.0316	18
O2	0.9707(4)	0.3041(4)	0.1667	1	0.0148	18
O3	0.1220(2)	0.2439(4)	0.1295(4)	1	0.0186	18
O4	0	0.2658(4)	0	1	0.0238	18
Cu1	0	0	0.115(2)	0.25(1)	0.002	6
Cu2	0.922(5)	0.729(5)	0.574(4)	0.047(4)	0.0205	36
Cu3	0	0	0.202(7)	0.10(1)	0.0345	6
D1	0	0	0.285(7)	0.12(2)	0.0890	6
D2	0.067(5)	0.134(9)	0.338(8)	0.08(1)	0.1257	18
D3	0	0	0.36(1)	0.10(1)	0.1283	6

A.4 XRD Analysis of Cu(I)-SSZ-13 (Si/Al = 12) Sample

Cu(I)-SSZ-13 (Si/Al = 12) sample prepared by exchanging Cu(I) in acetonitrile solution has been characterized by using a Phillips X'Pert diffractometer equipped with a Cu K α source ($\lambda = 1.5418 \text{ \AA}$).

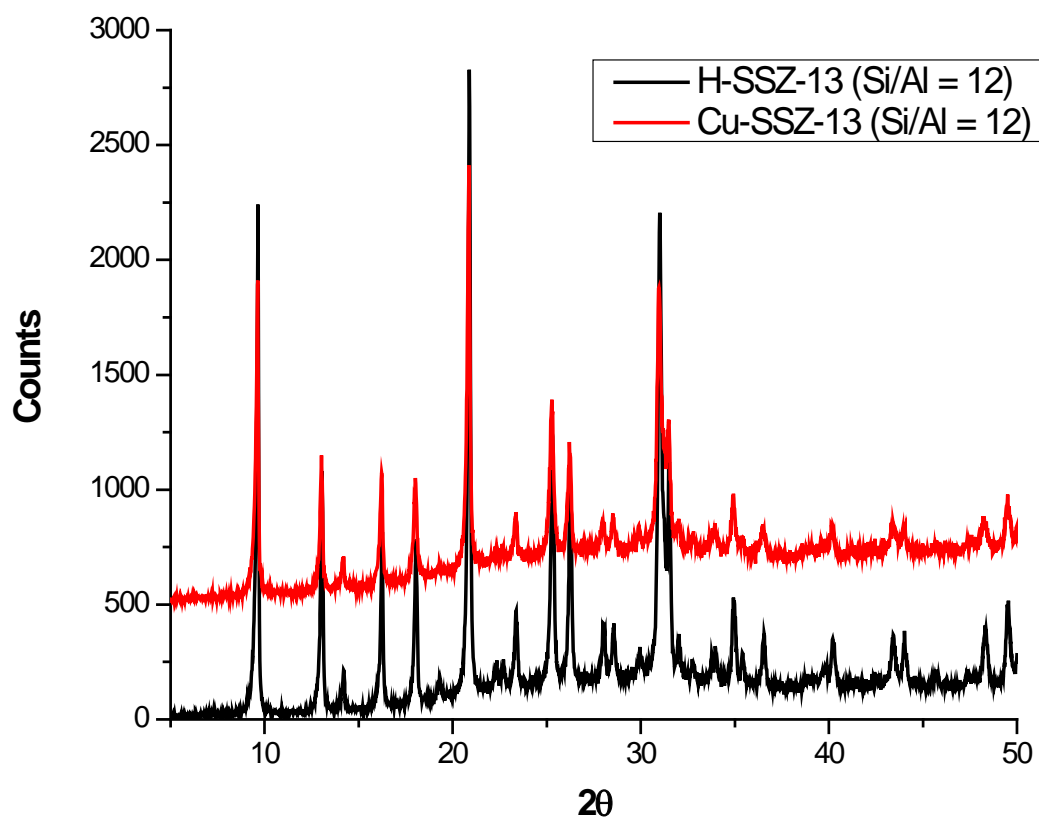


Figure A.4: Powder XRD pattern of H-SSZ-13 (Si/Al = 12), Cu-SSZ-13 (Si/Al = 12) samples, Cu K α , $\lambda = 1.5418 \text{ \AA}$. Samples were exposed to air during XRD data collection.

Appendix B

Cu(II) EXCHANGED SAMPLES FOR METHANOL FORMATION

B.1 Cu(II) Acetate Concentration Calibration for UV-vis Spectroscopy

A calibration curve was obtained for concentration of Cu(II) acetate solutions in de-ionized water. Solutions of Cu(II) acetate with concentrations ranging between 0.001 M and 0.02 M have been prepared using Cu(II) acetate (Aldrich, 98 wt.%). UV-vis spectra were obtained using using UV-vis spectrometer (JASCO, V-5500) and quartz cuvettes on transmission mode. The transmission spectra were converted to absorbance using:

$$Absorbance = -\log_{10} \frac{T}{100}$$

where T is the% transmittance.

A calibration curve of:

$$Concentration (M) = \frac{Absorbance+0.0384}{26.759}$$

has been obtained from linear regression with adjusted R² value of 0.9966 (Figure B.1).

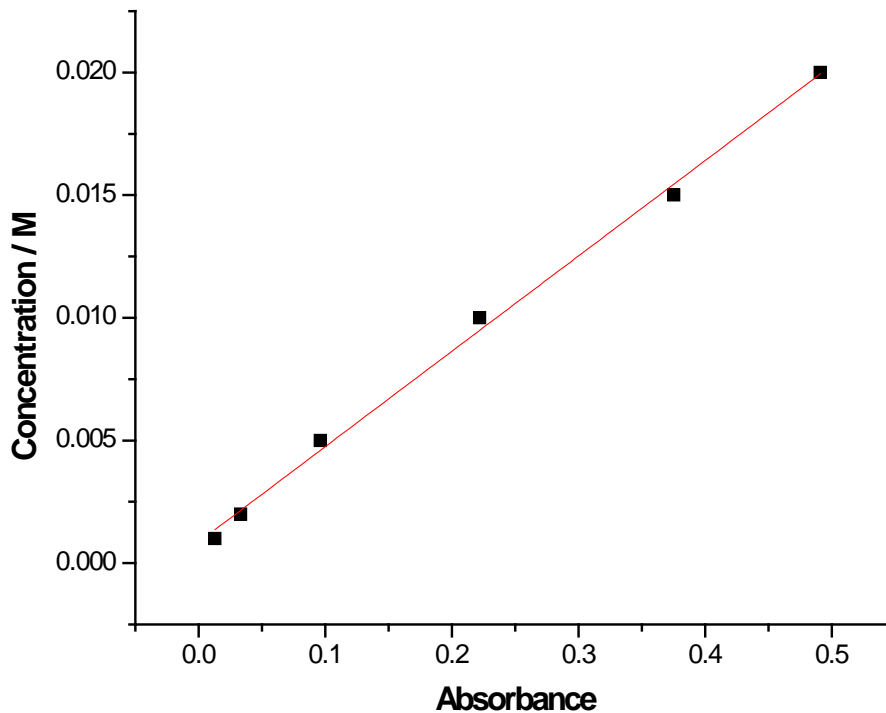


Figure B.1: Absorbance at 776 nm vs Cu(II) acetate concentration least square fitting with a straight line, $R^2_{adj} = 0.9966$

B.2 Methanol Formation on Cu(II)- exchanged Zeolites

Extracted methanol concentration in the effluent stream following the procedure given in Figure 3.1 on Na-Cu- samples (Table 3.2) are given in Figure B.2. The methanol concentration in the effluent stream was calculated from the methanol peak areas obtained in gas chromatogram (from Agilent 6890) using a response factor of 3.42 ppm/area obtained from methanol calibration. Then, the ppm methanol concentration was converted to the micromole of methanol flowing per minute using

0.0022 mol min⁻¹ (50 sccm) N₂ flow. The area under the micromole of methanol per min flow versus time (minutes) graph was calculated to obtain the total micromole of methanol that has been produced.

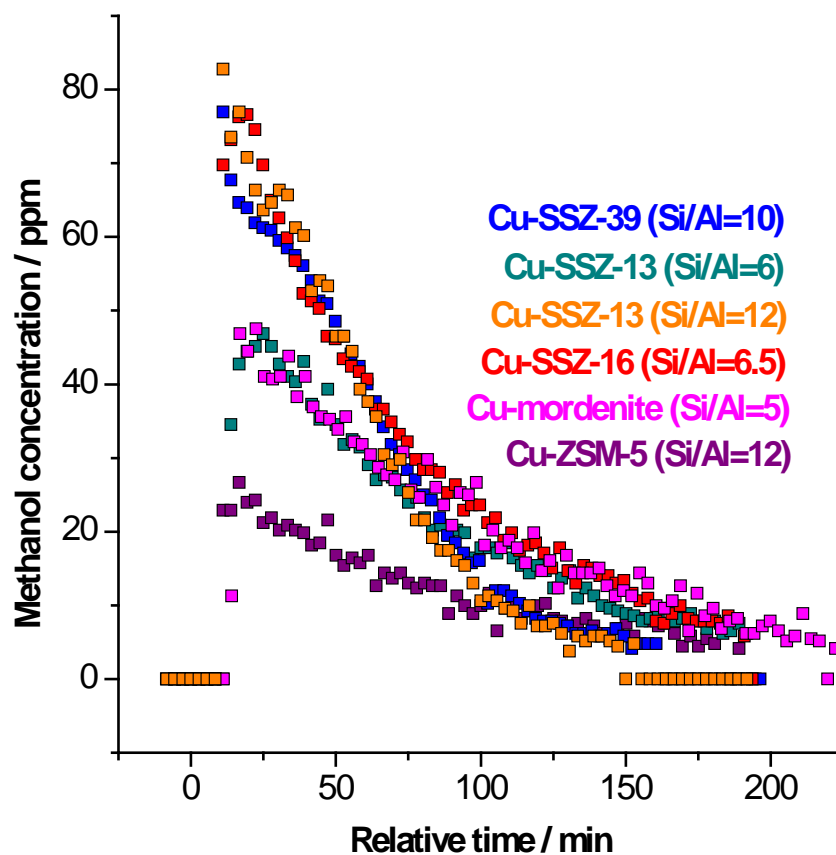


Figure B.2: The concentration of methanol in the effluent stream (obtained from GC) versus time after admission of steam (at time = 0 min) for Cu(II) exchanged samples from Na⁺.

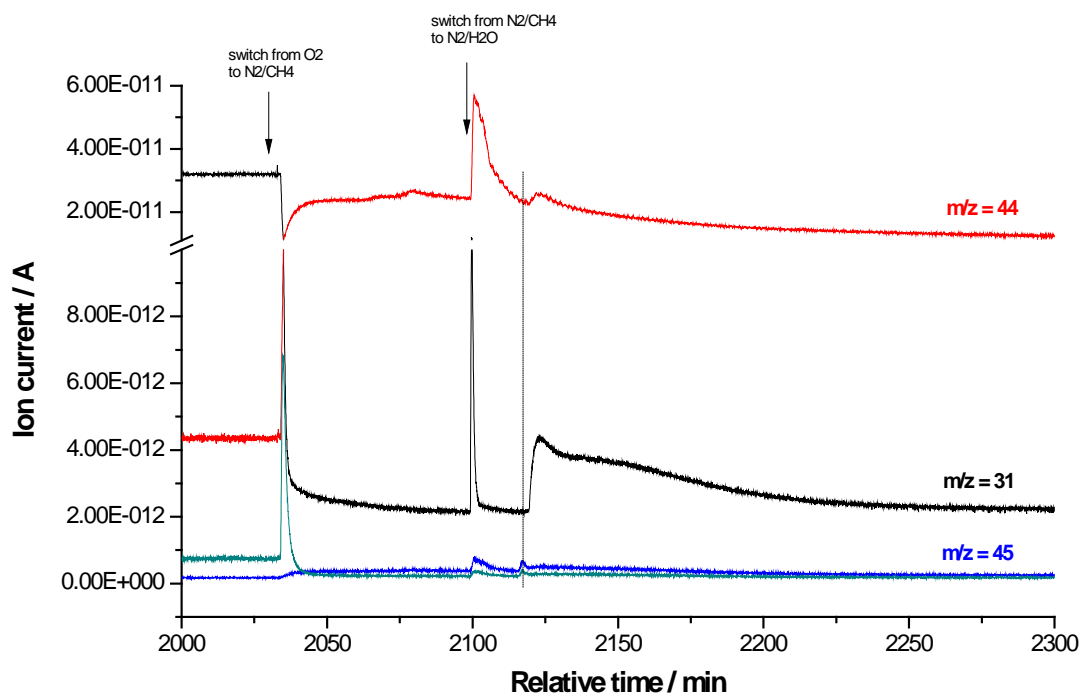


Figure B.3: Ion current versus time (min) obtained from MS analysis of the reactor effluent (for Na-Cu-SSZ-13 (Si/Al = 12, Cu/Al = 0.35)). The dashed line represents the time when the products were started to be observed. $m/z = 44$ is attributed to CO_2 and $m/z = 31$ is attributed to methanol. The produced CO_2 amount is calculated to be $1.6 \mu\text{mol g}^{-1}$ compared to $31 \mu\text{mol CH}_3\text{OH g}^{-1}$ produced methanol, resulting in 95% methanol selectivity.

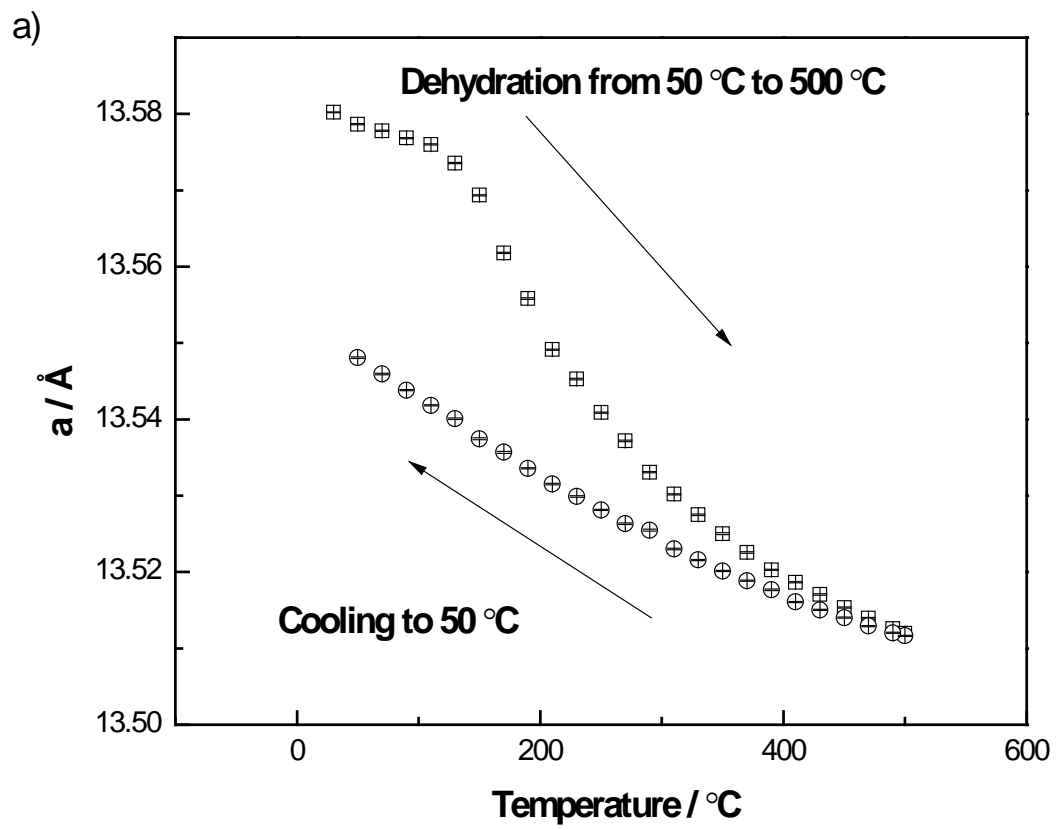
Appendix C

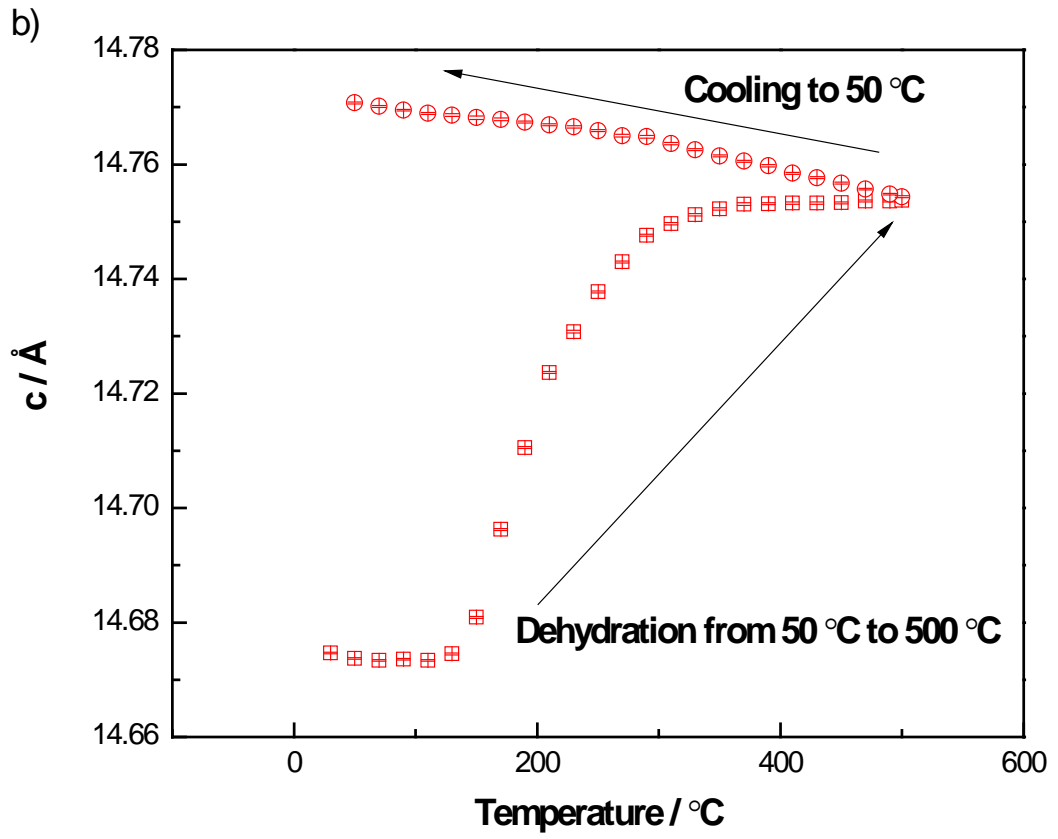
Cu_xO_y CHARACTERIZATION ON Cu-SSZ-13 AND Cu-SSZ-39

C.1 Synchrotron Powder X-ray Diffraction of Cu-SSZ-13

Table C.1: Atomic Parameters from Rietveld refinement of H-Cu-SSZ-13 (Si/Al = 12, Cu/Al = 0.4) data [APS, 17-BM-B](Trigonal, R-3m, Goodness of fit parameters $\chi^2 = 8.099$, $R_p = 1.68\%$, $wR_p = 2.24\%$ at 30 °C, $\lambda = 0.75009$ Å, $a = 13.5805(1)$ Å, $c = 14.6748(2)$ Å, $V = 2343.89(4)$ Å³

	<i>x/a</i>	<i>y/b</i>	<i>z/c</i>	Occupancy	$U_{iso}/U_{ani} / \text{Å}^2$	Multiplicity
Si	0.0001(2)	0.2277(2)	0.1047(1)	0.923	0.0258(4)	36
Al	0.0001(2)	0.2277(2)	0.1047(1)	0.077	0.0258(4)	36
O1	0.9024(2)	0.0976(2)	0.1245(3)	1	0.04043	18
O2	0.9805(3)	0.3139(3)	0.1667	1	0.03485	18
O3	0.1194(1)	0.2387(3)	0.1332(3)	1	0.03289	18
O4	0	0.2595(3)	0	1	0.04412	18
Cu1	0	0	0.242(6)	0.033(2)	0.10805	6
Cu2	0.133(1)	0.266(2)	0.371(2)	0.0505(8)	0.10552	18
O5/H ₂ O	0.066(1)	0.131(3)	0.451(4)	0.17(1)	0.15785	18
O6/H ₂ O	0.046(1)	0.092(3)	0.362(3)	0.21(1)	0.17972	18
	U_{11}	U_{12}	U_{13}	U_{22}	U_{23}	U_{33}
O1	0.016(3)	-0.001(4)	-0.006(2)	0.016(3)	0.006(2)	0.078(5)
O2	0.031(3)	0.017(4)	-0.004(2)	0.031(3)	0.004(2)	0.044(5)
O3	0.032(3)	0.018(2)	-0.006(2)	0.037(4)	-0.012(3)	0.031(5)
O4	0.041(4)	0.020(2)	0.008(4)	0.048(4)	0.004(2)	0.041(5)





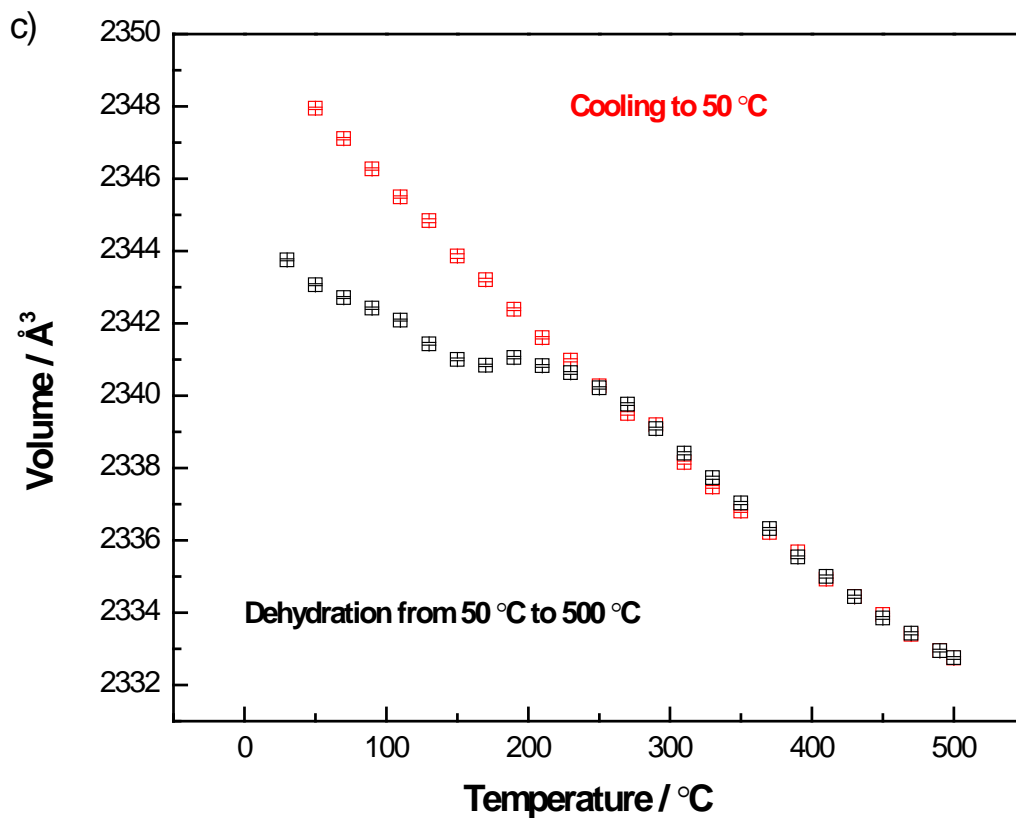


Figure C.1: a) Refined unit cell parameter a and b) unit cell parameter c and c) volume of the unit cell during dehydration and cooling of H-Cu-SSZ-13 (Si/Al = 12, Cu/Al = 0.4) with O₂ flow. (The unit cell parameters were refined with LeBail refinement)

Table C.2: Atomic Parameters from Rietveld refinement of H-Cu-SSZ-13 (Si/Al = 12, Cu/Al 0.4, H_{0.3}Cu_{1.2}Al_{2.7}Si_{33.3}O₇₂) data [APS, 17-BM-B](Trigonal, R-3m, Goodness of fit parameters $\chi^2 = 2.610$, R_p = 1.51%, wR_p = 1.99% at 50 °C, $\lambda = 0.75009$ Å, $a = 13.5494(2)$ Å, $c = 14.7720(2)$ Å, V = 2348.59(8) Å³)

	x/a	y/b	z/c	Occupancy	$U_{iso}/U_{ani} / \text{Å}^2$	Multiplicity
Si	0.0009(2)	0.2276(1)	0.10396(8)	0.923	0.0317(4)	36
Al	0.0009(2)	0.2276(1)	0.10396(8)	0.077	0.0317(4)	36
O1	0.9025(1)	0.0975(2)	0.1216(3)	1	0.04618	18
O2	0.9784(2)	0.3118(2)	0.1667	1	0.03772	18
O3	0.1201(1)	0.2401(3)	0.1323(3)	1	0.04793	18
O4	0	0.2637(3)	0	1	0.04177	18
Cu1	0	0	0.132(2)	0.043(2)	0.03427	6
Cu2	0.047(4)	0.283(5)	0.293(3)	0.0083(6)	0.03977	36
Cu3	0.178 (3)	0.356(5)	0.251(4)	0.013(1)	0.02000	18
	U_{11}	U_{12}	U_{13}	U_{22}	U_{23}	U_{33}
O1	0.024(2)	-0.001(3)	-0.002(1)	0.024(2)	0.002(1)	0.074(5)
O2	0.036(3)	0.021(3)	0.004(1)	0.031(3)	-0.004(1)	0.060(4)
O3	0.027(2)	0.028(2)	-0.012(2)	0.056(4)	-0.023(3)	0.071(6)
O4	0.043(3)	0.021(2)	-0.005(3)	0.047(3)	-0.003(2)	0.034(3)

Table C.3: Atomic Parameters from Rietveld refinement of Cu-SSZ-13 (Si/Al = 5, Cu/Al = 0.39, $H_{1.2}Cu_{2.4}Al_6Si_{30}O_{72}$) data [APS, 17-BM-B] (Trigonal, R-3m, Goodness of fit parameters $\chi^2 = 4.211$, $R_p = 2.52\%$, $wR_p = 3.59\%$ at 50 °C, $\lambda = 0.75009 \text{ \AA}$, $a = 13.4932(5) \text{ \AA}$, $c = 15.1027(7) \text{ \AA}$, $V = 2381.3(2) \text{ \AA}^3$)

	x/a	y/b	z/c	Occupancy	$U_{iso}/U_{ani} / \text{\AA}^2$	Multiplicity
Si	0.0000(4)	0.2285(3)	0.1006(3)	0.8333	0.039(1)	36
Al	0.0000(4)	0.2285(3)	0.1006(3)	0.1667	0.039(1)	36
O1	0.9079(5)	0.0921(5)	0.1128(7)	1	0.07604	18
O2	0.9738(5)	0.3072(5)	0.1667	1	0.03986	18
O3	0.1213(4)	0.2425(7)	0.1269(7)	1	0.06077	18
O4	0	0.2703(6)	0	1	0.06782	18
Cu1	0	0	0.121(1)	0.27(1)	0.02911	6
Cu2	0.3333	0.16667	0.16667	0.020(4)	0.02597	9
Cu3	0.182(4)	0.365(8)	0.270(7)	0.017(2)	0.01917	18
Cu4	0.038(8)	0.08(2)	0.152(8)	0.017(4)	0.01505	18
	U_{11}	U_{12}	U_{13}	U_{22}	U_{23}	U_{33}
O1	0.056(6)	0.016(8)	0.005(5)	0.056(6)	-0.005(5)	0.10(2)
O2	0.038(6)	0.024(8)	0.005(3)	0.038(6)	-0.005(3)	0.049(9)
O3	0.058(7)	0.048(6)	0.000(4)	0.01(1)	0.000(9)	0.04(1)
O4	0.11(1)	0.054(6)	0.007(9)	0.087(7)	0.003(5)	0.02(1)

C.2 MAS NMR Spectra

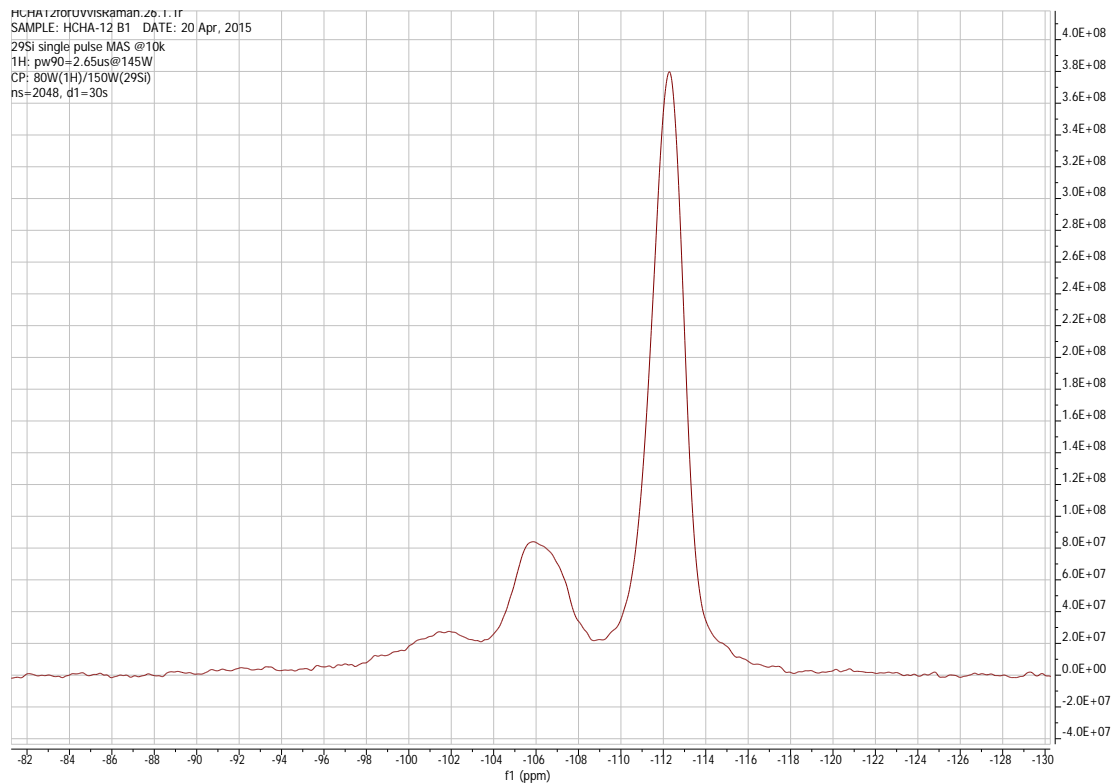


Figure C.2: ^{29}Si single pulse MAS NMR of H-SSZ-13 (Si/Al = 12) obtained at 10 kHz

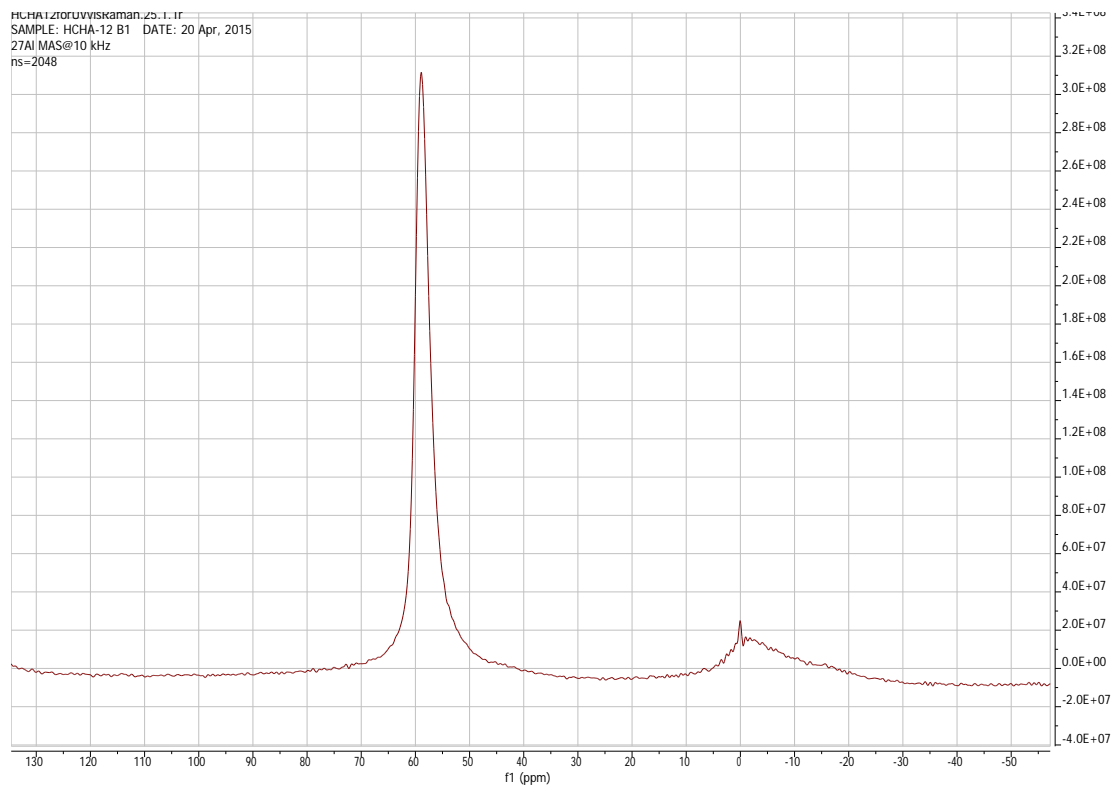


Figure C.3: ^{27}Al single pulse MAS NMR of H-SSZ-13 (Si/Al = 12) obtained at 10 kHz

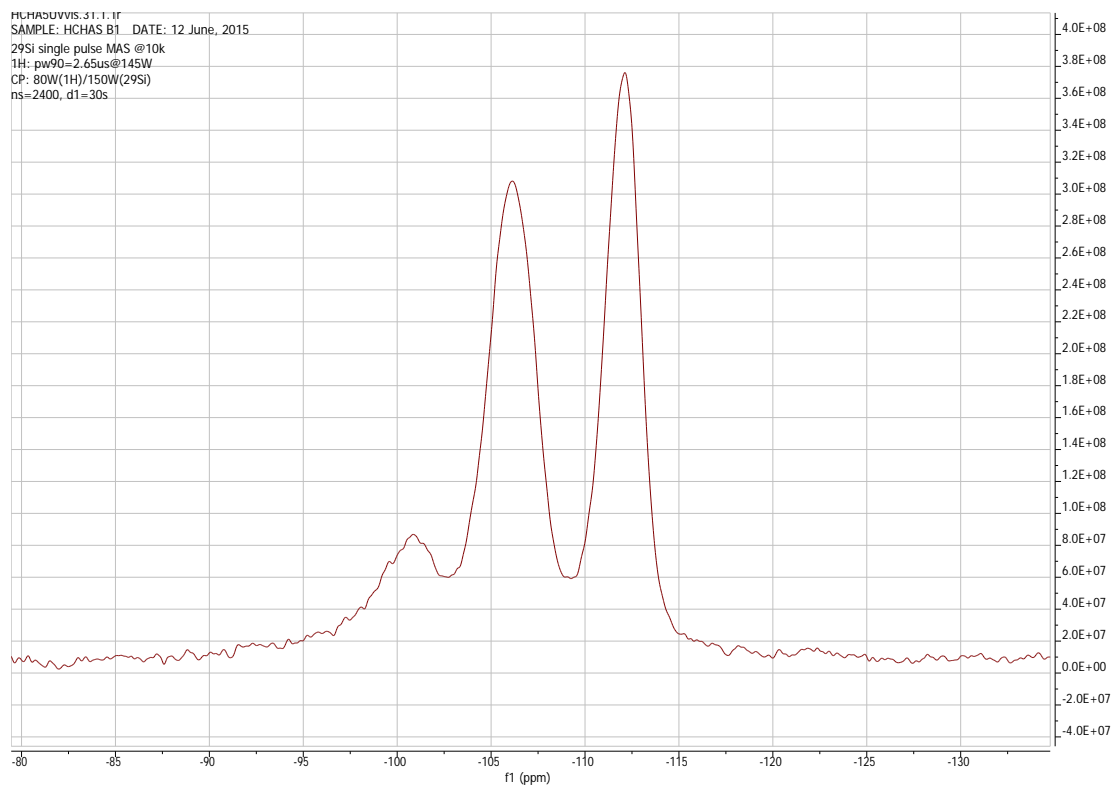


Figure C.4: ^{29}Si single pulse MAS NMR of H-SSZ-13 (Si/Al = 5) obtained at 10 kHz

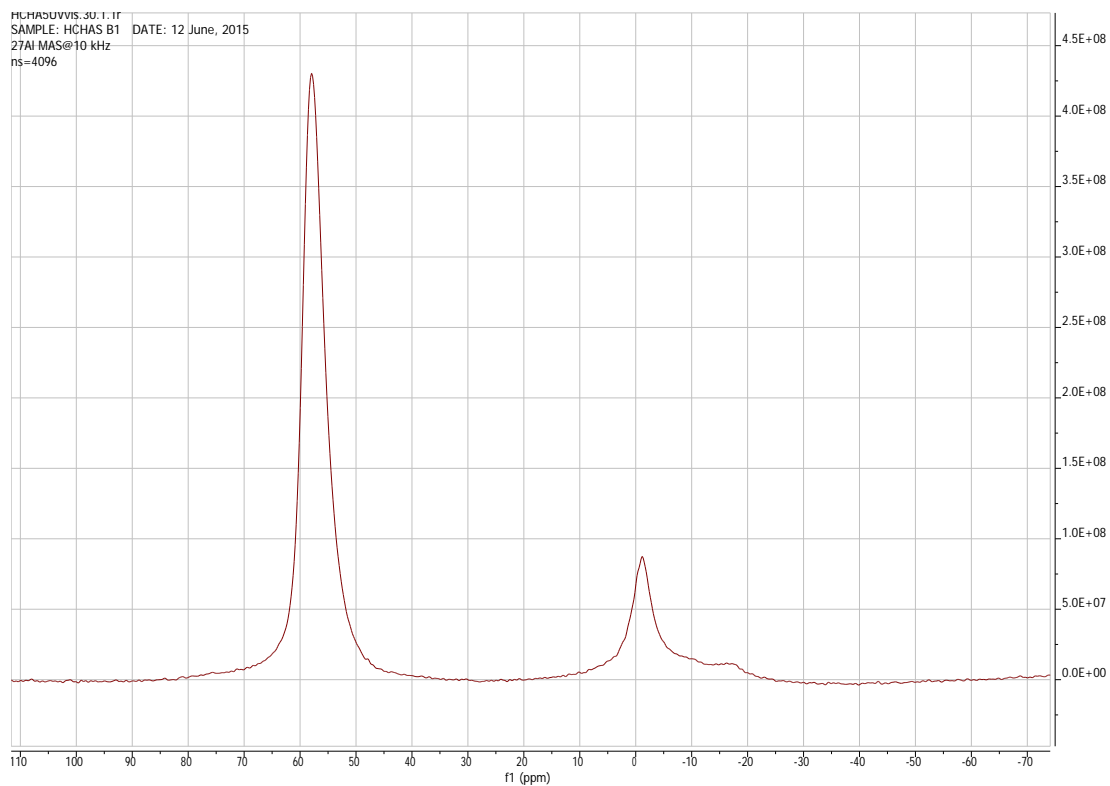


Figure C.5: ^{27}Al single pulse MAS NMR of H-SSZ-13 (Si/Al = 5) obtained at 10 kHz

C.3 DR UV–vis Spectroscopy

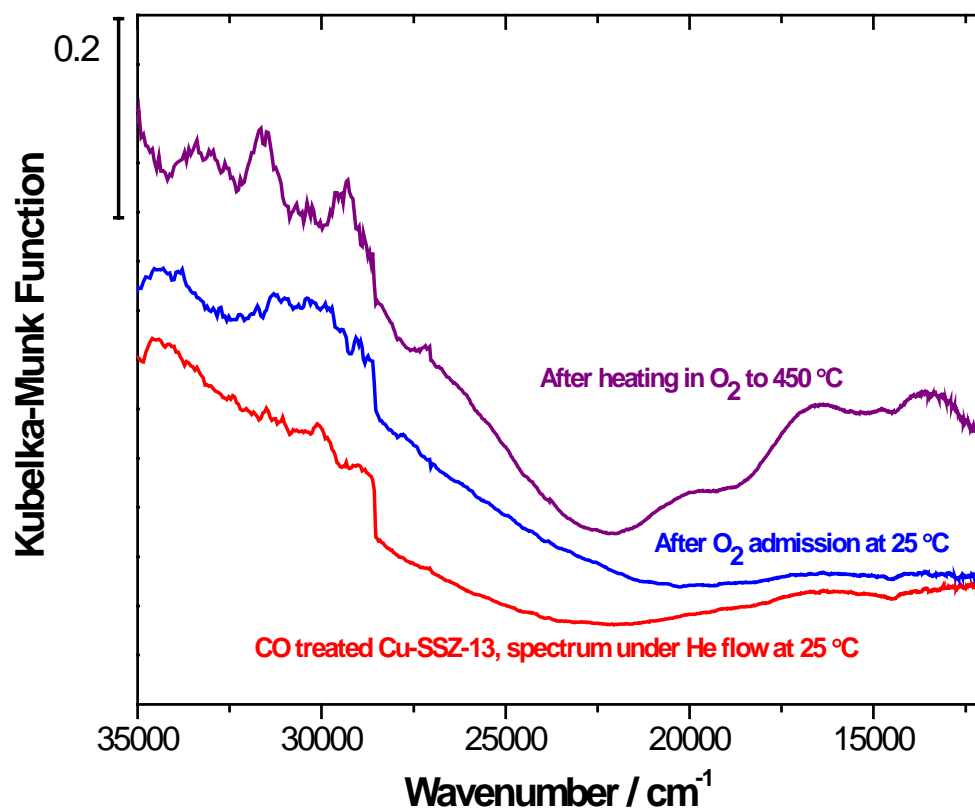


Figure C.6: DR UV–vis spectra before (red spectrum) and after (blue spectrum) O₂ admission for H-Cu⁺-SSZ-13 (Si/Al = 12, Cu/Al = 0.4) as given in Figure 4.13. Purple line is the spectra taken after heating the O₂ exposed sample to 450 °C with 20 cm³ min⁻¹ O₂ flow. The feature observed at 28,500 cm⁻¹ was caused by a lamp switch in the spectrometer.

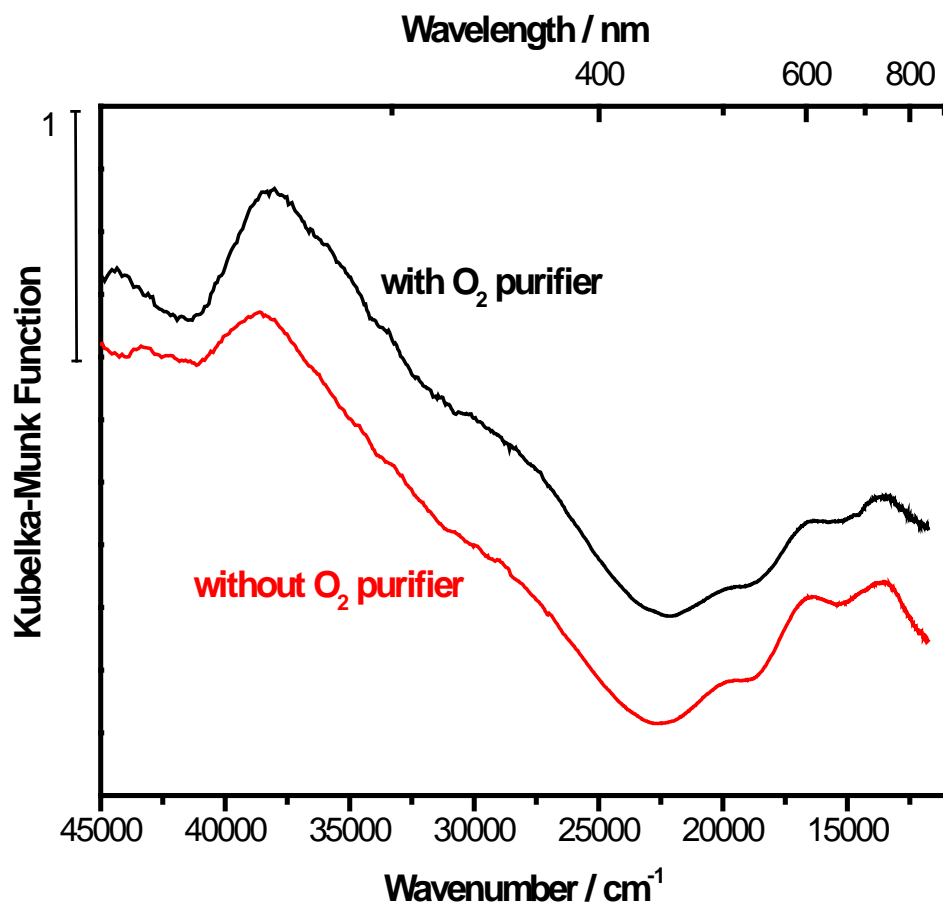


Figure C.7: DR UV-vis spectra with (black spectrum) and without (red spectrum) O₂ purifier for H-Cu-SSZ-13 (Si/Al = 12, Cu/Al = 0.4) treated with 20 cm³ min⁻¹ He flow at 450 °C for 4 h. The spectra are taken at 25 °C under flowing He.

Appendix D

CATALYTIC METHANOL SYNTHESIS ON Cu-SSZ-13

D.1 CH₃OH, CO and CO₂ Calibrations

D.1.1 CH₃OH calibration of GC FID chromatogram

CH₃OH calibration peak areas are obtained on gas chromatograph (GC) (Agilent 7890A) with flame ionization detector and a HP-PLOT Q column (Agilent19091P-Q04, 30 m x 0.32 mm x 0.02 mm) at 140 °C keeping the method the same. Methanol/ toluene solutions having 525 to 2100 ppm of methanol are prepared by adding 2, 4, and 8 µl of methanol in 10 ml of toluene. Then, 1 µl of the solution is injected manually at the injection port of the GC with a splitting ratio of 15:1. The calibration curve for methanol response factor (in ppm area⁻¹ units) is obtained from least square fitting of the data in Figure D.1.

Table D.1: Concentrations of methanol in 10 ml toluene solutions and corresponding peak areas obtained at 1.87 min residence time using HP-PLOT Q column

CH₃OH concentration / ppm	Peak area
525.33	127.3
1050.66	298.85
2101.32	568.05

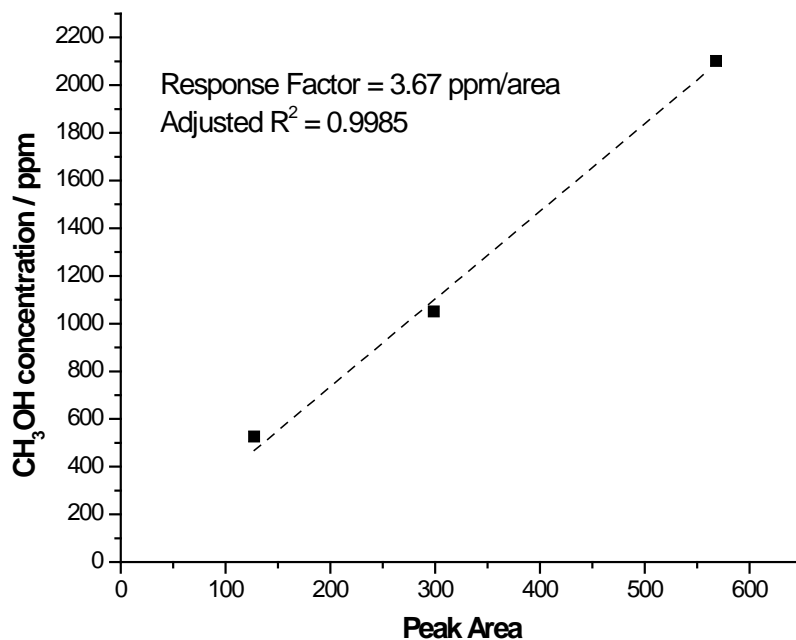


Figure D.1: The concentration of methanol in prepared toluene solutions versus observed methanol peak areas at 1.87 min residence time on HP-PLOT Q column at 140 °C

D.1.2 CO calibration of GC TCD chromatogram

CO calibration peak areas are obtained on gas chromatograph (GC) (Agilent 7890A) with a thermal conductivity detector and a HayeSep Q column (Agilent G3591-81121, 12 ft 1/8" 2 mm) at 140 °C keeping the method the same. The response factor for CO peak (with residence time = 2.243 min) is obtained using single point calibration. An average area of 3370.5 was obtained for 24 cm³ min⁻¹ 5.15% CO (Matheson, 99.999%) flow in He. The corresponding response factor was 15.3 ppm area⁻¹.

D.1.3 CO₂ calibration of GC TCD chromatogram

CO₂ calibration peak areas are obtained on gas chromatograph (GC) (Agilent 7890A) with a thermal conductivity detector and a HayeSep Q column (Agilent G3591-81121, 12 ft 1/8" 2 mm) at 140 °C keeping the method the same. The response factor for CO₂ peak (with residence time = 3.564 min) is obtained using three different concentrations of CO₂ in He (Table D.2). The calibration curve can be seen in Figure D.2.

Table D.2: Concentrations of CO₂ and corresponding peak areas obtained at 3.564 min residence time using HayeSep Q column

CO₂ Concentration / ppm	Peak area
50000	2948.1
24600	1487.3
12705	747.4

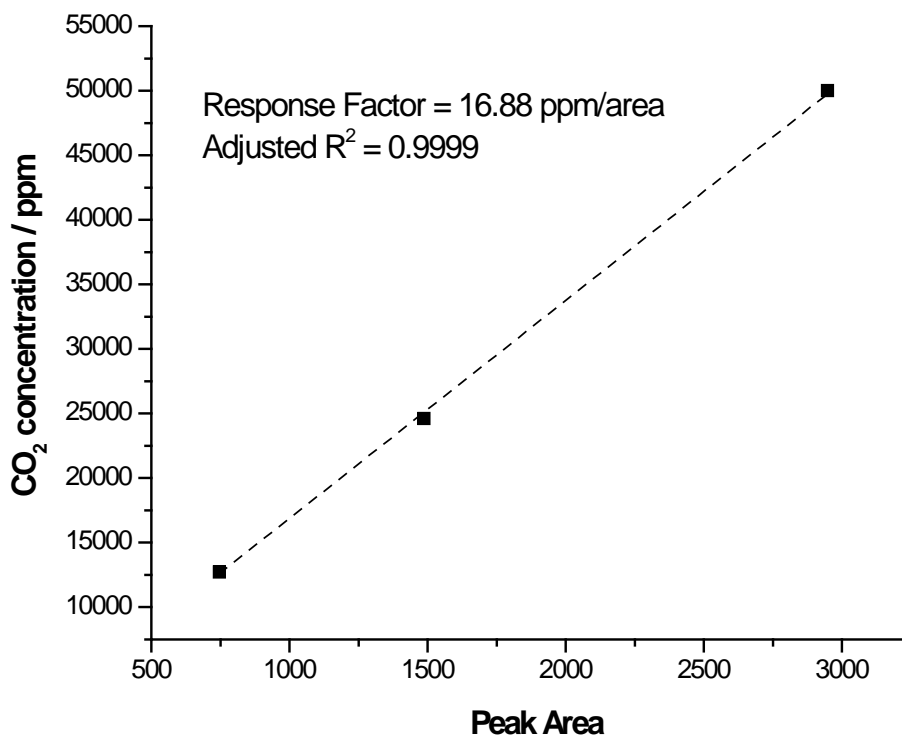


Figure D.2: The concentration of CO₂ on He versus observed CO₂ peak areas at 3.564 min residence time on HayeSep Q column at 140 °C

D.1.4 CO calibration using Mass Spectrometer

CO ($m/z = 28$) ion currents on a mass spectrometer (Pfeiffer OmniStar GSD 320) are calibrated using $18.8 \text{ cm}^3 \text{ min}^{-1}$ 2.4% and 3.7% CO (Matheson, 99.999%) flow in He. The response factor is found to be $24368.98 \text{ mol min}^{-1} \text{ ion current}^{-1}$ for $120 \text{ cm}^3 \text{ min}^{-1}$ flow (Figure D.3). The difference in $m/z = 28$ ion current during reaction are used to calculate CO production rate in mol min^{-1} using this response factor.

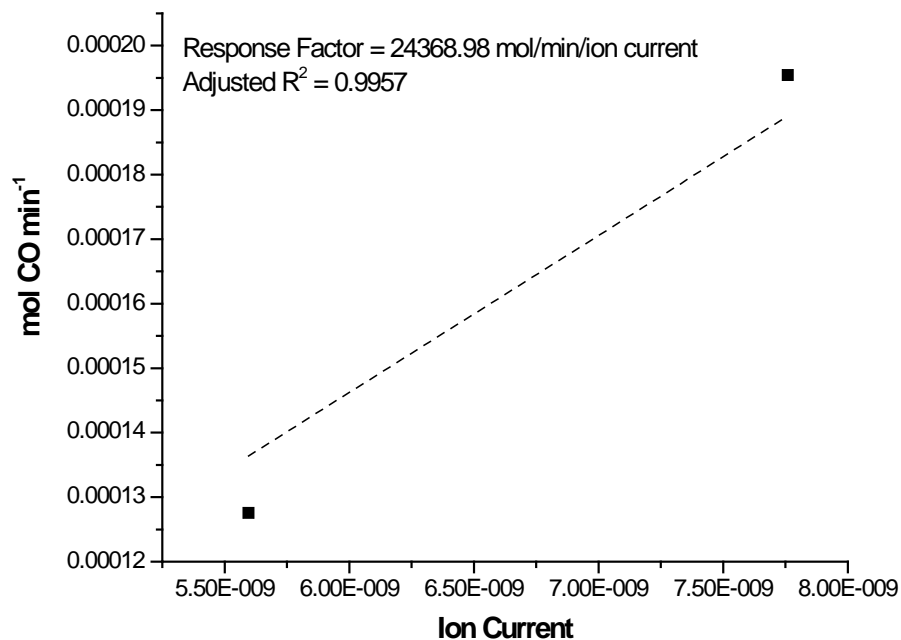


Figure D.3: The molar flow rate of CO assuming 120 cm³ min⁻¹ mixture (CO and He) flow versus Ion Current of Pfeiffer OmniStar GSD 320 mass spectrometer.

D.2 N₂O Treatment of Cu-SSZ-13

Hydrated Cu-SSZ-13 (Si/Al = 12, Cu/Al = 0.4) sample was treated with 5 cm³ min⁻¹ N₂O (Keen Gas, medical purity) and 50 cm³ min⁻¹ He in the reactor set-up as described in Section 3.2.3 as the temperature was increased to 450 °C with a heating rate of 5 °C min⁻¹. The temperature was kept at 450 °C for 2 h. The effluent analysis of the system using a mass spectrometer (Pfeiffer OmniStar GSD 320) showed a sudden decrease in N₂O concentration and relative increase in O₂ and N₂ concentrations for

temperatures higher than 350 °C indicating catalytic decomposition of N₂O into N₂ and O₂.

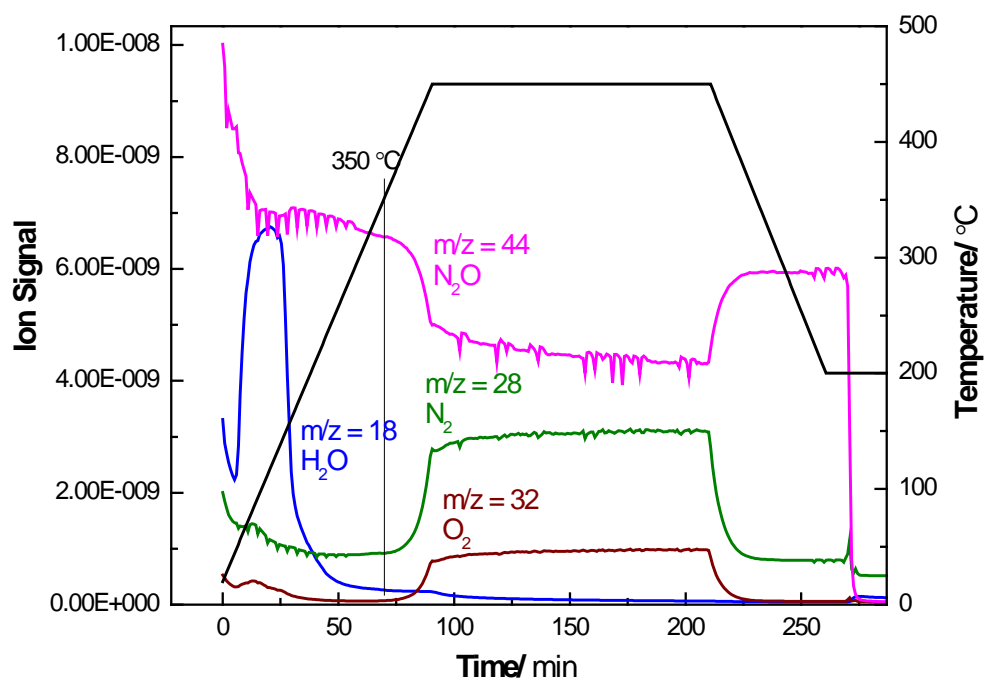


Figure D.4: Mass spectrometer ion current vs time upon 10% N₂O treatment of hydrated Cu-SSZ-13 with a heating rate of 5 °C min⁻¹

D.3 Catalytic Tests

The catalytic methanol production tests were performed as explained in section 5.2.2.3. Obtained chromatogram peak areas have been converted to ppm values using the response factors given in sections D.1.1–1.3. Then, the production rates have been calculated using the molar flow rate ($0.0053 \text{ mol min}^{-1}$) and catalyst weights (Table D.3)

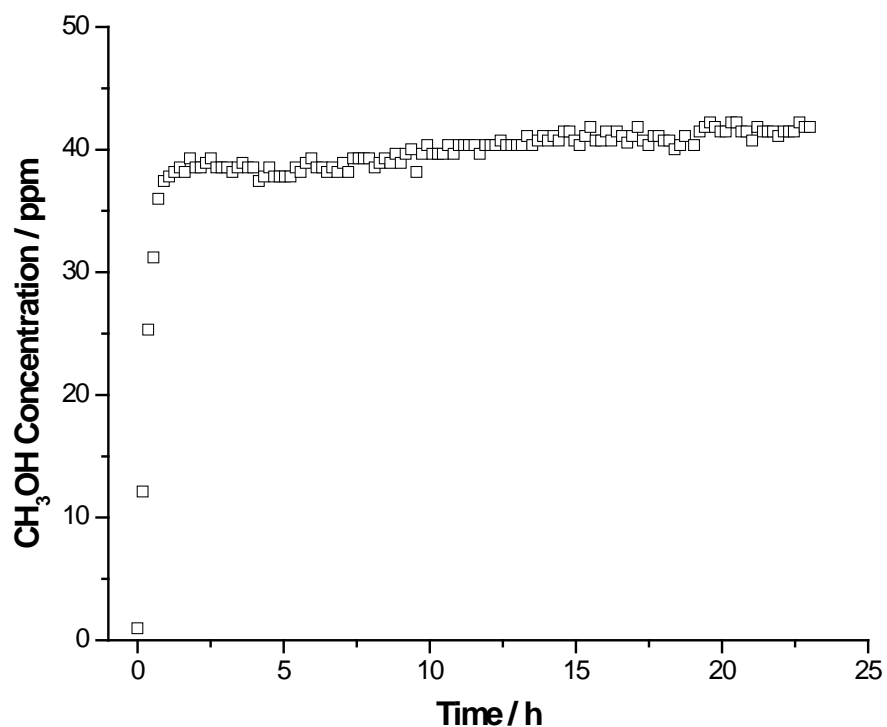


Figure D.5: Steady state concentration of methanol in the exit stream at 270 °C. Feed: 30% CH₄, 30% N₂O, 3% H₂O balance helium; flow rate 120 cm³ min⁻¹, WHSV = 19,650 g_{feed} g_{cat}⁻¹ h⁻¹

Table D.3. Loaded catalyst weights for catalytic methanol production^a

Sample	Reaction Temperature / °C	Catalyst weight (hydrated) / mg	Cu concentration / mmol Cu g ⁻¹	CH ₃ OH rate / μmol CH ₃ OH g ⁻¹ h ⁻¹
Cu-SSZ-13	250	298	0.50	12±1
Cu-SSZ-13	260	299	0.50	19±1
Cu-SSZ-13	265	300	0.50	22±5
Cu-SSZ-13	270	299	0.50	28±1
Cu-SSZ-13	275	300	0.50	34±1
Cu-SSZ-13	300	301	0.50	55±1
Cu-SSZ-13	300 ^b	300	0.50	49±3
Cu-SSZ-13	270 ^c	299	0.50	12±3
Cu-SSZ-13	300 ^c	301	0.50	9±1
Cu-mordenite	270	301	0.94	10±3
Cu-ZSM-5	270	300	0.57	6±1

^a: Reaction conditions: feed 30% CH₄, 30% N₂O, 3% H₂O balance helium; flow rate 120 cm³ min⁻¹, WHSV = 19,650 g_{feed} g_{cat}⁻¹ h⁻¹

^b: Same conditions with ^a except 20% H₂O instead of 3% H₂O

^c: Same conditions with ^a, 30% O₂ instead of 30% N₂O

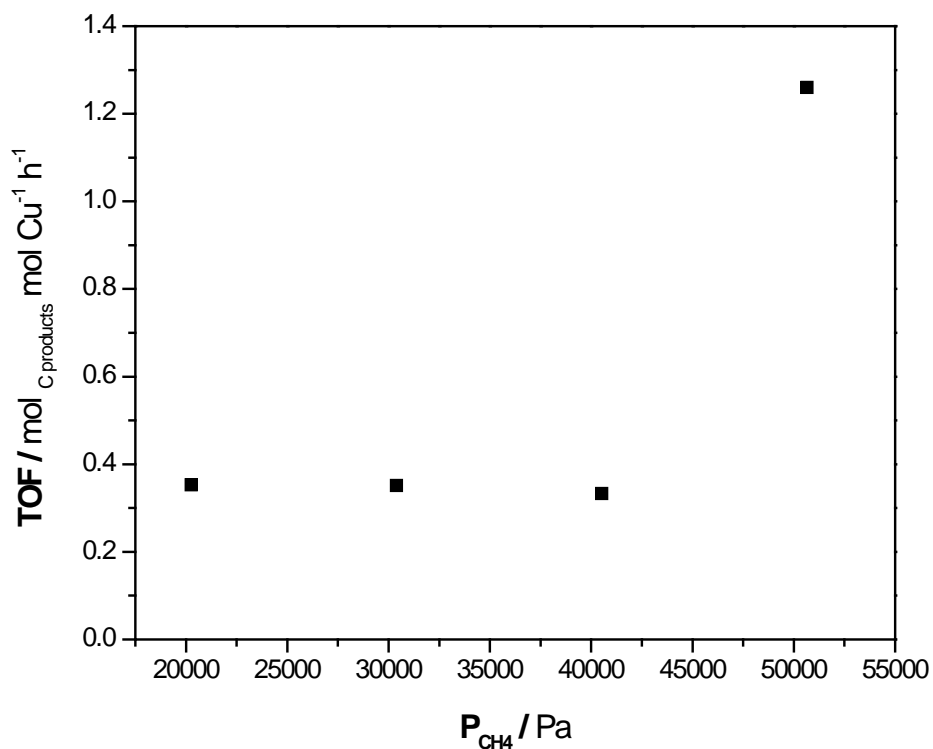


Figure D.6: Methane oxidation rate (mol_{CH₄ converted} mol_{Cu}⁻¹ h⁻¹) versus partial pressure of CH₄ (between at 20265 Pa and 50662 Pa) at 270 °C on Cu-SSZ-13 (feed gas composition: 20– 50% CH₄, 30% N₂O, 3% H₂O, balance He; flow rate: 120 cm³ min⁻¹)

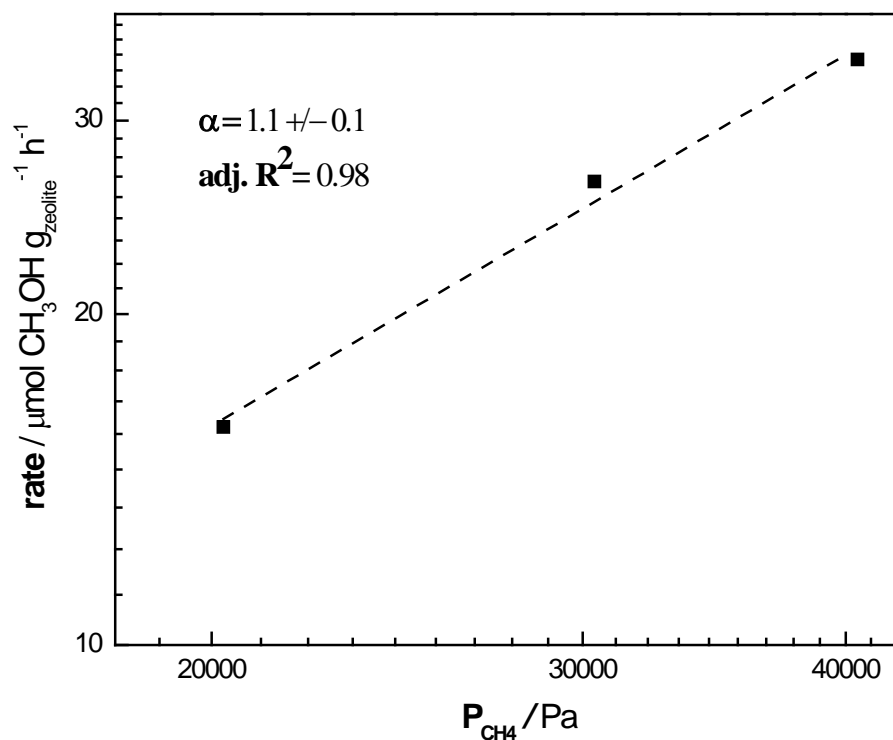


Figure D.7: log-log plot of methanol production rate versus partial pressure of CH_4 (between at 20265 Pa and 40530 Pa) at 270 °C on Cu-SSZ-13 (feed gas composition: 20– 40% CH_4 , 30% N_2O , 3% H_2O , balance He; flow rate: $120 \text{ cm}^3 \text{ min}^{-1}$). The order is calculated based on : $r_{\text{CH}_3\text{OH}} =$

$$k_{app} P_{\text{CH}_4}^\alpha P_{\text{N}_2\text{O}}^\beta$$

Table D.4: Effect of methane partial pressure on methane conversion (TOF: mol_{CH₄} converted mol_{Cu}⁻¹ h⁻¹) and methanol production rates at 270 °C on Cu-SSZ-13 (Cu concentration : 0.50 mmol Cu g⁻¹), feed gas composition: 20–50% CH₄, 30% N₂O, 3% H₂O, balance He; flow rate: 120 cm³ min⁻¹

CH₄ Partial Pressure / Pa	CH₃OH rate / μmol CH ₃ OH g ⁻¹ h ⁻¹	CO rate / μmol CO g ⁻¹ h ⁻¹	CO₂ rate / μmol CO ₂ g ⁻¹ h ⁻¹	CH₃OH Sel / %	TOF / h⁻¹
20265	16.6±0.7	125±3	34±5	9	0.353
30400	28±1	124±12	22±3	16	0.351
40530	33.7±0.8	109±10	22±5	20	0.333
50660	57.0±0.6	510±120	59±15	9	1.260

Table D.5: Effect of N₂O partial pressure on methane conversion (TOF: mol_{CH₄} converted mol_{Cu}⁻¹ h⁻¹) and methanol production rates at 270 °C on Cu-SSZ-13 (Cu concentration : 0.50 mmol Cu g⁻¹), feed gas composition: 30% CH₄, 3–30% N₂O, 3% H₂O, balance He; flow rate: 120 cm³ min⁻¹

N₂O Partial Pressure / Pa	CH₃OH rate / μmol CH ₃ OH g ⁻¹ h ⁻¹	CO rate / μmol CO g ⁻¹ h ⁻¹	CO₂ rate / μmol CO ₂ g ⁻¹ h ⁻¹	CH₃OH Sel / %	TOF / h⁻¹
3040	27.2±0.7	50±12	34±5	26	0.208
10133	26.7±0.5	87±12	22±3	20	0.288
20265	32±1	128±10	22±5	18	0.393
30400	28±1	124±12	22±3	16	0.351

D.4 DR UV-vis Spectra After CH₄ Treatment Cu-SSZ-13

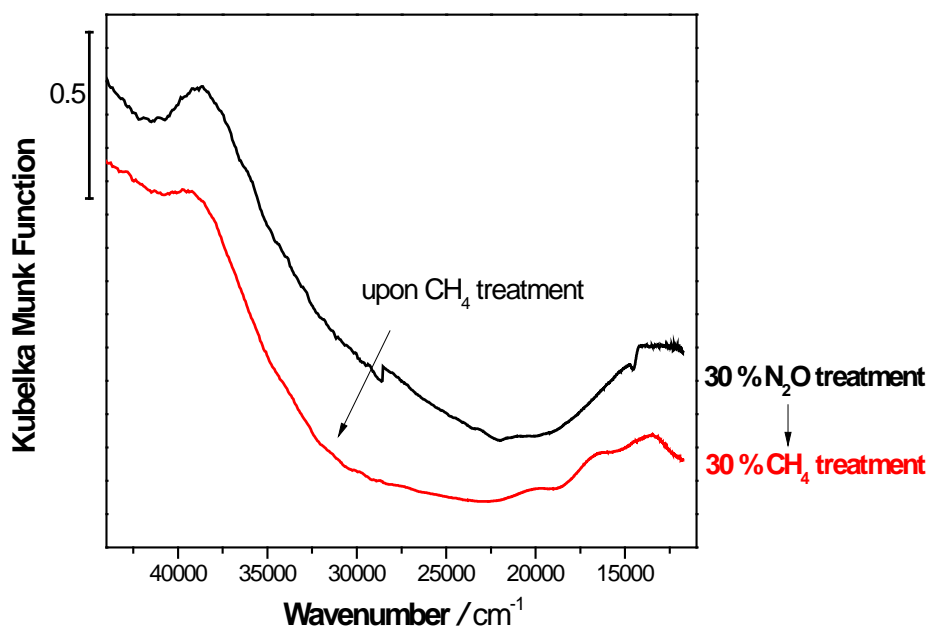


Figure D.8: Diffuse reflectance UV-vis spectra of Cu-SSZ-13 (Si/Al =12) following 2 h 30% N₂O/He treatment at 270 °C (black) followed by 1 h 30% CH₄/He treatment at 270 °C (red). Before each spectrum was collected, the quartz sample holder was cooled to room temperature with continuing N₂O/He or CH₄/He flow

Appendix E

PERMISSIONS

Some of the work in Chapter 3 have been reproduced from Wulfers, M. J.; Teketel, S.; Ipek, B.; Lobo, R. F. *Chem. Commun.* **2015**, *51*, 4447–4450. The webpage related to the Licences, Copyright and Permissions of the Royal Society of Chemistry (<http://www.rsc.org/journals-books-databases/journal-authors-reviewers/licences-copyright-permissions/#reuse-rsc-third-party>, accessed on July 2016) states as below:

Rights retained by authors

When the author accepts the exclusive licence to publish for a journal article, he/she retains certain rights that may be exercised without reference to the Royal Society of Chemistry.

Reproduce/republish portions of the article (including the abstract).

Photocopy the article and distribute such photocopies and distribute copies of the PDF of the article for personal or professional use only (the Royal Society of Chemistry makes this PDF available to the corresponding author of the article upon publication. Any such copies should not be offered for sale. Persons who receive or access the PDF mentioned above must be notified that this may not be made available further or distributed.).

Adapt the article and reproduce adaptations of the article for any purpose other than the commercial exploitation of a work similar to the original.

Reproduce, perform, transmit and otherwise communicate the article to the public in spoken presentations (including those that are accompanied by visual material such as slides, overheads and computer projections).

The author(s) must submit a written request to the Royal Society of Chemistry for any use other than those specified above.

All cases of republication/reproduction must be accompanied by an [acknowledgement](#) of first publication of the work by the Royal Society of Chemistry, the wording of which depends on the journal in which the article was published originally. The acknowledgement should also include a hyperlink to the article on the Royal Society of Chemistry website.

The author also has some rights concerning the deposition of the whole article.